Simple quantum-mechanical models for defects in titanium and iron—how far can they take us?

Tigany Noor Abubaker
Tigany Zarrouk
Department of Physics
King's College London

A thesis submitted in partial fulfilment of the requirements for the degree of Doctor of Philosophy at King's College London.

May 2022

Acknowledgements

I'd like to thank, first and foremost, my first supervisor Prof. Tony Paxton, for all of his guidance, patience and belief in the project. I am grateful for the support from my second supervisor Prof. Andrew Horsfield during this time, in addition to Lev Kantorovich for helping me in the latter stages.

Rolls-Royce for sponsorship and support, with thanks to Dave Rugg for the belief in the project and special thanks to Nigel Martin who was a wonderful supervisor during my time at Elton Road. I also give thanks to Kate Fox, Anna Radecka, Chris Collins and Christos Argyrakis who supported me before, and during, my time there.

Sebastián Echeverri Restrepo and Predrag Andric of SKF for their continued help and stimulating discussions both during and after my internship in the Netherlands.

Miguel Caro for hosting me at Aalto University in Finland, and the HPC-Europa 3 scheme, especially Marina Bouianov and Atte Sillanpää for organising and coordinating the trip.

The following are in no particular order. Alexander Lozovoi for his kindness, patience and meticulousness, the latter of which I am still trying to learn. Luke Simpson, for enduring my incessant questioning, and for his solidarity in being an accident-prone Irishman. Eleftherios Andritsos, whose relaxed spirit still permeates my linux sysadmin style to this day. Ivaylo Katzarov, who reminded me of my own mortality every group meeting. Emilie Gachon, for our continued friendship, coffee breaks and for regaling me with gossip every morning. Martina Ruffino, for being jubilant and lovely, always. Guy Skinner, for being almost too smart. Dimitar Pashov, for being really far too smart, and generous with any help I needed. Jarvist Moore Frost for kindness and support in the first year, and trusting me to hold your offspring.

Also, of course, Rachel Zarrouk, my twin, along with my parents, Doreen and Bakry Zarrouk, for all their support. And my friends who have seen me burn the midnight (scented) oil in the house: Seb, Edmund, Chris, Rinn and Abigail, along with my North-West London friends, Ü.

Publications

The following publications are mentioned in this thesis

- I. H. Katzarov, L. B. Drenchev, D. L. Pashov, T. N. A. T. Zarrouk, and O. Allahham, and A. T. Paxton, "Dynamic strain aging and the role of the Cottrell atmosphere", *Physical Review Materials*, Vol. 6, June 2022.

Abstract

Tight-binding has historically been a method of great importance for predicting properties and gaining insight into transition metals—it explicitly includes quantum mechanical effects, thereby being accurate in comparison to empirical potentials, while circumventing large computational overheads of Density Functional Theory (DFT). This preferential scaling makes it well-suited for the simulation of defects, which can require large simulation cells due to constraints of periodicity and the generation of large strain fields. Modern titanium tight-binding models have so far been lacking in their description of defects compared to DFT. All have had erroneous stacking fault energies, which are necessary for an adequate description of dislocations, the defects which control plasticity in metals. As such, simple tight-binding models of titanium were fitted: a *d*-electron only model, and one with both *s* and *d*-electrons, both of which gave good agreement with bulk properties and energetics of titanium polymorphs in comparison to DFT and empirical data. These models were meshed with a re-fitted polarisable-ion tight-binding parameterisation of titanium dioxide and water, resulting in the first tight-binding model able to describe: bulk Ti, TiO_2, TiH_2, H_2O and H_2. This combined model was used to simulate oxygen/hydrogen dissolution in titanium and adsorption of water on titanium, the results of which agreed well with DFT, testing model transferability. This model allows for many applications, such as novel electrochemical simulations within tight-binding. The correct ordering of stacking fault energies in hcp Ti was successfully reproduced by the titanium models, but relaxations of the $\frac{1}{3}\langle 1\bar{2}10\rangle$ screw core found a larger prismatic spreading, with exhibition of a reduced number of metastable core structures compared to DFT. The predicted prismatic Peierls stress was, however, in agreement with experiment. Oxygen-dislocation interactions were investigated to provide insight into the large strengthening effect of oxygen in titanium, at more realistic concentrations. A new mechanism for jog formation was found, which was in agreement with *ab-initio* γ-surface data. This new mechanism could explain the observation of increased slip planarity and frequency of jog formation with oxygen content in titanium. Further

investigations were made in a tight-binding parameterisation describing iron and carbon, to understand potential mechanisms of dislocation-assisted carbon migration, as theorised in bearing steels. This was achieved by a multi-scale modelling approach, involving a line-tension model, which was parameterised on tight-binding simulations of the 2d Peierls potential exhibited in bcc iron, and carbon-dislocation interactions. This model was able to show a reduction of the kink-pair formation enthalpy of dislocations as a function of carbon content and stress, resulting in carbon-enhanced localized plasticity, surprisingly to a lesser degree than the effect shown by hydrogen in iron. Tight-binding was able to reproduce the stabilisation of the metastable hard-core, which is not apparent in empirical potentials, and it was shown that this hard dislocation core is the most likely to be exhibited, even in high-purity iron, due to the large binding energy of carbon to the screw core. Furthermore, carbon diffusion barriers around the hard core were shown to be greatly reduced compared to that of bulk diffusion, thereby validating a mechanism for dislocation-assisted carbon migration in iron and bearing steels; in addition to explaining the softening effect of carbon on the temperature dependence of the flow stress. The aforementioned calculations push what can be achieved with simple tight-binding models, in terms of scalability and transferability, allowing for many novel simulations to be attempted using an explicit description of quantum mechanics.

List of Abbreviations

ACE	Atomic Cluster Expansion
BOP	Bond-order potential
CI-NEB	Climbing-image nudged-elastic band
CRSS	Critical resolved shear stress
DER	Dark-etching region
DFT	Density Functional Theory
EAM	Embedded-atom Method
GAP	Gaussian-approximation Potential
ISM	Interstitial shuffling mechanism
LCAO	Linear combination of atomic orbitals
MEAM	Modified Embedded-Atom Method
MEP	Minimum energy path
NEB	Nudged-elastic band
PITB	Polarisable-ion tight-binding
RCF	Rolling cycle fatigue
SCTM	Self-consistent charge transfer model
TB	Tight-binding
WEB	White-etching band

Table of contents

List of figures

List of tables

Chapter 1

Introduction

1.1 Titanium

Titanium is a ubiquitous metal. Its alloys are used in many applications: from aerospace, due to its high strength-to-weight ratio, toughness and temperature resilience; to biomedical applications, due to corrosion resistance from the TiO_2 oxide layer and a biocompatible bulk modulus [1].

The alluring properties of titanium are mainly due to its allotropes, of which the most desirable phases are the hcp (α) phase and the bcc (β) phase. In high purity titanium, the hcp phase is found at low temperatures, with transition to the bcc phase occurring at temperatures above the β-transus, $\sim 885°C$ in pure Ti, where it is dynamically stabilised by entropic contributions [2]. ω is a brittle titanium phase, observed at high pressure. It can be formed from a martensitic transformation of the β phase due to the collapse of two (111) planes, which can proceed near the speed of sound, interfering with the desired ductility of β alloys [3, 4]. Other phases, such as fcc (γ) and δ (distorted bcc) have been observed at high pressure [5, 6].

Understanding the motion of *dislocations* is paramount to understanding plasticity in metals. Dislocations are line defects in the crystal structure of a material, characterised by a Burgers vector $\mathbf{b}$. These defects allow for the slip of a crystal along a plane at a reduced shear stress: for a dislocation to propagate slip, only a line of atomic bonds need to be broken, rather than a whole plane [7]. They are therefore the mediators of plasticity. There are two extremal characters of dislocations: edge and screw. Edge components generally have a high mobility, hence it is the *screw* components which control plasticity. The dislocation core is the centre of the defect (around $1b$ in radius) which accommodates most of the deformation. The displacements found

in the core region form the *core structure* of the dislocation, which dictates how the dislocation can move. Different planes have different resistances to dislocation motion, due to the accommodation of deformation in distinct local atomic environments. Screw dislocations can change the plane on which they move: they undergo cross-slip, whereas edge dislocations are confined to slip in their glide plane. The theory of dislocations will be described in more detail in section 2.6.

The hcp crystal structure has four slip planes: basal (B, $\{0001\}$), prismatic (P, $\{10\bar{1}0\}$), first-order pyramidal plane (π_1, $\{10\bar{1}1\}$) and second-order pyramidal plane (π_2, $\{11\bar{2}2\}$, as seen in figure 1.1.

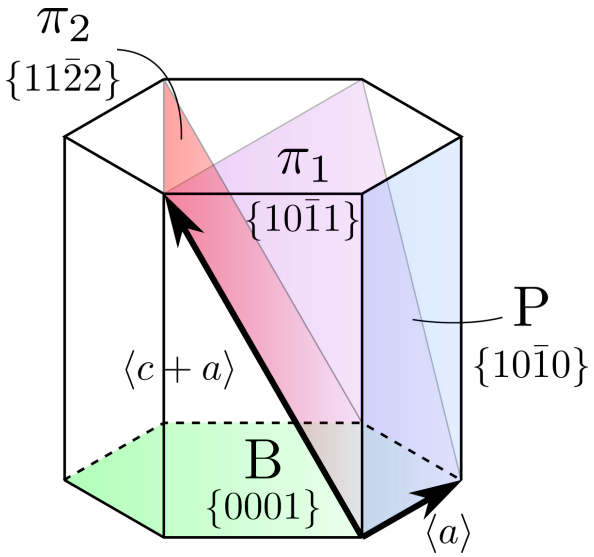

Fig. 1.1: Diagram of planes in hcp showing the Burgers vectors of $\mathbf{b} = \langle a \rangle$ and $\mathbf{b} = \langle c+a \rangle$ dislocations.

The von Mises criterion states that five independent slip systems are necessary for deformation in a crystal which preserves volume [7]. Enumerating the independent slip modes for the slip systems of an $\mathbf{b} = 1/3\langle 1\bar{2}10 \rangle = \langle a \rangle$ dislocation, one finds only four independent slip systems. As such, other deformation modes, notably twinning modes, are necessary to be activated, for adherence to the constraint of compatibility. Deformation twinning is the accommodation of shear such that the crystal structure is mirrored along the twin plane. The bcc crystal has 12 independent slip systems, which confers the high ductility of β titanium to that of α.

With the addition of alloying elements, the α and β phases can be stabilised. For α phase, C, N, O and Al act as stabilisers, whereas the β phase is stabilised by, H and larger elements, which are mainly substitutional, such as V, Mo, Cr.

By variation of the alloying content, solution temperatures, cooling rates, amount of work, ageing and other process parameters, α, $\alpha + \beta$ and β phase alloys can be created. The variation of the resulting microstructure is complex, and can be tailored to the application of its use. The interfaces between the α and β phases are barriers to the motion of dislocations, and play an important role in the yield strength of the alloy, hence the microstructure of the material is a vital consideration.

Many alloys are worked in the β/α-β phase field to give a small β grain size, to increase hardness of resulting grains on crystallisation by Hall-Petch strengthening: smaller grains increase strength due to a reduced probability of dislocation pile-ups on grain boundaries. The primary α precipitates from the β phase as laths [8], which are formed in a Burgers orientation relationship with the β phase. Slow and fast cooling rates can form colonies of α phase or basket-weave structures. If worked, the α phase colonies can be broken up, becoming equiaxed, allowing for a more random grain orientation distribution in the polycrystal. Depending on solute content of the alloy, one can find secondary and tertiary α which are interspersed in the fine β between the primary α laths, which can form from ageing and recovery respectively, which enhance the strength of the material by Hall-Petch strengthening. Grain boundary α precipitates between prior β grains, which are known to be crack initiation sites [9]. Fractures have been seen to arise from conditions which enhance planar slip and strain localisation from dislocation movement, which are found in the α phase with oxygen content [1]. As cracks have been seen to initiate in the α phase, we will mainly consider the effects of dislocations in this phase hereon, with the effect of oxygen being addressed later, both of which are pertinent to the simulations performed in this thesis.

HCP metals are generally thought to obey the Schmid law [10]

$$\sigma_n = \sigma_0 \cos\phi \cos\xi = \sigma_0 m, \tag{1.1}$$

where plasticity by slip is initiated when the resolved shear stress on a given plane, σ_n, from an applied tensile stress σ_0, reaches a critical value [11]. The factor $m = \cos\phi\cos\xi$ is the Schmid factor, where the angles ϕ and ξ are both measured from the tensile axis to a vector in the slip plane, or to the slip plane normal respectively. This law was verified by Schmid and Boas for hcp metals which preferentially slip on the basal plane, such as Md, Cd and Zn. However, in titanium, the Schmid law has been observed to fail. This was detailed by Naka *et al.* [12], where $\langle a \rangle$ screw dislocations—the primary active dislocations in titanium—were found to cross-slip

from the prismatic to π_1 planes at temperatures of 300-500K, suggesting a pyramidally spread core structure can exist at these temperatures, as theorised by Šob *et al.* [13]. Akhtar [14] found basal slip and twinning in single crystals with failure of the Schmid law, in agreement with recent work by Barkia *et al.* [15]. As suggested by Naka [12], the failure of the Schmid law suggests that the Peierls frictional force—the force generated from the *Peierls potential*, the energy landscape which dislocations experience moving through the crystal—can control glide, due to the response of the spread core structure to different stress tensor components [16].

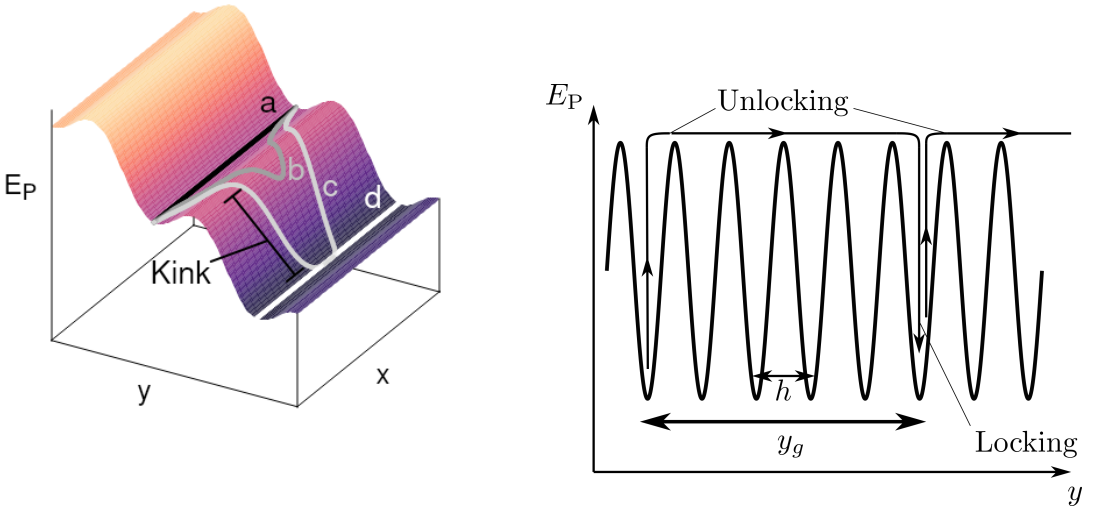

Fig. 1.2: Peierls (kink-pair) mechanism (left) and locking-unlocking mechanism (right) of dislocation glide in hcp titanium, as suggested by Farenc [17–19]. E_P is the Peierls potential. Left: kink-pair mechanism of glide occurs by dislocation overcoming potential, starting from a Peierls valley (a), thermal activation causes dislocation to bulge over Peierls barrier hump (b), with a sufficient activation energy, stable kink-pair is formed (c), causing full transition to next valley on kink migration (d). Application of increasing stress increases the incline of the potential, reducing activation energy for transition. Right: the locking-unlocking mechanism is where sessile, ground-state core, in the Peierls valleys, can gain energy, allowing for transformation to glissile metastable core, found at the peaks. This dislocation core moves quickly a distance y_g, the jump distance, after which it decays back to the sessile ground-state in the Peierls valley. Kink-pair formation is where dislocations traverse a distance h by overcoming the peak of the potential, and falling into the next valley.

Dislocations controlled by frictional forces undergo glide by a *Peierls (kink-pair) mechanism*, see figure 1.2, left. In this mechanism, dislocations glide by moving from

an initial valley in the potential (a Peierls valley) to the next. To do this, segments of the dislocation line must overcome the Peierls potential by thermal activation. When a large enough portion of the dislocation line has transitioned over the barrier, a stable kink-pair has formed—which is a critical (saddle point) configuration—after which the dislocation can easily transit to the next valley. The enthalpy change necessary to form this configuration from the initial Peierls valley is the *kink-pair formation enthalpy*. One can think of a dislocation in this potential as a string weighted with beads, which one pulls over the Peierls potential: when enough beads (thermally activated segments) are in the next valley (when a stable kink-pair has formed), the rest of the string will follow over the barrier, causing glide. If there are not enough beads over the barrier, the kink-pair is unstable, so it annihilates, resulting in the dislocation line staying in the original Peierls valley. With application of increasing stress, the activation energy necessary to overcome the potential decreases, and at some critical stress, no activation energy is necessary, which gives the Critical Resolved Shear Stress (CRSS). Farenc *et al.* [17, 18], proposed the jerky glide of screw dislocations between 150-473K is controlled by a locking-unlocking mechanism, as described in figure 1.2, right, where the $\langle a \rangle$ screw dislocation cores change between a metastable glissile prismatic core (unlocking) and ground-state pyramidal sessile core (locking). The metastable core can "skip" over the Peierls potential a certain distance, y_g, before decaying to the ground-state. Each of the aforementioned studies suggest that glide of $\langle a \rangle$ dislocations in titanium mainly occurs on the prismatic plane.

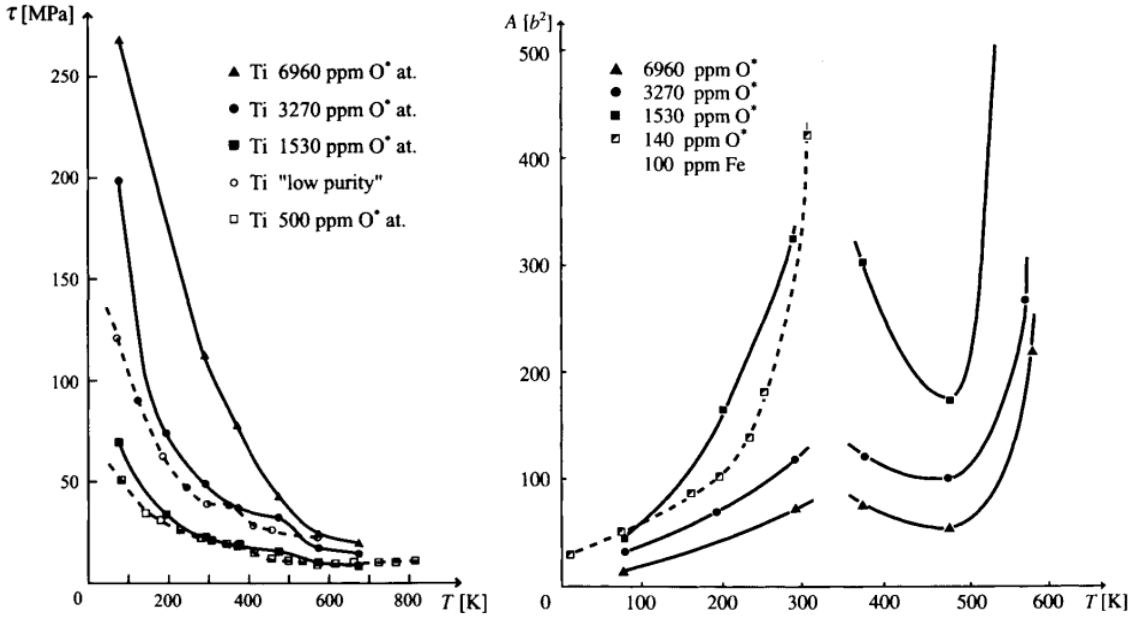

Fig. 1.3: Flow stress and activation area variation with temperature in Ti, oriented for prismatic slip from Caillard [16] with results from various authors [12, 20, 21].

Discontinuities in the temperature dependence of the activation area (the change in Gibbs free energy with respect to change in stress, per unit b) are found in titanium around 300K [12, 16–18, 20], indicating there are different thermally activated mechanisms which act in different temperature ranges, as seen in figure 1.3. Biget and Saada [22] found in very high purity titanium ($\sim$ 50 ppm O*) and at very low temperatures (4K), a σ^{-2} stress dependence of the activation area, which is consistent with the bowing of a dislocation, implying a sessile ground-state core configuration in the low temperature limit. This critical bowing theory was originally proposed by Friedel to explain prismatic cross-slip in hcp metals [23]. Farenc *et al.* [17] suggest this σ^{-2} dependence gives evidence to a locking-unlocking mechanism, initially in opposition that of a Peierls mechanism, where activation areas have a σ^{-1} or $\sigma^{-1/2}$ dependence [18], but later reneged, to include a Peierls mechanism in conjunction with locking-unlocking [17]. This explains the experimental observations of a reduction in dislocation jump distance with increasing temperature (ranging from 150-473K) [16, 17]. Farenc *et al.* proposed three regimes: a low temperature, high stress regime where dislocations bow out due to locking giving rise to the σ^{-2} dependence of activation area; an intermediate regime of both temperature and stress, where large kinks (macrokinks) form, where locking-unlocking still occurs, but a kink-pair mechanism

is active and then a high temperature, low stress regime, where a kink-pair mechanism dominates. Rectilinear dislocations have been observed, suggesting some form of kink-pair mechanism operates at a large range of temperatures [12, 15, 16, 24]. Considerations by Orawa [25], state that there could be two mechanisms occurring at the same time at low temperature—that of a Peierls mechanism and dislocation-solute interactions—which is apparently consistent with the activation area results found in high purity titanium [20]. Conclusions by Caillard suggest a Peierls mechanism in conjunction with a locking-unlocking mechanism [16].

Oxygen has profound effects on titanium. There are dramatic increases in the yield strength [26, 27], with reductions in ductility and toughness [28], and changes in slip behaviour [1]. The increases in hardness are not in-keeping with standard solute hardening mechanisms, such as that of Fleischer [26, 29, 30]. This suggests that hardening occurs from chemical interactions of oxygen with the core of dislocations [31]. How oxygen affects slip in titanium is not well understood, with conflicting results in the literature. Williams found a wavy-to-planar slip transition with an increase in oxygen content [24], which has also been observed by Chong *et al.* [28], who further showed that this transition was also a function of decreasing temperature and increasing strain rate. However, *in situ* tensile tests of Barkia *et al.* [15], note an increased instability of prismatic glide with oxygen content [15], suggesting that the ratio of the π_1 CRSS to prismatic CRSS decreases with increasing oxygen content, which is consistent with a lack of π_1 slip activation seen at low ($\sim$ 100ppm. O) oxygen content in other studies [32]. A suppression of prismatic slip was also seen with an increase in oxygen content in work by Zaefferer [33]. Barkia *et al.* remark that homogeneity in slip with high oxygen content, as found in nanopillar compression tests [26], could be due to the high stresses involved, which activate other slip systems, such as $\langle c+a \rangle$ [26], which was not seen in Barkia *et al.*'s work. From these conflicting results, more work is necessary to understand the influence of oxygen on slip in titanium. The main questions that need to be answered are:

1. What is the mechanistic origin of the dramatic increase in yield strength with oxygen content?

2. What is the origin of slip planarity with oxygen content?

3. Why is prismatic slip destabilised in some studies but not in others with oxygen content?

1.2 Iron

Many technologies central to modern society rely on bearings. Hence the study of martensitic bearing steels, and specifically, understanding the fundamental processes behind their failure, is critical to improving their performance. One particular pathway of failure is that of *rolling cycle fatigue* (RCF), where the microstructure of the steel decays on repeated stress cycles [34–39]. To understand the mechanism behind this decay, we will first focus on martensitic steels.

Martensitic steels are created from carbon-enriched austenite (γ/fcc iron) where the iron is heated to around 840–860° C (austenitisation) [34]. On quenching, the famous martensitic transformation occurs, where the carbon-enriched austenite transforms to a supersaturated ferrite phase (α/bcc iron), in which carbon becomes trapped, forming a body-centred tetragonal structure. The martensitic transformation creates numerous dislocations, which strengthen the steel. After tempering (at 160–170°C), which allows for diffusion of solutes, one finds the following phases in the material: tempered martensite, austenite which has not transformed (retained austenite), residual cementite (Fe_3C)—cementite which did not dissolve during austenitisation, tempered cementite and tempered transition carbides (M_3C, where M is one of the metals Mn, Cr or Fe).

As will be discussed in chapter 5, one finds that the martensite in bearing steels can decay, forming ferrite, among other carbon-rich phases. Therefore, we will focus on the properties of the bcc phase of iron hereon.

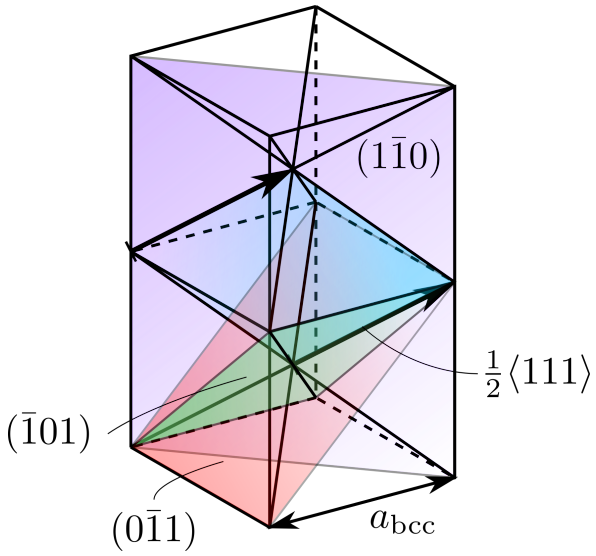

Fig. 1.4: Diagram of slip planes in bcc showing $\mathbf{b} = \frac{1}{2}\langle 111\rangle$ dislocation. Blue area swept as a dislocation glides on the $(1\bar{1}0)$ plane.

The low-temperature properties of bcc metals were one of the first known to be determined by a Peierls-type mechanism for dislocation motion, and iron is no exception [16]. Dislocations in iron are generally $\mathbf{b} = \frac{1}{2}\langle 111\rangle$ type, as seen in figure 1.4, and again, due to the high mobility of edge dislocations, screw dislocations control plasticity. There is a deviation from the Schmid law, equation (1.1), where the CRSS of iron changes with the sense of stress ("twinning/anti-twinning asymmetry") and whether tension/compression is applied ("tension/compression asymmetry") [40–43]. These can be attributed to the symmetry of the bcc structure along the $\langle 111\rangle$ direction, where screw dislocation displacements have a three-fold symmetry, and the core structure of dislocations, where small edge components respond to the non-glide components of the stress tensor [44].

Carbon is generally found in octahedral sites in the lattice, where it generates a tetragonal distortion: a reduction in the lattice parameter on the z axis, and an increase on the x–y axis. This produces dilatational and shear components of stress, which results in a binding of carbon to *both* edge and screw dislocations: solutes usually just produce a dilatational strain field, which only interacts with the dilatational field of an edge dislocations. Therefore Cottrell atmospheres are formed, where carbon segregates to the environment around edge and screw dislocations [7].

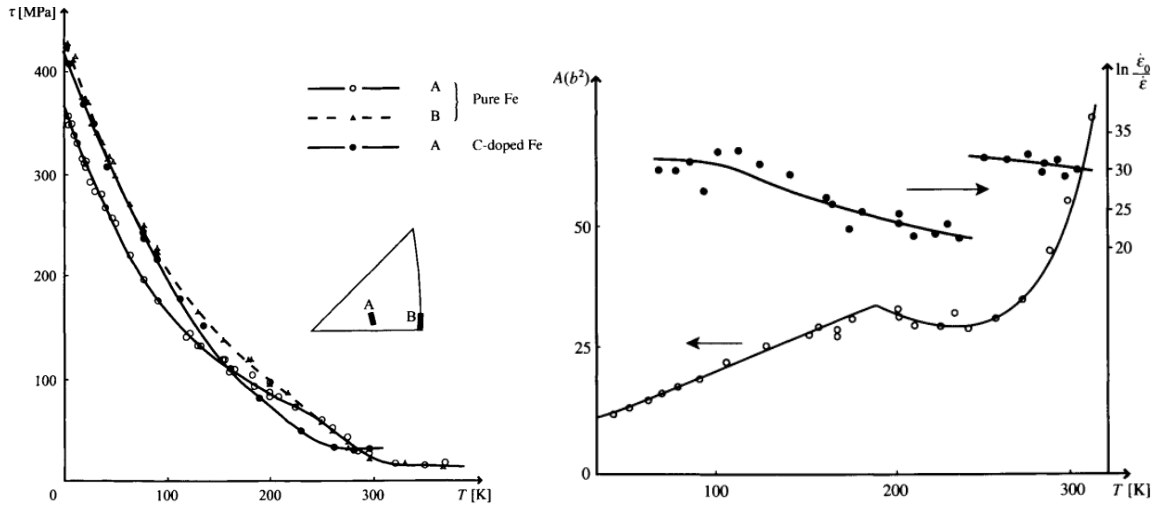

Fig. 1.5: Flow stress and activation area variation with temperature in Fe, oriented for $\frac{1}{2}\langle 111\rangle$ $\{110\}$ slip, from Caillard [16] with results from various authors [45–47]. We see at two different stress axes (A and B) that there is a different flow stress corresponds to the twinning/anti-twinning asymmetry. Carbon decreases the CRSS at intermediate temperatures, and increases it at high temperatures.

Carbon has pronounced effects on the flow stress in iron. One sees that carbon does not have a uniform effect, generating a softening effect, reducing the CRSS, at intermediate temperatures, while increasing the CRSS at higher temperatures, causing hardening, as seen in the flow stress/activation area curves in figure 1.5. Other studies have also found a hardening effect at very low temperatures [48]. The softening effect is interesting, given that one would expect the opposite to occur due to dislocation pinning by solutes. It has been suggested that a locking-unlocking mechanism occurs with iron at low temperature [48], which has been used to explain the peak found in the dependence of flow stress with temperature, where in the low temperature, high stress limit, there is a small bulge, which becomes a large bulge/macro kink-pair at an intermediate temperature, with higher temperatures being dominated by a kink-pair mechanism.

As found by Cottrell and Bilby [49], the dynamic strain ageing of iron—the phenomenon of a serrated stress-strain curve—can be attributed to carbon being attracted to screw dislocations, forming Cottrell atmospheres, where a carbon environment surrounds the dislocation line, which pins/inhibits dislocation motion. Upon action of sufficient shear stress, these dislocations break away from the environment of carbon which inhibits them. The usual accepted theory is that after periods of quiescence, carbon can equilibriate with the dislocation forming another atmosphere. It is usually

assumed that, due to the large barrier for migration (the energy barrier that carbon needs to overcome to hop to a new octahedral site: the diffusion barrier) carbon is simply left behind by the dislocation at temperatures around 300K. However, in bearing steels, there have been reports of a degradation of the microstructure, with a migration of carbon which is not commensurate with that of bulk diffusion [35, 39, 50–53]. It has been theorised that this is due to dislocations being able to drag carbon at these temperatures by a *dislocation-assisted carbon migration* mechanism, but this has not been verified by atomistic simulations and it cannot be probed experimentally. Hence, more research is needed, particularly to answer the questions:

1. Is carbon able to migrate with dislocations?
2. If so, what are the mechanisms of migration?
3. Under what regimes of stress, temperature and carbon concentration can this mechanism occur?

1.3 Computational modelling

From the above review, we see there is a need for atomistic modelling of oxygen in titanium, to understand the mechanisms behind large increase in the yield stress with oxygen content, which is theorised from oxygen-dislocation interactions. Furthermore, an investigation into the hypothesis of dislocation-assisted carbon migration in iron is necessary, and if it is indeed possible, the atomistic mechanisms by which this process occurs need to be ascertained. To tackle these problems, one must choose an appropriate method by which one can describe atomic interactions, to accurately elucidate the mechanisms of origin.

A key requirement of these models is the ability to accurately simulate dislocations to find the ground-state core structure. This is the most important feature to determine. Dislocation core structures dictate the glide planes on which dislocations can move, which in-turn, provide insights into plasticity and hardening upon solute interactions. These are solely determined by the description of atomic bonding. Therefore, it is paramount that one uses a method which gives an accurate description of atomic bonding/forces. But, the simulation of these defects requires a large number of atoms, due to the long-ranged strain fields which are generated. An insufficient number of atoms will result in a dislocation core structure which is not representative of the ground-state, thus hindering the prediction of potential mechanisms.

There is a trade-off which must be balanced: with increased capability of computational scaling comes the cost of more approximations being taken on-board, which could reduce the accuracy of the description of atomic bonding. Improved scaling allows for a broadening of potential simulations that can be performed—such as determining energy barriers for solute migration around dislocation cores [54–56], as would be necessary for investigation into dislocation-assisted carbon migration, or finding kink-pair formation enthalpies directly from atomistic calculations [57], simulation of dislocation loops [58] or the ability for novel simulations altogether, such as electrochemical simulations at the quantum scale for elucidating corrosion mechanisms *et cetera*. The required accuracy is that of dislocation core structures which are commensurate with experimental observations of dislocation glide—a prismatic/pyramidal core structure for titanium, for example. This suggests a method which describes the quantum mechanics of bonding and the resulting forces, sufficiently well.

The current gold-standard in the calculation of interatomic forces is that of DFT (Density Functional Theory), as will be explained in the theory section 2. Regular DFT methods scale as $\mathcal{O}(N^3)$, where N is the number of atoms, due to the diagonalisation of the dense Hamiltonian matrix.

DFT has an advantage that it is *ab-inito*: it is derived from first-principles quantum mechanics and does not rely on empirical results, or parameter fitting. But, one should not take this as a statement of DFT producing objective truth. The success of DFT relies on the choice of exchange-correlation functional [59]. Furthermore, systematic errors are included which cannot be avoided, resulting in erroneous phenomena, such as a poor reproduction of band gaps, of which accurate reproduction necessitates a higher-order technique describing quasi-particle excitations and not ground-state properties [60], and delocalisation phenomena [61]. In addition, the scaling of DFT is rather prohibitive, and it would be ideal if the method used could scale to include many atoms for the study of more complex systems and phenomena.

One way of improving the scalability of an interatomic force method is to *parameterise* them. This is where one compresses many complexities of reality/a higher-order model into numbers, which typically define some function of interest: say a repulsive energy between two atomic species (a pair potential). To obtain these numbers, one *fits* to data which one wants to reproduce, such as empirical lattice parameters, or particular energies from a higher-order method *et cetera*. How one goes about fitting depends on the particular method used. The ultimate goal in fitting these models is *transferability*—one model which can be used in many situations, which are far re-

moved from the data that was used to fit it, thereby showing a level of generality. The only way to test this is by use of empirical data.

Possibly one of the most simple paradigms of parameterised, interatomic force model is that of the *Embedded-atom Method* (EAM) [62], a generalisation of Finnis-Sinclair second-moment models [63], which scale as $\mathcal{O}(N)$. In this method, one obtains a per-atom energy, which is the value of an embedding function and a sum of pair potentials. The former function describes the energy necessary to place the atom within a background electron density. An extension of this method is the *Modified Embedded-atom Method* (MEAM) [64], where angular variation of the electron density is introduced to the EAM, allowing for more flexibility [64]. In modern EAM methods, arbitrary functional forms with many parameters—which are not based on physical considerations—are used to fit to the supplied data, but, typically they are not transferable: one iron EAM may be applicable to the bulk, but it will likely be inaccurate in simulating surfaces, for example [65].

More complex, data-driven schemes have been introduced in the past decade to capture the complexities associated with the local atomic environment and bonding, in a hope to create transferable models. *Gaussian approximation potentials* (GAPs), introduced by Bartók and Csyáni [66–68] try to reproduce the energy functional obtained in electronic structure calculations (usually DFT), by the fitting of local energy functionals parameterised by suitable descriptors defined for the potential, *e.g.* bond angles, atom-centred contributions etc. These models are fitted by Gaussian process regression, which uses kernel/covariance functions to measure correlation between descriptors. This has provided potentials which encapsulate DFT results reasonably well, with $\mathcal{O}(N)$ scaling, but with the rather large caveat that very large amounts of data are necessary to fit to: in the case of a recent study of pure silicon, this amassed 171,815 separate atomic environments [69]. The memory overhead is sizeable too, with some current GAP potentials needing *terabytes* of RAM to fit/use, thereby decreasing computational expense at the increase of memory expense.

The *Atomic Cluster Expansion* (ACE) is another data-driven method of interatomic potential fitting, which scales linearly ($\mathcal{O}(N)$). It consists of performing Gaussian-process regression to a fitting database, but using a kernel function which can be physically interpreted: it can be thought of as a generalisation of empirical potentials, such as the Finnis-Sinclair method, to higher multi-body order terms [70]. This has advantages, as one can treat magnetism in a natural way [71]. But, again, one needs a large database of environments to fit these potentials.

The aforementioned data-driven models have an advantage in that they are, in theory, systematically improvable: by adding more data you could improve your result. But, these models have a large disadvantage: the fitting database must account for all the environments one expects to find in the simulations of interest, as there is no physics-based model to rely on: data *is* the physics. In addition, the inclusion of more than one species means an $\sim \mathcal{O}(N_\mathrm{s}^2)$ increase in the amount of *ab-initio* calculations to fit to, where N_s is the number of species. As such, with a larger number of species, the amount of training data to fit to is usually pared down to those specific scenarios one wishes to simulate, creating a model which is not transferable.

Due to the necessity of a good description of atomic bonding for accurate resolution of dislocation core structures, one can use a simple quantum mechanical method to describe electronic bonding, but with better scaling by parameterisation. This can be achieved with *tight-binding*. These models circumvent the need for a very large fitting database when trying to describe multiple species, in addition to a reduction in the large memory overheads compared to data-driven parameterisation methods. Another advantage is that they are physically interpretable: energy contributions can be analysed naturally, allowing for the physical origin of phenomena to be discerned.

Tight-binding models can be thought of as approximations to DFT, as discussed in section 2.3.1. In these models, one describes the bonding between atomic species, typically, just the valence orbitals. This allows for a smaller basis, and therefore a smaller Hamiltonian, allowing for faster diagonalisation compared to DFT. Furthermore, many computationally-heavy complexities which come with DFT (such as the requirement of solving Poisson's equation for the potential) are dealt with in a less computationally taxing way, or swept into a pair potential, reducing the computational cost further. So although these models scale as $\mathcal{O}(N^3)$, under a direct-diagonalisation scheme, the prefactor to this scaling is orders of magnitude less than DFT. This allows for the simulation of many more atoms: it has been shown that DFT method can reproduce the core structures of dislocations, with $\sim$ 200–580 atoms [72–77], whereas for equivalent computational resources in tight-binding, simulations can be $\sim$ 600–1200 atoms, depending on the level of approximation one uses for the tight-binding model. Furthermore, scaling can become $\mathcal{O}(N)$, by using a *Bond-Order Potential* (BOP) [78–80] approach to approximately diagonalise the Hamiltonian, increasing the number of atoms which can be simulated to many thousands.

1.4 Overview and Objectives

In this thesis, the focus is on the parameterisation and use of *simple* tight-binding models, due to their: explicit description of atomic bonding by quantum-mechanics; physical interpretability; and scalability, compared to DFT methods and more complex tight-binding models. The limits of their scalability will be demonstrated by the simulation of dislocation-solute interactions which require large system sizes. In addition, the limits of transferability with these tight-binding models will be tested by parameterisations which simultaneously describe starkly different materials: titanium, titanium dioxide, titanium hydride and water. Using these models, potential mechanisms for hardening in titanium and dislocation-assisted carbon migration in iron, are sought. With the preferential scaling of these models, simulations beyond what is possible in DFT can be achieved, allowing for novel simulations which need both an explicit description of quantum mechanics and scalability, such as electrochemical simulations and elucidation of interfaces *et cetera*.

The outline of the structure of this thesis is as follows.

In chapter 2, the theory behind DFT, tight-binding and dislocations is described, along with saddle-point search methods, the latter of which are pertinent in chapter 5.

In chapter 3, one will show the process of fitting simple tight-binding models to describe bulk titanium, in addition to the parameterisation of titanium interactions with other species (oxygen and hydrogen), giving models for titanium dioxide and titanium hydride. In performing this fitting, and meshing with a previous model of water, the first ever transferable tight-binding model, which can simultaneously describe bulk titanium, titanium dioxide, titanium hydride and water is created, paving the way for future simulations of stress-corrosion cracking and electrochemistry at the quantum scale. An evaluation of the models, and their appropriateness for the simulation of defects, is achieved by various validation tests.

Upon the success of the validation tests, in chapter 4, the titanium and titanium-oxygen interactions which result from the fitting process are used to simulate oxygen-dislocation interactions, to determine the mechanistic origins of solute-hardening in titanium with oxygen content. These simulations are also used as a means to test the scalability of the tight-binding models, by use of large system sizes for dislocation simulations, and transferability, by comparison to DFT and empirical data.

In chapter 5, a simple tight-binding model describing iron and carbon is used to

investigate a dislocation-assisted carbon migration mechanism, theorised in bearing steels. This is achieved by simulation of carbon-dislocation interactions, in which the kink-pair formation enthalpy is calculated as a function of carbon content by a line-tension model. Further diffusion barrier calculations push tight-binding to its limits of computational time with a magnetic system. Analysis of carbon migration barriers in the vicinity of screw dislocations show novel mechanisms where carbon can keep up with dislocations in the operating temperatures of bearing steel, validating the dislocation-assisted carbon migration mechanism, and explaining the origin of carbon-induced changes to the flow stress with temperature in iron.

Chapter 2

Theory

2.1 Introduction

To accurately model the behaviour of an assembly of atoms we must use quantum mechanics. The first postulate of quantum mechanics states that a quantum mechanical system can be described by a wavefunction, a function of the positions of the quantum mechanical entities, and time, which satisfies the Schrödinger wave equation. As such we know that the state of the system can be fully described by a *many body wavefunction*: a wavefunction which is a function of the positions of each of the electrons and nuclei in the system, which also depends on time.

Assuming that we have non-relativistic electrons, and the Born-Oppenheimer approximation (that electrons instantaneously relax into their ground-state with nuclei movement) the Schrödinger equation one must solve is then [81, 82]

$$\hat{\mathcal{H}}\mathbf{\Psi}(\{\mathbf{r}\};t) = i\hbar\frac{\mathrm{d}\mathbf{\Psi}(\{\mathbf{r}\};t)}{\mathrm{d}t}, \tag{2.1}$$

where

$$\hat{\mathcal{H}} = \sum_i -\frac{1}{2}\nabla_i^2 + \frac{1}{2}\sum_i\sum_j \frac{1}{|\mathbf{r}_i - \mathbf{r}_j|} + \sum_i\sum_I \frac{-Z_I}{|\mathbf{r}_i - \mathbf{R}_I|} + \frac{1}{2}\sum_I\sum_J \frac{Z_I Z_J}{|\mathbf{R}_I - \mathbf{R}_J|} \tag{2.2}$$

and $\mathbf{\Psi}(\{\mathbf{r}\};t) = \mathbf{\Psi}(\{\mathbf{r}\})e^{-iEt/\hbar}$ is a many-body eigenstate of a set of electrons at $\{\mathbf{r}\} = \{\mathbf{r}_1, \ldots, \mathbf{r}_i, \ldots \mathbf{r}_n\}$, the form of which depends on nuclei positions at $\mathbf{R}_I$. The many-body Hamiltonian is $\hat{\mathcal{H}} = \hat{\mathcal{T}} + \hat{\mathcal{V}}$, where $\hat{\mathcal{T}}$ and $\hat{\mathcal{V}}$ are the kinetic energy (first term in equation (2.2)) and potential operators. The second, third and fourth terms in equation (2.2) correspond to the potential from electron-electron, electron-nucleus

and nucleus-nucleus interactions. Hartree units have been used here ($e = m = \hbar = 4\pi\epsilon_0 = 1$).

A time-independent observable which has operator $\hat{O}$, is given by the expectation value with a particular eigenstate,

$$\left\langle \hat{O} \right\rangle = \frac{\langle \mathbf{\Psi} | \hat{O} | \mathbf{\Psi} \rangle}{\langle \mathbf{\Psi} | \mathbf{\Psi} \rangle}. \tag{2.3}$$

The electronic density operator is defined as

$$\hat{\rho}(\mathbf{r}) = \sum_{i=1}^{N} \delta(\mathbf{r} - \mathbf{r}_i), \tag{2.4}$$

giving the expectation of the electron density as

$$\rho(\mathbf{r}) = \frac{\langle \mathbf{\Psi} | \hat{\rho}(\mathbf{r}) | \mathbf{\Psi} \rangle}{\langle \mathbf{\Psi} | \mathbf{\Psi} \rangle}. \tag{2.5}$$

The total energy is the expectation value of the many-body Hamiltonian $\hat{\mathcal{H}}$:

$$\begin{aligned} E &= \frac{\langle \mathbf{\Psi} | \hat{\mathcal{H}} | \mathbf{\Psi} \rangle}{\langle \mathbf{\Psi} | \mathbf{\Psi} \rangle} \\ &= \left\langle \hat{T} \right\rangle + \left\langle \hat{V}_{\text{int}} \right\rangle + \int \rho(\mathbf{r}) V_{\text{ext}} \mathrm{d}\mathbf{r} + E_{ZZ}, \end{aligned} \tag{2.6}$$

where

$$V_{\text{ext}}(\mathbf{r}) = \sum_{I} -\frac{Z_I}{|\mathbf{r} - \mathbf{R}_I|} \tag{2.7}$$

is the external potential due to the Coulomb interaction between the electrons and the nuclei. V_{int} is the electron-electron interaction energy and E_{ZZ} is the classical electrostatic nucleus-nucleus interaction energy, which are expectation values of the second and fourth terms in equation (2.2) respectively. $\left\langle \hat{T} \right\rangle$ is the expectation value of the electronic kinetic energy.

Stationary points in the total energy correspond to eigenstates of the many-body Hamiltonian. To find these stationary points, one can vary $\langle \mathbf{\Psi} | \hat{\mathcal{H}} | \mathbf{\Psi} \rangle$ subject to to the constraint of orthonormality ($\langle \mathbf{\Psi} | \mathbf{\Psi} \rangle = 1$), which is possible with the use of Lagrange multipliers. One finds that upon variation of the bra $\langle \mathbf{\Psi} |$ that the ket must satisfy the *time-independent* Schrödinger equation:

$$\hat{\mathcal{H}} \left| \mathbf{\Psi}_n \right\rangle = E_n \left| \mathbf{\Psi}_n \right\rangle, \tag{2.8}$$

where $|\mathbf{\Psi}_n\rangle$ is an eigenstate. From hereon we shall only be looking for these stationary eigenstates with time-independence.

Quite often, the state we would most like to find is the lowest energy state (*ground state*) of the system, as this is the fundamental state which other mechanisms return to or start from. To find this state for the full system, one must minimise the energy with respect to the variables in the many-body wavefunction, while satisfying the Schrödinger equation and appropriate symmetry constraints (e.g. for electrons, $\mathbf{\Psi}$ must be antisymmetric). This quickly leads to an explosion of complexity without making approximations: to only describe the $N = 22$ electrons present in a single titanium atom, using a grid of $N_\mathrm{p} \times N_\mathrm{p} \times N_\mathrm{p}$ points, and taking a coarse grid $N_\mathrm{p} = 10$, one would need to tabulate $(N_\mathrm{p}^3)^N = 10^{66}$ complex numbers to describe the electronic wavefunction. Clearly, minimising a function of this complexity is impossible. To make the problem tractable, we must make a few approximations.

2.2 Self-Consistent Mean-Field Theory

A major development on the path to tractable calculations is that of Hartree and Hartree-Fock theory. An ansatz is made for the many-electron wavefunction, whereby we assume it is a product state between single particle orbitals $\phi_i(\mathbf{r}_i)$. These orbitals are the product of spatial function and a spin function. This reduces the complexity to describe the wavefunction: we only need $3N \times N_\mathrm{p}^3$ numbers to describe the wavefunction.

We will first treat the simple case, without accounting for antisymmetry of the electronic wavefunction, with the ansatz

$$\mathbf{\Psi}(\{\mathbf{r}\}) = \phi_1(\mathbf{r}_1)\phi_1(\mathbf{r}_2)\dots\phi_N(\mathbf{r}_N). \tag{2.9}$$

We assume that electrons move in a *mean-field*: they are all in an *effective potential*, which consists of the average Coulomb interaction of all other electrons in addition to the potential from the nuclei $V_\mathrm{ext}(\mathbf{r})$ [83]. Denoting the i^th and j^th electrons as $\mathbf{r}$ and $\mathbf{r}'$ respectively, we have

$$V_\mathrm{eff}(\mathbf{r}) = V_\mathrm{ext}(\mathbf{r}) + \int \frac{\rho(\mathbf{r}')}{|\mathbf{r} - \mathbf{r}'|}\mathrm{d}\mathbf{r}', \tag{2.10}$$

where $\rho(\mathbf{r}) = \sum_i |\phi_i(\mathbf{r})|^2$. This is the Hartree approximation.

Upon making this approximation, one finds that the many-body Hamiltonian can be expressed as a sum of single-particle Hamiltonians $\hat{H}_i = \hat{T}_i + \hat{V}_i$ pertaining to each electron i:

$$\left(\sum_i \hat{H}_i\right) \mathbf{\Psi}(\{\mathbf{r}\}) = \left(\sum_i \left[-\frac{1}{2}\nabla_i^2 + V_{\text{eff}}(\mathbf{r})\right]\right) \mathbf{\Psi}(\{\mathbf{r}\}) = E\mathbf{\Psi}(\{\mathbf{r}\}). \tag{2.11}$$

One must minimise the functional

$$E[\mathbf{\Psi}] = \frac{\langle \mathbf{\Psi}|\hat{\mathcal{H}}|\mathbf{\Psi}\rangle}{\langle \mathbf{\Psi}|\mathbf{\Psi}\rangle}. \tag{2.12}$$

by the variational principle to find the ground state. A functional is analogous to function: a function maps a variable to a number, whereas a functional maps a function to a number. An orthonormal set of single-particle wavefunctions $\phi_n \equiv |n\rangle$, minimise this functional. From these orbitals, we can obtain the expectation value of full Hamiltonian to obtain the total energy.

The total energy in the Hartree approximation is given by [84]

$$E_{\text{H. approx}} = T + E_{\text{ext}} + E_{\text{H}}, \tag{2.13}$$

where the energy of the Hartree term E_{H} is given by

$$E_{\text{H}} = \frac{1}{2}\sum_m \sum_n f_n \int \frac{\phi_n^*(\mathbf{r})\phi_n(\mathbf{r})\phi_m^*(\mathbf{r}')\phi_m(\mathbf{r}')}{|\mathbf{r}-\mathbf{r}'|}\mathrm{d}\mathbf{r}\mathrm{d}\mathbf{r}', \tag{2.14}$$

and the energy from the external potential is

$$E_{\text{ext}} = \sum_n f_n \int \phi_n^*(\mathbf{r}')\phi_n(\mathbf{r}')V_{\text{ext}}(\mathbf{r}')\mathrm{d}\mathbf{r}'. \tag{2.15}$$

The expectation value of the kinetic energy is given by

$$T = \sum_n f_n \langle n|\hat{T}|n\rangle = \sum_n f_n \int \phi_n^*(\mathbf{r}) - \frac{1}{2}\nabla_n^2\phi_n(\mathbf{r})\mathrm{d}\mathbf{r}, \tag{2.16}$$

where f_n (included here for generality) is the occupancy of the eigenstate $|n\rangle$, which in the case of Hartree and Hartree-Fock theory, we take to be one.

To preserve the antisymmetry of the wavefunction, one must take the approach of Hartree-Fock theory. We can reformulate the ansatz in equation (2.9) by taking the Slater determinant of the orbitals, which imposes the required antisymmetry property

of the wavefunction, giving

$$\mathbf{\Psi}(\{\mathbf{r}\}) = \det\left(\phi_1(\mathbf{r}_1), \phi_2(\mathbf{r}_2), \ldots, \phi_N(\mathbf{r}_N)\right). \tag{2.17}$$

This gives the effective potential in Hartree-Fock theory as

$$V_{\text{eff}}^{\text{HF}}(\mathbf{r}) = V_{\text{ext}}(\mathbf{r}) + \int \frac{\rho(\mathbf{r}') - \rho_i^{\text{HF}}(\mathbf{r}, \mathbf{r}')}{|\mathbf{r} - \mathbf{r}'|} \mathrm{d}\mathbf{r}', \tag{2.18}$$

where we see there is now a non-local term $\rho_i^{\text{HF}}(\mathbf{r}, \mathbf{r}')$ given as

$$\rho_i^{\text{HF}}(\mathbf{r}, \mathbf{r}') = \sum_{\substack{k \\ \parallel \text{ spin}}} \frac{\phi_k^*(\mathbf{r}')\phi_i(\mathbf{r}')\phi_i^*(\mathbf{r})\phi_k(\mathbf{r})}{\phi_i^*(\mathbf{r}')\phi_i(\mathbf{r}')}. \tag{2.19}$$

This is the exchange charge density, which enforces Pauli exclusion for electrons. Only a summation over parallel spins is necessary due to spin function orthogonality.

The Hartree-Fock total energy is given by [84]

$$E_{\text{HF}} = T + E_{\text{ext}} + E_{\text{H}} + E_{\text{x}}, \tag{2.20}$$

with the exchange energy as

$$E_{\text{x}} = -\frac{1}{2} \sum_m \sum_n \int \frac{\phi_m^*(\mathbf{r}')\phi_n^*(\mathbf{r})\phi_n(\mathbf{r}')\phi_m(\mathbf{r})}{|\mathbf{r} - \mathbf{r}'|} \mathrm{d}\mathbf{r}\mathrm{d}\mathbf{r}', \tag{2.21}$$

where we see that exchange reduces the energy, as electrons of like spin are kept automatically apart, lowering the energy from Coulomb repulsion. The exchange energy also cancels the spurious self-interaction found in the Hartree energy, equation (2.14), for each electron eigenstate (with a given spin). Electronic correlations from effects other than exchange are not included in this theory.

With Hartree-Fock, there is still a vast amount of complexity, with typical calculations scaling as $\mathcal{O}(N^4)$. In addition, Hartree-Fock predicts that metals are insulators, with a singularity being found in the density of states at the Fermi energy due to the long-range Coulomb interaction [85]. As such, we would like a description which has better scaling, allowing for larger system sizes, while having a correct description of metals, with the inclusion of correlation effects which are not soley from exchange. We can achieve this with *Density Functional Theory*.

2.3 Density Functional Theory

Hohenberg and Kohn's seminal paper in 1964 [86] proved that there exists an energy functional of the electron density which can provide the exact ground-state energy and density upon minimisation. This reduces the number of variables to that of only $3N_{\mathrm{p}}^3$ for *any* number of electrons N in the system of interest.

In 1965, Kohn and Sham [87] developed a formalism to practically calculate this ground-state density via a set of self-consistent equations: the Kohn-Sham equations.

The main tenet of Density Functional Theory is: given a system that consists of N electrons, there exists an energy functional of the local electron density $E[\rho(\mathbf{r})]$, which corresponds to an antisymmetric wavefunction $|\mathbf{\Psi}\rangle$, which upon minimisation by variation of the electron density, subject to the constraint that the number of electrons is conserved

$$\int \rho(\mathbf{r})\mathrm{d}\mathbf{r} = N, \tag{2.22}$$

the resulting density is unique and the value of the functional is the ground-state energy. To obtain this result we can go through the following theory.

Assuming $\rho(\mathbf{r})$ is the exact ground state density, and $|\mathbf{\Psi}\rangle$ is a wavefunction, by the variational principle we can write,

$$\langle\mathbf{\Psi}|\,\hat{\mathcal{T}} + \frac{1}{2}\sum_i\sum_j \frac{1}{|\mathbf{r}_i - \mathbf{r}_j|}\,|\mathbf{\Psi}\rangle + \int \rho(\mathbf{r})V_{\mathrm{ext}}(\mathbf{r})\mathrm{d}\mathbf{r} \geq E_0. \tag{2.23}$$

where $V_{\mathrm{ext}}(\mathbf{r})$ is the external potential due to electron-nuclei interactions and E_0 is the ground-state energy. The state $|\mathbf{\Psi}\rangle$ may not be unique. To make it so, one can subject equation (2.23) to the constraints that the number of electrons is conserved and that ρ is fixed [88]. This defines the functional:

$$F[\rho] = \min_{\mathbf{\Psi}\to\rho} \langle\mathbf{\Psi}|\,\hat{\mathcal{T}} + \frac{1}{2}\sum_i\sum_j \frac{1}{|\mathbf{r}_i - \mathbf{r}_j|}\,|\mathbf{\Psi}\rangle = T[\rho] + E_{ee}[\rho], \tag{2.24}$$

where the notation $\mathbf{\Psi} \to \rho$ is to show that the minimisation is with respect to all $\mathbf{\Psi}$ that can make the density ρ.

The functional with the minimum value as the ground-state energy is then

$$E[\rho] = F[\rho] + E_{\mathrm{ext}}[\rho], \tag{2.25}$$

where

$$E_{\text{ext}}[\rho] = \int \rho(\mathbf{r}) V_{\text{ext}}(\mathbf{r}) \mathrm{d}\mathbf{r}, \tag{2.26}$$

of which its functional derivative with respect to the density is $V_{\text{ext}}(\mathbf{r})$.

By the Euler-Lagrange equations, one finds that the ground state must satisfy

$$\frac{\delta F[\rho]}{\delta \rho(\mathbf{r})} + V_{\text{ext}}(\mathbf{r}) = \mu, \tag{2.27}$$

where μ is the corresponding Lagrange multiplier.

To actually find this density, one can use the Kohn-Sham equations to find a self-consistent solution for the electron density [87]. To obtain the eigenvalues, one can replace the problem of solving a fully-interacting electronic system, with a given electronic density, by an auxiliary non-interacting electronic system which has the same electronic density. The resulting eigenvectors can be used to find the expectation value of the kinetic energy functional, $T_s[\rho]$, which corresponds to the kinetic energy of the non-interacting (Kohn-Sham) system.

The Hohenberg-Kohn-Sham (HKS) functional can be defined as

$$E_{\text{HKS}}[\rho] = T_{\text{s}}[\rho] + E_{\text{H}}[\rho] + E_{\text{xc}}[\rho] + E_{\text{ext}}[\rho] + E_{\text{ZZ}}, \tag{2.28}$$

where

$$E_{\text{H}}[\rho] = \frac{1}{2} \int \frac{\rho(\mathbf{r})\rho(\mathbf{r}')}{|\mathbf{r} - \mathbf{r}'|} \mathrm{d}\mathbf{r}\mathrm{d}\mathbf{r}', \tag{2.29}$$

is the Hartree energy, $E_{\text{xc}}[\rho]$ is the exchange-correlation energy and $T_{\text{s}}[\rho]$ is the kinetic energy of the fictitious non-interacting auxiliary system acting in the same effective potential $V_{\text{eff}}[\rho]$, where one can obtain $T_{\text{s}}[\rho]$ from equation (2.16). The assumption made here is that the ground state density of the non-interacting, auxiliary system is equal to that of the system with full electronic interactions.

This definition of the HKS functional redefines the exchange-correlation functional $E_{\text{xc}}[\rho]$: the energy associated with Coulombic contributions from electron correlation and exchange in addition to the difference between the true kinetic energy and that of the non-interacting system. This gives the true exchange-correlation functional as

$$E_{\text{xc}}[\rho] = \Big(\left\langle \hat{T} \right\rangle - T_{\text{s}}[\rho] \Big) + \Big(\left\langle \hat{V}_{\text{int}} \right\rangle - E_{\text{H}}[\rho] \Big), \tag{2.30}$$

where we can interpret the first term as being the increase in kinetic energy from electronic correlation in a fully interacting system, compared to a non-interacting

one—correlations cause electrons to move to more energetically favourable areas of the potential, thus increasing the kinetic energy. The second term is the difference in energy between a system with full electron-electron interactions $\left(\hat{V}_{\text{int}} = \frac{1}{2}\sum_{\mathbf{r},\mathbf{r}'}\frac{1}{|\mathbf{r}-\mathbf{r}'|}\right)$, which includes exchange and correlation effects, and the standard Hartree energy, which represents the energy purely from an electronic density, with no exchange-correlation.

To solve the Kohn-sham equations, the following process can be performed. One solves Poisson's equation for the Hartree potential $\nabla^2 V_{\text{H}}^{\text{in}}(\mathbf{r}) = -4\pi\rho^{\text{in}}(\mathbf{r})$, given an initial input density $\rho^{\text{in}}(\mathbf{r})$, which in the first iteration is a sum of atomic charge densities. Then, the total effective potential for the system is constructed,

$$V_{\text{eff}}^{\text{in}}(\mathbf{r}) = V_{\text{H}}^{\text{in}}(\mathbf{r}) + V_{\text{ext}}^{\text{in}}(\mathbf{r}) + V_{\text{xc}}^{\text{in}}(\mathbf{r}). \tag{2.31}$$

The set of single-particle Schrödinger equations (the Kohn-Sham equations) are subsequently solved

$$\left[-\frac{1}{2}\nabla_n^2 + V_{\text{eff}}^{\text{in}}(\mathbf{r}_n)\right]\phi_n(\mathbf{r}_n) = \epsilon_n\phi_n(\mathbf{r}_n), \tag{2.32}$$

yielding the single-particle eigenstates (Kohn-Sham orbitals) from which a new electron density is found, $\rho^{\text{out}}(\mathbf{r}) = \sum_n f_n|\phi_n(\mathbf{r})|^2$. This density can be put back into the Poisson's equation, giving a new $V_{\text{H}}^{\text{in}}(\mathbf{r})$, starting a new cycle to get a new $\rho^{\text{out}}(\mathbf{r})$. Once the input and output densities are within some tolerance of each other, one can say that the $\rho^{\text{out}}(\mathbf{r}) = \rho^{\text{exact}}(\mathbf{r})$, and the resulting total energy is the ground-state energy.

2.3.1 From Density Functional Theory to Tight-Binding

One can apply perturbation theory to more closely understand the relationship between the input and output densities upon solving the Kohn-Sham equations (2.32). We can expand the HKS functional, equation (2.28), to second order in deviations of

the input density to obtain the second-order HKS functional [81]:

$$\begin{aligned} E^{(2)}_{\mathrm{HKS}}[\rho] = & \sum_n f_n \langle n|\hat{H}^{\mathrm{in}}|n\rangle \\ & - \int \mathrm{d}\mathbf{r}\rho^{\mathrm{in}}(\mathbf{r})V^{\mathrm{in}}_{\mathrm{xc}}(\mathbf{r}) + E_{\mathrm{xc}}[\rho^{\mathrm{in}}] - E_{\mathrm{H}}[\rho^{\mathrm{in}}] + E_{\mathrm{ZZ}} \\ & + \frac{1}{2}\int \mathrm{d}\mathbf{r}\int \mathrm{d}\mathbf{r}'\left\{\frac{\delta\rho(\mathbf{r})\delta\rho(\mathbf{r}')}{|\mathbf{r}-\mathbf{r}'|}\right. \\ & \left. + \delta\rho(\mathbf{r})\frac{\delta^2 E_{\mathrm{xc}}}{\delta\rho(\mathbf{r})\delta\rho(\mathbf{r}')}\delta\rho(\mathbf{r}')\right\}. \end{aligned} \tag{2.33}$$

where, $\delta\rho(\mathbf{r}) = \rho^{\mathrm{out}}(\mathbf{r}) - \rho^{\mathrm{in}}(\mathbf{r})$. The first line represents the energy from the input Hamiltonian, the second line subtracts the exchange-correlation energy from the first term, to encapsulate all exchange-correlation effects in the second term on the second line, the third term on the second line removes the Hartree contribution from the first line, which is the double-counting correction term, with the final term on the second line being the classical nucleus-nucleus interaction.

Minimising the above functional with respect to ρ, furnishes us with the equation one needs to solve for the ground-state:

$$\hat{H}^{\mathrm{in}}|n\rangle = (\hat{T} + \hat{V}^{(2)}_{\mathrm{eff}})|n\rangle = \epsilon_n|n\rangle, \tag{2.34}$$

where

$$V^{(2)}_{\mathrm{eff}}(\mathbf{r}) = V^{\mathrm{in}}_{\mathrm{eff}}(\mathbf{r}) + \int\left(\frac{1}{|\mathbf{r}-\mathbf{r}'|} + \frac{\delta^2 E_{\mathrm{xc}}[\rho]}{\delta\rho(\mathbf{r})\delta\rho(\mathbf{r}')}\Big|_{\rho^{\mathrm{in}}(\mathbf{r})}\right)\delta\rho(\mathbf{r}')\mathrm{d}\mathbf{r}', \tag{2.35}$$

Omitting the final two lines in equation (2.33), we obtain the first-order functional, the Harris-Foulkes functional. This is the basis for the tight-binding bond model.

2.4 Tight Binding

2.4.1 The Tight-Binding Bond Model

As with many tight-binding models, we represent our Hamiltonian in a Linear Combination of Atomic Orbitals (LCAO) basis [89, 90]. These basis functions are localised to a particular site $\mathbf{R}$ with an orbital described by angular momentum ℓ with magnetic quantum number m. We shall denote this orbital by the composite index L, giving the basis as $|\mathbf{R}L\rangle$.

To solve the single-particle Schrödinger equation, we first must convert equa-

tion (2.34), into a matrix eigenvalue problem. Using the local orbitals we define for tight-binding, one can expand the eigenstate with coefficients $C^n_{\mathbf{R}'L'}$ as $|n\rangle = \sum_{\mathbf{R}'L'} C^n_{\mathbf{R}'L'} |\mathbf{R}'L'\rangle$, which upon projection of $\langle \mathbf{R}L|$ gives

$$\sum_{\mathbf{R}'L'} H_{\mathbf{R}L\mathbf{R}'L'} C^n_{\mathbf{R}'L'} = \epsilon_n \sum_{\mathbf{R}'L'} S_{\mathbf{R}L\mathbf{R}'L'} C^n_{\mathbf{R}'L'}, \tag{2.36}$$

where $S_{\mathbf{R}L\mathbf{R}'L'}$ is the overlap matrix $S_{\mathbf{R}L\mathbf{R}'L'} = \langle \mathbf{R}L|\mathbf{R}'L'\rangle$ and $H_{\mathbf{R}L\mathbf{R}'L'}$ are the Hamiltonian matrix elements. $\phi_{\mathbf{R}L}(\mathbf{r})$ is the basis function of $|\mathbf{R}L\rangle$ in the $\mathbf{r}$-representation, which gives matrix elements as

$$H_{\mathbf{R}L\mathbf{R}'L'} = \int \langle \mathbf{R}L|\mathbf{r}\rangle \, H(\mathbf{r}) \, \langle \mathbf{r}|\mathbf{R}'L'\rangle \, \mathrm{d}\mathbf{r} = \int \phi^*_{\mathbf{R}L}(\mathbf{r}) H(\mathbf{r}) \phi_{\mathbf{R}'L'}(\mathbf{r}) \mathrm{d}\mathbf{r}. \tag{2.37}$$

Central to tight-binding are the numerous approximations one makes. The first, is that we assume we can write the effective potential as a sum of atom-centred contributions $\hat{V}_{\text{eff}} = \sum_{\mathbf{R}} \hat{V}^{(\mathbf{R})}_{\text{eff}}$. From this, one can represent the matrix element of the effective potential as

$$\langle \mathbf{R}L| \, \hat{V}_{\text{eff}} \, |\mathbf{R}'L'\rangle = \langle \mathbf{R}L| \, \hat{V}^{(\mathbf{R})}_{\text{eff}} \, |\mathbf{R}'L'\rangle + \langle \mathbf{R}L| \, \hat{V}^{(\mathbf{R}')}_{\text{eff}} \, |\mathbf{R}'L'\rangle + \sum_{\mathbf{R}'' \neq \mathbf{R}', \mathbf{R}} \langle \mathbf{R}L| \, \hat{V}^{(\mathbf{R}'')}_{\text{eff}} \, |\mathbf{R}'L'\rangle \, , \tag{2.38}$$

We take the two-centre approximation for the Hamiltonian matrix elements in this thesis: where the final summation in equation (2.38), is dropped, which has the effect of removing an environmental dependence of the matrix elements. The matrix elements of the kinetic energy operator $\hat{T}$ are two-centre terms, as can be easily seen.

The two-centre Hamiltonian matrix elements are generated by use of the Slater-Koster relations [91], which provide the angular dependencies of the atomic orbitals in the LCAO basis, in conjunction with the distance dependencies of these matrix elements, which are given by fundamental *bond integrals* $V_{\ell\ell' m}(r)$. These are the parameterised functions which describe the distance dependence r of the bonding orbital m, between atomic orbitals ℓ and ℓ', as seen in figure 2.1. One can parameterise the elements of the $\mathbf{S}$ matrix in the same way, using the Slater-Koster relations and distance dependences given by some function $S_{\ell\ell' m}(r)$.

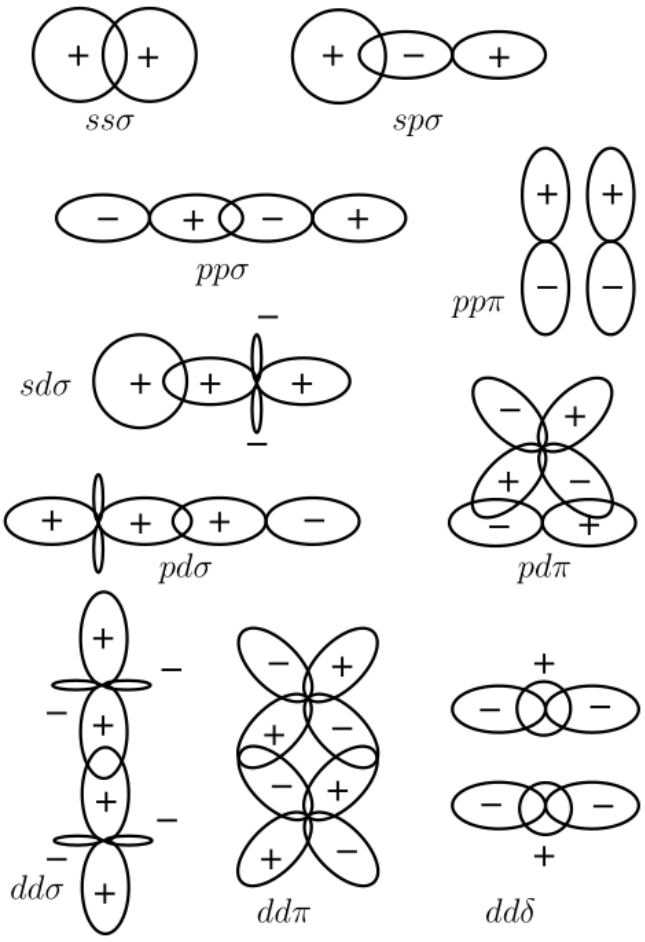

Fig. 2.1: Fundamental bond integrals, $V_{\ell\ell' m}(r)$, between atomic orbitals [89, 92].

The diagonal elements of the Hamiltonian in equation (2.36), $H_{\mathbf{R}L\mathbf{R}L}$ correspond to *on-site* terms. These are simply the energy of a particular orbital e.g. ϵ_s, ϵ_p, ϵ_d for the s, p and d orbitals. These are parameters along with the assumed orbital occupancies of the free atoms $N_{\mathbf{R}\ell}$. Off-diagonal terms between different sites, $H_{\mathbf{R}L\mathbf{R}'L'}$, correspond to the potential of overlapping atomic orbitals on different sites, as given by the Slater-Koster rules.

Given the matrix elements, prior to solving anything, there are useful quantities to define. An operator $\hat{A}$, can have expansion coefficients related to the local orbitals by

$$A^{\mathbf{R}L\mathbf{R}'L'} = \sum_{\mathbf{R}''L''\mathbf{R}'''L'''} S^{-1}_{\mathbf{R}L\mathbf{R}''L''} \langle \mathbf{R}''L'' | \hat{A} | \mathbf{R}'''L''' \rangle S^{-1}_{\mathbf{R}'''L'''\mathbf{R}'L'}, \tag{2.39}$$

The expression for the expansion coefficients are similar to that of matrix elements $A_{\mathbf{R}L\mathbf{R}'L'} = \langle \mathbf{R}L | \hat{A} | \mathbf{R}'L' \rangle$, but are only equivalent if $\mathbf{S} = \mathbf{I}$, which is an *orthogonal*

tight-binding model: the type of models we will encounter in this thesis. One can interpret the overlap matrix as a quantity akin to the metric tensor as in General Relativity, where the action of it is to raise/lower indices, changing between covariance and contravariance [93].

We can obtain the electron density as

$$\rho(\mathbf{r}) = \sum_{\mathbf{R}L\mathbf{R}'L'} \langle \mathbf{r}|\mathbf{R}L\rangle \, \rho^{\mathbf{R}L\mathbf{R}'L'} \, \langle \mathbf{R}'L'|\mathbf{r}\rangle \,, \tag{2.40}$$

where

$$\rho^{\mathbf{R}L\mathbf{R}'L'} = \sum_n f_n C^n_{\mathbf{R}L} C^{n*}_{\mathbf{R}'L'}, \tag{2.41}$$

are the expansion coefficients of the density operator

$$\hat{\rho} = \sum_n f_n \, |n\rangle \, \langle n| \,. \tag{2.42}$$

where f_n is the occupancy. This occupancy can be given by $2f_{\mathrm{F}}(\epsilon_n)$, where f_{F} is the Fermi distribution function, assuming spin degeneracy. At 0K we have f_n given by zero or one. In collinear magnetism at 0K, we have the occupancy dependent on spin f^σ_n, which has values either zero or one, as such there are two density matrices constructed.

We can define Mulliken charges on a site as

$$q_{\mathbf{R}} = \sum_{\mathbf{R}L} \rho^{\mathbf{R}L\mathbf{R}L} + \frac{1}{2} \sum_{LL'} \left(\rho^{\mathbf{R}L\mathbf{R}'L'} O_{\mathbf{R}'L'\mathbf{R}L} + \rho^{\mathbf{R}'L'\mathbf{R}L} O_{\mathbf{R}L\mathbf{R}'L'} \right)$$

(2.43)

where $\mathbf{O} = \mathbf{S} - \mathbf{I}$.

The band energy is then given by,

$$E_{\mathrm{band}} = \mathrm{Tr}\hat{\rho}\hat{H} = \sum_n f_n \epsilon_n, \tag{2.44}$$

This band energy is the sum of the electron kinetic energies and electron-ion interaction energies, which is the first term in the functional, equation (2.33).

To obtain more insight into systems using tight-binding, can define the cohesive

energy, $E_{\text{coh}} = E_{\text{tot}} - E_{\text{free}}$, where E_{free} is the energy of free atoms prior to bonding and E_{tot} is the energy which comes, at the moment, from the Harris-Foulkes functional, the first two lines in equation (2.33). One can partition cohesive energy to understand the different energy contributions apparent when atoms undergo bonding, which is the central result of the tight-binding approximation [81, 94]

$$E_{\text{coh}} = E_{\text{cov}} + E_{\text{prom}} + E_{\text{cf}} + E_{\text{polar}} + E_{\text{mb}} + E_{\text{rep}}, \tag{2.45}$$

where the terms will be explained below.

One must first account for the energy in going from free atoms, in which electrons are allowed to spin-polarise due to Hund's rule, to that of an atom which is not spin-polarised. Then we prepare the electrons for bonding in the solid by the promotion energy E_{prom}

$$E_{\text{prom}} = \sum_{\mathbf{R}L} \left\{ q_{\mathbf{R}L} - N^{\text{free}}_{\mathbf{R}\ell} \right\} \epsilon_\ell \tag{2.46}$$

where we redistribute charge from the initial occupancies of the orbitals $N_{\mathbf{R}\ell}$ to the orbitals appropriate for bonding. Here, $q_{\mathbf{R}L} = \sum_{\mathbf{R}'L'} \rho^{\mathbf{R}L\mathbf{R}'L'} S_{\mathbf{R}'L'\mathbf{R}L}$. Then we bring the atoms together and do not allow for hybridisation. The on-site energies of the atoms change as the potential the electrons experience is not just the potential of the free atom, but also the local atomic environment: this is the crystal-field splitting term E_{cf}

$$E_{\text{cf}} = \sum_{\mathbf{R}L} q_{\mathbf{R}L} \left(H_{\mathbf{R}L\mathbf{R}L} - \epsilon_\ell \right). \tag{2.47}$$

Allowing for hybridisation of the orbitals on each of the sites gives the polarisation energy E_{polar}

$$E_{\text{polar}} = \sum_{\mathbf{R}L\mathbf{R}L'} \rho^{\mathbf{R}L\mathbf{R}L'} \left(H_{\mathbf{R}L\mathbf{R}L'} - \delta^{\mathbf{R}L}_{\mathbf{R}L'} H_{\mathbf{R}L\mathbf{R}L} \right), \tag{2.48}$$

Then, allowing for hybridisation of orbitals localized at different sites, we gain the covalent bond energy E_{cov},

$$E_{\text{cov}} = \sum_{\substack{\mathbf{R}L\mathbf{R}L' \\ \mathbf{R}\neq\mathbf{R}'}} \rho^{\mathbf{R}L\mathbf{R}'L'} \left(H_{\mathbf{R}'L'\mathbf{R}L} - S_{\mathbf{R}'L'\mathbf{R}L} H_{\mathbf{R}L\mathbf{R}L} \right). \tag{2.49}$$

We have the small many body energy term given by E_{mb} and E_{rep} is the sum of the pair potential contribution to the double counting term with the ion-ion interaction.

Here, we can see that the band energy consists of $E_{\text{band}} = E_{\text{cov}} + E_{\text{prom}} + E_{\text{free}}$. In tight-binding, one usually uses a pair potential to approximate the other terms,

$E_{\text{pair}} \approx E_{\text{cf}} + E_{\text{polar}} + E_{\text{mb}} + E_{\text{rep}}$, if there are no extra additions to the model. This gives the cohesive energy from tight-binding, to first order

$$E_{\text{coh}}^{(1)} = E_{\text{cov}} + E_{\text{prom}} + E_{\text{pair}}. \tag{2.50}$$

This is the tight-binding *bond* model, as developed by Sutton *et al.* [90]. Using this scheme for tight-binding, a condition is imposed: that atoms should be charge-neutral. This *local charge neutrality* condition is a reasonable approximation to make in metallic systems due to the strong screening of conduction electrons. It is not satisfied after a näive first calculation: on analysis of the resulting charges from the output density matrix, one finds a redistribution of charge which can lead to inconsistencies, such as non-conservation of charge and insufficient potential variation from flowing charges [89, 90]. Imposing local charge neutrality introduces an elementary form of self-consistency, whereby $H_{\mathbf{R}L\mathbf{R}L}$, the on-site matrix elements of the Hamiltonian—the energies of each atom—are changed iteratively until the change in the resulting local atomic charges is approximately zero. This results in the satisfaction of the force theorem, which states that there is no contribution to the force upon a self-consistent redistribution of the charge following a virtual displacement of an atom [90, 95, 96].

2.4.2 Self-Consistent Polarisable-Ion Tight-Binding

The approximation of local charge neutrality for atoms as a basic form of self-consistency is well satisfied for bulk metals, as one expects a large amount of screening of metallic ions from the conduction electrons. This is not the case for solids composed of atoms with very different electronegativities, or metal surfaces, as there will be large charge transfers [81, 89, 97]. Allowing for these charges, there will be an electrostatic interaction between atoms which distorts the orbitals, breaking their spherical symmetry, resulting in charge polarisation.

To account for charge transfer and charge polarisation within tight-binding, one can introduce the effect of the second-order term in the second-order HKS functional, equation (2.33), which we will denote as E_2

$$E_2 = \int \mathrm{d}\mathbf{r}\mathrm{d}\mathbf{r}'\delta\rho(\mathbf{r})\delta\rho(\mathbf{r}')\left(\frac{1}{|\mathbf{r}-\mathbf{r}'|} + \frac{\delta^2 E_{\text{xc}}}{\delta\rho(\mathbf{r})\delta\rho(\mathbf{r}')}\right) = \int \mathrm{d}\mathbf{r}\mathrm{d}\mathbf{r}'\delta\rho(\mathbf{r})\delta\rho(\mathbf{r}')C_{\text{in}}(\mathbf{r},\mathbf{r}'), \tag{2.51}$$

This term describes the change in the Hartree and exchange-correlation potentials to first order in the change of the charge density. By adding this term, one must

self-consistently solve the Schrödinger equation, as there is now the term $V_2^{\text{eff}} = \int \mathrm{d}\mathbf{r}' \delta\rho(\mathbf{r}') C_{\text{in}}(\mathbf{r}, \mathbf{r}')$, the second term in equation (2.35), in the effective potential which itself is a functional of the density.

To describe monopoles of charge, we can start by developing the self-consistent charge transfer model (SCTM), approximating E_2 as

$$E_2^{\text{SCTM}} = \frac{1}{2} \sum_{\mathbf{R}} U_{\mathbf{R}} \delta q_{\mathbf{R}}^2 + \frac{1}{2} \sum_{\mathbf{R}' \neq \mathbf{R}} U_{\mathbf{R}\mathbf{R}'} \delta q_{\mathbf{R}} \delta q_{\mathbf{R}'}, \tag{2.52}$$

resulting in the Hamiltonian

$$H_{\mathbf{R}L\mathbf{R}'L'}^{\text{SCTM}} = H_{\mathbf{R}L\mathbf{R}'L'}^{\text{in}} + \left(U_{\mathbf{R}} \delta q_{\mathbf{R}} + \sum_{\mathbf{R}' \neq \mathbf{R}} U_{\mathbf{R}\mathbf{R}'} \delta q_{\mathbf{R}'} \right) \delta_{\mathbf{R}\mathbf{R}'} \delta_{LL'}, \tag{2.53}$$

for an orthogonal model, where we have assumed that the induced charges at each site are well-described by the change in the Mulliken charges at those sites $\delta q_{\mathbf{R}} = q_{\mathbf{R}} - q_{\mathbf{R}}^{\text{in}}$. These terms only change the on-site energies of the Hamiltonian. We have defined a Hubbard U parameter $U_{\mathbf{R}}$, which is a penalty for the addition of charge to a site. We assume this parameter is constant in tight-binding. $U_{\mathbf{R}\mathbf{R}'} = 1/|\mathbf{R} - \mathbf{R}'|$ is the standard Coulomb term relating the change in the Coulomb energy due to the change in atom-centred charges. $\delta_{LL'}$ and $\delta_{\mathbf{R}\mathbf{R}'}$ are Kronecker deltas. $H_{\mathbf{R}L\mathbf{R}'L'}^{\text{in}}$ is the Hamiltonian matrix which comes from the standard two-centre construction, as in the tight-binding bond model.

To include the effect of charge polarisation, we need self-consistent Polarisable-Ion tight-binding (PITB). Assuming the basis functions of tight-binding are composed of a radial and a spherical part:

$$\langle \mathbf{r} | \mathbf{R}L \rangle = f_{\mathbf{R}L}(|\mathbf{r} - \mathbf{R}|) Y_L(\theta, \phi), \tag{2.54}$$

and inserting the expression for the expansion of the density, equation (2.40), into equation (2.51), and differentiating with respect to the wavefunction coefficients, one finds the Hamiltonian as [81]

$$H_{\mathbf{R}L\mathbf{R}'L'}^{\text{PITB}} = H_{\mathbf{R}L\mathbf{R}'L'}^{\text{in}} + \sum_{\mathbf{R}''L''\mathbf{R}'''L'''} C_{\mathbf{R}L\mathbf{R}'L'\mathbf{R}''L''\mathbf{R}'''L'''} \left(\rho^{\mathbf{R}''L''\mathbf{R}'''L'''} - \rho_{\mathbf{R}''}^{\mathbf{R}''L''\mathbf{R}''L''} \right), \tag{2.55}$$

where $\rho_{\mathbf{R}''}^{\mathbf{R}''L''\mathbf{R}''L''}$ is subscripted with $\mathbf{R}''$ to emphasise these are atom-centred charges.

This general Hamiltonian provides us with a plethora of matrix elements to account for the response of the system to changes in the charge density. Of note are the on-site terms which relate different orbitals together, $L \neq L'$. These are polarisation terms, which provide distortions to the orbitals due to the electrostatic interactions.

In free atoms, the atomic orbital basis is spherically symmetric, as they include the spherical harmonic terms $Y_L(\theta, \phi)$. In a solid, there is much lower symmetry, generally the point group of the solid. This reduction in symmetry induces a splitting of the energy levels, coming from the crystal field, which arises from potential of the neighbours and the resulting polarisation of the charge. To describe the reaction of these orbitals to the symmetry of the potential, one can incorporate on-site matrix elements between different orbitals on a site, induced by the surrounding charges, causing distortion away from spherical symmetry. We do not include the simple crystal field terms, related to the change in on-site energies upon insertion into the crystal—these are still swept into the pair potential.

There are also off-site matrix elements which respond to changes in the charge density. These terms are able to be parameterised to include the effects of exchange to remove self-interaction, and even non-local correlation effects [81].

In order to keep the number of parameters to a minimum, we will omit the contribution of the off-site, off-diagonal contributions to the matrix elements. Thus, we want to only include the effect of on-site, off-diagonal terms. We can extend the SCTM model to do this.

One can expand the Coulomb term in equation (2.52), in charge multipoles, while keeping the Hubbard U as the monopole ($Q_0(\mathbf{R}) \equiv \delta q_{\mathbf{R}}$), which results in

$$E_2^{\mathrm{PITB}} = \frac{1}{2}\sum_{\mathbf{R}} U_{\mathbf{R}} \delta q_{\mathbf{R}}^2 + \frac{1}{2} \sum_{\mathbf{R}L\mathbf{R}'L'\mathbf{R}\neq\mathbf{R}'} Q_L(\mathbf{R}_I) B_{LL'}(\mathbf{R}, \mathbf{R}') Q_{L'}(\mathbf{R}'), \tag{2.56}$$

where $Q_L(\mathbf{R})$ is a charge multipole which is defined as $Q_L(\mathbf{R}) = \int \mathrm{d}\mathbf{r} \rho(\mathbf{r}) r^\ell Y_L(\mathbf{r})$, the $B_{LL'}(\mathbf{R}, \mathbf{R}')$ are coefficients defined by

$$B_{LL'}(\mathbf{R}, \mathbf{R}') = 16\pi^2 \sum_{L''} (-1)^\ell \frac{(2\ell'' - 1)!!}{(2\ell + 1)!!(2\ell' + 1)!!} C_{L'LL''} K_{L''}(|\mathbf{R} - \mathbf{R}'|), \tag{2.57}$$

where $K_{L''}(\mathbf{R}) = R^{-\ell-1} Y_L(\theta, \phi)$ are solid Hankel functions, $C_{L'LL''} = \iint \mathrm{d}\Omega Y_{L'} Y_L Y_{L''}$ are Gaunt coefficients, and the summation is restricted such that $L'' = L + L'$, with ℓ being the multipole component of interest, from the $L = (l, m)$ combined index.

To restrict the number of parameters which would result from equation (2.56), we

can expand $Q_L(\mathbf{R})$ in terms of the charge density and real spherical harmonics, to obtain

$$Q_L(\mathbf{R}) = \sum_{LL'} \rho^{\mathbf{R}L\mathbf{R}L'} \Delta^{\mathbf{R}}_{\ell'\ell\ell''} C^{\mathbf{R}}_{L'LL''}, \tag{2.58}$$

where $\Delta^{\mathbf{R}}_{\ell'\ell\ell''}$ are coupling strengths, which are the new parameters. We restrict the number of $\Delta^{\mathbf{R}}_{\ell'\ell\ell''}$ necessary by the symmetries of the Gaunt coefficients, resulting in seven new coefficients for an s, p, d basis,

$$\Delta^{\mathbf{R}}_{spp}, \Delta^{\mathbf{R}}_{ppd}, \Delta^{\mathbf{R}}_{sdd}, \Delta^{\mathbf{R}}_{pdp}, \Delta^{\mathbf{R}}_{ddd}, \Delta^{\mathbf{R}}_{pdf}, \Delta^{\mathbf{R}}_{ddg}. \tag{2.59}$$

This gives the Hamiltonian for an orthogonal PITB model as

$$\begin{aligned} H^{\mathrm{PITB}}_{\mathbf{R}L\mathbf{R}'L'} =& H^{\mathrm{in}}_{\mathbf{R}L\mathbf{R}'L'} + U_{\mathbf{R}} \delta q_{\mathbf{R}} \delta_{\mathbf{R}\mathbf{R}'} \delta_{LL'} \\ &+ \sum_{\mathbf{R}'' \neq \mathbf{R}} \sum_{LL'} \left(\sum_{L''L'''} \Delta^{\mathbf{R}}_{\ell''\ell\ell'''} C^{\mathbf{R}}_{L''LL'''} \right) B_{LL'}(\mathbf{R}, \mathbf{R}'') Q_{L'}(\mathbf{R}'') \delta_{\mathbf{R}\mathbf{R}'}. \end{aligned} \tag{2.60}$$

2.4.3 Stoner Magnetism

Magnetism must be taken into account in materials where it is exhibited, such as iron. It has been shown to explain the stability of different iron phases [98, 99]. This effect can be introduced into tight-binding by use of Stoner's model of itinerant magnetism [100–102].

We will not delve into the theory of itinerant magnetism in-depth in this thesis, but the reader is directed to Paxton and Finnis [103] and Pettifor [104] both of whom detail Stoner's theory in the context of tight-binding descriptions of transition metals. To keep it brief, one must solve the Schrödinger equation for both minority and majority spins, obtaining two density matrices: ρ^+ and ρ^- for spin-up and spin-down electrons respectively. The difference in these densities gives the magnetic moment $\delta m = \rho^+ - \rho^-$. The Stoner parameter I is a fitted parameter which controls the exchange splitting. There is an extra contribution to the energy, $E_{\mathrm{mag}} = \delta T - \frac{1}{4} I \delta m^2$, where δT is the change in electron kinetic energy. For ferromagnetic states, there is an increase in the electron kinetic energy, by spin-down states, which are just below the nonmagnetic Fermi level, flipping to spin-up states, which must occupy states above the nonmagnetic Fermi level. This leads to the Stoner criterion of spontaneous ferromagnetic order

$$I D(E_{\mathrm{F}}) > 1, \tag{2.61}$$

where $D(E_\mathrm{F})$ is the nonmagnetic density of states per spin.

All calculations with magnetism in this thesis start from a ferromagnetic ground-state.

2.4.4 Forces

To obtain the forces from tight-binding, one must take the derivative of the cohesive energy with respect to ion position. A small change in the position of an ion at $\mathbf{R}$, $\delta\mathbf{R}$ gives a change in the total energy δE_tot of [81]

$$\delta E_\mathrm{tot} = \left.\frac{\partial E_\mathrm{tot}}{\partial \mathbf{R}}\right|_{\{C^n_{\mathbf{R}L}\}} \cdot \delta\mathbf{R} + \sum_{n\mathbf{R}'L'} \left.\frac{\partial E_\mathrm{tot}}{\partial C^n_{\mathbf{R}'L'}}\right|_{\mathbf{R}} \delta C^n_{\mathbf{R}'L'}, \tag{2.62}$$

where $\frac{\partial E_\mathrm{tot}}{\partial \mathbf{R}}$ is the vector gradient with respect to the components of the ion position

$$\frac{\partial E_\mathrm{tot}}{\partial \mathbf{R}} \equiv \left(\frac{\partial E_\mathrm{tot}}{\partial R_x}, \frac{\partial E_\mathrm{tot}}{\partial R_y}, \frac{\partial E_\mathrm{tot}}{\partial R_z}\right). \tag{2.63}$$

The term $\frac{\partial E_\mathrm{tot}}{\partial C^n_{\mathbf{R}'L'}}$ is the change in the total energy with respect to the wavefunction coefficients, where the change in the wavefunction coefficient is constrained to those which satisfy the matrix eigenvalue equation (2.36) and the normalisation condition, $\sum_{\mathbf{R}L\mathbf{R}'L'} C^{n*}_{\mathbf{R}L} C^n_{\mathbf{R}'L} S_{\mathbf{R}'L'\mathbf{R}L} = 1$. Considering these constraints, one finds [81]

$$\left.\frac{\partial E_\mathrm{tot}}{\partial C^n_{\mathbf{R}'L'}}\right|_{\mathbf{R}} = \sum_{n\mathbf{R}'L'\mathbf{R}''L''} f_n \epsilon_n C^{n*}_{\mathbf{R}'L'} \frac{\partial S_{\mathbf{R}'L'\mathbf{R}''L''}}{\partial \mathbf{R}} C^n_{\mathbf{R}''L''} \cdot \delta\mathbf{R}. \tag{2.64}$$

The total energy in the tight-binding bond model is given as $E_\mathrm{tot} = E_\mathrm{cov} + E_\mathrm{prom} + E_\mathrm{free} + E_\mathrm{pair} = E_\mathrm{band} + E_\mathrm{pair}$. The derivative of the pair potential is trivial, as it is an analytic function. To evaluate the derivative of the band energy, equation (2.44), we make use of the Hellmann-Feynman Theorem [105, 106], where the derivative of the band energy is given by the expectation value of derivative of the Hamiltonian operator

$$\left.\frac{\partial E_\mathrm{band}}{\partial \mathbf{R}}\right|_{\{C^n_{\mathbf{R}L}\}} = \sum_{n\mathbf{R}L\mathbf{R}'L'} f_n \epsilon_n C^{n*}_{\mathbf{R}'L'} C^n_{\mathbf{R}L} \left\langle \mathbf{R}'L' \right| \frac{\partial}{\partial \mathbf{R}} \hat{H}^\mathrm{in} \left| \mathbf{R}L \right\rangle, \tag{2.65}$$

We know only the dependence of the parameterised terms in tight-binding: the matrix elements $H_{\mathbf{R}'L',\mathbf{R}L}(\mathbf{R})$, and the overlap matrix $S_{\mathbf{R}'L',\mathbf{R}L}(\mathbf{R})$. Therefore, to obtain the expectation of the derivative of the Hamiltonian operator in equation (2.65), we can use the full expression for the derivative of a matrix element from the

Hellmann-Feynman theorem to furnish us with quantities we know how to calculate

$$\frac{\partial}{\partial \mathbf{R}} H^{\text{in}}_{\mathbf{R}'L'\mathbf{R}L} = \langle \mathbf{R}'L' | \frac{\partial}{\partial \mathbf{R}} \hat{H}^{\text{in}} | \mathbf{R}L \rangle + \langle \frac{\partial}{\partial \mathbf{R}} \mathbf{R}'L' | \hat{H}^{\text{in}} | \mathbf{R}L \rangle + \langle \mathbf{R}'L' | \hat{H}^{\text{in}} | \frac{\partial}{\partial \mathbf{R}} \mathbf{R}L \rangle \tag{2.66}$$

Rearranging (2.66) to obtain an expression for $\langle \mathbf{R}'L' | \frac{\partial}{\partial \mathbf{R}} \hat{H}^{\text{in}} | \mathbf{R}L \rangle$ one obtains from equation (2.65),

$$\frac{\partial E_{\text{band}}}{\partial \mathbf{R}}\Big|_{\{C^n_{\mathbf{R}L}\}} = \sum_{n\mathbf{R}L\mathbf{R}'L'} f_n \epsilon_n C^{n*}_{\mathbf{R}'L'} C^n_{\mathbf{R}L} \left[\frac{\partial}{\partial \mathbf{R}} H^{\text{in}}_{\mathbf{R}'L'\mathbf{R}L} - \langle \frac{\partial}{\partial \mathbf{R}} \mathbf{R}'L' | \hat{H}^{\text{in}} | \mathbf{R}L \rangle - \langle \mathbf{R}'L' | \hat{H}^{\text{in}} | \frac{\partial}{\partial \mathbf{R}} \mathbf{R}L \rangle \right] \tag{2.67}$$

which after some manipulation by expanding the terms, and using the identity $\frac{\partial S_{\mathbf{R}'L'\mathbf{R}L}}{\partial \mathbf{R}} = \langle \frac{\partial}{\partial \mathbf{R}} \mathbf{R}'L' | \mathbf{R}L \rangle + \langle \mathbf{R}'L' | \frac{\partial}{\partial \mathbf{R}} \mathbf{R}L \rangle$ leads to [107]

$$\frac{\partial E_{\text{band}}}{\partial \mathbf{R}}\Big|_{\{C^n_{\mathbf{R}L}\}} = \sum_{\mathbf{R}L\mathbf{R}'L'\mathbf{R}' \neq \mathbf{R}} \rho^{\mathbf{R}L\mathbf{R}'L'} \left[\frac{\partial H^{\text{in}}_{\mathbf{R}'L'\mathbf{R}L}}{\partial \mathbf{R}} - \epsilon_n \frac{\partial S_{\mathbf{R}'L'\mathbf{R}L}}{\partial \mathbf{R}} \right], \tag{2.68}$$

giving the necessary terms to evaluate the force.

In the tight-binding bond model, there is no contribution to the force from the on-site elements due to the condition of local charge neutrality [81, 89]. Therefore, one obtains the force in an orthogonal model as [81]

$$F^{\text{TBBM}}_{\mathbf{R}} = - \sum_{L\mathbf{R}'L'\mathbf{R}' \neq \mathbf{R}} \rho^{\mathbf{R}L\mathbf{R}'L'} \frac{\partial H^{\text{in}}_{\mathbf{R}'L'\mathbf{R}L}}{\partial \mathbf{R}} - \sum_{\mathbf{R}' \neq \mathbf{R}} \frac{\partial V_{\text{pair}}}{\partial \mathbf{R}}, \tag{2.69}$$

where V_{pair} is the pair potential.

For an orthogonal SCTM model, one includes the on-site terms again, giving

$$F^{\text{SCTM}}_{\mathbf{R}} = - \sum_{LL'} \rho^{\mathbf{R}L\mathbf{R}L'} \frac{\partial H^{\text{in}}_{\mathbf{R}'L'\mathbf{R}L}}{\partial \mathbf{R}} - \sum_{L\mathbf{R}'L'\mathbf{R}' \neq \mathbf{R}} \rho^{\mathbf{R}L\mathbf{R}'L'} \frac{\partial H^{\text{in}}_{\mathbf{R}'L'\mathbf{R}L}}{\partial \mathbf{R}} - \sum_{\mathbf{R}' \neq \mathbf{R}} \frac{\partial V_{\text{pair}}}{\partial \mathbf{R}} - \sum_{\mathbf{R}'} \delta q_{\mathbf{R}} \delta q_{\mathbf{R}'} \frac{\mathbf{R} - \mathbf{R}'}{|\mathbf{R} - \mathbf{R}'|^3}, \tag{2.70}$$

For an orthogonal PITB model, one obtains

$$F_{\mathbf{R}}^{\mathrm{PITB}} = -\sum_{LL'} \rho^{\mathbf{R}L\mathbf{R}L'} \frac{\partial H^{\mathrm{in}}_{\mathbf{R}'L'\mathbf{R}L}}{\partial \mathbf{R}} - \sum_{L\mathbf{R}'L'\mathbf{R}'\neq\mathbf{R}} \rho^{\mathbf{R}L\mathbf{R}'L'} \frac{\partial H^{\mathrm{in}}_{\mathbf{R}'L'\mathbf{R}L}}{\partial \mathbf{R}} - \sum_{\mathbf{R}'\neq\mathbf{R}} \frac{\partial V_{\mathrm{pair}}}{\partial \mathbf{R}} - \sum_{L} Q_{\mathbf{R}L} \nabla V_{\mathbf{R}L}. \tag{2.71}$$

where the derivative of the final term is easily evaluated from the derivative of the structure constant matrix (2.57), which is composed of analytic Hankel functions.

2.5 Saddle Search Methods

In many physics models, one wants to find configurations of the system which have the lowest energy, when starting from an initial configuration. In terms of the potential energy surface of the system, these states are wells, corresponding to a local minimum in configuration space. It is common in systems of multiple dimensions to have many local minima, and in real systems, one sees there are transitions between local minima due to thermal activation. In such cases, one might ask the question, what is the rate of transition between these states? To answer this, one can use the machinery of transition-state theory [108], in which the harmonic approximation of Vineyard [109] can be used to obtain the attempt frequency ν^*, which is the prefactor for the rate of transition, given by the Arrhenius expression $\Gamma = \nu^* \exp\{-\Delta E/k_{\mathrm{B}}T\}$. However to obtain ν^* and the energy barrier ΔE, we must first obtain the transition state between the two systems.

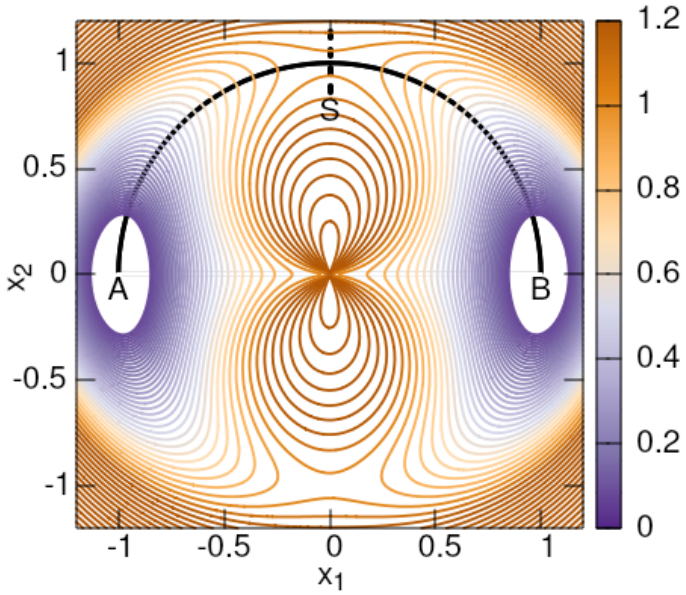

Fig. 2.2: Diagram of minimum energy pathway between two local minima A and B, the black line, on a potential energy surface, the orange contours. The saddle point S is given where the dashed line meets the black line. Function shown is of $(1 - x^2 - y^2)^2 + y^2/(x^2 + y^2)$, where the minimum energy pathway (MEP) is a unit circle.

The point on the potential energy surface which corresponds to the smallest barrier along the minimum energy path (MEP) between the two minima is necessarily a saddle point: from it, the potential energy should increase for all degrees of freedom bar that which pertains to transition between the states, along which the energy decreases in both directions. This can be visualised in figure 2.2.

To find these saddle points between two minima, one can use methods such as the Nudged-Elastic Band method [110] and the String method [111, 112], where the latter method is a special case of the former. Here we follow the notation of Makri *et al.* [113].

Given a potential $V(\mathbf{x})$, which has two minima at $\mathbf{x}_A$ and $\mathbf{x}_B$, we wish to obtain the saddle point between them $\mathbf{x}_S$, which corresponds to the maximum of a minimum energy path on the potential energy surface between these minima. To obtain this, we can parameterise the path between the two endpoints as $\mathbf{x}^*(s)$, where $s \in [0, 1]$

with $\mathbf{x}^*(0) = \mathbf{x}_A$ and $\mathbf{x}^*(1) = \mathbf{x}_B$. The minimum energy path between the endpoints is defined by the equation

$$\nabla^{\perp} V(\mathbf{x}^*) \equiv \mathbf{0}, \tag{2.72}$$

where $\nabla^{\perp} V(\mathbf{x}) = \left(\mathbf{1} - \frac{\mathbf{x}'}{||\mathbf{x}'||} \otimes \frac{\mathbf{x}'}{||\mathbf{x}'||}\right) \nabla V(\mathbf{x})$ is the force perpendicular to the path direction, and $\mathbf{x}' = \frac{\mathrm{d}\mathbf{x}}{\mathrm{d}s}$. We denote the second derivative with respect to s as $\mathbf{x}'' = \frac{\mathrm{d}^2\mathbf{x}}{\mathrm{d}s^2}$, with double vertical bars denoting the norm of the vector.

To find this minimum energy path, we can initially take N discrete points in configuration space, labelled $\mathbf{x}_n$ between the endpoints, N images, from which we can sample the potential energy surface.

In the NEB method, we introduce spring forces $\boldsymbol{\eta}_n$ which act between the images along the line of the path. These act to keep images distributed evenly along the path in configurational space.

To optimise the minimum energy path, one can introduce a pseudo-temporal coordinate τ, which we make equivalent to the force $\mathbf{F} \equiv \frac{\mathrm{d}\mathbf{x}}{\mathrm{d}\tau}$, so we wish to solve the system of ODEs

$$\mathbf{F} \equiv \frac{\mathrm{d}\mathbf{x}_n}{\mathrm{d}\tau} = -\nabla^{\perp} V(\mathbf{x_n}) + \boldsymbol{\eta}_n(\mathbf{x}_n', \mathbf{x}_n'') \tag{2.73}$$

where in the case of NEB, we have

$$\boldsymbol{\eta}_n^{\mathrm{NEB}}(\mathbf{x}_n', \mathbf{x}_n'') = \kappa \left(\mathbf{x}_n'' \cdot \frac{\mathbf{x}_n'}{||\mathbf{x}_n||}\right) \frac{\mathbf{x}_n'}{||\mathbf{x}_n||}, \tag{2.74}$$

where κ is the spring constant, and for the string method, we have $\boldsymbol{\eta}_n^{\mathrm{string}} = \mathbf{0}$.

Then one can evolve the system of images by using an appropriate solver. Using Euler's method, one finds the usual update at iteration k of,

$$\mathbf{x}_n^{k+1} = \mathbf{x}_n^k + \alpha^k \left[-\nabla^{\perp} V(\mathbf{x_n}) + \boldsymbol{\eta}_n^k(\mathbf{x}_n^{k'}, \mathbf{x}_n^{k''})\right], \tag{2.75}$$

where α^k is the timestep at iteration k. We can evolve the images until the maximum root mean square difference of the forces from equation (2.73) between iterations, are below some specified tolerance.

2.6 Dislocations

To understand the deformation characteristics of materials, one must understand dislocations, the fundamental defects which control plasticity. Dislocations are line defects

in the crystal structure of a material. They allow for the flow and accumulation of plasticity through glide and multiplication.

One can imagine a dislocation in an isotropic continua, as in figure 2.3. If one applies a shear stress to the material, deformation may occur. In figure 2.3, one sees that this displacement is along the y direction, by the vector $\mathbf{b} = b\hat{\mathbf{y}}$ relative to the perfect crystal, and the displacement is of the material is bounded by the blue-red line. This is the dislocation line.

The *Burgers vector* $\mathbf{b}$, defines the dislocation, and it is an invariant quantity along the dislocation line. It can be determined by taking a Burgers circuit: integrating the displacement around the dislocation line in a closed loop and comparing that to the perfect lattice. The convention taken in this thesis is "FS/RH" convention [7], where a clockwise circuit is taken around a dislocation with a line-sense that goes into the page. The Burgers vector is the difference of the final position from the initial, when the same path has been taken on a perfect lattice. Dislocation character can be determined by the line-sense $\boldsymbol{\xi}$, and the Burgers vector. There are two possible characters of pure dislocations, edge (as seen in blue, denoted by the symbol $\perp$) where the Burgers vector is perpendicular to the line-sense, and screw (as seen in red, denoted by the symbol §) where the Burgers vector is parallel to the line-sense. Between these characters we have mixed dislocations, given by the purple region between the two.

The *glide plane* of a dislocation is that which contains both the Burgers vector and the line-sense. Edge dislocations can only glide in one plane, the plane in which it was formed. However the glide plane for screw dislocations is ambiguous, and in fact, screw dislocations can glide in any close-packed plane. When a screw dislocation changes glide plane, it is said to have undergone *cross-slip*.

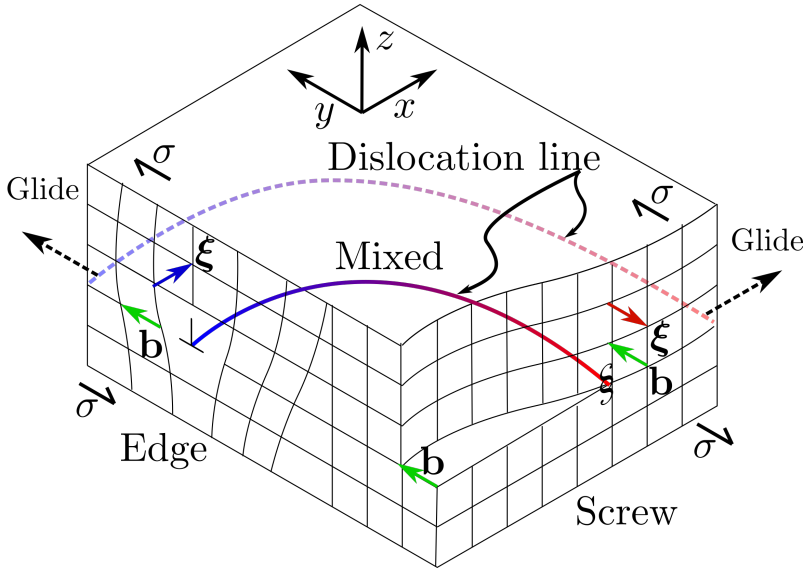

Fig. 2.3: Diagram showing edge and screw dislocation as part of the whole dislocation line. Blue to red gradient shows the dislocation line character, which changes from pure edge (blue) to pure screw (red). When the shear stress σ is imposed, glide of pure screw segments occurs along the x direction, with pure edge segments gliding on the y direction. Dislocation which has undergone glide is given by the dotted line, with the same gradient colour scheme.

The movement of dislocations can occur by application of stress above a critical value, which causes segments of the dislocation line to move. If one applies a large enough shear stress σ, in figure 2.3, the pure screw segments, the red part of line, can glide along the x direction, and the edge segments, the blue part of the line, can glide along the y direction, causing the dislocation line to move (dashed blue-red line). The general equation for the force per unit length on a dislocation, from an applied stress $\boldsymbol{\sigma}$, is the Peach-Koehler force

$$\mathbf{F} = (\boldsymbol{\sigma} \cdot \mathbf{b}) \times \boldsymbol{\xi}. \tag{2.76}$$

In real materials, the stress necessary to cause dislocation glide depends on the character of the dislocation, the crystal structure, the elements which compose the crystal and impurity content. The nature of dislocation glide is also not smooth, as suggested by the isotropic continua diagram. This is due to the oscillating energy landscape in which a dislocation resides, of which is generated from atomic potentials of

the deformed crystal structure: the *Peierls potential*. Without stress, dislocations will reside in valleys of this potential, which correspond to zone axes of the crystal: between rows of atoms. Dislocations glide by the movement of a dislocation segment into a neighbouring Peierls valley by a kink-pair mechanism, as seen in figure 1.2, left. This occurs by a segment of the dislocation line having gained enough energy, from thermal activation or a lowering of the Peierls potential by application of stress, to overcome the Peierls barrier. This creates a *kink-pair*, where two new segments of dislocation, which have opposite signs, are formed in the glide plane of the dislocation, which adjoin the pioneering segment which has undergone migration to the next valley, as shown in the diagram in figure 2.4. If the kink-pair formed is stable—if the oppositely signed dislocations do not come together and annihilate—the kinks may migrate along the length of the dislocation line, which causes the whole of the dislocation line to move to the next Peierls valley.

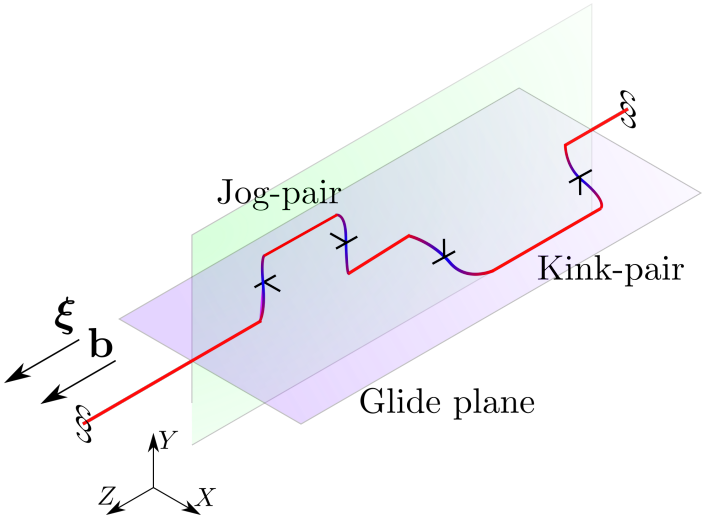

Fig. 2.4: Diagram of jogs and kinks on a screw dislocation with edge segments in blue and screw segments in red.

Segments of the dislocation line may also be formed which are not in the glide plane of the dislocation. These segments are called *jogs*, and can be formed under thermal activation or by interactions, as seen in figure 2.4. Large jogs, those of multiple atomic spacings in length, are called superjogs. For edge dislocations, jogs are just edge dislocations, and movement along the initial glide plane is uninhibited. However, jogs on screw dislocations (relative to a particular glide plane of interest) create segments of edge character in which the applied stress necessary to move them is perpendicular

to that which enacts screw dislocation glide. This can severely inhibit the motion of screw dislocations, thus causing an increase in lattice friction and strengthening.

2.7 Anisotropic Elasticity

Defects in materials cause deformations in the parent material, which can lead to long-ranged interactions. Given deformations which are sufficiently small in magnitude, such that the gradients in displacement are not too large, the stresses generated by these defects can be well-described by *linear elasticity theory*. Here we follow the book of Sutton [114], with slight changes in notation for consistency with Stroh [115] and Hirth and Lothe [7].

Given an arbitrary point $\mathbf{x}'$ in a material with a defect, there will be a displacement of the material $\mathbf{u} = \mathbf{x}' - \mathbf{x}$ from its perfect state $\mathbf{x}$. Within linear elasticity, if the displacement gradient around the point is assumed to be small, one can define a *Lagrangian strain tensor*

$$\varepsilon_{kl} = \frac{1}{2}\left(\frac{\partial u_k}{\partial x_l} + \frac{\partial u_l}{\partial x_k}\right). \tag{2.77}$$

The strain field generated from the defect can be related to a stress through Hooke's law,

$$\sigma_{ij} = C_{ijkl}\varepsilon_{kl}, \tag{2.78}$$

where σ_{ij} is the stress tensor and C_{ijkl} is the elastic constant tensor. The Einstein summation convention, where it is implied that repeated indices are summed over, is used here throughout the rest of this section. A particular component of the stress tensor is the force per unit area, which acts through a particular area, in a particular direction.

Consider a region $\mathcal{R}$, bounded by a surface $\mathcal{S}$, within a body. For each infinitesimal volume element in $\mathcal{R}$, one can state there is a force acting on that element, a body force $\mathbf{f}$, which is a force per unit volume: a typical example of a body force is that of gravity. These forces cause the material around $\mathcal{R}$ to deform in response. Under mechanical equilibrium, the sum of the body forces acting within $\mathcal{R}$, must be balanced by the stresses which act through the surface $\mathcal{S}$, which were generated in response to the body forces. This results in the stress tensor at every point in the body satisfying the equation,

$$\frac{\partial \sigma_{ij}}{\partial x_j} + f_i = 0, \tag{2.79}$$

where f_i is a component of a body force, within $\mathcal{R}$. Under the requirement of no resultant torque at equilibrium—conservation of angular momentum—the stress tensor becomes symmetric.

To simulate dislocations, one must be able to calculate the displacement field which defines them. This can be achieved with the *anisotropic elasticity solutions*. Here, we use the extended formalism as developed by Stroh [115] following the notation of Hirth and Lothe [7].

A dislocation is a line defect. The direction of the line can be defined by a unit vector $\boldsymbol{\xi}$ which is the *line sense*. Orthogonal vectors to this line sense can be defined, $\mathbf{m}$ and $\mathbf{n}$, where $\mathbf{n}$ defines the cut-plane normal of the dislocation, and $\mathbf{m}$ is a vector in the cut plane, where $\boldsymbol{\xi} = \mathbf{m} \times \mathbf{n}$.

From the definition of the strain tensor, equation (2.77), and by use of Hooke's law, equation (2.78), one wishes to find the displacements of

$$\sigma_{ij} = C_{ijkl} \frac{\partial u_k}{\partial x_l}, \tag{2.80}$$

where the indexes $i, j, k, l = 1, 2, 3$. We consider only the internal strain in the body, and therefore take the body force acting per unit volume as zero, reducing the equation for mechanical equilibrium, equation (2.79), to $\frac{\partial \sigma_{ij}}{\partial x_j} = 0$, which in conjunction with equation (2.80), gives the equations we can solve for the displacements

$$C_{ijkl} \frac{\partial^2 u_k}{\partial x_j \partial x_l} = 0. \tag{2.81}$$

To solve equation (2.81), we can seek trial solutions for $\mathbf{u}$ of the form

$$\mathbf{u} = \mathbf{A} f(\eta), \tag{2.82}$$

where $\mathbf{A}$ is a vector and $f(z)$ is an analytic function of the complex variable z, which will be defined later. η is defined as

$$\eta = \mathbf{m} \cdot \mathbf{x} + p\mathbf{n} \cdot \mathbf{x}. \tag{2.83}$$

We define a shorthand notation: given two vectors $\mathbf{a}$ and $\mathbf{b}$, the matrix (ab) is defined by $(ab)_{jk} = a_i C_{ijkl} b_l$. Using this notation, we see equation (2.82) is a solution if $\mathbf{A}$ satisfies

$$\left\{ (mm) + \left[(mn + nm) \right] p + (nn) p^2 \right\} \mathbf{A} = 0, \tag{2.84}$$

Non-trivial solutions for $\mathbf{A}$ can be determined if p is a root of the sextic equation

$$\det\left((mm) + [(mn + nm)]\, p + (nn)p^2\right) = 0. \tag{2.85}$$

The roots of this equation are complex, giving three roots with their complex conjugate pairs. The three roots with positive imaginary components are denoted by p_α, $\alpha = 1, 2, 3$, with their complex conjugates as p_α, $\alpha = 4, 5, 6$. The value of $\mathbf{A}$ obtained by the root p_α is hereon denoted by $\mathbf{A}_\alpha$ and similarly for other quantities.

Related to $\mathbf{A}_\alpha$ is the quantity $\mathbf{L}_\alpha$, given by

$$\mathbf{L}_\alpha = -\left[(nm) + p_\alpha(nn)\right]\mathbf{A}_\alpha, \tag{2.86}$$

which obey the orthogonality relations

$$2\mathbf{A}_\alpha \cdot \mathbf{L}_\alpha = 1, \tag{2.87}$$

for each α.

Along the cut plane of a dislocation, considering a component of the displacement u_k there is, by definition, a discontinuity in the displacement which is equal to the Burgers vector component b_k. Considering the form of the function $f(\eta)$, one finds that the form for $f(\eta)$ which is commensurate with real dislocations is

$$f(\eta_\alpha) = \frac{D(\alpha)}{2\pi i}\ln(\eta_\alpha), \tag{2.88}$$

where $D(\alpha)$ is a constant.

These $D(\alpha)$ can be determined from the orthogonality relations, equation (2.87), and from the boundary conditions related to the discontinuity of the Burgers vector and the requirement of no force to be found at the core of the dislocation

$$\sum_{\alpha=1}^{6} \pm D(\alpha)\mathbf{A}_\alpha = \mathbf{b}, \tag{2.89}$$

$$\sum_{\alpha=1}^{6} \pm D(\alpha)\mathbf{L}_\alpha = \mathbf{0}, \tag{2.90}$$

where $\pm$ is defined by the sign of the imaginary component of the corresponding p_α.

These relations produce $D(\alpha)$ by the equation

$$D(\alpha) = \pm \mathbf{L}_\alpha \cdot \mathbf{b}. \tag{2.91}$$

With this, the displacements are fully determined by

$$\mathbf{u} = \frac{1}{2\pi i} \sum_{\alpha=1}^{6} D(\alpha) \mathbf{A}_\alpha \ln \eta_\alpha, \tag{2.92}$$

from which the distortion tensor can be found

$$\frac{\partial u_k}{\partial x_l} = \frac{1}{2\pi i} \sum_{\alpha=1}^{6} \pm \left[m_l + p_\alpha n_l \right] A_{\alpha k} \left[\mathbf{L}_\alpha \cdot \mathbf{b} \right] \frac{1}{\eta_\alpha}, \tag{2.93}$$

which relate to the stresses by Hooke's law (2.78)

$$\sigma_{ij} = \frac{1}{2\pi i} \sum_{\alpha=1}^{6} \pm C_{ijkl} \left[m_l + p_\alpha n_l \right] A_{\alpha k} \left[\mathbf{L}_\alpha \cdot \mathbf{b} \right] \frac{1}{\eta_\alpha}, \tag{2.94}$$

The force along the cut-plane of the dislocation is given by resolved stress

$$\boldsymbol{\sigma} \cdot \mathbf{n} = -\frac{1}{2\pi i} \sum_{\alpha=1}^{6} \pm \mathbf{L}_\alpha \left[\mathbf{L}_\alpha \cdot \mathbf{b} \right] \frac{1}{\mathbf{m} \cdot \mathbf{x}}. \tag{2.95}$$

To create the dislocation, work is done against this force to create the displacement discontinuity $\mathbf{b}$. The work done per unit length is given by $\mathbf{b} \cdot \boldsymbol{\sigma} \cdot \mathbf{n}/2$ in linear elasticity, giving

$$\frac{W}{L} = -\frac{1}{4\pi i} \left(\sum_{\alpha=1}^{6} \left[\mathbf{b} \cdot \mathbf{L} \right] \left[\mathbf{L} \cdot \mathbf{b} \right] \right) \ln \frac{R}{R_c}, \tag{2.96}$$

where R is the radius around the dislocation considered and R_c is the core radius. This gives the energy-coefficient tensor, for the logarithmic prefactor, as the tensor product of the $\mathbf{L}_\alpha$ vectors

$$\mathbf{K} = i \sum_{\alpha=1}^{6} \pm L_{\alpha k} L_{\alpha l}. \tag{2.97}$$

Chapter 3

Fitting tight-binding models of titanium systems

3.1 Introduction

To describe and predict the properties of fundamental defects controlling plasticity in titanium, one can fit simple quantum mechanical models, such as tight-binding models, to describe atomic interactions. This allows for an explicit description of atomic bonding due to electronic structure, which is vital for defect structures and energies, quantities which empirical potentials have difficulty reproducing [116–118]. In addition, tight-binding methods have better scalability than DFT, due to a many-fold reduction of the $\mathcal{O}(N^3)$ scaling prefactor, allowing for thousands of atoms to be simulated using the same computational resources as that for hundreds of DFT atoms. Furthermore, there is an ease of interpretation compared to DFT, due to the partitioning of the total energy into different energy contributions, as discussed in section 2.4.

In the literature, there have been many previous tight-binding titanium models. Legrand pioneered titanium defect calculations using tight-binding in the 1980's [119, 120], with a simple d-band model parameterised on the LMTO-DFT results of Jepsen [121]. This model used the Gaussian density of states approach with the recursion method to approximately diagonalise the tight-binding Hamiltonian [122–124]. This predicted a prismatically dissociated core structure for the $\langle a \rangle \equiv 1/3\langle 11\bar{2}0 \rangle$ screw dislocation in titanium, which agrees with the prevalence of prismatic glide in titanium [12, 15, 24]. Girshick *et al.* [125, 126] similarly parameterised a d-only bond order potential—another recursion method scheme—by fitting the d-band width to

calculations of Harrison [84], and the pair potential to the empirical elastic constants by splines—however this resulted in a model which did not generalise well enough to dislocations, predicting a basal dissociation for the ground-state $\langle a \rangle$ screw core structure, due to the opposite energetic ordering of prismatic and basal stacking fault energies. The modified tight-binding scheme of Trinkle *et al.* [118] parameterised a non-orthogonal s, p, d-valence tight-binding model by fitting to density functional theory data, using splines to curtail the bond integrals at short range to circumvent the need for short-range Coulomb interactions. This model was able to describe hcp and omega phases, but ultimately fell foul of instability issues [127]. Urban *et al.* also parameterised an s, p, d-electron non-orthogonal tight-binding model on DFT data [128], from which a d-only model was determined by Löwdin orthogonalisation [129]. Neither of these models were used in applications outside of the paper in which they were presented, with the group moving on to perform a new parameterisation by Ferrari *et al.* [130], implying that the models did not generalise well to defect modelling. The bond order potential of Ferrari *et al.* is based on a non-orthogonal tight-binding parameterisation fit to DFT data, which has been orthogonalised and optimised, similar to the Urban model, but with the inclusion of an EAM-like embedding potential to model s-electrons [130]. This model could describe transformation path energies between the bcc $\leftrightarrow$ hcp and bcc $\leftrightarrow$ omega phases, but stacking fault energies on the prismatic plane did not allow for realistic dislocation simulations, obtaining a prismatic fault energy ~ 5 times less than the DFT prediction [19].

Interestingly, the only models which have explicitly simulated dislocations in the literature are the simplest: the bond-order potential of Girshick *et al.*, which predicted an erroneous basal spreading [131], and the Legrand model, which produced a prismatically spread core structure, in-keeping with current theory, but with use of a sizeable approximation, that of a Gaussian local density of states. More complex models have not simulated dislocations, perhaps partly due to the expense of non-orthogonal/direct-diagonalisation tight-binding, but more likely, dissuasion arises from poor preliminary results of defect energies, such as stacking faults, from the models themselves, given that more computationally-taxing DFT methods have been able to perform dislocation relaxations [19, 132, 133]. This agrees with the deviation of validation tests from literature data in derived models, such as that of Ferrari *et al.* [130], suggesting that these models are overfit to the data they were supplied with during fitting. The chance of overfitting increases with model complexity: the number of parameters to fit [134, 135]. Hence, it would be of use to create a new titanium

tight-binding model which contains enough physics/parameters to agree with the experimental and *ab-initio* results—elastic constants, cohesive energies, stacking fault energies, dislocation core structures *etc*—while being simple enough to mitigate the problem of overfitting, allowing for a transferable tight-binding model, which additionally welcomes the benefit of scalability to large numbers of atoms.

There are many-fold benefits to increased scalability. In explicit dislocation simulations, there is a reduction of the influence of boundary conditions on dislocation relaxation, allowing for accurate core structure resolution. There is also an enhanced scope of simulations available, which would be prohibitively expensive in DFT, such as explicit calculations of the Peierls stress of dislocations on different glide planes, NEB calculations for kink-pair formation energies of dislocations and solute migration in the vicinity of dislocations, and so on.

In this work, two separate titanium tight-binding models were fitted: one with only d valence electrons, and another with s and d valence, hereon referred to as the d and sd models respectively. Both models were parameterised with the aim of modelling defects, in particular modelling of dislocations and their solute interactions in titanium alloys, to improve upon the aforementioned tight-binding models, and to shed light on the dramatic solute-hardening effect of oxygen in titanium with oxygen content. The sd tight-binding model was also fitted for integration with the polarisable-ion tight-binding model of TiO_2/H_2O, originally developed by Lozovoi and Paxton *et al.*, in which the Ti-Ti parameters give unsatisfactory results for bulk Ti properties [136]. Ti-H parameters were fitted to properties of TiH_2. Integration of the sd titanium model with the $TiO_2/TiH_2/H_2O$ model would result in a tight-binding model with many applications, allowing for simulations of water on a titanium surface, electrochemistry simulations and the modelling of stress-corrosion cracking.

3.2 Methods

3.2.1 Ti-Ti parameters

The bond integrals for both the d and sd-models were chosen to have a simple exponential distance dependence.

$$V_{\ell\ell' m}(r) = V^0_{\ell\ell' m} \exp\{-p_{\ell\ell' m} r\}, \tag{3.1}$$

where $V_{\ell\ell' m}$ is the bond integral between orbitals ℓ and ℓ', with bonding orbital m, $p_{\ell\ell' m}$ is the exponent and r is the distance between the atoms of interest. The bond integrals $V_{\ell\ell' m}$, will be denoted as $\ell\ell' m$ for convenience. For the d model, only $dd\sigma$, $dd\pi$ and $dd\delta$ bond integrals were used. Additional $ss\sigma$ and $sd\sigma$ bond integrals were used in the sd-model.

Analysis of the hybridisation of d states with nearly-free electron states in transition metals gives rise to d-band resonances, which suggest a fifth-degree power law distance dependence of d-orbitals for the matrix elements [84, 104, 137–139]. However, it has not been shown that a power-law dependence exhibits better transferability over a simple exponential dependence [140, 141]. Many power-law models have not fared well in predicting data outside of their fitting range [118, 125, 142–144]. Furthermore, power laws have large first or second derivatives compared to exponentials, when modified by a cutoff function. The large derivatives of power laws can complicate fitting for elastic properties, and would provide noisy forces [145].

Canonical band theory [89, 139] suggests that the bond integrals are in the ratio

$$dd\sigma : dd\pi : dd\delta = -6 : 4 : -1. \tag{3.2}$$

It has been shown in an sd non-orthogonal model of titanium, which has subsequently been orthogonalised to a d-band only model, that bond integral ratios can deviate from canonical band theory; in the case of Urban *et al.* [128], the ratio turned out to be $dd\sigma : dd\pi : dd\delta = -4.3 : 3.6 : -1$. This orthogonalisation procedure results in bond integrals which approximately account for environmental dependence by bond screening [79, 128, 146]. This provided an estimate for how much one could allow the canonical band ratios to vary during fitting. For the purpose of fitting these models, the canonical band ratios were allowed to deviate from the ideal ratio by 25%.

In tight-binding, each orbital has a finite extent. To achieve this, the bond integrals and pair potential are modified by a cutoff function, which forces these functions to decay to zero from a given radius r_1 to the extent r_c. A fifth-order multiplicative polynomial was used in these models as the cutoff function, with r_1 chosen to be between first and second neighbours in the hcp structure, and r_c between second and third-neighbours. This gave the value of the function of interest in the tail, f_{tail}, when

between r_1 and r_c, as

$$f_{\text{tail}}(r) = (R)^{-5}(f(r)R^2 + (r-r_1)((R\frac{\mathrm{d}f(r)}{\mathrm{d}r} - 3f(r))R + (r-r_1)(\frac{1}{2}\frac{\mathrm{d}^2f(r)}{\mathrm{d}r}R - 3\frac{\mathrm{d}f(r)}{\mathrm{d}r})R + 6f(r)))(r-r_c)^3, \quad (3.3)$$

where $R = r_1 - r_c$ and $f(r)$ is the function which is being cut off (the bond integrals or the pair potential). It was verified that the cutoffs were not close to neighbour shells found in titanium polymorphs, such that in future simulations, there would be no large and sudden forces arising from the inclusion of extra neighbours, as would be the case in molecular dynamics or defect simulations. A multiplicative cutoff type was preferred over augmentative as it has been shown to mitigate the effect of large second-derivatives, which can cause difficulty in replicating experimental elastic constants and phonon dispersion [145].

In fitting, it was found that having only first-neighbour interactions, for our particular paradigm of functional forms for bond integrals and the pair potential, did not give desirable properties for the hcp phase: elastic constants generated for the hcp phase resulted in negative Cauchy pressures and a poor description of the energy difference between titanium polymorphs. Increasing the range of the interactions to second-neighbours produced more favourable results.

The form of the pair potential was chosen to be a simple sum of two exponentials, with a rapidly decaying power law term included only in the *d*-model.

$$V_{\text{pair}}(r) = A_1 \exp\{-p_1 r\} - A_2 \exp\{-p_2 r\} + A_3 r^{-b_3}, \quad (3.4)$$

where r is the distance between two species, and A_i, p_i and b_i are parameters. Of these terms, the exponentials, which have one large positive term, and a smaller negative term, contribute the most over the range of interaction, with the power law chosen to only increase the repulsion at smaller distances. The addition of this power law was to give γ-surface energies reminiscent of DFT due to the close proximity of atoms at particular stacking faults. This will be discussed in section 3.2.2.3. The resultant pair potential was highly repulsive at short distances, yet became slightly attractive at larger distances. This allowed for one to approximately account for the attractive effect of *sd* hybridisation in this simple *d*-orbital only model, as done in previous, exclusively *d*-orbital, tight-binding models for titanium [125]. Even though hybridisation is not pairwise in character, we did not deem it necessary to add in extra parameters or

effects to complicate, or risk overfitting, the model. The results of parameter fitting and a summation of the functional forms used will be found later in section 3.3.1.

The data used to fit to was a mix of DFT and empirical data. Great importance was given to the hcp lattice parameter, and the structural energy differences between the titanium polymorphs, all of which were compared to GGA-LMTO calculations using the QUESTAAL suite [147]. Bandwidths at the high symmetry points of the hcp bands were used as targets, and calculated from DFT by ascertaining bands of dominant d character and taking the difference between the highest and lowest eigenvalues. d character was determined by decomposition of the eigenvector norm by summation over corresponding orbital subsets, similar to a Mulliken analysis.

To fit the parameters, an objective function was defined as

$$E(\mathbf{x}) = \sum_i w_i (f_i(\mathbf{x}) - \hat{f}_i)^2 + (\alpha ||\mathbf{x}||_2 + (1-\alpha)||\mathbf{x}||_1)\,, \tag{3.5}$$

where $\mathbf{x}$ is a vector of input parameters, $f_i(\mathbf{x})$ are quantities calculated from the input parameters and $\hat{f}_i$ are the respective target quantities from DFT or empirical data. w_i are the weights for each quantity, which act as feature scalers. The L2 norm is $||\mathbf{x}||_2 = \sqrt{\sum_j x_j^2}$ and the L1 norm is $||\mathbf{x}||_1 = \sum_j \mathrm{abs}(x_j)$, where x_j are the components of the input vector.

The absolute error $\mathrm{Err}_{\mathrm{abs.}}(\mathbf{x}_i)$ was used for the initial calculation of these weights $\tilde{w}_i = 1/\mathrm{Err}_{\mathrm{abs.}}(\mathbf{x}_i)^2$, $w_i = \tilde{w}_i / \sum_k \tilde{w}_k$. The absolute error for each quantity was chosen by hand. Quantities which were only given a small absolute error were of high importance, such as lattice and elastic constants, as such, the optimiser would have a preference to minimise these quantities. Barzdajn *et al.* [148] have proposed other objective functions which have resulted in a transferable tight-binding model for Fe, but this metric was deemed to be sufficient for our purposes.

To mitigate the overfitting of parameters, an Elastic Net regularisation term was added to the objective function, the final term in equation (3.5), which consists of the L1 and L2 norms of the input parameter vector $\mathbf{x}$, which was scaled prior to calculation of the regularisation term. The addition of these L1 and L2 penalties forced the parameters obtained after optimisation to be more similar, reducing the variance, and therefore the dependence on the user-chosen data in the training dataset. The L1 norm has the added benefit of allowing sparsity of the parameters during optimisation: it allows redundant parameters, say in the pair potential—the final term—to go to zero [134, 135]. One can think of this penalty as an incentive for the optimiser to

"distribute" the magnitude of the parameters more optimally, so that quantities which explain most of the behaviour will be of greater importance, and hence will be allowed a large value if necessary, and vice versa for parameters of little importance.

To hasten the fitting of parameters, if a set of parameters produced a quantity which was out of an acceptable range, the evaluation of the objective function would immediately cease and submit a large value to the optimiser, dissuading the optimisation algorithm from searching close to that area in parameter space.

The objective function was minimised within predefined constraints by use of the CMA-ES (Covariance Matrix Adaptation-Evolution Strategy) algorithm, using the python implementation by Hansen [149]. Parameters put into the CMA-ES algorithm were first transformed to have similar sensitivities with respect to the bounds in which they are sought. We achieved this by the transformations detailed by Hansen [150]. This allows for the initial assumption of the CMA-ES algorithm, that the covariance matrix is unity, to be more readily satisfied, resulting in a better conditioned parameter space for the CMA-ES to search [151, 152]. This mitigates premature convergence. Parameters were transformed back when passed into the objective function, allowing for evaluation. This objective function value was then fed into the CMA-ES optimiser.

The fitting of both the *sd*-model and *d*-model was achieved in the same fashion, with the modification that in the *sd*-model the on-site energy splitting was determined prior to full parameter fitting. Initially the levels were simply hand-tuned to reproduce the energy difference between the GGA-LMTO s and d bands. However, with the incorporation of the *sd*-model into the titania model, the band gaps for the anatase and rutile phases became non-existent, which was not apparent for the *d*-model. This was due to the bulk titanium s-states being lower in energy than the d-states, which are both found in the valence bands of anatase and rutile band structures. The addition of the s states therefore reduced/removed the band gap. To rectify this, without introducing s and d overlap integrals—which would reduce the scalability of the model due to the $\mathbf{S}$ matrix not being unity—the Ti–s on-site energy was allowed to be increased with respect to the d states, which as a consequence, increased the amount of hybridisation between the s and d bands. The choice of the s–d splitting was achieved by a rough fitting of Ti-Ti bond integrals, with additional checks that the band gaps in TiO_2 phases were preserved. The best s–d energy splitting value was chosen from the best parameter set of 10 CMA-ES optimisation runs. Then it was fixed during the last, finer stage of parameter fitting, where all parameters but the splitting were allowed to vary.

All calculations for each of the phases, bar the $4h$ and $6h$ phases, were done with a k-point mesh of $30 \times 30 \times 30$. The $4h$ and $6h$ phases had their k-points along the c-axis reduced by 2 and 4 times respectively due to the length of their cells, to keep a similar k-point density. Optimal lattice parameters were found by minimisation of the cohesive energy with respect to the given lattice constant(s) using the Nelder-Mead algorithm. Elastic constants were determined by the dependence of the energy with respect to particular strains of the structure, about the optimal lattice parameters [153, 154]. A fifth-order polynomial was fitted, to each of these dependencies, and the curvature extracted from the minimum, from which the elastic constants and bulk modulus could be calculated.

When evaluating the C_{11}, C_{12} and C_{66} elastic constants, it was necessary to fully relax the structure, to find the minimum energy at each strain, prior to the polynomial fitting. Application of certain homogeneous strains to a hcp lattice may reveal internal degrees of freedom which are not able to relax [155]. One can determine the change to these three constants by calculating internal elastic constants, as in the paper by Cousins [156]. Two of these internal elastic constants are related to phonon frequencies of the optical branches at the Γ-point. Therefore to improve agreement with phonon data, relaxation prior to elastic constant evaluation was performed when fitting the models.

Results from the first rounds of fitting found that soft modes (imaginary frequencies) would appear in the phonon spectra for omega and hcp phases, despite structural stability indicated by their elastic constants [157, 158]. This has been observed in other tight-binding models during fitting [146]. As such, it was necessary to calculate the phonon density of states during objective function evaluation, to verify there were no negative densities resulting from these imaginary frequencies. These calculations were achieved with the PHONOPY code [159].

3.2.2 Ti-Ti Validation

For a model to provide any predictive capability, it must first pass tests in which it can adequately replicate phenomena/data which it was not supplied with during the fitting phase. If a model can do so, then it gives an indication whether it generalises well to situations outside of which it was shown. If it cannot, then it is either too biased—the model is too simple—or it is overfit to the data it was trained on.

To validate the fitting of the tight-binding models, one can compare calculated quantities to empirical/density functional theory data. Vacancy formation energies

provide a measure of the bond strength between atomic species; phonon spectra show the dispersion relation of the simulated lattice under small deformations and γ-surfaces show the energies associated with the shearing of the lattice on a particular glide plane, from which one can predict dislocation dissociation distances. Further validation of the model, by calculation of solution energies, is described in section 4, due to their pertinence in dislocation modelling.

3.2.2.1 Vacancy formation energies

The vacancy formation energies were calculated using a $5 \times 5 \times 4$ titanium cell, where one titanium atom was removed, resulting in a cell of 199 atoms. The perfect cell and cell with a vacancy underwent structural and volume relaxation until all forces were below 1×10^{-5} Ry/bohr, where the k-point mesh was $6 \times 6 \times 8$. The vacancy formation energy was then calculated simply as [81]:

$$E_{\text{vac. form}} = E(\text{Ti}_{N-1}) - \frac{N-1}{N} E(\text{Ti}_N), \tag{3.6}$$

where $N = 200$ is the number of atoms in the perfect lattice and $E(\text{Ti}_{N-1})$ and $E(\text{Ti}_N)$ are the energies of relaxed cells with and without a vacancy respectively.

3.2.2.2 Phonons

Phonon spectra show the dispersion characteristics of lattice vibrations. From these spectra, one can compare how well the simulated lattice performs under small deformations to DFT methods. From numerous phonon spectra calculations, one can also predict the stability of the different phases with temperature by calculation of the Gibbs free energy. To do this one can use the quasi-harmonic approximation. By calculating the Helmholtz free energy from the phonon density of states at different volumes and using the Legendre transform, we get the Gibbs free energy

$$G(T, p) = \min_V [E_{\text{coh}}(V) + F(T; V) + pV], \tag{3.7}$$

where, $E_{\text{coh}}(V)$ is the energy of the cell at a given volume V, F is the Helmholtz free energy from the phonon density of states, with T, p and V being the temperature, pressure and volume respectively. This was achieved within the PHONOPY code [159]. $2 \times 2 \times 2$ cells were used in the phonon calculations for each of the α, β and ω phases. The k-point density was kept similar for all phases, with k-point meshes of $15 \times 15 \times 10$,

$15 \times 15 \times 15$ and $10 \times 10 \times 15$ for the α, β and ω phonon cells respectively.

3.2.2.3 Gamma surfaces

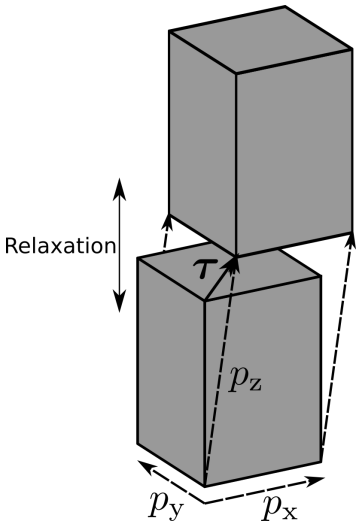

Fig. 3.1: Diagram showing sampling of γ-surface energies by shearing of a block by a fault vector $\boldsymbol{\tau}$.

A crystal can be sheared along preferential planes. In doing so, a stacking fault is created and the energy increases—assuming the crystal is stable upon the action of the shear. The variation of the excess energy of a lattice, undergoing shear by a fault vector $\boldsymbol{\tau}$, on a particular plane γ, is called a γ-surface, as shown in figure 3.1. By calculation of γ-surfaces, one can determine where *stable* stacking faults are—local minima on these surfaces—from which one can determine energetically favourable splittings of full dislocations into partials, which are necessarily bordered by stable stacking faults [160, 161]. These split configurations strongly influence the plasticity of the material, and are of great importance in hcp and fcc metals [11].

Generally, a dislocation of Burgers vector $\mathbf{b}_1$ will dissociate into partials $\mathbf{b}_2$ and $\mathbf{b}_3$ if

$$E^{\text{disl.}}_{\mathbf{b}_1} - \left\{ E^{\text{disl.}}_{\mathbf{b}_2} + E^{\text{disl.}}_{\mathbf{b}_3} + E^{\text{disl. int}}_{\mathbf{b}_2,\mathbf{b}_3} + \gamma \cdot A \right\} > 0, \tag{3.8}$$

where $E_{\mathbf{b}_1}$ is the energy of the perfect dislocation, $E_{\mathbf{b}_2}$ and $E_{\mathbf{b}_3}$ are the energies of the partial dislocations, $E^{\text{disl. int}}_{\mathbf{b}_2,\mathbf{b}_3}$ is the interaction energy between the partials, γ is the γ-surface energy and A is the area of the produced stacking fault upon dissociation.

In a tight-binding model, it is crucial that we are able to obtain the correct ordering of these stacking fault energies, such that we are more likely to obtain correct splitting

of partial dislocations when performing dislocation relaxations, thereby allowing for physical simulations. It has been shown that there is a great deal of difficulty in reproducing stacking faults in hcp titanium using methods other than DFT [119, 162, 163]. There is particular issue in reproducing the stable stacking fault on the prismatic plane, which has the associated dissociation

$$\frac{1}{3}\langle 1\bar{1}20\rangle \rightarrow \frac{1}{6}\langle 1\bar{1}20\rangle + \frac{1}{6}\langle 1\bar{1}20\rangle. \tag{3.9}$$

DFT calculations show there is a stable stacking fault along this direction, however in all the titanium tight-binding models and empirical potentials which have calculated this quantity, one does not find a minimum at the expected position. In fact, all of the models, bar that of the recursion method results of Legrand, found the prismatic fault energy was less than that of the basal fault [119, 120, 154, 164].

For the basal plane, one expects the dissociation

$$\frac{1}{3}\langle 1\bar{1}20\rangle \rightarrow \frac{1}{3}\langle 1\bar{1}00\rangle + \frac{1}{3}\langle 0\bar{1}10\rangle. \tag{3.10}$$

which is required by the symmetry of the hcp lattice, and corresponds to fcc stacking [162].

To obtain γ-surface energies, one followed a similar prescription to that of Yin *et al.* [161]. A diagram can be found in figure 3.1. First, a perfect supercell with a chosen number of planes was created, where the normal vector of the plane of interest is oriented along the Z axis. The imposition of a faulted surface was achieved by modifying the perfect lattice vector along this direction, $\mathbf{p}_z^{\text{perfect}}$, by adding the fault vector $\boldsymbol{\tau}$, giving a new principal lattice vector $\mathbf{p}_z = \boldsymbol{\tau} + \mathbf{p}_z^{\text{perfect}}$. This introduced faulted surfaces on the top and bottom of the supercell. These faulted supercells were then allowed to relax only perpendicularly to the fault (along the Z axis only).

These calculations were done in tight binding with 15 layers for both basal and prismatic γ-surfaces. The k-point meshes for the convergence were $20 \times 30 \times 2$, $30 \times 20 \times 2$ and $8 \times 30 \times 10$ for the basal, prismatic and pyramidal γ-surfaces respectively, which all gave energies within ± 0.1 mRy of a $40 \times 40 \times 10$ mesh giving an error for the gamma surface energies of ± 3 mJm^{-2}. Relaxation was performed until all forces were below 1×10^{-5} Ry/bohr.

Upon looking along the direction normal to the first-order pyramidal (π_1) plane in hcp, one finds that there is no periodicity in the stacking of planes. One must therefore use a cell which approximately has periodicity. A 32 atom cell was found to suffice, as

used by Ready *et al.* [165] in their reproduction of the full pyramidal gamma surface on the wide plane in hcp Ti using pseudopotentials. There are both narrow and wide π_1 planes. The narrow π_1 plane is relevant to $\langle a \rangle$ screw dislocation dissociation [166], with dissociation occurring by the equation [160]

$$\frac{1}{3}\langle 1\bar{1}20\rangle \rightarrow \left(\frac{1}{6}\langle 1\bar{1}20\rangle + \frac{4c^2-9a^2}{2(4c^2+3a^2)}\langle 1\bar{1}02\rangle\right) + \left(\frac{1}{6}\langle 1\bar{1}20\rangle - \frac{4c^2-9a^2}{2(4c^2+3a^2)}\langle 1\bar{1}02\rangle\right). \tag{3.11}$$

The fault vector for this dissociation corresponds to a two-layer disconnection of the $\left\{\bar{1}011\right\}$ twinning system [167]. The wide π_1 plane, is relevant to the splitting of $\langle c+a \rangle$ dislocations, which split into three Burgers vectors [165].

For the basal and prismatic planes, relaxation perpendicular to the fault plane is sufficient to obtain accurate γ-surface energies. However, as Curtin and Kwasniak detail [166, 168], to obtain realistic stable stacking fault energies for the first-order pyramidal plane, one must allow for full, unconstrained relaxation in addition to optimisation of the $\mathbf{p}_z$ lattice vector, or use the NEB method. This has been found to be necessary to obtain the true stable stacking faults in the first-order pyramidal and prism II planes, due to in-plane atomic shuffling [166]. In these tight-binding calculations, full unconstrained relaxation with volume optimisation was only performed for the narrow first-order pyramidal energies along the line equal to $\frac{1}{6}\langle 11\bar{2}0\rangle$, as the minimum along this line is pertinent $\langle a \rangle$ screw dislocation dissociation, as found in equation (3.11). The $\mathbf{p}_z$ lattice vector component normal to the surface was optimised using the Nelder-Mead algorithm. The k-point sampling and relaxation criteria for each step was identical to the initial relaxation for the full first-order pyramidal γ-surface.

3.2.2.4 Dissociation Distances

We see from equation (3.8) that there is a balance of the energy when dislocations dissociate into partials. The interaction of partials is repulsive, and goes as $1/r$ from elasticity theory. Therefore, the partials would prefer to maximise their distance, creating a large stacking fault area. However, the energy penalty in creating a stacking fault increases linearly with area, thus, there must be a compromise for the distance between the partials: the dissociation distance. One can calculate the dissociation distances of dislocations in tight-binding and compare to other interatomic force methods using the γ-surface energies and dislocation energy coefficient matrices found from each

method. These results can give indications of dislocation behaviour prior to performing full relaxations.

Following Clouet [155], we can use the result of the self-energy of a dislocation [7, 169] as in equation (2.96), to compute the dissociation distance of a dislocation in particular planes. The energy variation caused by a dissociation of a dislocation of length d is given by

$$\Delta E_{\text{diss}}(d) = -b_i^{(1)} K_{ij} b_j^{(2)} \ln\left(\frac{d}{r_c}\right) + \gamma d, \tag{3.12}$$

where $b^{(k)}$ are the Burgers vectors of the dissociated dislocations. γ is the corresponding gamma surface energy, r_c is the dislocation core radius and K is the energy-coefficient matrix. Minimising this expression, one can find the equilibrium dissociation distance as

$$d_{\text{b}}^{\text{eq}} = \frac{b_i^{(1)} K_{ij} b_j^{(2)}}{\gamma}, \tag{3.13}$$

With the orientation of the simulation cell as, $X = \langle 10\bar{1}0\rangle$, $Y = \langle 0001\rangle$, $Z = \langle 1\bar{2}10\rangle$, one finds the components of the energy prefactor matrix as [155]:

$$K_{11}^{\text{screw}} = \frac{1}{2\pi}\left(\bar{C}_{11} + C_{13}\right)\sqrt{\frac{C_{44}\left(\bar{C}_{11} - C_{13}\right)}{C_{33}\left(\bar{C}_{11} + C_{13} + 2C_{44}\right)}} \tag{3.14}$$

$$K_{22}^{\text{screw}} = \sqrt{\frac{C_{33}}{C_{11}}} K_{11}^{\text{screw}} \tag{3.15}$$

$$K_{33}^{\text{screw}} = \frac{1}{2\pi}\sqrt{\frac{1}{2} C_{44}\left(C_{11} - C_{12}\right)} \tag{3.16}$$

here, $\bar{C}_{11} = \sqrt{C_{11}C_{33}}$.

For the basal plane one expects the dissociation as found in equation (3.10). This gives the dissociation length of the $\langle a\rangle$ screw dislocation in the basal plane as

$$d_{\text{b}}^{\text{screw}} = \frac{(3K_{33}^{\text{screw}} - K_{11}^{\text{screw}})a^2}{12\gamma_{\text{b}}}, \tag{3.17}$$

For the prism plane, the $1/3\langle 1\bar{2}10\rangle$ dislocation can dissociate according to equation (3.9). It has been found in EAM potentials, that the stacking fault minimum can be displaced along the [0001] into resulting in two partials, $1/6[1\bar{2}10] \pm \alpha(c/a)[0001]$, where the parameter α controls the position along the [0001] direction. The dissociation

length is therefore

$$d_{\mathrm{p}}^{\mathrm{screw}} = \frac{(K_{33}^{\mathrm{screw}} a^2 - 4\alpha^2 K_{22}^{\mathrm{screw}} c^2)}{4\gamma_p}, \tag{3.18}$$

For the basal $\{0001\}$ $\langle a \rangle$ edge dislocation, one can use the expressions of Savin, who corrected the initial work of Foreman [170, 171] to obtain the elements of the energy prefactor matrix,

$$K_{11}^{\text{b. edge}} = \frac{1}{2\pi}\left(\lambda^2 C_{33} + C_{13}\right)\sqrt{\frac{C_{44}\left(\lambda^2 C_{33} - C_{13}\right)}{C_{11}\left(\lambda^2 C_{33} + C_{13} + 2C_{44}\right)}} \tag{3.19}$$

$$K_{22}^{\text{b. edge}} = \lambda^2 K_{11}^{\text{b. edge}} \tag{3.20}$$

$$K_{33}^{\text{b. edge}} = \frac{1}{2\pi}\sqrt{\frac{1}{2}C_{44}\left(C_{11} - C_{12}\right)} \tag{3.21}$$

where, $\lambda = \sqrt{C_{11}/C_{33}}$. Savin [170] also gave an expression for prismatic $\{10\bar{1}0\}$ edge dislocation matrix element, where only the the K_{11} prefactor is necessary

$$K_{11}^{\text{p. edge}} = \frac{C_{11}^2 - C_{13}^2}{2C_{11}}. \tag{3.22}$$

For the first-order pyramidal plane edge dislocation, $\{10\bar{1}1\}$ $\langle a \rangle$, the energy coefficient matrix was evaluated numerically from the anisotropic elasticity solutions rotated into the appropriate dislocation coordinate system, where the x_3 axis was rotated by $\theta = \arccos 2q/\sqrt{3+4q^2}$, where q is the c/a ratio, about x_1, such that the dislocation line was on the π_1 plane. It should be noted that the full anisotropic description, as detailed in section 2.7, must be used. Simplified equations for the anisotropic solutions, such as those found in Hirth and Lothe [7] may only describe systems which have the $x_1 - x_2$ plane as a mirror plane, which is not the case with pyramidal stacking, as there is no periodic stacking of planes along this direction [165].

From these energy coefficients, one used equation (3.13) to evaluate the dissociation distances numerically, using the partial Burgers vectors found in equations (3.17), (3.9) and (3.11) for the basal, prismatic and first-order pyramidal dissociation distances respectively.

3.2.3 Ti-O and Ti-H parameters

To obtain a model of both bulk titanium and titanium dioxide, one had to replace the Ti-Ti parameters from the model of Lozovoi and Paxton [172], with the newly-fitted

Ti-Ti model, and subsequently refit the Ti-O parameters. The original paper had a Ti-Ti model which only had a description of d hopping integrals, with the addition of a further two s-electrons included on each Ti, which had no hopping allowed between them. These s-electrons are essential as they fill up the oxygen p-states in TiO_2. To describe both pure titanium and TiO_2, the sd-model was chosen for integration with the Lozovoi model, as it explicitly incorporated fitted Ti–s states.

Within the parameterisation of the aforementioned paper, there was no explicit description of hydrogen interacting with titanium, despite the inclusion of O-H interactions for the description of water. To complete the description of the physics when water approaches a titanium/titanium-dioxide surface, Ti-H bond integrals were fitted with $ss\sigma$ and $sd\sigma$ bond integrals. These were fit simply to the bands, optimised lattice constant and bulk properties calculated from LMTO-GGA simulations of fluorite TiH_2.

To mesh the new Ti-Ti parameters with the TiO_2 model, the Ti-O parameters model had to be refitted to replicate the properties found in the Lozovoi and Paxton paper: lattice parameters, structural energy differences, bulk moduli and band gaps for the anatase and rutile TiO_2 polymorphs. The data was obtained from DFT and experiment. Additional data pertinent to electrochemical simulations was also included, in particular, the energies associated with an oxygen/hydrogen approaching and penetrating the bulk titanium (0001) surface on the hollow hcp and fcc sites. The target data was generated by self-consistent LMTO-DFT calculations of an oxygen approaching a 2×2 titanium (0001) surface from a distance of $1.5c$, where c is the structurally optimised lattice parameter of the α titanium phase within the DFT. The total energies obtained were subtracted from the reference distance of oxygen at $1.5c$. This data was fitted similarly to that of the Ti-Ti parameters, using the objective function defined in equation (3.5), using the CMA-ES algorithm.

3.2.3.1 Water on titanium

To demonstrate the transferability and stability of the models created, the first ever tight-binding simulations of water on titanium, known to the author, were performed. This tested the Ti-Ti, Ti-O, Ti-H, H-O parameter sets. Molecular dynamics using an NVT ensemble with a Nosé-Hoover thermostat was performed at 100K with a small system size for testing: $2 \times 2 \times 3$ slab of titanium atoms (24 atoms), with 16 water molecules placed on either side of the slab. The cell used had a length of $\mathbf{p}_z = 12c_{\text{hcp}}\hat{\mathbf{z}}$, where the titanium slab was placed in the centre. The configuration of water molecules

was taken from a slice of an 128 water molecule cubic cell which had been equilibriated over 100ps (using the same temperature and ensemble) to obtain the correct radial distribution function of water. The timestep used in these simulations was 0.25fs. Charge tolerance was 1×10^{-3}. These simulations can be easily scaled to double or triple the system size, and allow for calculations which are simply not possible in DFT due to scaling issues, both with atom number and cell size: one can add vacuum at no cost in tight-binding, whereas most DFT codes must have plane waves defined in the vacuum.

3.3 Results

3.3.1 Ti-Ti parameters

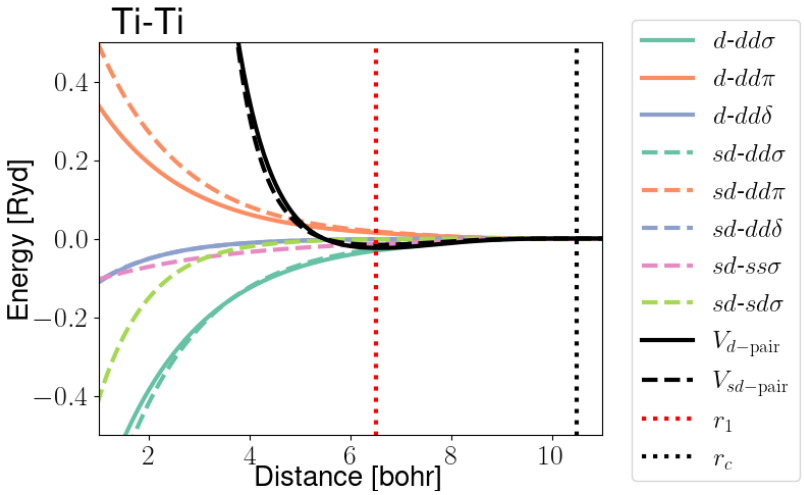

Fig. 3.2: Bond integrals and pair potential of both *d* and *sd* titanium tight-binding models.

The parameters obtained from optimisation are shown in table 3.1, with the titanium bond integrals being shown in figure 3.2.

One finds that the canonical band ratios for the titanium models are $dd\sigma : dd\pi : dd\delta = -6.0 : 3.0 : -1.2$ and $dd\sigma : dd\pi : dd\delta = -6.0 : 3.8 : -1.0$ for the *d*-model and *sd*-model respectively, which are in good agreement with canonical band theory, equation (3.2), $dd\sigma : dd\pi : dd\delta = -6 : 4 : -1$. The canonical ratios for the *d*-model are coincidentally similar to the *d*-orbital only model of Ferrari *et al.* in their bond-order potential parameterisation [130]: $dd\sigma : dd\pi : dd\delta = -6.0 : 3.0 : -0.9$.

Table 3.1: Parameters of the tight-binding models which describe titanium, titanium dioxide, titanium hydride, diatomic hydrogen and water. Notation for the functional form of the scaling law for bond integrals and pair potential is clarified in Table 3.2. All values are given in atomic Rydberg units.

On-site parameters

Ti		O		H	
ε_s	–0.3764	ε_s	–2.1164	ε_s	–1
ε_d	–0.2282	ε_p	–1.1492		
U	0.8287	U	1.0775	U	1
Δ_{ddd}	8.0	Δ_{spp}	–0.9430		
Δ_{ddg}	28.0	Δ_{ppd}	0		

Bond integrals, $V_{\ell\ell' m}$, and scaling

Ti–Ti *sd*		Ti–Ti *d*		Ti–O		Ti–H		O–H		O–O		H–H	
Function	EXP			Function	GSP	Function	EXP	Function	EXP	Function	GSP	Function	EPL
$V^0_{ss\sigma}$	–0.150			$V^0_{ss\sigma}$	–0.037	$V^0_{ss\sigma}$	–0.26	$V^0_{ss\sigma}$	–0.5018	$V^0_{ss\sigma}$	–0.015	$V^0_{ss\sigma}$	–0.88
$V^0_{sd\sigma}$	–1.110			$V^0_{sp\sigma}$	0.062	$V^0_{sd\sigma}$	–0.16			$V^0_{sp\sigma}$	0.002		
$V^0_{dd\sigma}$	–1.410	–1.175		$V^0_{ds\sigma}$	–0.147			$V^0_{ps\sigma}$	–0.4362	$V^0_{ps\sigma}$	–0.002		
$V^0_{dd\pi}$	0.899	0.597		$V^0_{dp\sigma}$	–0.144					$V^0_{pp\sigma}$	0.050		
$V^0_{dd\delta}$	–0.229	–0.241		$V^0_{dp\pi}$	0.084					$V^0_{pp\pi}$	–0.020		
$p_{ss\sigma}$	0.370			$n_{ss\sigma}$	3	$q_{ss\sigma}$	0.54	$n_{ss\sigma}$	2.0963	$n_{ss\sigma}$	2	$n_{ss\sigma}$	1.5
$p_{sd\sigma}$	1.000			$n_{sp\sigma}$	3	$q_{sd\sigma}$	0.28			$n_{sp\sigma}$	2		
$p_{dd\sigma}$	0.610	0.559		$n_{ds\sigma}$	4			$n_{ps\sigma}$	1.5019	$n_{ps\sigma}$	2		
$p_{dd\pi}$	0.600	0.569		$n_{dp\sigma}$	2.1					$n_{pp\sigma}$	3		
$p_{dd\delta}$	0.751	0.774		$n_{dp\pi}$	3.356					$n_{pp\pi}$	3		
				n_c	8			n_c	4.0561	n_c	6		
				r_0	3.685			r_0	1.8094	r_0	5.6		
				r_c	7.37			r_c	3.7985	r_c	9.0		

Pair potentials, ϕ, and scaling

Ti–Ti *sd*		Ti–Ti *d*		Ti–O		Ti–H		O–H		O–O		H–H	
Function	EPL			Function	EPL	Function	EPL	Function	GSP	Function	EPL	Function	EPL
ϕ^0_1	75.73	59.09		ϕ^0_1	30687	ϕ^0_1	194.15	ϕ^0	0.73669	ϕ^0_1	4.0306×10^{-3}	ϕ^0_1	1.631
m_1	0	0		m_1	12	m_1	–1.3	n	3.3502	m_1	10	m_1	–2.38
p_1	1.198	1.219		p_1	0	p_1	1.857	n_c	6.3096	p_1	0	p_1	0
ϕ^0_2	–3.78	–3.22		ϕ^0_2	238.8			r_c	3.3550	ϕ^0_2	-2.0265×10^{-3}	ϕ^0_2	0.1
m_2	0	0		m_2	1					m_2	6	m_2	–12
p_2	0.650	0.686		p_2	1.5609					p_2	0	p_2	0
ϕ^0_3	0	593519.11											
m_3	0	–11.5											
p_3	0	0											
r_0	1.0	1.0						r_0	1.8094	r_0	5.6		

Cut-off distances $[r^{(1)}_{\text{cut}}; r^{(2)}_{\text{cut}}]$

Ti–Ti		Ti–O		Ti–H		O–H		O–O		H–H	
$r^{(1)}_{\text{cut}}$	6.5	$r^{(1)}_{\text{cut}}$	4	$r^{(1)}_{\text{cut}}$	4.34	$r^{(1)}_{\text{cut}}$	2.1	$r^{(1)}_{\text{cut}}$	8	$r^{(1)}_{\text{cut}}$	4
$r^{(2)}_{\text{cut}}$	10.5	$r^{(2)}_{\text{cut}}$	8	$r^{(2)}_{\text{cut}}$	10.85	$r^{(2)}_{\text{cut}}$	5.5	$r^{(2)}_{\text{cut}}$	11	$r^{(2)}_{\text{cut}}$	5.8

Table 3.2: Explicit form of the scaling laws referred to in Table 3.1. Prefactor A denotes $V^0_{\ell\ell' m}$ in case of bond integrals and ϕ^0 in case of pair potentials.

Notation	Function	Explicit form
GSP	Goodwin–Skinner–Pettifor[173]	$f(r) = A\,(r_0/r)^n \exp\left\{n\left[-(r/r_c)^{n_c} + (r_0/r_c)^{n_c}\right]\right\}$
EPL	Exponential × power law	$f(r) = \sum_i A_i\,(r_0/r)^{m_i}\,\exp\left[-p_i(r-r_0)\right]$
EXP	Exponential	$f(r) = \sum_i A_i\,\exp\left[-p_i r\right]$

The results of the fitting to the training data set are shown in table 3.3.

Both the d and sd-model fit the target data well, with the d-model obtaining better agreement with lattice and elastic constants compared to the sd model. The cohesive energies of the α phase for the models agree well with experiment $E_{\text{coh.}}^{\alpha\ \text{Exp.}} = -4.85$ eV/Atom [176], but this cohesive energy per atom is less negative than what is found in DFT, $E_{\text{coh.}}^{\alpha\ \text{LMTO-GGA}} = -6.64$ eV/Atom (this work), $E_{\text{coh.}}^{\alpha\ \text{VASP}} = -6.68$ eV/Atom [130]. Despite the difference in the absolute cohesive energy from DFT, the small structural energy differences between titanium polymorphs are well produced by tight-binding, especially for the sd-model.

It was thought that with the addition of s-electrons, the sd-model would be able to reproduce the DFT result of ω phase being marginally lower in energy than the hcp phase—due to the increased cohesion of titanium by the inclusion of s-electrons in conjunction with the compactness of the ω phase compared to α, as seen in pair correlation functions of each optimised phase in DFT. In pure d-orbital bond-order potential models, the effect of s-electrons is usually approximated by an "embedding" potential, which is of Finnis-Sinclair/EAM form. This extra term was included in the titanium bond-order potential model by Ferrari [130], which replicated the energetics of $\omega \leftrightarrow \alpha$ and $\beta \leftrightarrow \alpha$ transitions from DFT. They attribute 60% of the cohesive energy to their s-electron embedding term, which agrees well with the projection of cohesive energy contributions from a previous non-orthogonal tight-binding parameterisation [128]. Due to the strong hybridisation of the s-electrons with the d in the sd-model, as will be shown in the tight-binding bands, figure 3.3, there is a smaller amount of cohesive strength from s-electrons. In the sd-model, the s-states are pushed up relative to the expected splitting from DFT or s, p, d tight-binding [128]. Therefore the centre-of-gravity of the s-electron contribution to the density of states is higher in energy relative to the contribution from d-states, and with hybridisation, there is more s-electron density of states above the Fermi level, causing a reduction in the cohesive contribution of s-states. As such, this particular feature could not be replicated, but, as the focus of the model is for the simulation of pure titanium, it is not expected to hinder predictions or insights obtained from the model.

hcp | α							
	Lattice Parameters				Elastic Constants (GPa)		
	d-TB	*sd*-TB	Reference		*d*-TB	*sd*-TB	Reference
a (bohr)	5.585	5.674	5.574[a]	C_{11}	171.6	167.3	176.1[b]
c/a	1.584	1.586	1.587[a]	C_{33}	198.9	205.2	190.5[b]
				C_{44}	47.4	46.6	50.8[b]
				C_{12}	94.7	96.7	86.9[b]
				C_{13}	61.2	60.9	68.3[b]

Other Hexagonal Phases							
	Omega | ω						
	d-TB	*sd*-TB	Reference				
a (bohr)	8.935	9.039	8.733[c]				
c (bohr)	5.387	5.486	5.323[c]				
	4h				6h		
	d-TB	*sd*-TB	Reference		*d*-TB	*sd*-TB	Reference
a (bohr)	5.576	5.681	5.563[c]	a (bohr)	5.574	5.676	5.546[c]
c (bohr)	18.098	18.328	17.759[c]	c (bohr)	27.184	27.579	26.771[c]

Cubic Phases							
	bcc | β				fcc | γ		
	d-TB	*sd*-TB	Reference		*d*-TB	*sd*-TB	Reference
a (bohr)	6.201	6.201	6.179 [c]	a (bohr)	7.873	8.013	7.887 [c]

Cohesive Energy [eV/Atom] / Energy differences [mRy/Atom]			
	d-TB	*sd*-TB	Reference
$E(\alpha)$ cohesive	–4.413	–5.086	–6.646[c]
$E(\omega) - E(\alpha)$	0.588	0.357	–0.633[c]
$E(\text{4h}) - E(\alpha)$	1.580	1.663	3.172[c]
$E(\text{6h}) - E(\alpha)$	2.483	2.400	3.720[c]
$E(\text{bcc}) - E(\alpha)$	5.351	7.958	7.635[c]
$E(\text{fcc}) - E(\alpha)$	3.780	3.825	4.519[c]

[a] Expt. Ref [174]
[b] Expt. Ref [175]
[c] LMTO-GGA DFT (this work)

Table 3.3: Table of the titanium objective function values compared to experimental and DFT target data. The hcp lattice parameter, and the structural energy differences between titanium polymorphs were given large weights in the objective function.

3.3.1.1 Bands

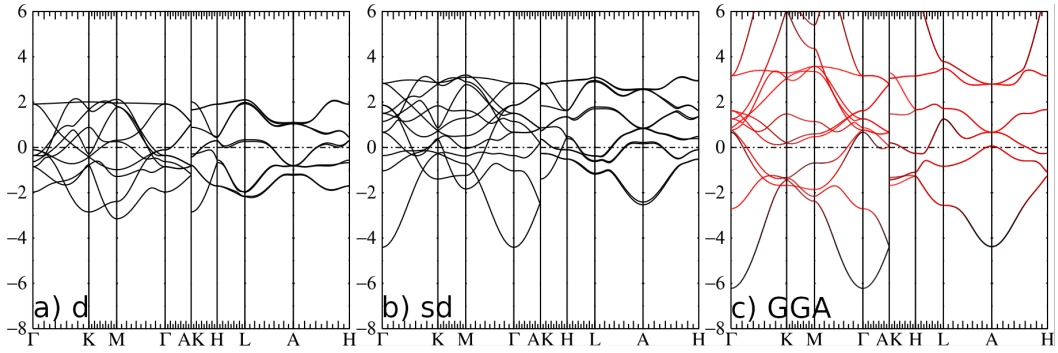

Fig. 3.3: Band structure for the titanium a) *d* and b) *sd* tight-binding models compared to c) LMTO-GGA DFT. The *d*-orbital character of the GGA bands is shown in red for clarity.

A comparison of the *d* and *sd* bands compared to LMTO-GGA can be found in figure 3.3. We find that the shape of the tight-binding bands match well with those found in DFT, but the *d*-band width is a little smaller than found in DFT. This is consistent with other parameterisations, notably that of Urban *et al.* where the orthogonal *d*-only model, which was derived from a full s, p, d non-orthogonal model, had a reduced *d* bandwidth [128]. The *sd* model exhibits *s*-bands which are well hybridised, which have a smaller deviation from the centre of gravity of the *d* bands compared to GGA from the aforementioned raising of the Ti-*s* on-site energy, such that the TiO_2 anatase and rutile bands have a sufficient band gap.

3.3.2 Ti-Ti Validation

Quantity	*d*-model	*sd*-model	BOP [130]	BOP [125]	NOTB [118]	DFT [177]	Experiment [178]
$E_{\text{Vac.Form.}}$	2.64	3.27	2.80	2.30	1.80	1.97	1.27

Table 3.4: Vacancy formation energies of the titanium tight-binding models compared DFT and experiment. Energies are in eV.

The first validation test of the titanium tight-binding models was to measure the vacancy formation energy, as found in table 3.4. The vacancy formation energies are significantly higher than those found in DFT and experiment. This implies that the energy to break bonds in a simulated hcp lattice, with the *d* and *sd* tight-binding models is larger than what is found in DFT or experiment. This large difference is

likely due to the inclusion of charge transfer in these tight-binding models, where charge transfer is exaggerated compared to BOP and DFT.

The deviation from BOP can be explained by the fact that it is based on the concept of *local charge neutrality*, where atoms are taken to be charge neutral. Framing this in a self-consistent charge transfer tight-binding model, a subset of the PITB used in the *d*-model and *sd*-model, the Hubbard U parameter, the penalty for charge transfer due to Coulomb repulsion, may be taken to be infinity. This simulates a perfectly screened metal where no effective charge transfer exists as the penalty is too great [81]. In the *d* and *sd* models, the Hubbard U is fit to reproduce properties if TiO_2. It is finite, allowing charge transfer. These deviations of charge increase the electrostatic energy of the defected lattice, increasing the vacancy formation energy.

These differences in the vacancy formation energy may result in larger surface energies compared to DFT, with a further possibility of large dislocation excess energies, especially for simulated edge dislocations, and γ-surface energies, however for these cases, it depends on the amount of charge transfer found upon reaching self-consistency.

3.3.2.1 Phonons

The *d* and *sd* tight-binding models give reasonable results for phonon dispersion, as seen in figure 3.4. Deviations in the α and ω phase phonons were found at A, with some larger deviation in some optical branches in the latter at K and M. The β phonons agree well with DFT. They exhibit imaginary frequencies (seen as negative in the figure), as the bcc phase is not stable at 0K. It was found for all tight-binding models that the bandwidths were a little larger than those found in DFT.

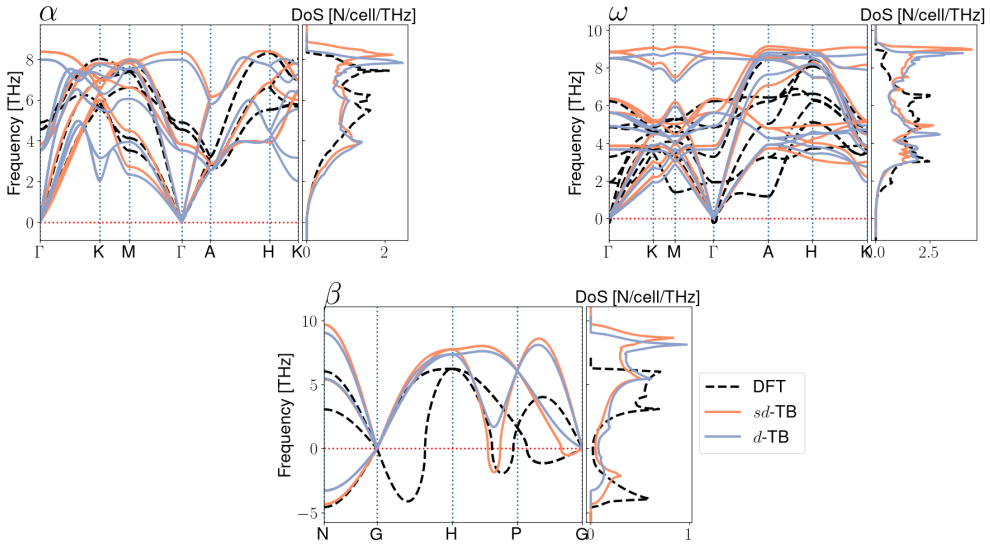

Fig. 3.4: Phonons for pure titanium for the α, β, and ω phases compared to LMTO-GGA.

The difference of the Gibbs free energy, with respect to the hcp phase is shown in figure 3.5.

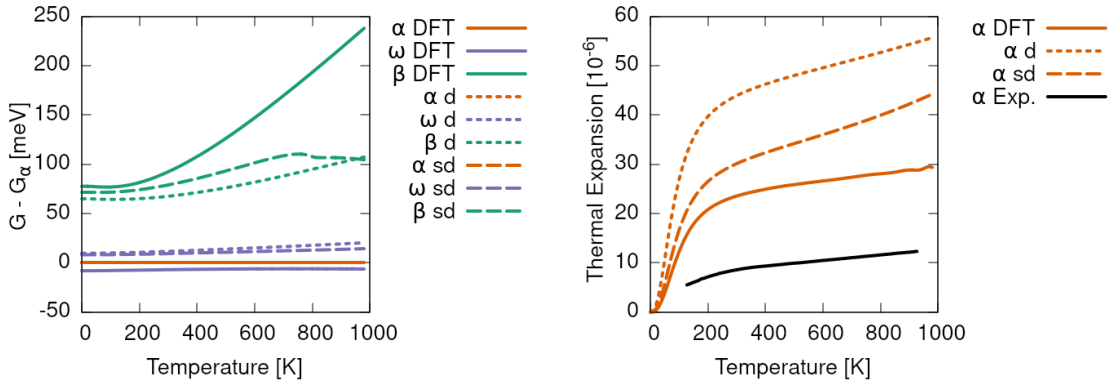

Fig. 3.5: The Gibbs free energy of the α, β and ω phases, relative to the hcp phase of titanium. The lowest difference corresponds to the most stable phase. Thermal expansion of α is compared to experiment where the units are in $10^{-6}\mathrm{K}^{-1}$ [179].

We see that neither of the tight-binding models can reproduce the stability of the omega phase, as found in DFT, as mentioned previously in the comparison of the bare cohesive energies. In both DFT and tight-binding, the free energy of the bcc phase diverges in an unphysical manner. This is because the bcc phase in titanium is dynamically stabilised, and it has been shown previously that quasi-harmonic models

are not able to capture dynamic stabilisation of these phases due to the omission of entropic contributions [2]. This stabilisation can be achieved with the self-consistent lattice-dynamical method [180] as was achieved by Kadkhodaei *et al.* in bcc Ti [181].

The thermal expansion of the hcp phases simulated from the *d*-model and *sd*-model are larger than that of DFT. All atomistic methods used show a thermal expansion much larger than the experimental value. This is likely due to the omission of entropic effects as mentioned above. In the simulations with this model, it is not expected that thermal expansion will hinder the predictive power of the results obtained in this thesis. However, it could play a role in the high temperature molecular dynamics simulations performed with the model.

3.3.2.2 Gamma surfaces

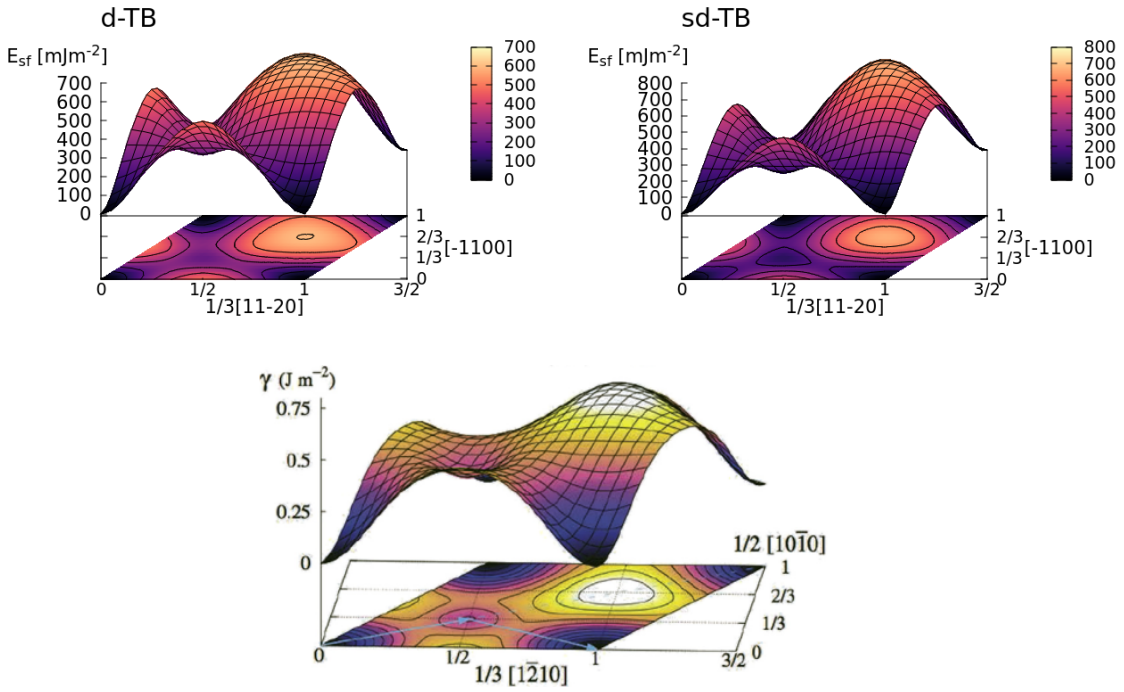

Fig. 3.6: Basal gamma surface in hcp compared to DFT (bottom) [160].

The basal and prismatic gamma surfaces can be found in figures 3.6 and 3.7. There is very good agreement in the morphology of *d* and *sd* tight-binding models with DFT. The intrinsic stacking fault on the basal surface, I_2, associated with fcc stacking, is found at $1/6[1\bar{2}10] + 1/6[10\bar{1}0]$, with energies of $\gamma_{\mathrm{b}}^{d\text{-TB}} = 215.0$ mJm^{-2} and $\gamma_{\mathrm{p}}^{sd\text{-TB}} =$

128.5 mJm^{-2} for the *d* and *sd* models respectively. These are $\sim$ 50 to 150 mJm^{-2} lower compared to DFT values, which range from 260 to 300 mJm^{-2} [162, 166].

The γ-surface for the prismatic plane is shown in figure 3.7. The expected dissociation of the $\langle a \rangle$ dislocation on the prismatic plane, is reproduced successfully in both tight-binding models. Both have a minimum, albeit slight, at $1/6[1\bar{2}10]$, with energies of $\gamma_{\mathrm{p}}^{d\text{-TB}} = 128.5$ mJm^{-2} and $\gamma_{\mathrm{p}}^{sd\text{-TB}} = 155.5$ mJm^{-2}. These are lower than those found by DFT by around 100 mJm^{-2} [162, 166], similar to the basal faults as detailed above, but close to the experimental value calculated by Akhtar and Teghtsoonian of 145 mJm^{-2} [21]. As such, it is expected that the expected dissociation distance of the partials is larger than would be found in DFT. These dissociation distances can be found in table 3.5.

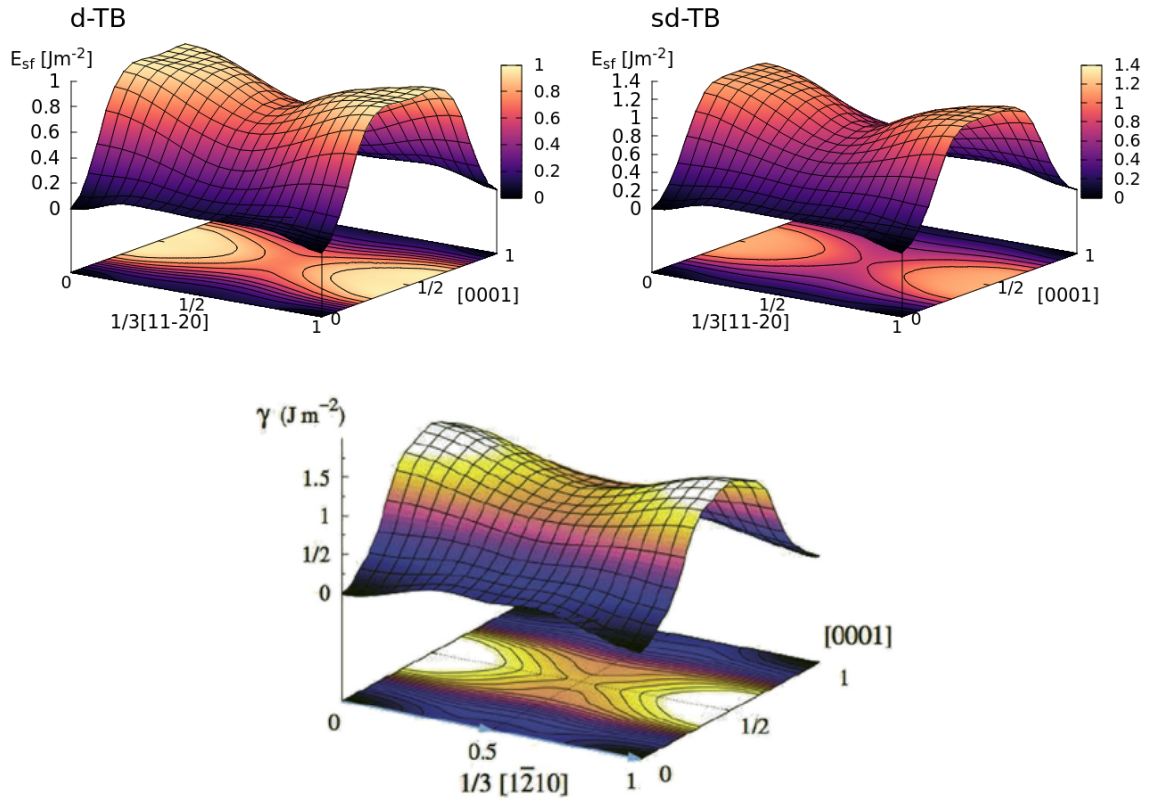

Fig. 3.7: Prismatic gamma surface in hcp compared to DFT (bottom) [160].

The results for the wide plane pyramidal plane, and the narrow pyramidal plane in figures 3.8 and 3.9 respectively. Both γ-surfaces reflect their DFT counterparts in terms of morphology and position of stable stacking faults, although the maximum

γ-surface energies are larger than DFT by around 200 mJm^{-2}.

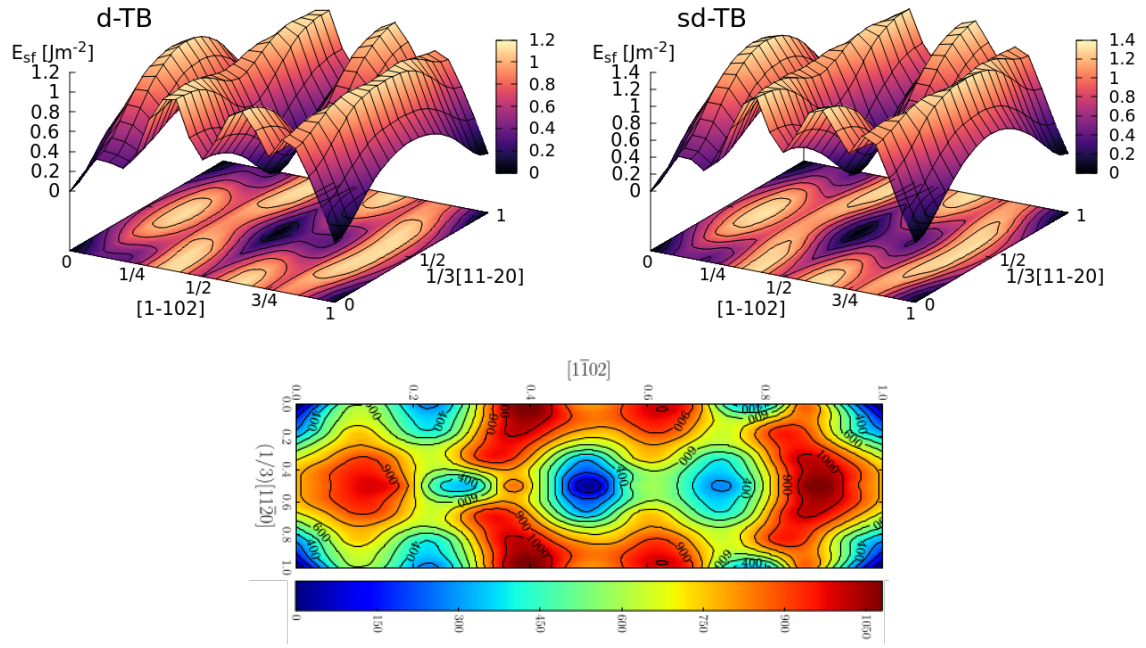

Fig. 3.8: First-order pyramidal gamma surface on the wide plane compared to DFT [165].

The π_1 wide gamma surface, figure 3.8, matches very well with DFT calculations of Ready [165]. One expects a similar splitting of the $\langle c+a \rangle$ screw dislocation, into three segments.

$$\begin{aligned}\frac{1}{3}[2\bar{1}\bar{1}3] \rightarrow & \frac{4}{18}[1\bar{1}02] \\ & + \left(\frac{1}{6}[11\bar{2}0] + \frac{1}{18}[1\bar{1}02]\right) \\ & + \frac{4}{18}[1\bar{1}02],\end{aligned}$$

where each line corresponds to a separate Burgers vector.

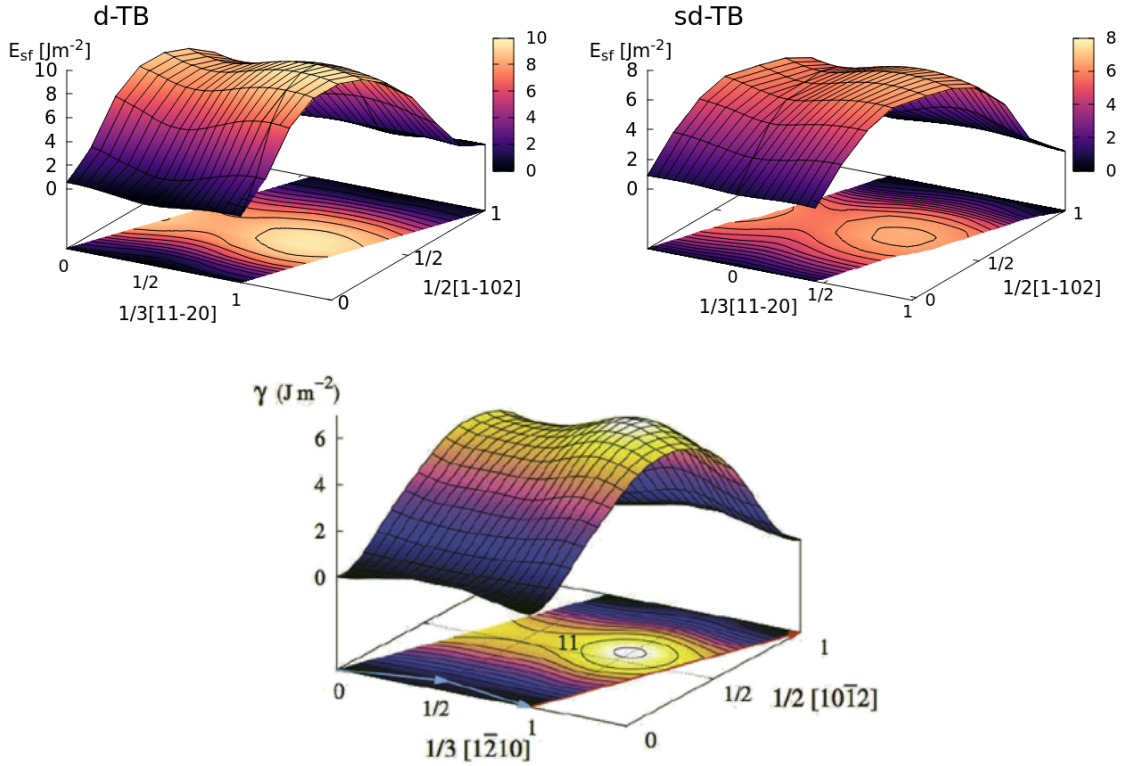

Fig. 3.9: First-order pyramidal narrow gamma surface, with relaxation constrained. Comparison to DFT from reference [160].

For the pyramidal gamma surface on the narrow plane, figure 3.9, one finds the expected splitting of the $\langle a \rangle$ dislocation, equation (3.11). Upon further volume and structural relaxation, one finds the stable stacking fault energies, of which the *d*-model, with a value of $\gamma_{\pi_1}^{d\text{-TB}} = 187.5\ \text{mJm}^{-2}$ agrees well with the value of Curtin *et al.* $\gamma_{\pi_1}^{\text{DFT}} = 200\ \text{mJm}^{-2}$. The volume relaxed stable gamma surface energies can be found in table 3.5.

3.3.2.3 Dissociation distances

Comparing our tight-binding model to the literature, one finds that both the *d*-model and *sd*-model fare well to the other titanium tight-binding models, with dissociation distances of screw dislocations are in good agreement with DFT, as seen in table 3.5. In both models, the dissociation of the $\langle a \rangle$ dislocation on the prismatic plane is expected to be exaggerated, due to the energy of the prismatic fault being underestimated by $\sim$ 80 to 100 mJm^{-2}. Note that the model of Girshick [125] which predicts a

—DFT—															
Method	$d^{\text{screw}}_{\text{pris}}$	$d^{\text{screw}}_{\text{basal}}$	$d^{\text{edge}}_{\text{pris}}$	$d^{\text{edge}}_{\text{basal}}$	$d^{\text{edge}}_{\text{pyr}}$	γ_{p}	γ_{b}	γ_{π_1}	a	c/a	C_{11}	C_{12}	C_{13}	C_{33}	C_{44}
Curtin VASP [161]	6.631	1.252	10.431	4.382	4.919	214.0	306.0	200.0	2.924	1.582	177.0	90.0	84.0	189.0	40.0
Trinkle VASP [182]	7.083	1.391	10.459	4.680	1.516	220.0	292.0	689.0	2.950	1.586	172.0	82.0	75.0	190.0	45.0
Clouet VASP [19]	5.628	0.898	8.738	3.971	-	220.0	292.0	-	2.920	1.581	169.0	97.0	84.0	189.0	37.0
Clouet PWSCF [19]	5.491	1.049	8.181	4.170	-	256.0	297.0	-	2.936	1.583	169.0	89.0	77.0	192.0	42.0
Tarrat SIESTA [162]	7.014	1.358	10.313	5.999	-	250.0	259.1	-	2.996	1.588	183.4	84.6	63.8	204.9	48.8
—Tight-Binding—															
Method	$d^{\text{screw}}_{\text{pris}}$	$d^{\text{screw}}_{\text{basal}}$	$d^{\text{edge}}_{\text{pris}}$	$d^{\text{edge}}_{\text{basal}}$	$d^{\text{edge}}_{\text{pyr}}$	γ_{p}	γ_{b}	γ_{π_1}	a	c/a	C_{11}	C_{12}	C_{13}	C_{33}	C_{44}
Girshick BOP [163]	6.782	5.484	9.656	13.262	-	260.0	110.0	-	2.950	1.587	176.1	74.0	83.3	190.5	50.8
Matous BOP [144]	20.233	2.334	35.760	9.668	-	55.0	160.0	-	2.922	1.604	170.0	96.0	86.0	144.0	29.0
d-model (this work)	11.461	0.824	16.138	6.334	5.165	128.5	215.0	187.5	2.955	1.584	171.6	94.7	61.2	198.9	47.4
sd-model (this work)	9.992	0.839	12.850	9.879	1.065	155.5	128.5	887.5	3.003	1.586	167.3	96.7	60.9	205.2	46.6
—Empirical Potential—															
Method	$d^{\text{screw}}_{\text{pris}}$	$d^{\text{screw}}_{\text{basal}}$	$d^{\text{edge}}_{\text{pris}}$	$d^{\text{edge}}_{\text{basal}}$	$d^{\text{edge}}_{\text{pyr}}$	γ_{p}	γ_{b}	γ_{π_1}	a	c/a	C_{11}	C_{12}	C_{13}	C_{33}	C_{44}
Hennig MEAM [118]	5.509	2.139	7.028	9.003	2.076	297.0	172.0	443.0	2.931	1.596	174.0	95.0	72.0	188.0	58.0

Table 3.5: Table of $1/3\langle 1\bar{1}20\rangle$ dislocation dissociation distances on the prismatic, pyramidal and basal planes. All distances, d_i, a, are in angstrom. Elastic constants C_{ij} are in GPa and stacking fault energies γ_i are in mJm^{-2}.

dissociation distance in-keeping with DFT, gives an erroneous ordering of stacking fault energies, which results in a spurious spreading on the basal plane, as exhibited in their dislocation calculations [154]. DFT has shown basal plane spreading to be highly unstable due to the high energy of the cores [131]. The 12.85Å dissociation distance of the *sd*-model prismatic edge dislocation which agrees remarkably well with that of the experimentally measured value of de Crecy *et al.* of 12Å [183]. de Crecy *et al.* also estimated the stacking fault energy (using isotropic elasticity theory) as $\gamma_{\text{p}} = 155\ \text{mJm}^{-2}$, which agrees almost exactly with the *sd*-model value.

One can make a connection with the Peierls-Nabarro model of a dislocation to interpret dislocation dissociation distances in terms of dislocation mobility. The Peierls-Nabarro stress, the critical stress on a glide plane necessary to initiate dislocation glide, is given by

$$\sigma_{\text{PN}} = \frac{2\mu}{1-\nu}\exp\left\{-\frac{4\pi\zeta}{b}\right\}, \tag{3.23}$$

where $\nu \approx 0.31$ for Ti is Poisson's ratio, μ is the shear modulus, d_{planar} is the distance between the glide planes and 2ζ is the dislocation core width. In the original formulation $2\zeta_{\text{edge}} = d_{\text{planar}}/(1-\nu)$ for edge dislocations, and $2\zeta_{\text{screw}} = d_{\text{planar}}$ for screws. As the width of dislocations of edge character are generally larger than that of screws (by $1/(1-\nu) \approx 1.45$ times) the Peierls-Nabarro stress, and therefore the mobility of edge dislocations, is higher, due to the exponentially decaying dependence of the stress on dislocation core width. To link to our dissociation distances, we can first

imagine projecting the Burgers vector distribution of our dissociated dislocation fully onto the dislocation glide plane. We can consider the half-width ζ, which is defined to be the value in the Peierls-Nabarro model at which the displacement along the glide plane of interest $u(x = \pm\zeta) = u(\pm\infty)/2 = \pm b/8$, or equivalently, when the disregistry $D(x)$, which is the cumulative Burgers vector along the glide plane, is $\pm b/4$ [7], or in the convention of Clouet, when $D(x) = b/4, 3b/4$. If one assumes that the glide-plane projected Burgers vector density of each partial is split evenly about each partial dislocation centre, then one can intuitively take $\zeta \approx d_{\text{diss}}/2$, as between $0 < x < d_{\text{diss}}/2$, the total integrated Burgers vector, the disregistry, will be $b/4$.

Therefore taking d_{diss} as an approximation to 2ζ, one expects that prismatic dissociation, and therefore edge dislocation mobility, to be high on the prismatic plane for all models, as we expect. Following the results of Curtin *et al.* in table 3.5 who I believe took the most careful treatment in calculating stacking fault energies of the included authors, allowing for full volume and structural relaxation, one finds the width of the basal and pyramidal edge dislocations, and therefore their mobilities, to be comparable. The *sd*-model dissociation distances agree with these results. These widths are not too dissimilar from the value of prismatic screw dislocation dissociation width. The basal screw dislocation for all models shows a very low mobility. This agrees with explicit DFT calculations of basal screw dislocations, showing that the $\langle a \rangle$ screw core is unstable and decays into a pyramidally dissociated core, even during glide along the basal plane, prismatic/pyramidal dissociation is maintained [131].

3.3.3 Ti-O and Ti-H parameters

Results of the fitting can be seen in table 3.6, with the bond integrals and pair potential as seen in figure 3.10.

TiO_2									
	Rutile			Anatase			Fluorite		
	d-TB	*sd*-TB	Expt	*d*-TB	*sd*-TB	Expt	*d*-TB	*sd*-TB	DFT
a (Å)	4.388	4.553	4.587[a]	3.629	3.772	3.782[a]	4.708[†]	4.854[†]	4.86[b]
c (Å)	2.827	2.932	2.954[a]	9.117	9.476	9.502[a]			
V/V_{target}	0.8756	0.9780	1	0.8833	0.9919	1	0.9088[†]	0.9965[†]	1
Internal parameter u/a	0.314	0.303	0.305[a]	0.203	0.208	0.208[a]			
Bulk modulus (GPa)	417.7	339.3	211±7[c]	369.3	283.6	179±2[d]	330.2[‡]	342.3[‡]	282[b]
Band gap (eV)	3.91	2.18	3.03[e]	4.78	2.96	3.20[f]			
E_{cohesive}/f.u. (eV)	–28.30	–25.31	–25.36[h]						
Energy differences (mRy per f.u.):									
E(rutile) – E(anatase)	–28.1	–45.2	–1.29[g]						
E(fluorite) – E(rutile)[†]	123.3	56.2	51.0[h]						

TiH_2			
	Fluorite		
	d-TB	*sd*-TB	Expt
a (Å)	9.566	9.324	8.356[h]
E_{coh}/f.u. (eV)	–14.562	–15.284	–14.844
Bulk modulus (GPa)	74.0	48.2	114.4[h]

[†] used in fitting with low weight.
[‡] not included into fitting.
[a] Neutron diffraction, Ref. [184].
[b] DFT LDA, Ref. [186].
[c] X ray diffraction, Ref. [188].
[d] Ref. [189].
[e] Ref. [190].
[f] Ref. [185].
[g] ΔH_{298}, heat capacity measurements, Ref. [187]. The actual target was set to zero.
[h] DFT LDA, present study

Table 3.6: Objective function results of Ti-O/Ti-H fitting, showing equilibrium crystal structure, bulk moduli, and band gaps of TiO_2/TiH_2 bulk phases. Experimental data was used to fit with the exception of fluorite TiO_2/TiH_2, where DFT targets were used.

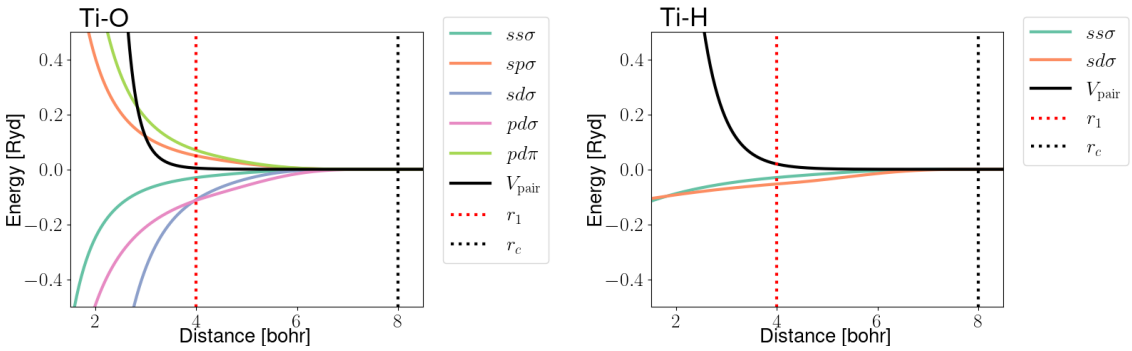

Fig. 3.10: Bond integrals for Ti-O and Ti-H.

From table 3.6, we see the *sd*-model has better agreement with experimental and empirical data than the *d*-model, with $\sim 2\%$ and $\sim 10\%$ deviations from the target values in TiO_2 respectively, excluding the bulk moduli and the band-gaps. This is expected due to the fitting procedure. The lattice constants and internal parameters are in good agreement with experiment [185]. There are discrepancies found in the band gaps of the rutile and anatase phases compared to experiment, where one finds they are smaller by 0.85 eV, and 0.24 eV respectively. These gaps, although reduced compared to experiment and GW simulations, are assumed to be sufficiently wide for defect (surface) states to be found within the gap. This is especially the case for rutile, when compared to the DFT LDA calculations, as found in figure 3.11. The bulk moduli of these phases are higher than expected by 60%, which is roughly twice the deviation found in the Lozovoi *et al.* paper. These could not be improved upon in the fitting of the Ti-O parameters, and were thus deemed to be due to the contribution of the Ti-Ti interactions, which were additionally thought to be the reason for the structural energy difference of the anatase phase deviating from the original parameterisation of the model: anatase is found to be higher in energy than rutile, rather than marginally lower, as found in DFT [186], however this does agree with experimental heat capacity measurements, as found in table 3.6.

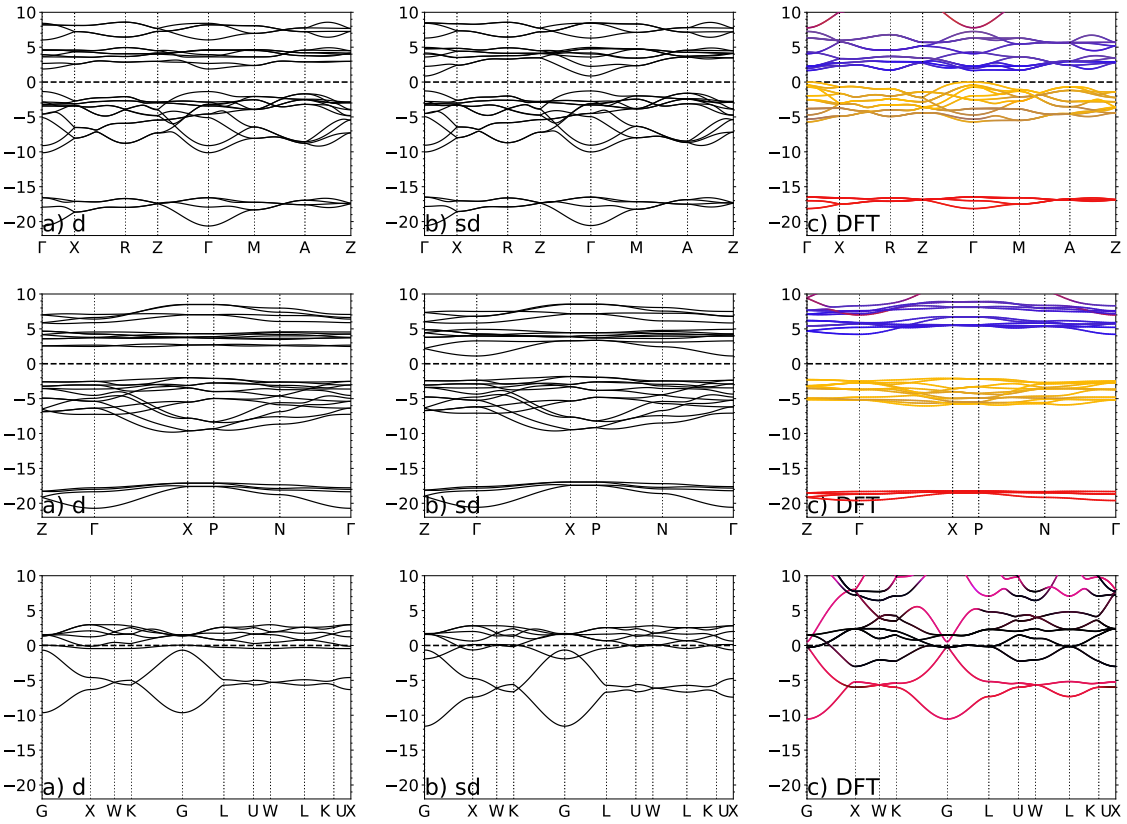

Fig. 3.11: Bands for TiO_2/TiH_2 phases compared to DFT. Top row: Rutile TiO_2 bands. Middle row: anatase TiO_2 bands. Bottom row fluorite TiH_2 bands. *d* and *sd* tight-binding shown compared to DFT. The DFT bands of the TiO_2 bands are shown with the O-*s* states in red, O-*p* states in orange and other orbital characters (mainly Ti-*d* states) in blue. The DFT bands of TiH_2 show the hydrogen *s* states in red. Eigenvalue energies are in eV.

The bands resulting from the tight-binding parameters agree well with DFT, as shown in figure 3.11. The splitting between the *s*, *p* and *d* states in TiO_2 is qualitatively similar to DFT, but the band gaps between the models, compared to DFT, are quite different between the *d* and *sd* models, as mentioned above. Bandwidths for the oxide phases are generally larger than their DFT counterparts, but for the hydrides the width of the *d* bands are smaller than what DFT finds, which can be attributed to the smaller *d*-band with in the corresponding pure hcp titanium simulations compared to DFT, see figure 3.3.

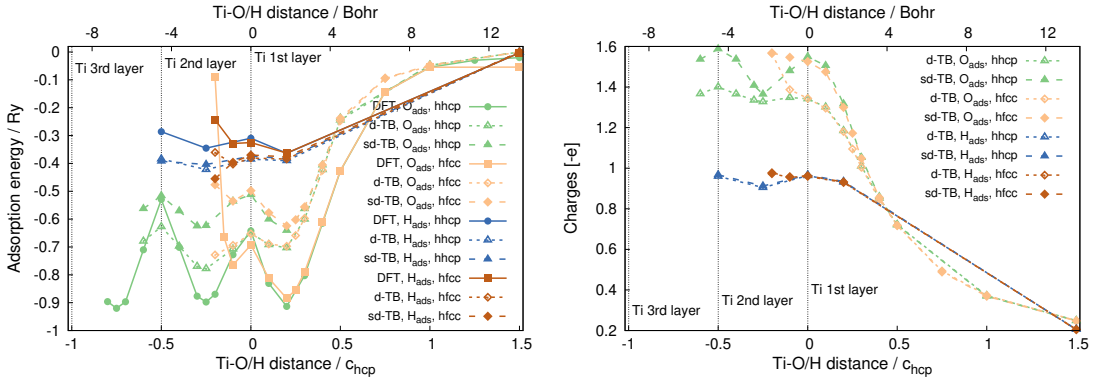

Fig. 3.12: Unrelaxed adsorption energies of oxygen and hydrogen relative to 1.5c from the Ti (0001) surface compared to LDA.

One finds qualitatively good agreement in the energy of adsorption of H/O species on the (0001) surface relative to the reference state at a distance of 1.5c. The energy minima found outside of the surface of the metal is reproduced for both oxygen and hydrogen, see figure 3.12.

The amplitudes of energy associated with the penetration into the metal is well produced by the Ti-H parameterisation, with some differences in behaviour between the *d*-model and *sd*-model with respect to DFT for the hollow fcc site, when the H species is very close to Ti. We see from observation of the corresponding charges of hydrogen, figure 3.12 right, that the amplitudes of the charge correlate well to the change of adsorption energy when the species in in the metal, with the rest of the contribution to the energy coming from the variation of the Ti-H pair potential.

For oxygen, we see that the Ti-O pair potential dominates the electrostatic contribution of the adsorption energy, as shown by the similar amplitudes of the adsorption energy for both the *d*-model and *sd*-model when going through the hollow hcp site, despite the large variation of the charge of oxygen in the *sd*-model compared to the *d*-model. The larger reservoir of electrons available for charge transfer in the *sd*-model, enables more Ti-O charge transfer, giving a larger Hubbard U penalty, resulting in larger overall adsorption energies in the *sd*-model compared to the *d*-model.

3.3.3.1 Water on titanium

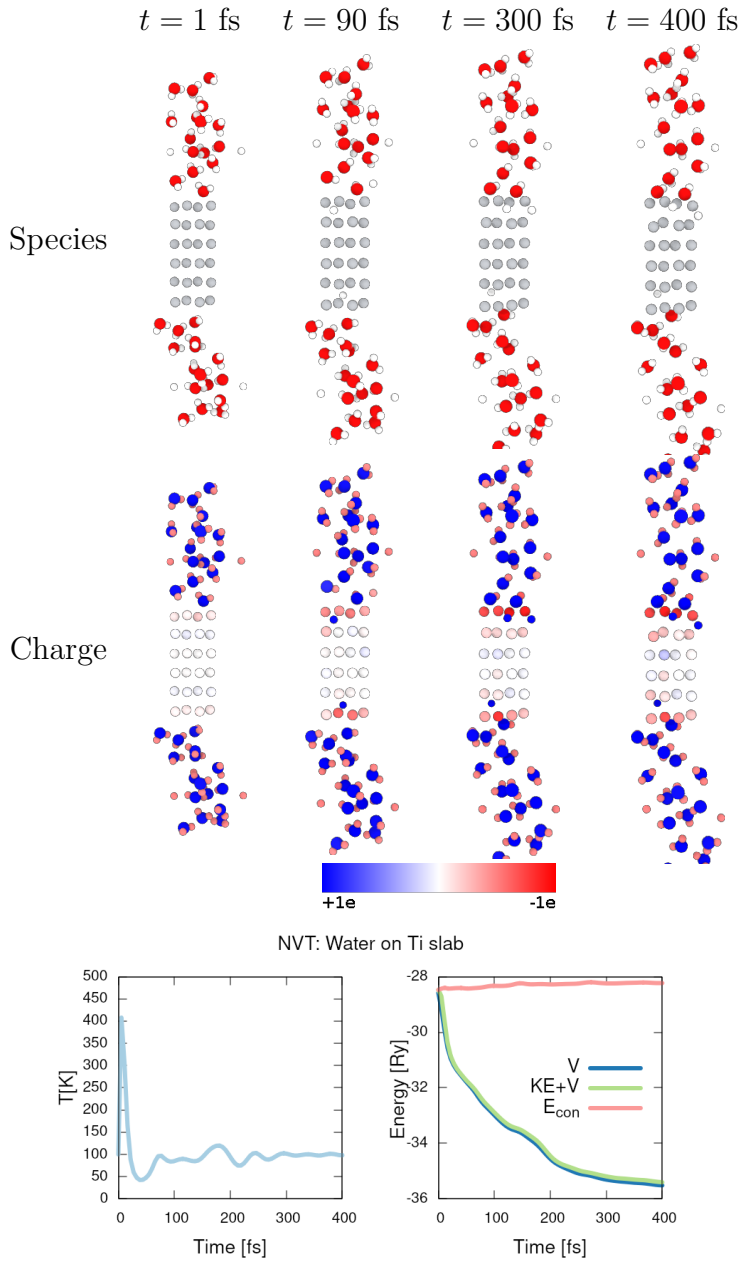

Fig. 3.13: NVT simulation of water on titanium (0001) surface at 100K using the *sd*-model. Original cells in top row, where grey denotes Ti, red O and white H. Cells coloured by charges in middle row: red shows absence of charge (positive charge) and blue denotes charge increase (negatively charged). Hydrogen gains charge from Ti species, becoming H^-, dissociating from water, and subsequently penetrating the titanium surface. The remaining OH group is adsorbed on the surface. Bottom: temperature and energy variation in the MD simulation.

As can be seen in figure 3.13, water was found to dissociate on the surface of titanium, where an OH group would adsorb on the titanium surface, and the hydrogen, which became H^-, would penetrate the first layer of titanium. Charge was transferred from titanium to hydrogen, which caused the dissociation. This behaviour was seen on both titanium-water interfaces in the simulation cell.

The model is shown to be reasonably stable in trials of molecular dynamics, as shown in figure 3.13, bottom. The conserved quantity increases initially but it stabilises, as does the temperature, during the equilbriation phase. A rather high charge tolerance was used here: 1×10^{-3}, and it has been shown in other test calculations, with a decreased charge tolerance, $\sim 1 \times 10^{-5}$ the conserved quantity does not increase.

3.4 Discussion

In the titanium parameterisations, one finds the *d* and *sd*-models to be rather similar. Both models agree well with validation tests against DFT.

Local minima on γ-surfaces suggest dislocation dissociations of the $\langle a \rangle$ and $\langle c+a \rangle$ screw dislocations from tight-binding will be in-line with DFT. The energies of stable stacking faults are closer to those of DFT results than previous titanium tight-binding models, in particular the *d*-model which predicts the narrow π_1 fault with only $\sim$ 15 mJm^{-2} difference from the DFT value. However, prismatic stacking faults are still $\sim$ 100 mJm^{-2} lower than those expected by DFT, as found by previous tight-binding parameterisations and empirical potentials. From these results, one expects atomistic simulations to exhibit larger dissociation distances of $\langle a \rangle$ screw dislocations on the prismatic plane with the *d*-model and *sd*-models, compared to DFT. With regards to this specific parameterisation, the lower stable stacking fault energy could be due to insufficient short-range repulsion, as shearing the crystal along the prismatic plane along the $\langle a \rangle$ direction, the stable prismatic fault corresponds to a configuration where atoms are atop of one another.

Dissociation distance calculations considering edge dislocations suggest the mobilities of basal and π_1 $\langle a \rangle$ edge dislocations to be comparable, with the *d*-model of tight-binding replicating the DFT data of Curtin *et al.* well [166].

Rather surprisingly, the MEAM potential of Hennig *et al.* produces remarkably similar dissociation distances to DFT for screw dislocations. Atomistic calculations have shown this potential to exhibit screw dislocation core structures which are prismatically and pyramidally spread, akin to DFT, despite the erroneous ordering of the

prismatic, and basal faults [191]. This is perhaps due to the flexibility of this MEAM potential, which used cubic splines to determine the functional forms of which it is constituted. These splines were not constrained or physically motivated. The functional forms of the *d* and *sd* titanium tight-binding models, in contrast, were constrained to certain forms motivated by physical insight, and therefore cannot reproduce arbitrary data it is supplied with, unlike the MEAM. The success of the MEAM potential may suggest that in the fitting of tight-binding models for titanium, functional forms with more parameters, such as sums of Goodwin-Skinner-Pettifor potentials, or even splines, despite their poor second derivative properties, might be beneficial in providing sufficient flexibility to reproduce dissociation distances. Furthermore, perhaps the inclusion of more varied data—such as vacancy formation energies and force data from DFT molecular dynamics simulations, as used in the MEAM parameterisation—is necessary to include in the objective function, supplying enough variation in the local environment of titanium in the training data for it to generalise to situations far from that on which it was trained. This is further supported by the recent success of a Deep Potential (neural network parameterised) interatomic potential of titanium, which replicates the DFT core structures, from parameterisation on DFT molecular dynamics data, using a total of 11,948 datasets [192, 193].

However, one should note there is a difference in the philosophies in the tight-binding approach used here and that of empirical/learned potentials. In tight-binding, the use of DFT data for fitting is a means by which one can tune the physics-based models of which it is composed—that of simple quantum interactions, polarisation *et cetera*—such that one can gain both physical insight into, and predictions of, systems of interest; on the other hand, empirical/learned potentials use DFT data as a means to circumvent the large computational cost of DFT calculations; gaining scalability at the cost of losing physical insight, due to the compression of all physics of the system into a sum of environmentally-dependent energies. The latter does not have a physics-based model to rely upon when extrapolating to unseen scenarios, as such vast amounts of data is paramount to their success.

Comparing the pure titanium models to literature, we see that a simple *d*-model may be more suited to bulk and dislocation modelling due to the elastic properties, stacking faults and γ-surface energies being closer to DFT than the *sd*-model, albeit by a marginal amounts for bulk properties. The addition of *s*-electrons does not improve, in this case, the fitting to the target data. This is similar to previous tight-binding models, where the canonical *d* model fit the target data, and generalised better, than an

sd model [54]. However, for application to dislocation-oxygen interactions in titanium, the *sd*-model is preferred due to its explicit description of *s*-electrons.

Substituting the new Ti-Ti parameter sets in the Lozovoi and Paxton titanium dioxide model [172], and subsequently refitting the Ti-O parameters, deviations from the expected experimental/DFT quantities were found for both *d* and *sd* Ti-Ti models. The band gaps of the TiO_2 phases were impacted the most: the band gap of rutile was decreased, relative to that of anatase. However the decrease is not expected to significantly affect simulations of surface phases. As the gaps are larger than 2 eV, the simulated titanium dioxide phases are still wide-bandgap semiconductors, and as such, it is not expected that this discrepancy will affect the phenomena observed in future TiO_2 simulations.

In the section of parameter space searched for the bond integrals and the pair potential of the Ti-O/Ti-H parameters, the above discrepancies could not be assuaged. But, importantly, the cohesive energy, and relative cohesive energies between the various phases in the fitting (α-Ti, fluorite TiH_2 and rutile TiO_2) was made commensurate with the cohesive energies found from DFT, which was not apparent in the original parameterisation of the model. As such, the relative strengths of bonding for these phases is expected to be similar to that of DFT. Therefore, it is only the cohesive strength of pure titanium which is around $\sim 20\%$ lower than expected, suggesting in simulations which include Ti-Ti and Ti-O/Ti-H interactions, Ti-Ti bonds will be weaker relative to the others in the system, when comparing to DFT. This could make solution energies more negative and increase the dislocation-oxygen interaction energies. This could also affect the amount of corrosion of the Ti surface in future electrochemical simulations, due to less energy being necessary to break Ti-Ti bonds on the surface. But it is uncertain as to how marked this effect will be, and if this deviation in cohesive energy would significantly alter solute-hardening/corrosion mechanisms and predictions found from the model.

The adsorption energies of hydrogen and oxygen qualitatively agree with DFT, with the Ti-H parameters almost exactly reproducing the depth and amplitude of energetic oscillations upon insertion of hydrogen in hcp titanium. The Ti-O parameters show differences between the *d*-model and *sd*-model due to the extra charge available in the *sd*-model, but again, there is agreement in the general trends compared to DFT. The depth of the adsorption energies suggest reasonable solution energies for H/O can be obtained from these Ti-H and Ti-O parameters, if the energies upon deformation of pure titanium are comparable to DFT.

In the small NVT simulations of water on titanium an OH group adsorbs on the Ti surface becoming OH^-. This is similar to DFT simulations of water on titanium, in which an OH^- is adsorbed on the titanium (0001) surface, but with a small potential applied [194, 195]. However H^- was not seen to penetrate the surface layer of the metal in these DFT simulations, suggesting that the barrier to entry of the surface, as seen in figure 3.12, is larger in the case of the basis set used in VASP compared to the FP-LMTO DFT calculations seen here. These calculations should be repeated using the FP-LMTO code, to verify that the behaviour seen in these tight-binding simulations is correct. It is also stated in the aforementioned papers that the dissociated species is H^+ in DFT, despite no mention of either Bader or Mulliken charge analysis being performed within the VASP calculations themselves, as such, a comparison of the actual charges on the species cannot be performed. In addition, if such an analysis is performed in the VASP calculations, the charges quoted will not be integer. Again, validation tests by DFT calculations, in conjunction with some form of charge analysis, need to be performed to confirm whether the behaviour seen is reasonable, and to suggest reasons for its deviation.

These simulations have shown that the model is reasonably stable in molecular dynamics. But perhaps the large charge tolerance/amount of charge transfer included in the model is too large, which gave rise to the differences in behaviour compared to DFT. This may suggest a limit of the model's transferability, however these simulations cannot be experimentally verified, leaving the final verdict on transferability as inconclusive.

3.5 Conclusion

In conclusion, the fitting of Ti-Ti, Ti-O and Ti-H parameters was successful, resulting in the first polarisable-ion tight-binding model which can describe bulk Ti along with TiO_2, TiH_2 and H_2O.

The Ti-Ti parameter set gave good agreement with experimental data for lattice constants and bulk properties of titanium, but the bulk moduli and band gaps of titania phases suffered somewhat upon integration, even with refitted Ti-O bond integrals. All band structures were well replicated, with reductions in the band width of Ti d states compared to DFT and band gaps of TiO_2 phases compared to experiment. The best TiO_2 results came from the *sd*-model Ti-Ti parameters, as expected.

Rutile TiO_2 and fluorite TiH_2 cohesive energies were found to agree well with DFT,

with anatase TiO_2 coming out to be less stable than rutile TiO_2, in contrast to DFT. The cohesive energy of pure titanium matches the experimental result, which is less negative than that found by *ab-initio* methods, resulting in a reduction of the relative bond strength of titanium compared to TiO_2 and TiH_2. The vacancy formation energy of pure Ti is 30% higher than DFT, even though the cohesive energy per atom of pure Ti is lower than that of DFT, suggesting exaggerated charge transfer, which indicates that surface energies might be larger.

Of importance are the gamma surfaces and stable stacking fault energies, in which one finds the correct morphology and ordering respectively, for the *d*-model, which has not been seen in modern titanium tight-binding models. The stable stacking fault energies suggest large dissociation distances of the $\langle a \rangle$ screw dislocation on the prismatic plane, implying a reduction in the critical resolved shear stress of the tight-binding models on the prismatic glide plane compared to DFT. The relative mobilities of $\langle a \rangle$ screw dislocations, estimated by the calculation of other dissociation distances, predict that basal and pyramidal edge dislocations are of similar mobility, which is markedly less than that of prismatic edge dislocations, but somewhat comparable to prismatic screw dislocations.

Adsorption energies show upon insertion of H or O in pure titanium, similar reductions in energy are found compared to DFT, implying a potentially good agreement of solution energies. Most of the effect of insertion is determined by the repulsive pair potential rather than electrostatic contributions from charge transfer.

The first tight-binding simulations of water on titanium show a dissociation of water due to hydrogen gaining charge from titanium on the surface. The remaining OH group adsorbs on the surface with the H^- ion penetrating the charge depleted Ti surface. This behaviour was similar to DFT simulations of water adsorption with a small applied potential [194]. The deviation demonstrates a potential limit to transferability in this case, but more DFT/experimental work is necessary to validate this behaviour; to provide a final say on transferability.

With the correct ordering of stacking fault energies, and solution energies which are expected to be comparable to *ab-inito* methods, one can perform defect calculations pertinent to plasticity in titanium. In the next chapter, this will be achieved, and used as a means by which we can compare these simple tight-binding models to DFT and empirical data, thereby determining their predictive limits, while gaining an intuition for such systems from the physics included within these models. Defect calculations are good validation tests, in that they take the models well outside of the training

data upon which they were fit, thereby testing the transferability of the models.

Chapter 4

Modelling of defects in titanium

4.1 Introduction

Titanium alloys are ubiquitous in aerospace applications, due to their high strength-to-weight ratio and corrosion resistance among other properties [1]. The high strength of these alloys arises from the resulting microstructure—which is highly dependent on solute content, solution and ageing temperatures/times, amount of work *et cetera*—and the influence of solutes on plasticity within the grains themselves, such as solute-dislocation interactions. However, with respect to certain alloying elements, the mechanistic origin of their influence on plasticity is not well understood. A well-reported example of this is the action of oxygen in titanium alloys, in which there are dramatic changes in the hardness, ductility, and yield strength of the material, which is not in-keeping with classical theories of solute hardening [12, 15, 26, 28].

The plasticity of titanium at low temperature is controlled by the motion of screw dislocations. This has been evidenced in the work of Naka *et al.* [12], who observed a large lattice friction acting on $\langle a \rangle$ screw dislocations, which were found to have a much lower mobility compared to that of edge dislocations, implied by the observations of long screw segments, as seen in the work of de Crecy [183].

At low temperatures, wavy slip of screw dislocations has been reported [12, 15, 183], which show a propensity for screw dislocations to cross-slip from prismatic to pyramidal slip planes, which has been hypothesised to be controlled by a kink-pair mechanism [12, 31] and/or by locking-unlocking [16–19], where a sessile dislocation core is the ground state, and a glissile core is metastable. A diagram of these mechanisms are found in figure 1.2.

The stability of core structures on the prismatic and π_1 planes have been cor-

roborated by DFT calculations of titanium screw dislocations [19, 26, 75, 191, 196], showing screw cores which are either prismatically or pyramidally spread, with the latter being deemed the most stable. However, whether the pyramidal core is indeed the most stable is contentious. Tarrat *et al.* [132, 162] found both pyramidal and prismatic dissociation of $\langle a \rangle$ dislocations using the SIESTA code, with only a $\Delta E_{\mathrm{Pris-Pyr}} = 5.5 \pm 16.8$ meV/Å difference in the excess core energies. PWSCF calculations by Clouet *et al.* [19], found that the ground state $\langle a \rangle$ screw dislocation structure in pure titanium is pyramidally dissociated, with other core structures, notably that of a fully prismatic dissociation, being metastable, with the difference in the core energies being $\Delta E_{\mathrm{Pris-Pyr}} = 4.7 \pm 13.6$ meV/Å. Liang [196], found that a prismatic dissociation was the most stable from an initial configuration, but with modification of the input elastic constants in the anisotropic elasticity solutions used to generate the dislocation displacement field, a lower energy pyramidally spread screw dislocation in DFT was obtained, with a difference between the cores as $\Delta E_{\mathrm{Pris-Pyr}} = 15.0 \pm 18.0$meV/Å using VASP. The errors stated for the core energy differences of Liang and Clouet *et al.* were estimated from the per-atom error given by Tarrat *et al.* [133], as the errors were not stated in their respective texts. The total error for a given cell was obtained by the product of the number of atoms used in the simulation with the per-atom error. Note that the error in core energy differences is larger than the stated difference in core energies, hence it cannot be said with certainty which is the most stable.

It has been shown in titanium that there are dramatic increases in the yield strength of the alloy with oxygen content in both nanopillar compression [26] and uniaxial tensile tests [28]. These increases do not follow the $\sqrt{c}$ concentration dependence, as in the classical theory of solid solution strengthening of Fleischer [12, 29] in the Friedel (strong-pinning) limit, which applies when the distance of interaction between the solute and the dislocation is sufficiently small [26, 30, 197, 198]. Oxygen has been shown to inhabit octahedral sites in the vicinity of screw dislocation cores, as evidenced in HAADF-STEM images, and basal interstitial sites in lightly strained titanium, which have been suggested to be at the intersection of several dislocations [26]. As evidenced by Barkia *et al.* and Yu *et al.* [15, 26], screw dislocations are modified more by oxygen content than near-edge dislocations. In Ti-0.3wt% O alloy, screw dislocations have a compact core structure where oxygen is found in adjacent prismatic planes. The extent of the core is far smaller than the extended in-plane displacement as found in higher purity Ti-0.1wt% O alloy. Oxygen content was not found to modify near-edge dislocations found in Ti-0.1/0.2/0.3wt% O alloy, where

oxygen has been found on the tension side of these dislocations, close to the core. As such, it has been surmised that the strengthening effect of oxygen is due to screw dislocation-oxygen interactions, given the influence of oxygen on screw core structure, and the greater mobility of edge dislocations compared to screw dislocations.

ab-initio calculations of oxygen-screw dislocation interactions have consistently shown observations of a repulsive interaction between oxygen and screw dislocations [26, 75, 196]. In calculations seen thus far, oxygen causes the screw dislocation to locally cross-slip onto a basal or π_1 plane. This causes jogs to form on the dislocation line, which are necessarily of edge character, limiting the glide of these jogs on their basal or π_1 planes respectively. These act as pinning points for these dislocations. See figure 4.1, for a diagram.

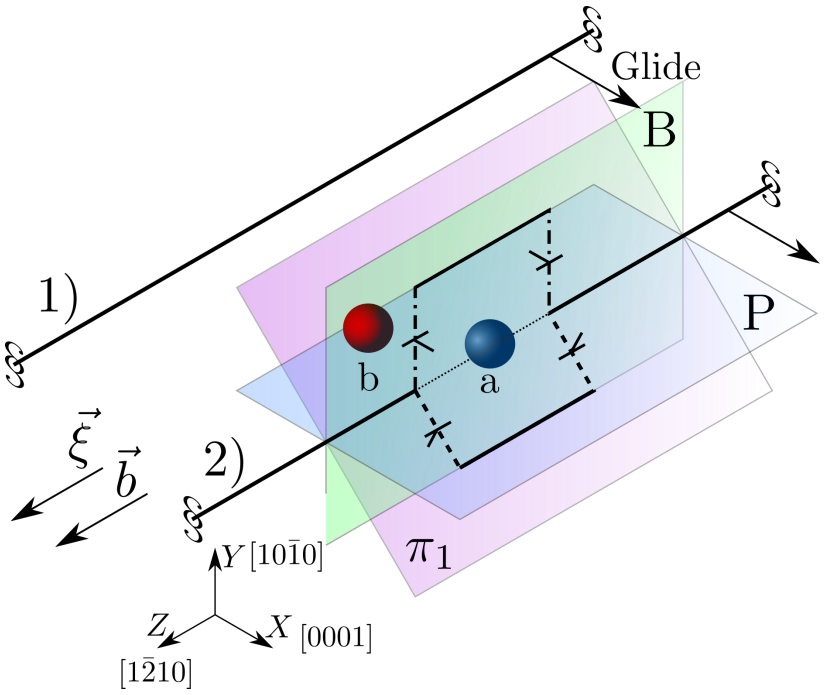

Fig. 4.1: Diagram of oxygen-screw dislocation interaction, forming a jog dipole on the basal and first-order pyramidal planes. Dashed lines correspond to π_1 edge segments, and dot-dashed lines correspond to basal edge segments. Oxygen causes cross-slip of dislocation at a, and then binds on the tension side of a jog segment at b.

It was first observed by Williams [24], that there exists a wavy-to-planar transition of slip in titanium, of which prevalence of planar slip increases with decreasing temperature and increasing oxygen content. Chong *et al.* extended this study, and observed a preference for planar slip with increasing oxygen content, decreasing tem-

perature, and increasing strain rate [28]. They attribute this to an interstitial shuffling mechanism (ISM), where oxygen causes cross-slipping events when dislocations move at low velocities, or when oxygen is fixed due to a lack of available energy for migration. Slip-plane softening (preference for planar slip) occurs when oxygen shuffles to a nearby hexahedral site, allowing for screw dislocations to move along the prismatic slip plane without being hindered by octahedral oxygen, which would give a large stacking fault energy, hindering dislocation motion, see figure 4.2. At higher temperatures, when oxygen diffusion is active, the oxygen can hop back from the hexahedral site to the octahedral, causing cross-slip. At high strain rates, oxygen cannot hop out of the hexahedral site, due to the proposed high flux of these screw dislocations past the same oxygen, as such oxygen will likely be in the preferred hexahedral site from a higher frequency of shuffling events. The preference for oxygen to be in the hexahedral site has been determined by DFT γ-surface calculations of both Yu *et al.* [26] and Kwasniak *et al.* [168].

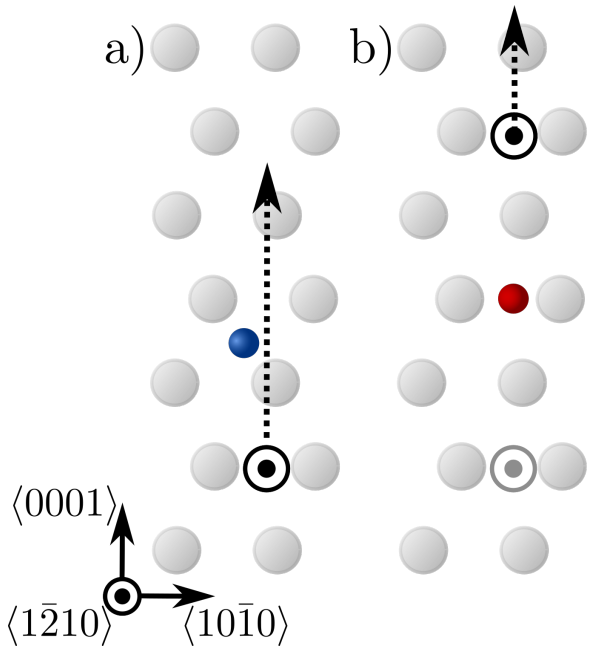

Fig. 4.2: Part of interstitial shuffling mechanism of Chong *et al.* to explain slip planarity in titanium [28]. Dislocation shown by ⊙, with direction of glide given by dashed arrows. At a high strain rate and low temperature, dislocations can pass by the oxygen on the prismatic plane, shuffling the oxygen from an octahedral site a), to a hexahedral site b), allowing for continued slip on the prismatic plane.

It is interesting to note that there has been no exploration in the literature of what

happens to oxygen, and the resulting effects on dislocation motion, *after* these cross-slip events occur. Oxygen has an attractive interaction between edge dislocations on the tension side, and a repulsive interaction with the compression side. On initial formation of the jog, there is no net binding energy to these edge segments, as such, the oxygen is not in a stable equilibrium with the jog dipole, as the system could lower its energy by allowing for oxygen to bind on the tension side of one of the jogs, by going from position a to b in figure 4.1. Furthermore, once bound, there will be a repulsive interaction between oxygen and the other jog of opposite sign, which can oppose jog-dipole annihilation. It is known that with small jog segments, upon action of a shear stress to move the whole dislocation line, there is a net force on the jogs which acts to annihilate them, due to dislocation bow out from the jog pinning points [199]. It is also likely that these jog segments would be small given the large expected Peierls stress on the basal/π_1 planes for screw dislocations. Oxygen-edge dislocation interactions could therefore stabilise jogs when oxygen diffusion is active, or after periods of quiescence, where oxygen can equilibriate with the edge dislocation. The diffusion barriers for oxygen migration could also be reduced around the dislocation core, as has been found in atomistic simulations of interstitial diffusion around dislocation cores in other metals [200, 201]. The stabilisation of jogs could allow for superjogs to form due to: the inhibition of jog glide which can discourage jog-dipole annihilation; the enhancement of screw dislocation cross-slip through the continued repulsive interaction of oxygen with the screw segment and the annihilation of screw dislocation segments upon further cross-slip and dislocation bow out [11, 202]. Indeed, it has been observed by Barkia *et al.* [15] that screw dislocations undergo jerky flow in both pure and oxygen-rich titanium, but whereas the origin of the jerky flow of screw dislocations in the former is due to the current, albeit contested, consensus of the locking-unlocking mechanism due to a metastable prismatic dislocation core [19], jogs and superjogs were formed with higher oxygen content which resulted in much shorter jump distances between pinning points, giving an additional character to the intermittent glide phenomena exhibited. Superjogs were seen to form and undergo loop expansion, causing dislocation multiplication. This was proposed to be due to cross-slip and consequent bowing of the jogged screw segment. This mechanism allowed for the formation of edge dipoles by the annihilation of screw segments. This work is supported by the experimental work of Williams, who found jogged screw dislocations and dislocation debris with higher oxygen content in titanium [24] and observations of "bursts" of dislocations with an increase of oxygen content in nanopillar compression

tests [26]. The binding energy of oxygen to these edge segments is important, as seen in the glide of superjogs in zirconium, another hcp transition metal with the same valence at titanium, where the glide velocity of the superjog is seen to be a linear function of the driving stress, consistent with a solute-dragging mechanism [203], influencing plasticity. The climb of jogs is an important consideration in creep regimes, with models of creep rate in titanium being controlled by jogged screw dislocations [204, 205].

The focus of this chapter is to investigate the tight-binding models which were created in section 3, to see:

1. How does tight-binding compare to other methods for the calculation of defect properties in titanium, such as solutes, dislocations and dislocation-oxygen interactions?

2. What does tight-binding predict for the mechanistic origin of the hardness increases of dislocations with oxygen content?

3. How does this compare to literature on the hardening mechanisms in titanium?

4.2 Methods

4.2.1 Oxygen/hydrogen interstitials

To further test the validity of the tight-binding models fitted, one calculated the solution energy of oxygen and hydrogen in various interstitial sites.

Within the scheme of tight-binding used, the energies one obtains are the cohesive energies, $E_{\text{coh}} = E_{\text{tot}} - E_{\text{free}}$, where E_{tot} is the energy functional we are approximating (either Harris-Foulkes or Hohenberg-Kohn-Sham) and E_{free} are the energy of the "free atoms" within the tight-binding scheme. These free atom energies are those which correspond to the initial on-site energy levels *neglecting* spin-polarisation.

In a standard calculation of the solution energy, upon the insertion of a species into a lattice in DFT, one calculates the total energies of the relaxed cells with and without the solute—$E(\text{Ti}_N\text{X})$ and $E(\text{Ti}_N)$ respectively—and subtracts the reference energy of the free atom calculated from DFT or other means (which accounts for if the exchange-correlation functional used includes spin-polarisation or not). In tight-binding, one can simulate isolated atoms, but the energies one obtains are not accurate, as the energy consists of a sum of occupied on-site levels, which are fit to reproduce properties of

bonding in a solid. However, one can work around this poor description of free atom energies by use of the tight-binding cohesive energy. To calculate a solution energy using the cohesive energy, one can use half of the experimental dissociation energy of the species of interest for a reference [81, 206]. Here, we use half the dissociation energy of O_2/H_2 dimers $\frac{1}{2}E_{\text{diss.}}(X_2)$, which furnish us with the equivalent reference energy, where $E_{\text{diss.}}(O_2) = -5.162$ eV [207] and $E_{\text{diss.}}(H_2) = -4.75$ eV [208] which agrees with quantum chemistry results [140]. We can then use the standard equation

$$E_{\text{sol}}(X) = E_{\text{coh}}(\text{Ti}_N\text{X}) - E_{\text{coh}}(\text{Ti}_N) - \frac{1}{2}E_{\text{diss.}}(\text{X}_2), \tag{4.1}$$

where $E_{\text{coh}}(\text{Ti}_N\text{X})$ and $E_{\text{coh}}(\text{Ti}_N)$ correspond to the cohesive energies of the cells mentioned above. The perfect cell used in these calculations was a $5 \times 5 \times 4$ cell of 200 atoms. The defected cells were created by simply placing an interstitial in the site of interest. All calculations were performed with a $6 \times 6 \times 8$ k-point mesh with relaxation performed until all forces were below 1×10^{-5} Ry/bohr.

4.2.2 Screw dislocations in pure titanium

4.2.2.1 Relaxation

As mentioned in section 4.1, the $\langle a \rangle$ screw dislocation in titanium is that which controls the plasticity of the alloy. The core structure—the displacement field of the resulting dislocation upon relaxation—determines the potential dynamics of the dislocation, *e.g.* the glide planes upon which it prefers to move. As such, determining all the different stable and metastable core structures is an important validation test for the titanium tight-binding models parameterised in chapter 3.

There have been no titanium tight-binding models in the modern literature, which have been able to reproduce the core structures of the of the $\langle a \rangle$ screw dislocation as seen in experiment. The pioneering work of Legrand [119, 120] found the correct prismatic dissociation using the recursion method, with just $dd\sigma$ and $dd\pi$ bond integrals, despite their ratios strongly deviating from the canonical band theory of Andersen [139]. All other tight-binding models, which have explicitly modelled dislocations thus far, notably the bond-order potentials of Girshick and Pettifor [125, 154] and Znam [164] have not exhibited the correct dissociation, finding basal dissociations for the ground-state, like that of EAM potentials [132], despite the basal core structures being high energy and unstable, as seen in the DFT work of Kwasniak and Clouet

[131]. Pyramidal or prismatic ground-state cores are preferred, as shown in DFT calculations and experimental considerations [12, 15, 17–19, 21, 24, 132, 133, 183].

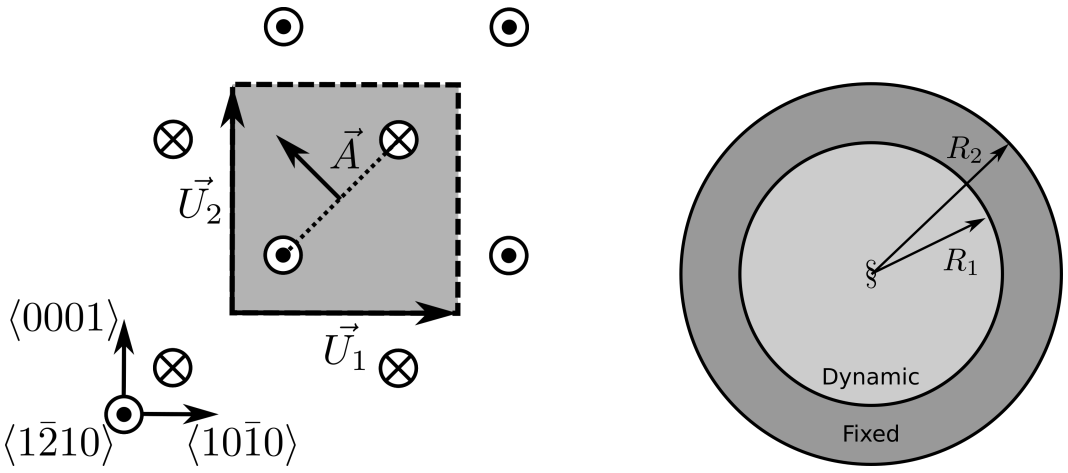

Fig. 4.3: Schematics of dislocation simulation methods. Left: quadrupolar arrangement of dislocations in a simulation cell (grey square). This arrangement minimises the stress experienced by each dislocation in a periodic simulation. Cell vectors $\vec{U}_1$ and $\vec{U}_2$ are shown; $\vec{A}$ defines the cut plane between the dipoles. The dislocation positions, and their corresponding Burgers vector direction, are denoted by the symbols $\otimes$ and $\odot$, which are antiparallel to each other. Tilt components added to cell vectors to accommodate for the plastic strain are not shown. Right: cluster method, where atoms are displaced according to the displacement field from the screw dislocation at the centre of the cluster, denoted by "§". Atoms in the annulus $R_2 - R_1$ are fixed in position to the anisotropic elasticity solutions. Within R_1, all atoms can relax. Periodicity is only imposed in the Z direction.

To determine the core structure of screw dislocations, there are multiple methods one may use, as seen in figure 4.3.

The cluster method, figure 4.3, right, simulates a single screw dislocation. Typically, a cylindrical disc of atoms, with depth of a Burgers vector, is created, in which a dislocation is placed in the centre. Periodicity is only imposed along the direction of the dislocation. The disc is split into two regions: a central region in which atoms are able to fully relax, and the remaining annulus around the former, in which atoms are fixed to the displacements arising from the anisotropic elasticity solutions. The thickness of the outer region is typically chosen to be just larger than the cutoff for atomic

interactions, such that the surface does not influence the relaxation of the dynamic region [209]. This simulation method is suitable for methods which can simulate a large number of atoms, as the boundary conditions of linear elasticity become more appropriate with larger cylinder radius; at smaller cell sizes, the boundary conditions can cause insufficient dislocation core relaxation [209].

In the cluster simulations performed in this chapter, one used cells which had $R_1 = 12a_{\mathrm{hcp}}$ and $R_2 = 15a_{\mathrm{hcp}}$, resulting in cells of 936 atoms: 728 atoms in the dynamic region and 208 atoms in the fixed region. The k-point mesh was $1 \times 1 \times 30$. The system was relaxed to a force tolerance of 1×10^{-5} Ryd/bohr.

The most prevalent method for dislocation simulation in DFT calculations is that of the periodic quadrupolar cell, in which a cell is constructed with a dislocation dipole, two dislocations of opposite Burgers vector, such that it, along with its periodic images, form a quadrupolar array of dislocations, see figure 4.3, left. This configuration minimises the stress which dislocations experience and allows them to relax without the imposition of fixed boundary conditions [155, 209]. With the inclusion of a dislocation dipole, a plastic strain is introduced into the cell, which results from the Burgers vector displacement introduced along the area swept out by the dislocation dipole cut plane [209]:

$$\varepsilon_{ij}^{\mathrm{plastic}} = \frac{b_i A_j + b_j A_i}{2\Omega}, \tag{4.2}$$

where b_i and A_j are components of the Burgers vector and the dipole cut plane normal respectively and Ω is the periodic supercell volume. This results in a back-stress, which can cause the dislocation dipole to annihilate. To accommodate this, the cell is strained by an opposing elastic strain $\varepsilon_{ij}^{0} = -\varepsilon_{ij}^{\mathrm{plastic}}$.

One must further modify the initial displacements which come from the dislocation dipole: the total displacement field generated from the two dislocations is not periodic. Artificial stacking faults are introduced at the edges of the simulation cell, which could inhibit relaxation. A correction term, found by Bulatov and Cai [209, 210], corrects for this by subtraction of the displacement fields from dipoles in the periodic array, and accounting for a conditionally convergent sum by measurement of a linear error term in the displacement.

The periodic displacement one wishes $\mathbf{u}^{\mathrm{periodic}}(\mathbf{r})$ is related to the sum of displacements resulting from periodic images $\mathbf{u}^{\mathrm{sum}}(\mathbf{r})$. For a quadrupolar array of screw dislocations, where the only non-zero displacement components are $u_z(\mathbf{r})$

$$u_z^{\mathrm{periodic}}(\mathbf{r}) = u_z^{\mathrm{sum}}(\mathbf{r}) - \mathbf{s} \cdot \mathbf{r}, \tag{4.3}$$

where $\mathbf{s}$ is the linear correction term to be determined and

$$u_z^{\text{sum}}(\mathbf{r}) = \sum_{\mathbf{R}_{\text{images}}} u_z(\mathbf{r} - \mathbf{R}), \tag{4.4}$$

where $u_z(\mathbf{r} - \mathbf{R})$ is the total displacement of the dislocation dipole from a periodic image which is at $\mathbf{R} = n_1\mathbf{U}_1 + n_2\mathbf{U}_2$, where n_1 and n_2 are integers and $\mathbf{U}_1$ and $\mathbf{U}_2$ are the x/y lattice vectors of the periodic simulation cell, which will be defined later. The correction term was determined by measuring $\mathbf{s}$ at four points in the simulation cell by use of the expression

$$u_z^{\text{sum}}(\mathbf{r} + \mathbf{U}_i) - u_z^{\text{sum}}(\mathbf{r}) = \mathbf{s} \cdot \mathbf{U}_i, \tag{4.5}$$

which allows for calculation of the periodic displacement from equation (4.3). All summations in this thesis were carried out with $n_i \in [-30, 30]$, which gave convergence in the components of $\mathbf{s}$ as $\sim 1 \times 10^{-6}$ compared to a large truncation limit of $n_i \in [-50, 50]$.

The quadrupolar cells used in this thesis had the "S" configuration, detailed by Clouet [155]. To construct this, dislocations of opposite Burgers vector had the initial dislocation coordinates placed at $\mathbf{r}_1 = \frac{1}{4}(\mathbf{U}_1 + \mathbf{U}_2)$ and $\mathbf{r}_2 = \frac{3}{4}(\mathbf{U}_1 + \mathbf{U}_2)$, where $\mathbf{U}_1 = n\frac{1}{2}a_{\text{hcp}}[10\bar{1}0]$, $\mathbf{U}_2 = mc_{\text{hcp}}[0001]$ and $\mathbf{U}_3 = l\mathbf{b} = la_{\text{hcp}}[1\bar{2}10]/3$ are the lattice vectors of the cell. The parameters $n = m = 12$ in all simulations, with $l = 1$ for initial dislocation relaxations. The dislocations had their cut plane along the diagonal towards the other dislocation centre. The cut plane normal $\mathbf{A}$ was obtained by a $\pi/2$ rotation of the vector joining the dipole, $\mathbf{D} = 1/2(\mathbf{r}_1 + \mathbf{r}_2)$. For the relaxation of dislocations, a $3 \times 3 \times 30$ k-point mesh was used for the 576 atom cell with $l = 1$, giving an error compared to a mesh size of $5 \times 5 \times 50$ of $\pm$1meV.

Dislocation excess energies were calculated as in Tarrat [133].

$$E_{\text{excess}} = E_{\text{disl.}} - E_{\text{perfect}}, \tag{4.6}$$

where $E_{\text{disl.}}$ is the energy of the dislocated cell, and E_{perfect} is the energy of the perfect cell prior to the inclusion of a dislocation.

Following each of these prescriptions one can obtain simulation cells of dislocations which can be subsequently relaxed. However, there still remains the choice of where to centre the screw dislocation(s). As noted by Tarrat *et al.* [132, 133], for the $\langle a \rangle$ screw dislocation in hcp, the differences in the choice of the elastic centre give rise to

different dislocation core structures. As such, dislocation relaxations were performed for each of the six different elastic centres, as done by Tarrat [133].

4.2.2.2 Peierls Stress

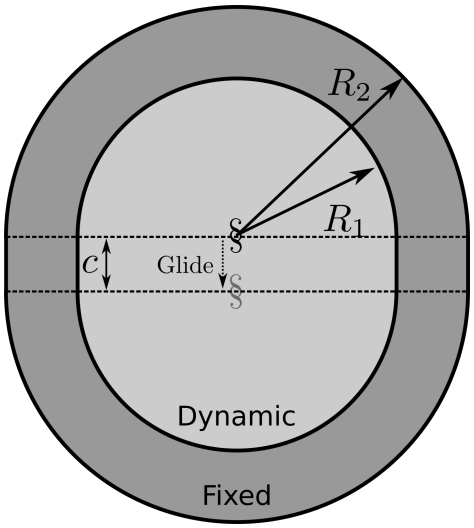

Fig. 4.4: Diagram of cell used to calculate Peierls stress.

The threshold resolved stress on a glide plane upon which a dislocation undergoes glide is the Peierls stress.

To find the Peierls stress from atomistic simulations, a method similar to Chen [211] and Trinkle [191] was followed: one incrementally applied strain and relaxed a cluster simulation cell containing a pre-relaxed dislocation to find the critical strain necessary to enact glide of the dislocation. For the Peierls stress on the prismatic plane, a simulation cell was constructed from two semi-discs of atoms, a top half and a bottom half, each with the same radii as in 4.2.2.1, $R_1 = 12a_{\mathrm{hcp}}$ and $R_2 = 15a_{\mathrm{hcp}}$. A $1c$ thick layer of titanium joined the two semicircles, elongating the cell along the $Y = [0001]$ axis, as seen in figure 4.4. The bulk and dynamic regions were commensurate between the two semicircles, where the aforementioned radii became the widths on the x-axis between which atoms were fixed to the anisotropic elasticity displacements, and the rest were dynamic. A dislocation was placed at the centre of the top semicircle and then relaxed using the same tolerances found in 4.2.2.1.

The resulting cell was then given an ε_{xz} strain, in increments of 1×10^{-4}, resulting in the imposition of the stress, by Hooke's law, $\sigma_{ij} = C_{ijkl}\varepsilon_{kl}$, as $0.0001C^{\mathrm{rot}}$, where C^{rot} is the elastic constant which has been rotated into the dislocation coordinate system

which is pertinent to the applied strain. The total strain increment necessary to move the centre of the dislocation to the centre of the other semicircle, was used to calculate the Peierls stress.

The dislocation centre was determined by differential displacement maps using an in-house code which followed Itakura *et al.* [76]. These figures show the displacement of atoms around a dislocation, where arrows point from one column of atoms to a neighbouring column if the neighbouring column has a larger differential displacement. The differential displacement was determined by first taking the minimum image convention for the atoms in the supercell for the displacement component of interest: where atoms only interact with the particles in the image with the smallest displacement. From the resultant cell, the differential displacement was calculated from the atomic displacements by the equation $u_{ij}^k = (u_i^k - u_j^k)/b$ where u_{ij}^k is the differential displacement for component k of the displacement vector $\mathbf{u}_i = (u_i^x, u_i^y, u_i^z)$. The requirement of $|u_{ij}| \leq \frac{1}{2}$ was always satisfied. A closed circuit of differential displacement arrows encapsulates the dislocation core—this is equivalent to a Burgers circuit.

The original elastic constant matrix in 6×6 Voigt form, in the reference hcp coordinate system is:

$$C = \begin{bmatrix} C_{11} & C_{12} & C_{13} & 0 & 0 & 0 \\ C_{12} & C_{11} & C_{13} & 0 & 0 & 0 \\ C_{13} & C_{13} & C_{33} & 0 & 0 & 0 \\ 0 & 0 & 0 & C_{44} & 0 & 0 \\ 0 & 0 & 0 & 0 & C_{44} & 0 \\ 0 & 0 & 0 & 0 & 0 & C_{66} \end{bmatrix} \tag{4.7}$$

Transforming it into the dislocation coordinate system of a prismatic screw, by the rotation

$$R_{\text{prismatic}} = \begin{bmatrix} 1 & 0 & 0 \\ 0 & 0 & -1 \\ 0 & 1 & 0 \end{bmatrix} \tag{4.8}$$

gives

$$C^{\text{rot.}} = \begin{bmatrix} C_{11} & C_{13} & C_{12} & 0 & 0 & 0 \\ C_{13} & C_{11} & C_{13} & 0 & 0 & 0 \\ C_{12} & C_{13} & C_{33} & 0 & 0 & 0 \\ 0 & 0 & 0 & C_{44} & 0 & 0 \\ 0 & 0 & 0 & 0 & C_{66} & 0 \\ 0 & 0 & 0 & 0 & 0 & C_{44} \end{bmatrix}. \tag{4.9}$$

4.2.3 Screw dislocation-oxygen interactions

From the relaxed core structures, one can insert oxygen into various octahedral sites to see how oxygen changes the dislocation core structure, to reveal potential hardening mechanisms with oxygen content in titanium.

We follow a method similar to that of Chaari *et al.* who performed oxygen-screw dislocation interactions in both titanium and zirconium using DFT [74, 75]. Starting from the relaxed cell of a dislocation dipole, the cell was repeated along the dislocation line to $l = 3$ giving $\mathbf{U}_3 = 3\mathbf{b}$. Within the central layer, oxygen was inserted into various octahedral sites around the dislocation at various distances on the prismatic glide plane and on adjacent prismatic planes. A single oxygen was placed next to both dislocations, such that during the simulation the reaction of each dislocation would be similar, thereby keeping the quadrupolar dislocation array balanced. Relaxation of this cell was performed using a $2 \times 2 \times 10$ k-point mesh to the same 1×10^{-5} Ryd/bohr force tolerance. It was verified that there was no significant difference between the core structures found using the cluster method and the quadrupolar method.

4.2.4 Edge dislocation-oxygen interactions in anisotropic elasticity

As will be shown in section 4.3.3, oxygen interactions with screw dislocations are repulsive, and hence screw dislocations will try to avoid oxygen. If there is avoidance by cross-slip—where the screw dislocation shifts onto an adjacent plane—basal/pyramidal edge segments will be created. The binding of oxygen to edge dislocations therefore becomes an important interaction in discerning how these edge segments, which become the primary pinning points of the dislocation, move: if there is a strong binding of oxygen to edge dislocations, and the migration barrier for oxygen to jump to the tension side of the edge dislocation is low/active, then the jog segments are pinned by

the oxygen. This can influence the motion of screw dislocations, and plays a role in dislocation creep [204, 205].

There is a dearth of work in the literature pertaining to atomistic calculation of edge dislocations in titanium in general, and there has been no work, to the knowledge of the author, pertaining to oxygen interaction with π_1 or basal edge dislocations. For the purposes of comparing the titanium tight-binding models and to DFT, one therefore used anisotropic elasticity theory, from which one can directly obtain the binding energies of oxygen to edge dislocations from the results of structural and volume relaxation of oxygen interstitials, by calculation of the elastic dipole tensor. as has been achieved for carbon in iron [212–215].

Relaxations of oxygen in the most stable interstitial site in hcp titanium, the octahedral site, were used to determine the elastic dipole tensor. After an initial structural relaxation was performed for the $\mathrm{Ti}_N\mathrm{O}_{\mathrm{oct.}}$ and Ti_N cells, with fixed lattice parameters, the volume was optimised by variation of the lattice vectors, using the same charge and force tolerances, allowing again for full structural relaxation upon a lattice vector change. Due to the symmetry of the hexagonal cell, the $\mathbf{p}_x$ and $\mathbf{p}_y$ lattice vectors were changed together, while the $\mathbf{p}_z$ vector was varied independently. The optimal lattice vectors were found using a grid search where the $\mathbf{p}_{x/y}$ and $\mathbf{p}_z$ lattice parameters were changed between $\pm 3\%$ or $\pm 4\%$, for the $3 \times 3 \times 2$ and $4 \times 4 \times 3$ cells respectively in increments of 1.5% or 2.0%. A fourth order 2D polynomial was fitted to the results, from which the minimum energy lattice vectors were estimated.

From the volume optimised cells, one can calculate the elastic dipole tensor of an interstitial. Following Bacon, Barnett and Scattergood [169] and Clouet [155], in continuum elasticity theory, one can model an interstitial in a lattice as an array of point forces from the interstitial defect position which act on the host material. The displacement arising from the point forces of the defect can be expressed as the sum of a Green's function, expanded in multipole moments, in product with the corresponding moments of the point force array. The elastic dipole tensor, P_{ij}, is the first moment of the point force array.

In a periodic atomistic simulation involving a point defect, if one allows the cell vectors to change, the cell takes on an homogeneous strain ε_{ij} to accommodate for the strain generated by the point defect. In elasticity theory, applying a strain to a body with a point defect gives rise to an energy E_ε which is that of the self-energy of the body, and the interaction with the elastic dipole of the interstitial:

$$E_\varepsilon = \frac{1}{2} V C_{ijkl} \varepsilon_{ij} \varepsilon_{kl} - P_{ij} \varepsilon_{ij}, \tag{4.10}$$

where V is the volume and C_{ijkl} is the elastic constant tensor. The strain that minimises this energy gives [212, 214]

$$P_{ij} = V C_{ijkl} \varepsilon_{kl}. \tag{4.11}$$

For an octahedral site in the hcp lattice, the elastic dipole tensor is diagonal and in the usual hcp coordinate system, has $P_{11} = P_{22}$ giving [216]:

$$P_{\text{hcp}} = \begin{bmatrix} P_{11} & 0 & 0 \\ 0 & P_{11} & 0 \\ 0 & 0 & P_{33} \end{bmatrix}. \tag{4.12}$$

On rotation of the tensor into a basal edge dislocation coordinate system, where $X = [11\bar{2}0]$, $Y = [0001]$ and $Z = [\bar{1}100]$, were the Z-axis is parallel to the dislocation line-sense, by the rotation matrix

$$R_{\text{basal}} = \begin{bmatrix} 1 & 0 & 0 \\ 0 & 0 & -1 \\ 0 & 1 & 0 \end{bmatrix} \tag{4.13}$$

using the relation $\mathbf{T}' = \mathbf{R} \cdot \mathbf{T} \cdot \mathbf{R}^T$ for a rank 2 tensor $\mathbf{T}$, one obtains the dipole tensor in the dislocation coordinate system as

$$P_{\text{basal}} = \begin{bmatrix} P_{11} & 0 & 0 \\ 0 & P_{33} & 0 \\ 0 & 0 & P_{11} \end{bmatrix}, \tag{4.14}$$

Similarly, one can rotate the tensor into the dislocation coordinate system of an edge dislocation with a first-order pyramidal glide plane using the rotation matrix

$$R_{\pi_1} = \begin{bmatrix} 1 & 0 & 0 \\ 0 & \cos\alpha & -\sin\alpha \\ 0 & \sin\alpha & \cos\alpha \end{bmatrix} \tag{4.15}$$

where $\alpha = \arccos \frac{2q}{\sqrt{3+4q^2}}$, where q is the c/a ratio, giving the dislocation coordinate

system as $X = [11\bar{2}0]$, $Y = [10\bar{1}1]$ and $Z = [11\bar{2}3]$, where the dislocation line is parallel to Z.

One can obtain the binding energies of an edge dislocation directly from elasticity theory using these expressions for these dipole tensors where:

$$E_{\text{bind.}}^{\text{edge}} = P_{ij}^{\text{disl.}} \varepsilon_{ij}^{\text{edge}}, \tag{4.16}$$

where $\varepsilon_{ij}^{\text{edge}}$ is the strain field generated by an edge dislocation in the dislocation coordinate system of interest. As in the elasticity calculations of carbon in iron by Douthwaite [215] and others [212, 217], the strain field of the dislocation can be obtained from the stress tensor in the dislocation coordinate system, $\sigma_{kl}^{\text{edge}}$ resulting from the anisotropic elasticity solutions by the relation

$$\varepsilon_{ij}^{\text{edge}} = S_{ijkl} \sigma_{kl}^{\text{edge}}, \tag{4.17}$$

where S_{ijkl} is the compliance tensor in the dislocation coordinate system, which can be obtained by inversion of the corresponding 6×6 elastic constant matrix in the Voigt representation [7]. The elastic constant matrix for the basal plane is exactly that found in equation (4.9), as expected due to the transverse isotropy of hcp crystals. For the π_1 $\langle a \rangle$ edge dislocation, the elastic constant matrix of the *sd*-model becomes, in 6×6 Voigt form:

$$C_{\pi_1}^{\text{rot.}} = \begin{bmatrix} 176.2 & 92.7 & 68.1 & 19.2 & 0 & 0 \\ 92.7 & 171.8 & 69.6 & 0.8 & 0 & 0 \\ 68.1 & 69.6 & 189.5 & -14.6 & 0 & 0 \\ 19.2 & 0.8 & -14.6 & 62.6 & 0 & 0 \\ 0 & 0 & 0 & 0 & 47.4 & -5.9 \\ 0 & 0 & 0 & 0 & -5.9 & 39.7 \end{bmatrix}, \tag{4.18}$$

where the constants are in GPa.

Elasticity theory has limitations, and cannot be applied close to the dislocation core due to the $1/r$ divergence of the dislocation stress field with decreasing distance to the dislocation core. As such, a core radius, the radius beneath which elasticity theory cannot be relied upon, must be defined, and was taken to be equal to half the dissociation distance found in table 3.5, giving the radius of the core region to be $r_c = \zeta = d_{\text{diss.}}/2(1-\nu)$, where $d_{\text{diss.}}$ is the dissociation distance and $\nu = 0.315$ is Poisson's ratio. This agrees with arguments in Hirth and Lothe, and Argon that the core radius can be given by the core width [7, 11]. As the dislocation core width

of $\{0001\}\ \langle a\rangle$ and $\{10\bar{1}1\}\ \langle a\rangle$ edge dislocations are smaller compared to that of the prismatic screw dislocation, it is expected that the binding energy of oxygen can be estimated reasonably well close to the core.

4.3 Results

4.3.1 Oxygen/hydrogen interstitials

The solution energies, without volume relaxation, for oxygen and hydrogen in various interstitial sites are shown in tables 4.1 and 4.2 respectively. It should be noted, in the DFT results there was additional volume relaxation performed, as such, these solution energies are upper bounds, and here to illustrate the behaviour of the Ti-Ti/Ti-O models in comparison to DFT. Results with volume relaxation for oxygen in the octahedral site are presented in section 4.3.4.

Site	$E_{\text{sol}}^{sd-\text{TB}}$ [eV]	$E_{\text{sol}}^{d-\text{TB}}$ [eV]	$E_{\text{sol}}^{\text{DFT}}$ [eV]	
Tetrahedral	Unstable (O)	Unstable (O)	Unstable (H) [218]	–4.37 [219]
Octahedral	–5.48	–6.78	–5.61 [218]	–5.54 [219]
Hexahedral	Unstable (O)	Unstable (O)	–4.38 [218]	–4.36 [219]
Basal Oct.	Unstable (O)	Unstable (O)	Unstable (N/A) [218]	–2.22 [219]
Crowdion	Unstable (O)	Unstable (O)	–4.30 [218]	–3.93 [219]
Basal C	Unstable (O)	Unstable (O)	–4.37 [219]	

Table 4.1: Oxygen solution energies in various interstitial sites using the tight-binding model which was fitted in chapter 3. Unstable (X) indicates that there is a decay of the interstitial from the initial site to site X, where X can be an octahedral (O) or hexahedral (H) site.

There is good agreement of the solution energy for the octahedral site in the *sd*-model, with simulations also showing that the oxygen is unstable in the tetrahedral site. There are differences in the stable site which the oxygen decays to however. In the DFT simulations of Scotti and Mottura [218], one finds that oxygen initially placed in a tetrahedral site decays to a hexahedral site, not an octahedral site as found in the *d*-model or *sd*-model. However this instability (or in fact, any instability of a solute in an interstitial site) has not been noted in the simulations of Nayak *et al.* [219]. One finds a difference in the solution energies of the *d*-model and *sd*-model, where the *sd*-model predicts less negative solution energies. The difference in behaviour is likely due to the enhanced charge transfer which takes place in the *sd*-model. In both models, the electronegative oxygen takes charge from the titanium atoms in range (the

Ti-O parameter range), however, as Ti-Ti s-electron hoppings are active, there is a movement of charge from those Ti species which neighbour the depleted Ti species. The s-electrons move to the depleted Ti to screen the charge depleted species in the sd-model, whereas this cannot happen in the d-model, due to the lack of s-electron bond integrals. This reduces the energy from electrostatics between Ti and O in the sd-model due to screening by Ti s-electrons, causing a less negative solution energy. This replicates the adsorption energy results seen in section 3.3.3, where the d-model showed a more negative adsorption energy overall upon insertion of oxygen into the unrelaxed hcp Ti lattice.

Site	$E_{\text{sol}}^{sd-\text{TB}}$ [eV]	$E_{\text{sol}}^{d-\text{TB}}$ [eV]	$E_{\text{sol}}^{\text{DFT}}$ [eV]	
Tetrahedral	Unstable (O)	Unstable (O)	–2.65 [220]	–2.62 [219]
Octahedral	–2.65	–2.75	–2.72 [220]	–2.72 [219]
Hexahedral	Unstable (O)	Unstable (O)	–2.59 [219]	

Table 4.2: Hydrogen solution energies in various interstitial sites using the tight-binding model which was fitted in chapter 3.

Similarly, we find a slightly more negative solution energy for hydrogen when using the d-model over the sd-model for the same reason as above. Hydrogen is not as electronegative, nor can it acquire as much charge as oxygen, hence there is only a 0.1 eV difference between the sd-model and the d-model. The solution energy here is in very good agreement with DFT, and it is not expected that volume relaxation would change the results significantly due to the small strain which hydrogen creates.

4.3.2 Pure screw dislocations in titanium

4.3.2.1 Relaxation

As detailed by the DFT calculations of Tarrat [132, 133], the core structure of screw dislocations in titanium depends on the position of the elastic centre for the anisotropic elasticity solutions. In figure 4.5, one finds the relaxed $\langle a \rangle$ pure screw dislocation structures from both the d and sd titanium tight-binding models for all initial positions of the elastic center (hereon referred to as IPs). The $\alpha_{33} \equiv \rho_{\text{b}}$ component of the Nye tensor is shown scaled by the hcp lattice parameter a for ease of comparison with literature [19]. The Nye tensor was calculated from the ATOMMAN python library, where the Nye tensor α_{ij} describes a distribution of infinitesimal dislocations, of Burgers vector $\mathrm{d}b_i = \int_A \alpha_{ij} n_j \mathrm{d}A$, where $\mathbf{n}$ is the unit vector normal of the infinitesimal area

dA which is enclosed by the Burgers circuit being taken [221]. The corresponding relaxations were also performed in the cluster cell, but the core structures obtained were found to be similar to those found by quadrupolar array simulations, for both the d and sd-models.

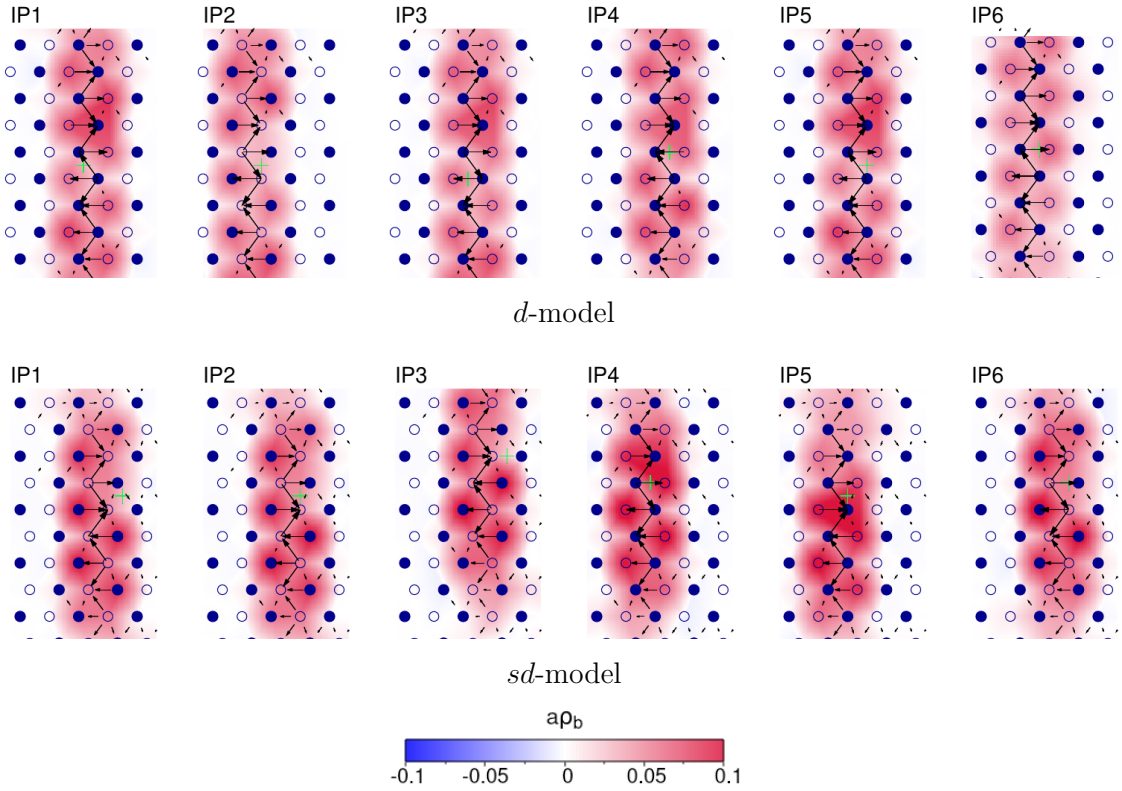

Fig. 4.5: Pure screw dislocation relaxations in the d and sd titanium models using a quadrupolar cell. Plots of the α_{33} component of the Nye tensor are shown to highlight spreading of the core along the prismatic plane. Differential displacement arrows also shown for the Z displacement component, with differential displacements less than $0.1b$ being omitted for clarity. The dislocation core is enclosed by a closed triad of arrows, which denotes a total displacement of b. Initial elastic centre of the dislocation shown by the lime-green cross.

For both tight-binding models, regardless of the initial configuration, one finds a prismatic spreading, which is more pronounced in the d-model than the sd-model; furthermore, the spreading found is larger than that in DFT results. This is corroborated by the dissociation distance data found in table 3.5, where the dissociation distance of the prismatic partials of the sd-model are less than that of the d-model, and both are larger than those found in DFT. There is no basal plane spreading as has been found

in previous tight-binding models. This is likely due to the correct ordering of the stacking fault energies in addition to a likely increased basal core energy, as implied by the γ-surfaces in chapter 3.

Notably, one does not find dissociation on the first-order pyramidal plane to be the ground state configuration in these tight-binding models, which differs from that of DFT simulations [19, 132, 133, 196]. Hence, one does not predict, in these tight-binding models, that wavy slip would occur by a locking-unlocking mechanism, as that suggested by Clouet *et al.* [19]. Only planar prismatic slip is expected.

Initial position	*d*-TB	*sd*-TB	DFT [133]
IP1	0.7328 (P)	0.44231 (P)	0.4396 (π_1)
IP2	0.7417 (P)	0.44231 (P)	0.4484 (π_1)
IP3	0.8111 (P)	0.44221 (P)	0.4419 (P)
IP4	0.7275 (P)	0.44222 (P)	0.4425 (P)
IP5	0.7430 (P)	0.44231 (P)	0.4364 (π_1)
IP6	0.7318 (P)	0.44221 (P)	0.4441 (P)

Table 4.3: Energies of the different dislocation cores in the *d* and *sd*-TB models compared to DFT. All energies in eV/Å. P and π_1 denote the observed dissociation of the core in the prismatic or π_1 planes respectively. The k-points used for these cells gives an error for each excess energy of $e^{\mathrm{TB}}_{\mathrm{excess}} = \pm 2 \times 1\mathrm{meV}/a_{\mathrm{hcp}} = \pm 0.678\mathrm{meV\AA}^{-1}$. The error in the results of Tarrat are $e^{\mathrm{DFT}}_{\mathrm{excess}} = \pm 16.4\mathrm{meV\AA}^{-1}$.

The dislocation excess energies, table 4.3, of the *sd*-model agree remarkably well in terms of magnitude with the DFT results by Tarrat *et al.* [133], with only a maximum difference of 6 meVÅ^{-1} for the resulting core structure at a given initial position. The core structures found in the paper of Tarrat *et al.* do differ in core structure however (for example, exhibiting pyramidal dissociations), whereas the core structures resulting from tight-binding are all prismatically dissociated, hence, there is little variation in the excess energies with a change of the initial dislocation position. The *d*-model screw dislocation core excess energies are ~ 1.6 times larger than that of the *sd*-model, which is a surprisingly large difference. The larger excess energy is due to the additional short-ranged power law contribution in the pair potential in the *d*-model. This increases the energy of Ti atoms if found too close to each other, as is found for the prismatic stacking fault associated with $\langle a \rangle$ dislocation dissociation at $[1\bar{2}10]/6$, as mentioned in the previous chapter.

The prevalence of prismatic dissociation implies that the π_1 stacking fault or the core energy associated with a $\langle a \rangle$ screw π_1 dissociation in these tight-binding models is too large in energy.

To try to induce a lower energy pyramidal core, further cells were created for both the *d*-model and *sd*-model in which the initial displacement field was generated from the expected pyramidal partial dislocations as in equation (3.11), using a method similar to Kwasniak and Clouet in their generation of basal $\langle a \rangle$ dislocation configurations from separated partials [131]. The only separation between the partials trialled was $\lambda = \sqrt{c_{\mathrm{hcp}}^2 + a_{\mathrm{hcp}}^2/4}$, which is approximately the dissociated distance of the π_1 partials in DFT. However, a prismatic dissociation was always preferred. Other separations could be attempted in future work, but it is likely that this core is high energy and metastable.

4.3.2.2 Peierls Stress

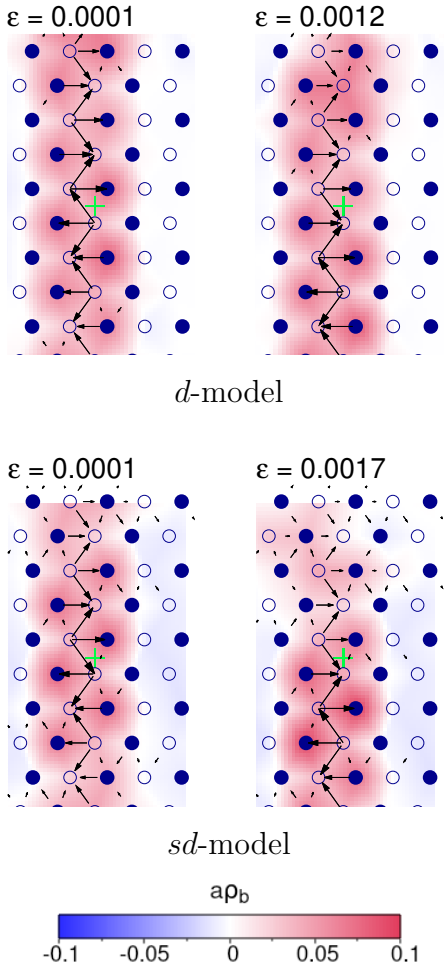

Fig. 4.6: Change in core structure of IP5 dislocation with strain in the *d* and *sd* titanium models, with critical Peierls stress. Plots of the α_{33} component of the Nye tensor are shown to highlight spreading of the core along with the differential displacement in Z, with differential displacements less than $0.1b$ being omitted for clarity. Initial elastic centre of the dislocation shown by the lime-green cross.

The core structures found upon straining to cause prismatic glide are found in figure 4.6. Using an increment in the ε_{xz} strain of $1 \times 10^{-4} C^{\text{rot}}$, where C^{rot} is the transformed elastic constant, with a value of $C_{44}^{d-\text{rot}} = 38.4749$ GPa, we find in the *d*-model that the dislocation glides along the prismatic plane at $\sigma_{xz}^{dc} = 0.0012 C_{44}^{d-\text{rot}}$, giving a Peierls stress of $\sigma_{xz}^{dc} = 2C_{44}\varepsilon_{xz} = 92.3$ MPa. For the *sd*-model one found the stress increment to be $\sigma_{xz}^{sdc} = 0.0017 C_{44}^{sd-\text{rot}} = 0.0017 \times 48.86$ GPa $= 166.124$ MPa. These strains are

smaller than those found by the MEAM potential of Trinkle *et al.* [191, 222], where a strain of $\varepsilon_{xz}^{\mathrm{MEAMc}} = 0.005 \implies \sigma_{xz}^{\mathrm{MEAMc}} = 580$ MPa, resulting in the tight-binding models being ~ 3 to 6 times easier to enact glide in than the MEAM. The tight-binding Peierls stresses do however agree with experimental results in high-purity titanium. Biget and Saada [22] find at 4K, a CRSS of ~ 100 MPa, which agrees especially well with the *d*-model value of 92.3 MPa. This value is lower than other flow stresses quoted in other studies due to the large effect of impurities, as noted by the authors.

Trinkle *et al.* [191] find that upon action of strain, basal or prismatic, on pyramidally dissociated cores, a transformation to the prismatic core always occurs. The core which undergoes *pyramidal* dissociation is metastable in the MEAM, with the prismatic core being the ground state. We find in tight-binding that there are no metastable cores upon relaxation of the anisotropic elasticity displacements, just prismatic dissociation, but the dislocation core structure remains in a prismatic configuration under strain, in agreement with this empirical potential.

4.3.3 Screw dislocation-oxygen interactions

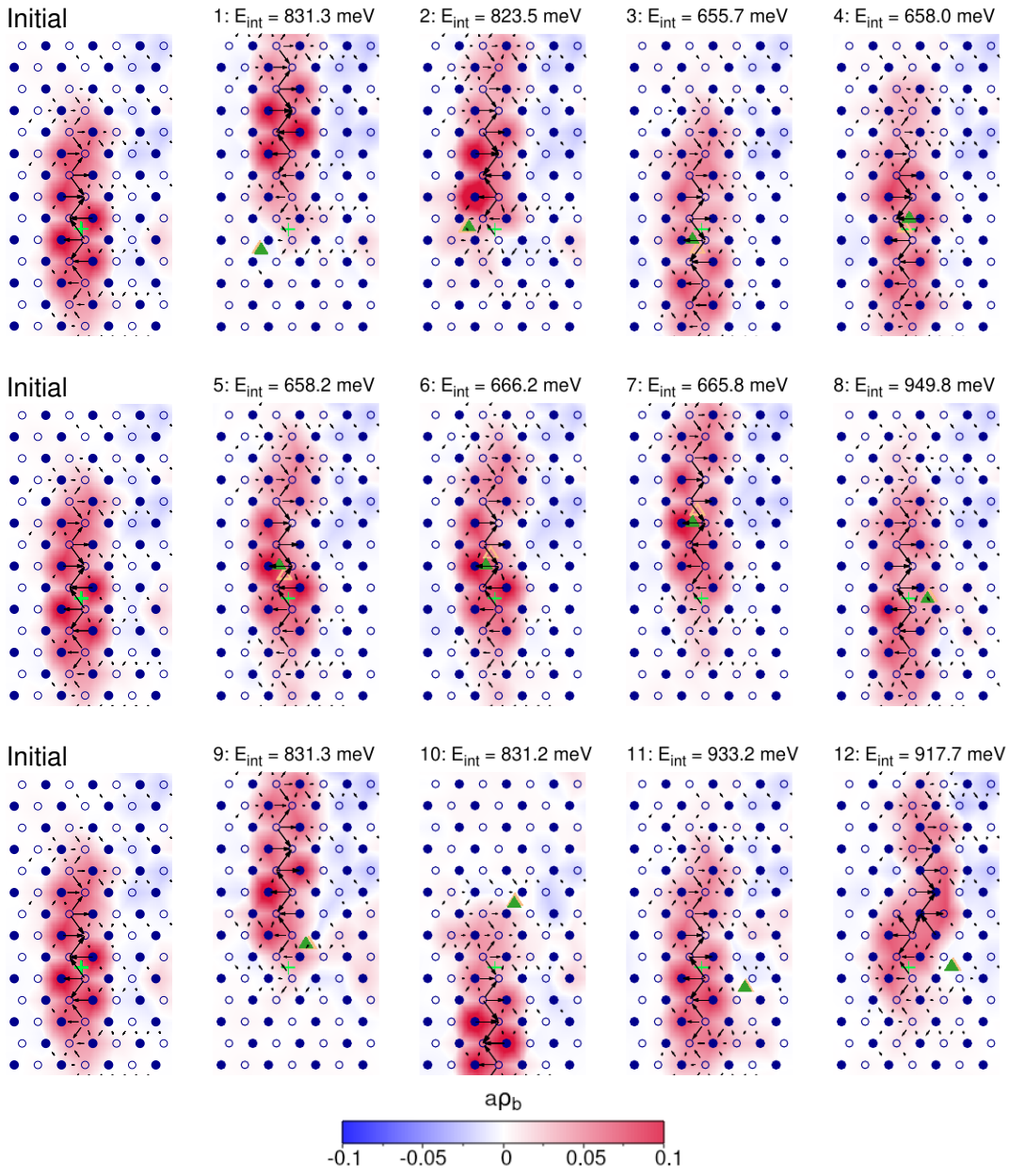

Fig. 4.7: Oxygen-screw dislocation relaxations in the *sd* titanium model using a quadrupolar cell. Initial position of oxygen given by orange, unfilled triangle, with final position given by filled green triangle. Initial elastic centre shown by lime-green cross for reference. Plots of the α_{33} component of the Nye tensor are shown of the middle layer which contains oxygen. Differential displacements less than $0.1b$ were omitted for clarity.

In figure 4.7, we see the screw dislocation core structure changes upon insertion of oxygen into different sites around the core. There are differences in some core configurations between tight-binding and DFT. In tight-binding, if oxygen is placed in an adjacent prismatic plane, and is placed further than the extent of the partial in the c direction, one finds that the repulsive interaction causes the dislocation to move along the prismatic plane away from the oxygen (figure 4.7: 1,10). When placed closer to the dislocation, the screw core moves a smaller distance along the prismatic plane, with a redistribution of the Burgers vector density towards the oxygen (figure 4.7: 2,9). When oxygen is placed in the prismatic plane upon which the dislocation has dissociated, if the oxygen is in the vicinity of the dislocation core, oxygen prefers to be in the hexahedral site which is created by the prismatic stacking fault (figure 4.7: 3–6). As the oxygen is placed at further distances from the dislocation elastic centre along the prismatic plane, there is a preference for the screw dislocation to move to the oxygen, which again, decays into the newly created hexahedral site created by the prismatic stacking fault (figure 4.7: 7). If oxygen is in an octahedral site on the basal plane which intersects with the elastic centre of the dislocation, the core stays in the same position, if the oxygen is in the closest prismatic plane (figure 4.7: 11). When placed in the second closest prismatic plane, on the same basal plane intersecting the elastic centre, one finds that the core reconfigures into a mixed prismatic-pyramidal core, where the prismatic partial is on same plane as the oxygen (figure 4.7: 12).

We find in tight-binding there is a tendency for oxygen to go into the hexahedral site created by the prismatic stacking fault, despite the instability in the usual lattice of the hexahedral site, as seen in table 4.1. This is due to the increased volume available in the site, as mentioned in work by Yu [26]. When this occurs there is a slightly enhanced dissociation of the partial dislocations on the glide plane due to the repulsive interaction with oxygen. This was also corroborated by NEB stacking fault calculations by Kwasniak [168].

Tight-binding predicts that the dislocation will locally create kinks on the prismatic glide plane, either by the repulsive effect of oxygen on the dislocation, figure 4.7: 1,2,9,10, or by the lowest energy configuration being that of the oxygen within the site created by the prismatic stacking fault, as found in the behaviour in figure 4.7: 3–6. Jogs on the π_1 plane can be formed as seen in figure 4.7: 12.

In figure 4.7: 12, it is interesting that the dislocation undergoes π_1 cross-slip towards the oxygen, allowing Burgers vector density onto the π_1 plane and the adjacent prismatic plane which contains the oxygen. When the oxygen is closer to the dis-

location, on the same basal plane, figure 4.7: 8, we do not see this behaviour: the dislocation stays where it is due to the equally repulsive interaction oxygen has with the partials on either side of it. This behaviour could be due to the reduction of the stable stacking fault energy on the π_1 plane with oxygen content, as observed by Kwasniak in DFT NEB calculations [168]. In this work, oxygen in the first and second nearest glide planes caused reductions in the stable stacking fault energy, with oxygen two planes away causing the greatest reduction to the stable π_1 fault energy. The stable prismatic stacking fault however, increased for all sites, albeit slight. Even though the stable stacking fault on the π_1 plane in the *sd*-model was higher than that found in DFT works, perhaps with oxygen there is an appreciable reduction, which allows for a lowering of the energy γ-surface energy penalty for dissociation on the π_1 plane compared to the prismatic plane.

The behaviour shown in figure 4.7: 12, indicates a mechanism which could tie together apparently conflicting experimental observations. The first is the suppression of prismatic slip, with observation of increased π_1 slip with oxygen content [15, 33], as seen by the π_1 cross-slip behaviour. The second, is that of increased slip planarity (increased amounts of prismatic slip), while also observing jogged screw dislocations [24, 28], due to the repelled partial dislocation evident on the adjacent prismatic plane, promoting prismatic glide of the cross-slipped dislocation, with the formation of a π_1 jog. The experimental observations all depend on the strain-rate, where lower strain rates find wavy slip (unstable prismatic glide), and higher strain rates find prismatic/planar slip. Intuitively, one can see there would be a strain-rate dependence on the mechanism exhibited in figure 4.7: 12, which is also shown schematically in figure 4.8: increased strain-rates imply large dislocation velocities, which result in a propensity for dislocations to continue accommodating plasticity along their usual prismatic path. The reduction in the stacking fault energy on the π_1 plane from oxygen causes cross slip, and the dislocation cross-slips again to continue on the prismatic plane, promoting slip planarity. At low strain-rates, the dislocation cross-slips onto the π_1 plane, but slip on the π_1 plane path can be continued. At low temperature, planar slip is promoted as the oxygen cannot migrate, allowing for a continued repulsive interaction of oxygen with the dislocation when on the same prismatic plane. Whereas at higher temperatures, the oxygen is able to migrate from the disfavoured site once cross-slip has occurred, which would allow for wavy slip. This is consistent with many experimental observations and the strain-rate and temperature dependence of these behaviours [15, 24, 28, 32].

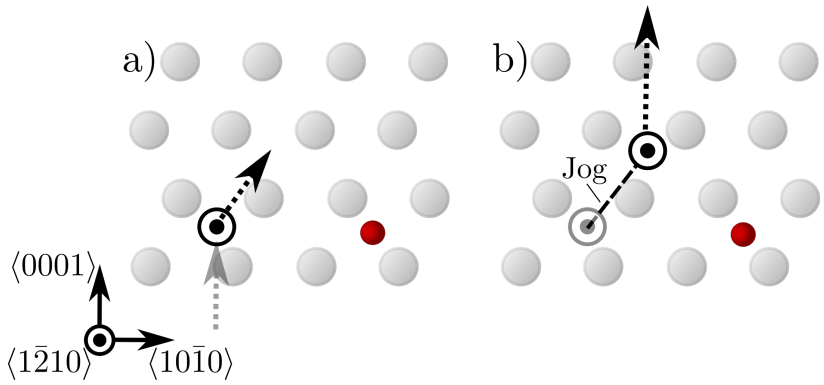

Fig. 4.8: Mechanism shown by tight-binding which could explain slip planarity in titanium with oxygen content. Dislocation shown by ⊙, with direction of glide given by dashed arrows. a) The dislocations interact with oxygen, which allows for favourability of dislocation cross-slip on the π_1 plane due to a reduction in the stacking fault energy with oxygen content, as seen by Kwasniak [168]. b) The dislocation can continue its path on the prismatic plane.

The mechanism just described seems to improve upon the explanation provided by Chong *et al.* [28]: the interstitial shuffling mechanism (ISM). The ISM only accounts for either slip planarity or jog formation separately and it *cannot* explain the increase in the number and size of jogged screw dislocations with temperature when slip planarity has been exhibited, as seen in the results of Williams [24]: there is no cross-slip mechanism which can occur in conjunction with slip planarity in the ISM model. However, the mechanism just described has only been observed in one configuration seen here, and it remains to be validated by other methods: no DFT calculations have been performed with oxygen interacting with a screw dislocation in this particular site. Perhaps the described mechanism also generalises to DFT work seen by others. Indeed, there is a reduction in stable stacking fault energy on the basal plane with oxygen content as in the results of Kwasniak [168], which suggest a similar mechanism could occur with basal jogs. Also, the *sd*-model exhibits a large positive γ_{π_1}–γ_{P} energy difference, whereas DFT has a negative difference, suggesting that such a mechanism would be more likely to occur in DFT, as π_1 dissociation would become even more favourable than prismatic.

The actual core structure of these dislocations upon interaction with oxygen is similar to what is found in DFT, in some cases. In the VASP calculations of Chaari *et al.* [75], the $\langle a \rangle$ screw core structure either becomes compact, upon a repulsive interaction with oxygen, creating basal or π_1 jogs, or there is a similar or enhanced spreading of the core along the original glide plane on which the $\langle a \rangle$ screw core was

originally dissociated. The DFT work here only sampled two octahedral sites and a hexahedral site for each metastable core structure. It remains to be seen if similar behaviour can be replicated in DFT for the other sites sampled.

The interaction energies of oxygen from tight-binding $\sim$ 600 to 900 meV are higher than those found in DFT ~ -80 to 600 meV. No oxygen-dislocation interactions were slightly attractive in tight-binding, but, these attractive interactions in DFT were attributed to a transformation of the metastable core structure to a lower energy core, confirming that oxygen-screw dislocation interactions are repulsive in all cases. The charges of species are consistent with that of solution energies, hence the larger repulsion can be attributed to the Ti-O pair potential, and how it is rather strong. Therefore, in a deformed lattice, there are larger energetic contributions compared to DFT. This is commensurate with results which will be presented later for the volume expansion of the titanium lattice with an oxygen interstitial, showing greater repulsion of Ti species in tight-binding compared to that of DFT, thereby increasing the magnitude of measured elastic dipole tensor components.

The minimum energy configuration of oxygen being in a hexahedral site is consistent with the theory of Chong *et al.*, that of the interstitial shuffling mechanism [28]. In this mechanism, dislocations gliding on the prismatic plane shuffle oxygen atoms into a hexahedral site. This allows for the glide of dislocations past oxygen at a higher strain rate due to the continued passage of dislocations past the shuffled oxygen. It is likely that the Peierls potential of dislocation glide with oxygen in this site is high, due to the repulsion of both partials from the oxygen. This could also be an effect which increases the yield strength: a pinning effect by hexahedral oxygen where there is a spring-like repulsive interaction with the partials, inhibiting glide.

4.3.4 Edge dislocation-oxygen interactions in anisotropic elasticity

The solution energies, allowing for the relaxation of cell volume, and the corresponding change in volume compared to that of the perfect cell, is shown in table 4.4.

The dipole tensor components extracted from the different cell sizes are shown in table 4.4. The data for the changes in volume for the DFT cells were taken from the paper of Aksyonov *et al.* [223] from the changes in the lattice vectors in the supplementary material and calculated in the same way as those for the tight-binding volumes. Note that the percentage change in each lattice vector was only quoted to

Size	E_{sol} [eV]	$P_{11}^{\text{oct.}}$ [eV]	$P_{33}^{\text{oct.}}$ [eV]	ΔV [Å^3]
$3 \times 3 \times 2$ *sd*-TB	–7.45	7.03	5.46	9.4
$4 \times 4 \times 3$ *sd*-TB	–7.40	6.75	5.58	10.3
$3 \times 3 \times 2$ DFT [223]	–5.61	3.81	4.47	6.7
$4 \times 4 \times 3$ DFT [223]	–5.59	4.67	4.49	7.0

Table 4.4: Solution energies of octahedral oxygen allowing for volume optimisation compared to DFT with calculation of dipole tensors. Volume difference of the cell with the octahedral site in comparison to that of the perfect lattice.

one decimal place in the aforementioned paper, which results in volume differences which are slightly larger (by ~ 2Å^3) than those that are found in the paper itself, resulting in an error of the DFT dipole tensor matrix elements of $\sim 30\%$.

The volumes increase with cell size as one expects. The dipole tensor components calculated are reasonably similar with cell size within tight-binding, but they do differ by a greater amount within DFT, due to the imprecision with the quoted changes in lattice vectors used, as mentioned above. One finds that there is a larger change in the volume of the cell upon relaxation compared to that of DFT. This suggests that the Ti-O repulsion from the pair potential is somewhat stronger than the repulsion from DFT.

In the coordinate system of a basal edge dislocation, one obtains the dipole tensor from the $4 \times 4 \times 3$ titanium cells as

$$P_{sd\text{-TB}}^{\text{oct. B}} = \begin{bmatrix} 6.75 & 0 & 0 \\ 0 & 5.58 & 0 \\ 0 & 0 & 6.75 \end{bmatrix}, \tag{4.19}$$

and

$$P_{\text{DFT}}^{\text{oct. B}} = \begin{bmatrix} 4.49 & 0 & 0 \\ 0 & 4.67 & 0 \\ 0 & 0 & 4.49 \end{bmatrix}, \tag{4.20}$$

from *sd*-TB and DFT respectively.

In the coordinate system of a first-order pyramidal edge dislocation, one obtains the dipole tensor from the $4 \times 4 \times 3$ titanium cells as

$$P_{sd\text{-TB}}^{\text{oct. } \pi_1} = \begin{bmatrix} 6.75 & 0 & 0 \\ 0 & 6.48 & 0.49 \\ 0 & 0.49 & 5.45 \end{bmatrix}, \tag{4.21}$$

and

$$P_{\mathrm{DFT}}^{\mathrm{oct.}\ \pi_1} = \begin{bmatrix} 4.49 & 0 & 0 \\ 0 & 4.63 & 0.07 \\ 0 & 0.07 & 4.54 \end{bmatrix}, \tag{4.22}$$

from *sd*-TB and DFT respectively.

The stress tensor and corresponding binding of edge dislocations is found in figure 4.9. The radius of the core region was taken to be the the half-width $r_c = \zeta_{\mathrm{edge}} = d_{\mathrm{diss}}/2(1-\nu)$, as in Argon [11], where $\nu = 0.315$ Poisson's ratio calculated from the hexagonal elastic constants in the *sd*-TB model, which is similar to the value of $\nu = 0.31$ pure titanium from the empirical elastic constants. The relevant dissociation distance was taken from table 3.5. These core radii are all above the usual method in the literature of assuming $r_c = b$.

The elastic constants were not determined for the reference data of Aksyonov *et al.* [223], so the same elastic constants of tight-binding were used, as they are close to the experimental values, and result in a more direct comparison of the dipole tensor components and the binding energies which result.

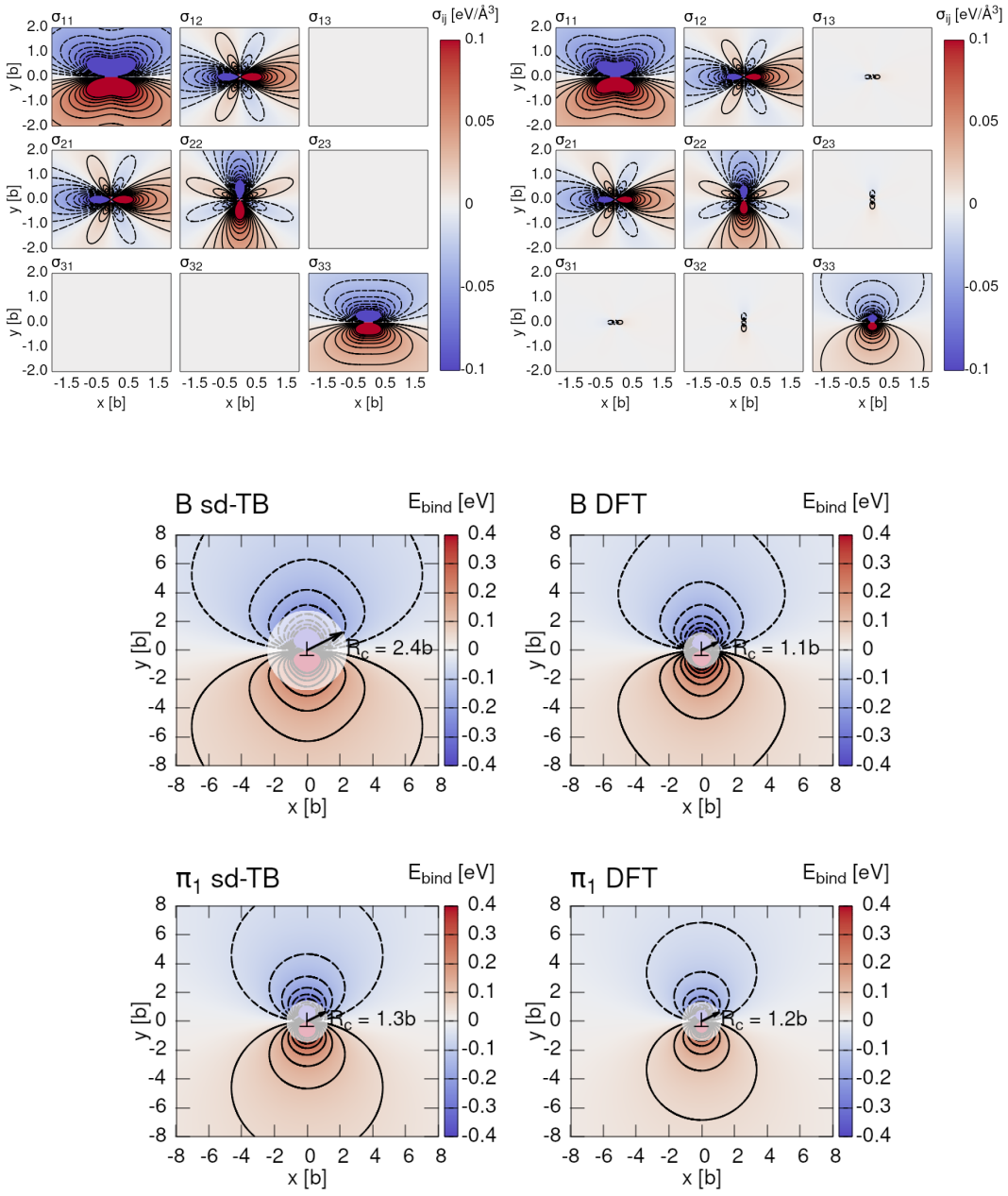

Fig. 4.9: Stress tensors and the resulting binding energies of oxygen to B $\{0001\}\ \langle a\rangle$ and $\pi_1\ \{10\bar{1}1\}\ \langle a\rangle$ edge dislocations. Basal stress tensor components found on top left with first-order pyramidal plane stress tensor components on the right, both from tight-binding elastic constants. Middle and bottom: binding energies resulting from calculated elastic dipole tensors of tight-binding (left) in comparison to that of DFT (right) for the basal (middle) and π_1 (bottom) planes. Contours range from -0.4 eV to 0.4 eV in increments of 0.05 eV. The outermost contours of the plot are -0.05 eV and +0.05 eV for the dashed and solid contours respectively. Core radii determined from explicit calculation from the energy coefficient matrix in the dislocation reference frame.

One finds in figure 4.9, that for a given distance from the core, oxygen can bind more strongly to basal edge dislocations rather than π_1 edge dislocations, on the tension side. The change in the morphology of the binding energy contours can be seen from the change in the stress tensors, where the σ_{33} component changes from a bow-like shape in the basal edge dislocation, to a leminscate in the π_1 edge dislocation.

The maximum binding energy which can be determined, and deemed to be accurate—the binding energy just outside of the core region—for DFT is 0.2 eV and 0.3 eV for the π_1 and basal edge dislocations respectively. From tight-binding, one finds the maximum binding energies just outside of the core region are 0.3 eV and 0.25 eV for the π_1 and basal edge dislocations respectively.

To make a connection with jogs, one must first address the assumption here: that jogs can be well-described by straight edge dislocations. In reality, there is a width to the jogs. An estimation of jog width is given in the appendix A. It was found, from anisotropic elasticity and stacking fault energies, that the jogs have widths around $w \approx 3b$. These are narrow compared to kinks on screw dislocations in iron, which are $\sim 10b$. Hence, one can say the approximation of the binding energy of oxygen to the jog is well represented by a straight dislocation, especially if the oxygen has migrated half the length of the kink $\sim 1.5b$, which represents a few diffusion events, which could be promoted by the reduction of interstitial diffusion barriers around dislocation cores.

Assuming a jog width $w \approx 3b$, and that the oxygen diffuses to the next octahedral site—by thermal activation of either the octahedral $\rightarrow$ octahedral, or the lower energy octahedral $\rightarrow$ crowdion $\rightarrow$ hexahedral $\rightarrow$ octahedral transitions—the vectorial distance traversed is $a_{\mathrm{hcp}} = b$ or $c_{\mathrm{hcp}}/2 \approx 0.8b$. Therefore, only two octahedral $\rightarrow$ octahedral transitions are necessary to reach the middle of jog, where the approximation of a straight dislocation becomes most accurate.

4.4 Discussion

4.4.1 General comments

Of the tight-binding models considered, one sees that the *d*-model, despite the good results of stacking fault energies, does not agree with DFT as well as the *sd*-model, of which exhibits a dissociation of the prismatic screw dislocation more comparable to DFT, in addition to very good agreement of the excess core energies for prismatically spread cores. However the Peierls stress of the *d*-model agrees remarkably well with

experiment [16, 22], especially compared to MEAM calculations of Trinkle *et al.* [191]. Both tight-binding models thankfully do not fall prey to a basal ground-state core structure, as has befallen past tight-binding models, resulting in the first modern tight-binding models which have a core structure which is more representative of current screw dislocation theory in titanium, in addition to the first models which produce realistic CRSS values compared to experiment.

The *sd*-model has solution energies of oxygen and hydrogen which are more in agreement with DFT than the *d*-model. As such, one hoped good agreement would be found for the repulsive energies between oxygen and screw dislocations. The repulsive interaction was overall greater using the tight-binding models parameterised here due to the strong Ti-O pair potential. Another effect of this increased repulsion was found in the larger volumes upon relaxation of oxygen in an octahedral site in titanium, which caused dipole tensor components to be larger in magnitude, resulting in the binding energies of oxygen to edge dislocations to be slightly higher than DFT.

The larger Ti-O repulsion, in conjunction with only one screw core structure, which had a larger dissociation distance than that of DFT, caused notable differences in screw dislocation-oxygen interaction, but there was reproduction of most mechanisms found in DFT, that of core compaction/elongation with jog formation, along with new mechanisms. Only slightly compacted cores were found due to the preference of a core structure spreading on the prismatic plane. This led to no basal jogs being formed, only π_1 jogs. New phenomena in support of the hypothesis of the interstitial shuffling mechanism, by Chong *et al.* was shown here, where lowest energy configuration is for oxygen to migrate to a hexahedral site in the site created by the prismatic stacking fault [28], which is in agreement with the NEB calculations of stacking fault energies on the prismatic plane with oxygen content, where oxygen goes to this hexahedral site [168].

With the new sites sampled around the dislocation core, one finds phenomena suggesting that the jerky flow of dislocations in titanium with oxygen content may be due to the local formation of kinks on the dislocation glide plane, in the direction which opposes glide, in addition to the formation of jogs, due to the repulsive interaction with oxygen. Kinks would inhibit dislocation motion due to an enhancement of the probability of stable kink-pair formation in opposition to the direction of dislocation glide. Furthermore, the new mechanism of jog formation due to a more preferable pyramidal stacking fault energy from oxygen interaction hints at another potential mechanism to describe jerky flow, which also explains the increased frequency and

number of jogged screw dislocations with temperature and oxygen content, as observed by Williams *et al.* [24], which the ISM cannot account for.

The results of oxygen binding to edge segments is relevant to the motion and formation of superjogs. The binding energy of oxygen to these edge segments can be used to estimate jog glide velocity, upon the estimation of the dislocation line-tension [203]. This work can also be important in the estimation of creep effects by the climb of these jogs, which may also drag oxygen.

4.4.2 Locking-unlocking vs π_1 metastability

The lack of metastable core structures found in the tight-binding models is seemingly due to a high π_1 core energy which is unstable for the one dissociation distance trialled. This may affect the prediction of core transformations seen in the screw dislocation-oxygen interactions. But, due to the error of energies associated with the core structures from DFT, one cannot totally refute the possibility that the prismatic core structure could be the ground-state. Trinkle *et al.* [191] claimed that pyramidally dissociated cores found from DFT and the MEAM are artefacts of relaxation from the initial anisotropic elasticity solution displacements, due to the fact that under strain there is a transformation of the pyramidal core, to that of a prismatic one. However, metastability of the pyramidal core has only been found in MEAM calculations, not in DFT; and rather conveniently, the dislocation excess energy from Trinkle *et al.*'s DFT calculations were not presented in their work, despite having performed similar DFT relaxations and core structures to Tarrat, of whom found the lowest energy core structure with a pyramidal dissociation [132, 133]. They also misquote which core structure has the lowest excess energy in the Tarrat *et al.* paper, which is also in conflict with their π_1 screw core metastability hypothesis. Within tight-binding, the π_1 screw core is metastable, as evidenced with its observation due to oxygen interaction, in agreement with the MEAM calculations.

If one were to take this hypothesis further—that the *prismatic* core is stable, and the pyramidal is *metastable*—one must re-examine the origin of jerky glide in titanium [12, 15, 17, 18, 24], which is usually attributed to a locking-unlocking mechanism (figure 1.2, right) where the *pyramidal* core is sessile but the ground-state, and the *prismatic* core is glissile but dependent on a thermally-activated core transformation [19]. We will now examine experimental results in the light of this hypothesis and compare to the current consensus of locking-unlocking, to determine whether this paradigm can satisfactorily explain the observed phenomena in titanium.

The higher propensity of planar slip at low temperature is consistent with this hypothesis, with higher temperatures giving rise to wavy slip [24, 28], which suggests a thermally activated transition from prismatic to the π_1 core, causing cross-slip. The higher planarity of slip with oxygen content in these studies can be explained away if the interstitial shuffling mechanism is indeed active in conjunction with the cross-slip phenomena, both with oxygen on the glide plane and the new observation of cross-slip by oxygen on further glide planes. But in high-purity titanium ($\sim$ 50ppm O*), *in situ* straining experiments by Farenc [19], show jerky motion and cross-slip at 150K. If the prismatic ground-state core hypothesis is true, jerky motion should not occur in high-purity titanium. It is likely these experiments are at a low strain-rate, as in other *in-situ* experiments [203], which show consistency with the locking-unlocking mechanism.

There are also problems with the assumption of a prismatic ground-state structure which is also glissile, which arises when considering the stress dependence of the activation area in titanium. In high purity, single crystals of titanium, many studies [17, 18, 20, 22] find a σ^{-2} dependence of the activation area, akin to the Friedel cross-slip mechanism arising from dislocation bowing [23]. This implies a sessile ground-state core configuration, in which the glissile dislocation segments can bow due to pinning of segments in their sessile ground-state, in line with the locking-unlocking hypothesis.

It was stated that the jump distances decreased with increasing temperature (ranging from 150-473K), which is consistent with locking-unlocking theory [16, 17]. However, the decrease in jump distance could be explained by the increased likelihood of promotion of the glissile prismatic core to a pyramidal one. Also, in the material studied, there was a very high effective oxygen content ($\sim$ 3000ppm O*), as such, the interstitial shuffling mechanism of oxygen jumping from a metastable hexahedral site to that of an octahedral one at higher temperatures could also impede glide, explaining the reduced jump distance.

The slip of zirconium, another hcp transition metal of d^2 valence, exhibits glide which has been said to be jerky at low temperature (24K) [16], and smooth in the range of 95 to 300 K [203]. The observation of smooth glide has been attributed to a ground-state prismatic core structure [19], unlike the metastable prismatic core structure for titanium, which exhibits jerky flow in the same study. There was a lack of any cross-slip of Zr seen at the range of temperatures tested, whereas for titanium, there was cross-slip between prismatic and pyramidal planes. These results suggest that zirconium may actually have a locking-unlocking mechanism, but there exists a

transition temperature, between 24–100K, in which dislocation motion becomes more smooth due to consistent activation of prismatic glide. This does not coincide however with the temperatures at which discontinuities are found in activation areas, where one expects a transition to a smooth kink-pair controlled glide mechanism in the higher temperature range above 300K [16]. The jerky glide seen in zirconium at low temperature suggests the same locking-unlocking mechanism is apparent in titanium, just with a higher transition temperature. These results put into question the *ab-inito* core structures found in the aforementioned study, and their predictive power, given that jerky flow, one of the observations which underpins the locking-unlocking hypothesis, was exhibited in zirconium at low temperature, despite the calculation of a prismatic ground-state at 0K from DFT, which has been stated in opposition to this hypothesis [19].

The discussion here suggests that a locking-unlocking mechanism—where a sessile pyramidal core is the ground-state, and a glissile prismatic core is metastable—describes the phenomena observed in titanium sufficiently well.

The transition between wavy and planar slip with oxygen content should be investigated further, for validation/exploration of potential mechanisms for slip planarity, as detailed earlier. The new mechanism proposed to explain slip planarity works well in conjunction with a locking-unlocking mechanism. Together, both can describe many observed phenomena in titanium, from jerky flow to increased slip planarity in tandem with increased frequency of jog formation at higher temperatures. Finite temperature atomistic simulations would be preferable to investigate this, but, the current state-of-the-art models cannot capture the subtleties of structures necessary, nor can many afford the complications which come with the inclusion of oxygen interactions.

4.4.3 Summary of solute-hardening by oxygen content in titanium

In the context of the results in this chapter and the current literature, one can discuss how oxygen causes hardening in titanium with oxygen content as follows. Screw dislocations control plasticity due to their low mobility compared to that of edge dislocations [12, 24, 183]. As a screw dislocation glides on the prismatic plane, there are multiple different modifications to the screw core structure which inhibit glide due to oxygen interactions. Oxygen atoms which are not found in the glide plane have a repulsive interaction with the gliding screw, which results in the formation of kinks

which oppose the direction of glide, inhibiting dislocation motion. Overcoming this repulsion, at low strain rate/high temperature the dislocation can get closer to oxygen, where the core, instead of being dissociated on the prismatic plane, can become compact, forming basal or π_1 jogs [26, 75], which could be promoted due to the reduction of the stable stacking fault energies on the basal and π_1 planes with oxygen content [168]. These jogs inhibit glide due to only responding to the action of a different shear stress component, causing pinning. This pinning causes bowing of the dislocation line, on continued action of shear stress. These jogs—which are likely small due to the large Peierls stress on the basal/π_1 planes—could annihilate due to the unequal line-tension components associated with bowing [199], but they are stabilised and pinned themselves by the binding of oxygen. The migration of oxygen could be incentivised by the reduction of interstitial diffusion barriers from the strain fields around dislocations, as evidenced in other systems. The stabilisation of the jog allows for superjogs to form due to the enhanced probability of further dislocation cross-slip. These superjogs can undergo loop expansion, causing dislocation multiplication and debris.

At a higher strain rate/low temperature, there are a two possible mechanisms. The first, as per the ISM, is that dislocations do not locally cross-slip, staying their course on the prismatic plane. This causes the oxygen to shuffle into the newly created hexahedral site within the prismatic stacking fault, as evidenced in the above dislocation calculations. For the dislocation to pass the oxygen, the repulsive action of oxygen with the dislocation partials must be overcome. This repulsion is increased due to the larger stable stacking fault of energy on the prismatic plane with oxygen content in the dislocation glide plane. With a high enough stress however, the dislocation can pass the oxygen, resulting in a hexahedral oxygen, which resides in the basal plane. This hexahedral oxygen stays in the site at low temperature after passage of the dislocation, as evidenced in lightly strained titanium [26], thus allowing for a more planar slip of screw dislocations past the oxygen on the prismatic plane, rather than cross-slipping onto a π_1 or basal plane. At higher temperature, the oxygen can hop out of the hexahedral site, which causes dislocation cross-slip/wavy slip due to interaction, and the mechanism in the previous paragraph applies.

The second regime which could act at a higher strain rate/low temperature, suggested in this thesis, is that jogs are formed, but due to oxygen-dislocation interactions where oxygen is not in the same plane as the screw dislocation, which differs from the low strain-rate case explained previously. There is a repulsive interaction of oxygen with the dislocation which can promote prismatic slip at higher strain rates. This

explains the increased frequency and size of jogs formed when planar slip occurs at high oxygen contents [24] and it additionally describes the instability of prismatic slip at low strain rates [15]. Furthermore, it describes the temperature dependence of wavy and planar slip, where oxygen jumps from the repulsive site upon the occurrence of cross-slip at high temperature, promoting wavy slip, and planar slip occurs at low temperatures as the oxygen cannot migrate, continuing its repulsive effect on the screw dislocation, promoting prismatic slip. All of this is consistent, and is an even more attractive proposal, with the locking-unlocking mechanism, due to the stability of π_1 core, which explains the σ^{-2} dependence of the activation area. This mechanism seems more likely to occur in DFT work due to the lower energy of the π_1 fault relative to the stable prismatic fault energy.

4.5 Conclusion

Performing calculations with the simple tight-binding models parameterised in the previous chapter, one finds reasonable agreement in solution energies, in addition to a prismatically dissociated screw dislocation core structure. This is in agreement with experimental observations of dislocation glide and metastable DFT screw dislocation core structures, resulting in the first modern tight-binding model for titanium which reproduces this behaviour. The parameterisation of the tight-binding models has been successful, with demonstration that the model is general enough to handle defects, while not being overly complex, allowing for good scalability, as shown in the simulation of dislocations with ~ 1000 atoms.

Metastable/pyramidal core structures were not found upon relaxation by the initial anisotropic elasticity displacements, which differs from DFT behaviour, but the error associated with these energies is appreciable, as such, one cannot discount a ground-state prismatic core structure, despite the attractiveness of the locking-unlocking mechanism which describes many phenomena exhibited in titanium, such as the σ^{-2} dependence of activation area, and decreasing dislocation jump distance with temperature. Peierls stresses from tight-binding agree with measurements of the CRSS in high-purity titanium, unlike empirical potentials.

Oxygen-screw dislocation interactions using the *sd*-model reproduce phenomena and hardening mechanisms found from *ab-inito* methods, such as the formation of jogs on the π_1 plane from the reduction of the respective stable stacking fault energy with oxygen content, despite larger repulsive interactions arising from the strong Ti-O

pair potential. New hardening phenomena was exhibited in tight-binding, showing a proclivity for kinks to form on the glide plane, in opposition to the glide direction, due to the repulsive effect of oxygen, which could explain the jerky glide of screw dislocations. In addition, a new explanation of the strain-rate dependence of slip planarity with oxygen content was given due to the observation of new phenomena in tight-binding: dislocation cross-slip induced by oxygen which is *not* in the glide plane of the dislocation. This was attributed to the favourability of the π_1 stacking fault with oxygen content, which is corroborated by DFT stacking fault energy calculations. This rectifies the lack of explanation for jogged screw dislocations with increased slip planarity in the ISM model.

Analysis of the binding energy of oxygen to edge segments, by a dipole tensor analysis, shows that oxygen binds more strongly to basal jogs rather than π_1 jogs, with calculation of narrow jog widths showing that the approximation of a straight edge dislocation is valid. This binding inhibits jog-dipole annihilation by pinning, resulting in a higher probability of cross-slip and superjog formation, explaining loop expansion and dipolar debris. These binding energies are beneficial for future analyses into dislocation creep, which is thought to be controlled by jogs on screw dislocations in titanium. Tight-binding and DFT oxygen-edge dislocation binding energies were in good agreement, but a larger volume expansion was found in tight-binding from the strong Ti-O pair potential.

Chapter 5

Dislocation-carbon interactions in Fe-C

5.1 Introduction

The martensitic microstructure of bearing steels can undergo decay. During operation, cyclic loading can exceed a given contact stress, which causes an accumulation of plasticity, signalling the onset of rolling contact fatigue (RCF). This increases the risk of failure from subsurface crack initiation. The microstructural decay corresponds to the observation of Dark Etching Regions (DERs) as seen in optical microscopy, where the darkness of these regions is due to the higher reactivity of DER phases to the etchant [34]. See figure 5.1.

Decay of the martensitic microstructure is complex, with the observation of many different phenomena. Martensite transforms to ferrite microbands as a result of strain localisation [35–39, 50, 224–226]. Residual carbides, untouched at the start of DER formation, gradually dissolve within ferrite and martensite [38, 39, 227]. Further RCF progression leads to the formation of low and high angle ferrite features, White Etching Bands (WEBs), composed of nanocrystalline [224, 227, 228] and elongated ferrite [50]. Lenticular carbides precipitate at the boundaries of these ferrite bands [39, 227]. Thickening of these carbides occurs during DER development and is correlated with WEB growth [35, 51–53]. Reductions of dislocation density in nanocrystalline (heavily deformed) ferrite have been observed in the later stages of DER formation [34, 229].

Carbon migration is thought to be the mechanism by which this degradation occurs, but it is not definitively known how or where carbon migrates with the onset of DER formation. The key questions are: where does excess carbon from the marten-

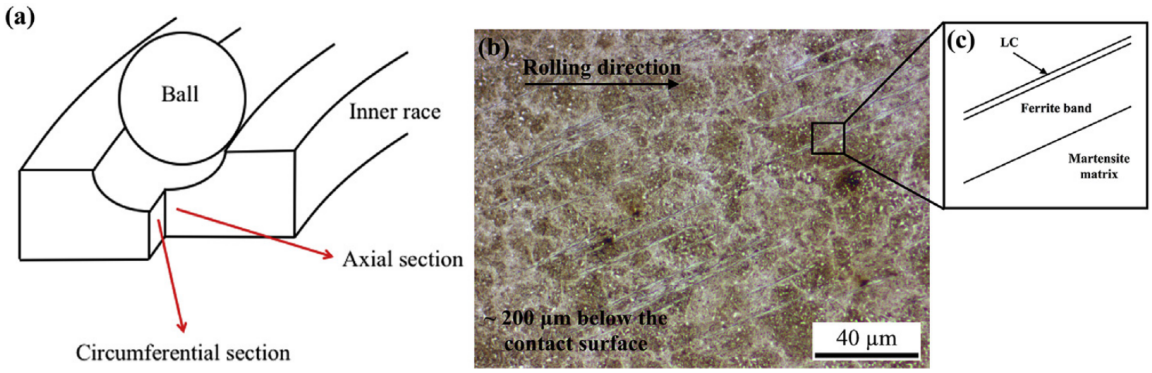

Fig. 5.1: Diagram of DER location within a bearing and its characteristics, taken from [51]. (a) Axial and circumferential sections of a bearing inner ring. (b) Circumferential section of a bearing inner ring under an optical microscope, where ferrite bands (white etching bands) are formed in the subsurface. (c) Diagram showing the structure of a WEB consisting of a ferrite band and a LC adjacent to it. One can see the DER region is composed of regions of ferrite interspersed in the parent martensite with lenticular carbides bordering the ferrite bands.

sitic matrix find itself when the structure decays to low solubility (0.02 wt%) ferrite? and how is the carbon transported, given its low diffusivity in martensite/DER phases [230]?

Fu *et al.* propose that carbon atoms inside the martensite would segregate to pre-existing/residual carbides, increasing their size [51]. This theory was successfully applied to the growth of lenticular carbides [35], however, problems arise with the application to temper carbide growth: if carbides were to form in martensite, they should follow the Bagaryatskii/Isaichev orientation relationship, but observations suggest a lack of any orientation relationship [231]. Temper carbides residing within DERs have irregular shapes/diffuse boundaries, which are seemingly due to the incomplete *dissolution* of *temper* carbides, which is at odds with the theory of Fu *et al.*.

A plausible mechanism for carbon migration is that it is driven by dislocation glide, which is as follows [35, 39, 51–53, 225]. Due to the high dislocation density exhibited in martensite, carbon segregates to dislocations in Cottrell atmospheres, causing pinning. Strain generated by cyclic stresses allow dislocations to escape their carbon rich environment. The free dislocations re-attract carbon, allowing the Cottrell atmospheres to reform, subsequently re-pinning the dislocations, creating a net carbon flux. This mechanism allows for the movement of carbon during the martensite-ferrite transition, while also explaining how excess carbon can move from the ferrite phases to

lenticular carbides at the boundaries, describing the process behind both WEB growth and carbide thickening. Moreover, it explains the dissolution of residual carbides, both in ferrite WEBs and martensite, due to dislocation rearrangement and pile ups at the carbide interface drawing carbon atoms out, due to a more favourable binding to dislocations. However, as to how this process occurs on the atomistic scale, or if it is indeed feasible, is unknown.

Experimentally probing dislocation-assisted carbon migration has proven difficult and inconclusive. As such, theoretical work needs to be done to understand dislocation-carbon interactions; more specifically: how could carbon move with dislocations within the temperature and stress regimes experienced during operation and where is carbon transported to and what are the resultant dislocation networks.

To shed light on this mechanism, a multi-scale modelling approach can be used. Atomistics can provide information of the 2d Peierls energy landscape which dislocations are subject to in iron; and how this landscape is modified by the binding of carbon to dislocations. The Peierls landscape and binding energy data can be used in a line-tension model of a dislocation to determine the kink-pair formation enthalpies of dislocations as a function of carbon content and stress. These enthalpies furnish us with the average velocities of dislocations undergoing glide by thermally activated kink-pair nucleation at different carbon concentrations. By the elucidation of carbon migration barriers around dislocations using atomistics, we can directly compare the average carbon velocities in the vicinity of dislocations, and determine whether it is feasible that carbon can keep up with dislocations undergoing thermally activated glide. Finally, one can use a kinetic Monte Carlo (kMC) model of dislocation glide by thermally activated kink-pair nucleation, in an environment of carbon, which can diffuse using the barriers found by atomistics. From this last stage of coarse-graining, one can determine in which regimes of temperature, stress and carbon concentration, dislocation-assisted carbon migration becomes a feasible mechanism behind DER formation. For this we need to predict dislocation velocity, dislocation configurations, and where carbon moves with dislocation glide.

In this chapter, the focus is on the atomistic and line-tension modelling portions of this project, all derived from the Fe-C magnetic tight-binding model of Paxton and Elsässer [206], to understand dislocation-carbon interactions in ferrite (bcc iron) in detail. This pushes the tight-binding technique to its limits in terms of scale and feasible computation time within a direct-diagonalisation framework. For example, each diffusion barrier calculation, as shown section 5.3.7, took 90,000+ core hours,

resulting in figure 5.22 being worth well over 1,000,000+ core hours, not accounting for the time taken to obtain the cells between which diffusion barriers were sought.

The aforementioned calculations are simply not feasible for calculation with DFT, due to the large prefactor associated with the $\mathcal{O}(N^3)$ scaling compared to tight-binding. It is only due to the preferential scaling of tight-binding, and the accuracy of the parameterisation—which satisfactorily replicates DFT results, unlike empirical potentials—which allows for the opportunity to obtain these barriers.

5.2 Computational Method

The tight-binding model of Paxton and Elsässer [206] has been shown to describe the binding energies of carbon complexes in bcc iron, in good agreement with DFT calculations. This model reproduces the two screw dislocation core structures—the easy and hard $1/2\langle 111\rangle$ cores—exhibited in bcc iron [54, 55]. Study of both is crucial to understanding solute-dislocation interactions. The easy core is the ground state in pure iron, but solutes, such as hydrogen and carbon, have been shown to reconstruct this core into the hard core configuration [232, 233]. Computationally cheaper models, which do not incorporate quantum mechanics, such as the EAM, cannot reproduce this behaviour.

5.2.1 Peierls Potential

To determine the Peierls potential of the $1/2\langle 111\rangle$ screw dislocation, one followed the procedure detailed by Itakura *et al.* [76]. Quadrupolar arrays of dislocations were constructed by placing dislocations of antiparallel $1/2\langle 111\rangle$ Burgers vectors in an "S" arrangement [155], with initial displacements determined by anisotropic elasticity solutions. See figure 5.2, left. A quadrupolar arrangement minimises the stress each dislocation experiences in the simulation. These displacements were modified to be periodic, thereby removing artificial stacking faults which would appear between periodic images after introduction of the dislocation dipole. This was achieved by the subtraction of a linear error term from the superposition of displacement fields arising from the dislocations in the simulation cell and its periodic images [209], as described in section 4.2.2.1. To accommodate for the internal stress upon introduction of a dislocation dipole into the simulation cell, an elastic strain was applied to the cell, resulting in an additional tilt component to cell vectors [155, 209, 234]. Simulation

cells were constructed with different initial core positions, which were sampled from the triangular region "EHS" (easy, hard and split) core positions, as detailed in figure 5.3. To fix the dislocation positions during relaxation, the three atoms surrounding the easy core, for each dislocation, were fixed in Z coordinate during relaxation, where Z is a $\langle 111 \rangle$ direction, along the dislocation line. The k-point sampling mesh for each of these cells was $5 \times 5 \times 30$. All tight-binding calculations in this chapter had a charge tolerance for self-consistency of 1×10^{-6}.

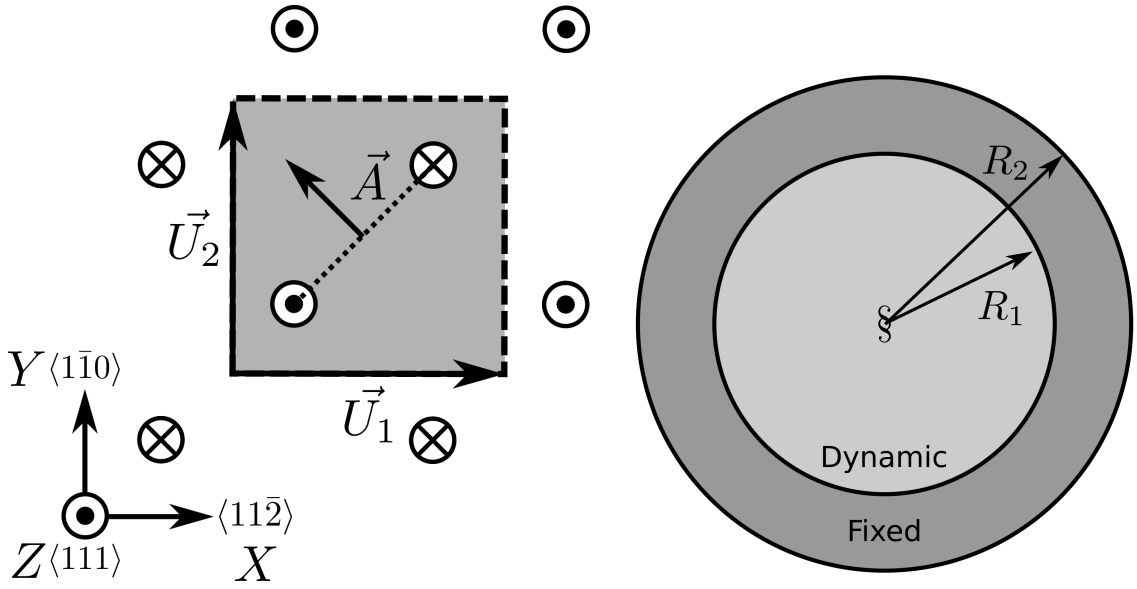

Fig. 5.2: Schematics of dislocation simulation methods as found in section 4.2.2.1, reproduced here for convenience with bcc screw dislocation coordinate system. Left: quadrupolar arrangement of dislocations in a simulation cell (grey square). This arrangement minimises the stress experienced by each dislocation in a periodic simulation. Cell vectors $\vec{U}_1$ and $\vec{U}_2$ are shown; $\vec{A}$ defines the cut plane between the dipoles. The dislocation positions, and their corresponding Burgers vector direction, are denoted by the symbols $\otimes$ and $\odot$, which are antiparallel to each other. Tilt components added to cell vectors to accommodate for the plastic strain are not shown. Right: cluster method, where atoms are displaced according to the displacement field from the screw dislocation at the centre of the cluster, denoted by "§". Atoms in the annulus $R_2 - R_1$ are fixed in position to the anisotropic elasticity solutions. Within R_1, all atoms can relax. Periodicity is only imposed in the Z direction.

The interaction energy between the dislocation dipole and periodic images was defined differently to Itakura *et al.* [76]. We followed the prescription of Bulatov and Cai [209] to find a regularised interaction energy, which is independent of the periodic truncation limit, in contrast to the formulas quoted in Itakura's papers. Details can

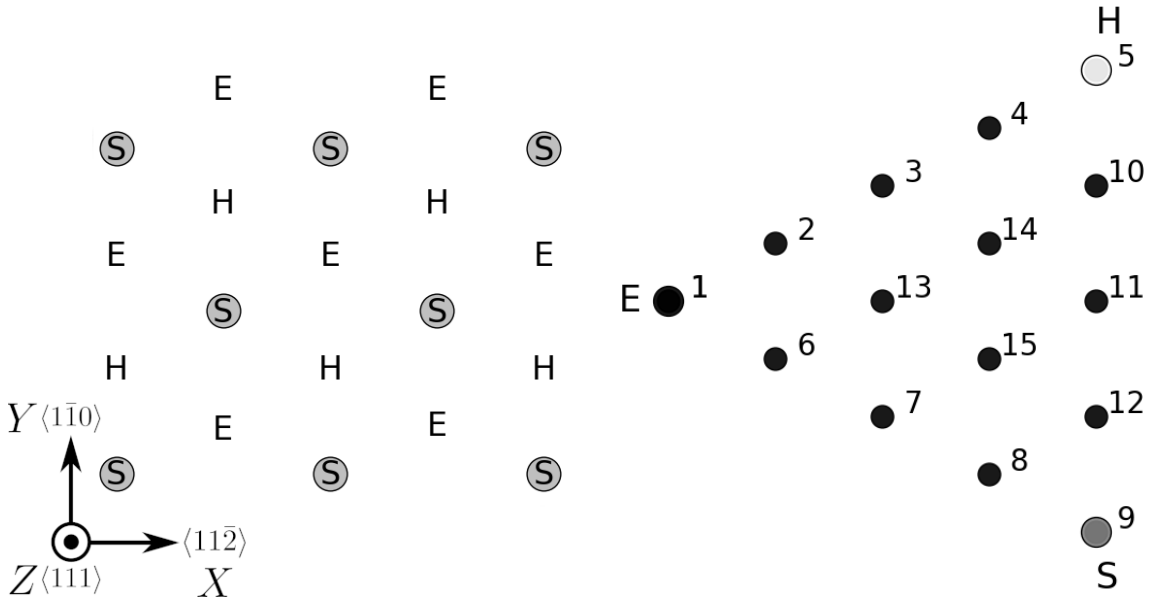

Fig. 5.3: Diagrams of dislocation core positions. "E", "H" and "S" correspond to the easy, hard and split core positions respectively. Left: core positions as seen along the $Z = \langle 111 \rangle$ direction, along the dislocation line. Atomic positions are shown as grey circles. Right: positions sampled within the triangle EHS used to determine the Peierls potential.

be found in appendix B.

The Peierls potential ΔE^i_{P}, for an isolated dislocation at the i^{th} core position, can be calculated from

$$\Delta E^i_{\mathrm{P}} = \Delta E^i_{\mathrm{tbe}} - \Delta E^i_{\mathrm{int}}, \tag{5.1}$$

where Δ refers to quantities, per dislocation, relative to the relaxed easy core configuration (labelled as E/1, as in figure 5.3). *e.g* $\Delta E^i_{\mathrm{tbe}} = \frac{1}{2}(E^i_{\mathrm{tbe}} - E^{\mathrm{E}}_{\mathrm{tbe}})$ is the difference in energy between a relaxed cell which has the two dislocation cores placed at position i, E^i_{tbe}, and a relaxed cell which has the two cores placed in easy core positions $E^{\mathrm{E}}_{\mathrm{tbe}}$, divided by the number of dislocations in each of the simulation cells. Dislocation-dislocation interaction energies are included in this term, due to dislocations in the simulation cell—and periodic images—interacting with each other, as can be readily seen in figure 5.2. To model the energy landscape of an isolated dislocation, these interaction energies must be subtracted, which is achieved by the correction term $\Delta E^i_{\mathrm{int}} = \frac{1}{2}(E^i_{\mathrm{int}} - E^{\mathrm{E}}_{\mathrm{int}})$.

5.2.2 Preliminary calculations

To determine the binding energy of carbon to dislocations, we used the cluster method, as shown in figure 5.2, right, such that one could study carbon-dislocation interactions without the effect of other elastic interactions and strains as found in a quadrupolar array. Simulation cells consisted of a cylindrical cluster of atoms, with a single dislocation introduced into the centre using displacements from anisotropic elasticity solutions. Each of the clusters were centred on the easy or hard core positions. The cluster of atoms was split into two regions: a central region of dynamic atoms with radius R_1, and an annulus of atoms, between R_1 and R_2, which were fixed in position to the displacements from anisotropic elasticity.

To confirm the anisotropic elasticity solutions were correct, we compared the displacements against the analytic solutions to the straight screw dislocation, as given in Hirth and Lothe [7]. In addition, energy scaling relations were verified. Dislocations were inserted into cells of varying radii: $R_1 = x\sqrt{2}a_{\mathrm{bcc}}$, and $R_2 = (x+1)\sqrt{2}a_{\mathrm{bcc}}$, where $x \in \{2 \ldots 5\}$. The excess energy was defined as the energy difference of a cell with a dislocation inserted, E_{d}, with respect to a perfect cell reference energy of the same geometry,

$$E_{\mathrm{excess}} = E_{\mathrm{core}} + E_{\mathrm{elastic}} = E_{\mathrm{d}} - E_{\mathrm{perfect}}, \tag{5.2}$$

where

$$E_{\mathrm{elastic}} = (\mu b^2/4\pi)\ln(R/r_c), \tag{5.3}$$

with $R = R_2$ and $r_c = b$.

Initially, large cells of $R_1 = 6\sqrt{2}a_{\mathrm{bcc}}$, and $R_2 = 7\sqrt{2}a_{\mathrm{bcc}}$ with depth of single Burgers vector, were relaxed for both the easy and hard cores, which consisted of 522 and 540 atoms respectively. The three atoms surrounding the core were constrained to only relax in X–Y plane, to fix the dislocation upon relaxation. The k-point sampling mesh for each of these cells was $1 \times 1 \times 24$.

From the relaxed cells, a smaller region of 174 atoms, with $R_1 = 3\sqrt{2}a_{\mathrm{bcc}}$, and $R_2 = 4\sqrt{2}a_{\mathrm{bcc}}$, was cut from the dynamic regions. This smaller cell was extended to a thickness of $3b$ in the Z direction. Carbon interstitials were inserted into octahedral sites near the dislocation core, in the middle layer. Exploiting reflection and rotational symmetry, only 10 interstitial sites needed to be used to obtain the binding energies of carbon $\sim$ 2 b from the core, denoted by iHj and iEj, where $j \in \{1 \ldots 10\}$. The final binding sites are denoted by Hk and Ej, where $k \in \{1 \ldots 7\}$. The three atoms

surrounding the core in the first and third layers were again constrained to relax only in the X and Y directions. No such constraints were imposed on the middle layer.

Other relaxation techniques were tried. Of note, if one tried to pre-emptively include the distortion induced carbon into the cell, by superposing the displacement field generated from carbon in an otherwise perfect cell of 3b depth, of the same geometry, thus modifying the dislocation core structure slightly—one does not find the ground state structures as predicted by dipole calculations which allow all degrees of freedom to be relaxed.

5.2.3 Fe-C binding energies

We calculated the carbon-dislocation binding energies as in Itakura [233]. The binding energy is given by

$$E_b = -(E_{\mathrm{d+C}} + E_{\mathrm{perfect}} - E_{\mathrm{d}} - E_{\mathrm{C\ ref.}}), \tag{5.4}$$

where $E_{\mathrm{d+C}}$ is the total energy of a relaxed cluster with a carbon interstitial and a dislocation, E_{d} is the total energy of a relaxed cluster with a dislocation and $E_{\mathrm{C\ ref.}}$ is the total energy of a relaxed perfect cluster with a single carbon in an octahedral site. A positive binding energy indicates favourable binding.

The zero-point energy (ZPE) is calculated as in Itakura. Details can be found in appendix C. The ZPE corrected binding energy is given by

$$E_b^{\mathrm{Z}} = E_b + \Delta E_z, \tag{5.5}$$

where $\Delta E_z = E_z - E_z^{\mathrm{C\ ref.}}$ and $E_z^{\mathrm{C\ ref.}} = 202.5\mathrm{meV}$ is the zero-point energy of carbon situated in an octahedral site in a perfect cluster of the same size.

5.2.4 Carbon concentration around the dislocation line

Using the Fe-C binding energies, one can predict the equilibrium carbon concentration of a carbon binding site c_d, using a thermodynamical mean-field model [232, 235, 236], under the assumption that carbon atoms around the core are sufficiently spaced such that intersite interaction energies are negligible.

The concentration is given by,

$$\frac{c_d^i}{1 - c_d^i} = \frac{c_{\mathrm{bulk}}}{1 - c_{\mathrm{bulk}}} \exp\Big(\frac{-E_{\mathrm{seg}}^i(c_d)}{k_{\mathrm{B}}T}\Big), \tag{5.6}$$

where i denotes the i^{th} carbon binding site. E^i_{seg} is the mean segregation energy defined as

$$E^i_{\text{seg}}(c_d) = -E^i_{\text{b}} + 2c_d V_{\text{CC}}, \tag{5.7}$$

where E^i_{b}, is the corresponding dislocation-solute binding energy (in the convention of attraction denoting a positive binding energy). c^i_d is the average concentration of the i^{th} carbon site bound to dislocations. c_{bulk} is the carbon concentration in the bulk, with c_{nom} the nominal carbon concentration per Fe atom. $V_{\text{CC}} = 0.30$eV is the carbon-carbon first-neighbour repulsion term, which is calculated as in Ventelon [232]. This repulsion term was calculated from carbon in the H1 prismatic site. It was assumed that this repulsion term is the same for carbon in other sites.

In a given volume V, the number of carbon sites along the dislocation cores is given by $N_d = \rho V/b$, with ρ the dislocation density, and the number of octahedral sites is $N_{\text{oct}} = 6V/a_{\text{bcc}}$. This imposes constraints on the carbon concentrations: $N_{\text{oct}}c_{\text{bulk}} + N_d c_d = N_{\text{oct}}c_{\text{nom}}/3$, where the factor of 3 is because there are three octahedral sites per Fe atom in the bcc lattice. Using this relation, equation (5.6) can be solved self-consistently to give the carbon concentration around the core, as a function of nominal carbon concentration and temperature. The nominal carbon concentration was taken to be the maximum solubility of ferrite in the DER region, 0.02 wt% $\approx$ 1000 appm [230]. Calculations of 10 and 500 appm were also performed. The dislocation density was varied between $1 \times 10^{12}\text{m}^{-2}$, $1 \times 10^{14}\text{m}^{-2}$ and $5 \times 10^{15}\text{m}^{-2}$, to see the effects of low densities up to the upper bound of dislocation densities $\sim 5 \times 10^{15}\text{m}^{-2}$ found in Fe-0.61wt%C martensite [237].

5.2.5 Line Tension Model

The kink-pair formation enthalpy is defined as the minimum energy necessary to create a kink-pair from a dislocation in a Peierls valley. One can find this by sampling the energy landscape seen by a dislocation line which moves from one Peierls valley to the next, from which the minimum enthalpy path can be sought. The difference between the maximum enthalpy image on this path, corresponding to a dislocation configuration in a transition state, and enthalpy of the initial state, is the kink-pair formation enthalpy. One can efficiently determine the minimum enthalpy path using the String/Nudged Elastic Band (NEB) algorithms. In these methods, a set of images, which interpolate between the initial and final states, are relaxed along the energy

landscape to find the barrier.

From atomistic calculations of the Peierls potential and carbon-dislocation binding energies, one can construct a line tension model of a dislocation from which we can obtain the kink-pair formation energies as a function of stress and carbon content [7, 76, 233]. This model views the dislocation as an elastic chain which moves in the Peierls potential ΔE_{P}.

The dislocation is modelled as a discretised line, with layer labels j. The enthalpy of the dislocation line is given by:

$$H_{\mathrm{LT}}(\sigma) = \frac{K}{2}\sum_{j}(\vec{P}_j - \vec{P}_{j+1})^2 + \sum_{j}\Delta E_{\mathrm{P}}(\vec{P}_j) + (\sigma\cdot\vec{b})\times\vec{l}\cdot\vec{P}_j - \sum_{j,k}E_{\mathrm{C}}(|\vec{P}_j - \vec{P}_k^{\mathrm{C}}|), \quad (5.8)$$

where K is a constant calculated from atomistics, ΔE_{P} is the Peierls potential, σ is the stress applied and $\vec{b}$ is the Burgers vector, with the dislocation line sense given by $\vec{l}$. $\vec{P}_j$ corresponds to the dislocation core position in a given layer. $E_{\mathrm{C}}(|\vec{P}_j - \vec{P}_k^{\mathrm{C}}|)$ is the binding energy of a particular carbon k, at position $\vec{P}_k^{\mathrm{C}}$, to a dislocation core positioned at $\vec{P}_j$. The kink-pair formation enthalpy can then be found using the string method to relax images which interpolate between the initial and final states (straight dislocations in adjacent Peierls valleys), to find the height of the transition-state barrier. A JULIA implementation of the string algorithm, accelerated by use of an ODE solver, was used to relax the images [113]. The implementation was validated on the dataset of Itakura *et al.* [76].

5.2.5.1 Line-tension model in a carbon environment

Dislocations form Cottrell atmospheres of carbon, which influence their motion. Analysis of the dynamics of a dislocation moving from one Peierls valley to the next, in an environment of carbon in equilibrium with the bulk, can provide estimates of: the mean energy barrier experienced by a straight dislocation segment upon glide, and the mean kink-pair formation enthalpy, both as functions of nominal carbon concentration. Results of the latter can be used as inputs of the aforementioned self-consistent kinetic Monte-Carlo (SCkMC) model of dislocation glide, which has been shown to predict dislocation structures in hydrogen-charged iron [238]. In addition to this, it provides estimates of mean dislocation velocity, in the limit of slow dislocation glide, by allowing carbon to equilibriate instantaneously with dislocation motion. This is an approximation. More accurate results would be possible by accounting for dislocation

velocity in a self-consistent manner as will be discussed in section 5.4.

The binding sites of carbon around the easy and hard core dislocation positions were found from atomistic simulations, detailed in section 5.3.3. Movement of a dislocation between Peierls valleys generates intermediate core positions which lie between the easy and hard cores. Carbon trap sites are not well-defined for these intermediate dislocation positions. To circumvent this, trap site positions were smoothly mapped between the easy and hard core positions by use of the dislocation core coordinate P_x by use of linear interpolation. Further information on the mapping of sites can be found in appendix D.

The total carbon concentration on the dislocation line was calculated by the self-consistent thermodynamical mean-field model, detailed in 5.2.4. The concentration was fixed to the value obtained using the H1 binding energy, $c_{\text{total}} = c_d^{\text{H1}}$, imposing the assumption that the dislocation neither rejects or absorbs carbon, despite changes in the carbon environment upon core movement. Thus carbon concentration on the dislocation line remained in equilibrium with the bulk during the simulations.

The concentration of carbon in a trap site i, c_i^{e} was determined by use of Maxwell-Boltzmann statistics [7], as done by Cottrell and Bilby [49], and Gong [238],

$$c_i^{\text{e}}(x) = c_{\text{total}} \frac{e^{-E_i(x)/k_{\text{b}}T}}{\sum_j e^{-E_j(x)/k_{\text{b}}T}}. \tag{5.9}$$

The total interaction energy of a dislocation in an environment of solutes is given by the sum of the binding energy of a particular site multiplied by the corresponding concentration

$$E_{\text{int}}^{\text{e}} = \sum_j c_j^{\text{e}} E_j(x). \tag{5.10}$$

Kink-pair formation enthalpies were obtained using the string method, as detailed in section 5.2.5, and were performed 320K.

5.2.6 Diffusion Barriers

5.2.6.1 Atomistic Calculations

Elucidation of carbon diffusion barriers around the hard dislocation core was achieved using the Climbing-Image Nudged Elastic Band (CI-NEB) method with either 5 or 9 images, with a spring constant of 6.8 eV/Å^2. The CI-NEB algorithm is a modification of the NEB algorithm mentioned in section 5.2.5, which allows for the highest energy

image to climb, by neglecting the spring forces acting on the highest image. This gives the true saddle point configuration, and therefore, an accurate energy barrier.

The fully-relaxed dislocation-carbon cells, resulting from the cluster method, as detailed in section 5.3.3, were used for the initial and final images. Intermediate images were initially determined by a linear interpolation between the two endpoints. The same k-point mesh, $1 \times 1 \times 12$ was used. The images were relaxed until all forces were below 40 meVÅ^{-1}. To prevent rotations and translations [239], six degrees of freedom were fixed (the forces resulting from these degrees of freedom were set to zero). Further constraints on NEB relaxation were imposed, as for the carbon-dislocation interactions in section 5.2.3: the three atoms surrounding the core in the top and bottom layers were fixed in Z, such that the dislocation core remained fixed during the saddle-point search: it was found that if these atoms were allowed to relax, the dislocation would move into positions which were not commensurate with the boundary conditions.

To validate this method, and to compare the migration barriers to other interatomic force methods, one performed CI-NEB calculations to find the migration barrier for carbon in bulk bcc, between two octahedral sites. The calculations were performed in a similar manner. Two cells of 250 atoms were created which each had carbon in octahedral sites which were displaced from each other by the lattice constant. These were relaxed to the same 1×10^{-5} Ry/bohr tolerance as above. These cells were taken as the initial and final images in the NEB calculation. These were interpolated between each other and then relaxed. Six degrees of freedom were fixed to prevent rotation and translation during image relaxation, as before.

5.2.6.2 Calculation of attempt frequencies and approximate carbon velocities around hard dislocation core

In determining the atomic configuration of the energy barrier, one can calculate attempt frequencies for carbon transitions in the bulk and the hard dislocation core. From these frequencies, one can approximate an effective diffusion coefficient prefactor for carbon diffusion perpendicular to the dislocation line, from which the velocity of carbon can be estimated. Comparison of the average velocities of carbon and dislocations will give insight into whether carbon does indeed diffuse faster around the dislocation core compared to the bulk, as suggested by EAM calculations of Nematollahi [56], proving the feasibility of a dislocation-assisted carbon migration. One can further use these frequencies in a discrete diffusion model of carbon migration around a dislocation core, which has a further extension to an SCkMC model of thermally

activated dislocation motion with carbon diffusion, which is detailed in the discussion, section 5.5.1.

Following the work of Jiang and Carter [240], with reference to the notation of Wert and Lu [241, 242], we have the diffusion coefficient given by

$$D = n\beta d^2 \Gamma = D_0 \exp\left(-E_\mathrm{a}/kT\right), \tag{5.11}$$

where n is the number of adjacent interstitial sites, β is the probability for diffusion in a given direction and d is the jump length projected onto the direction of diffusion. $\Gamma = \frac{1}{\tau} = \nu^* \exp\left(-E_\mathrm{a}/kT\right)$ is the transition rate—which is the inverse of the mean time-of-stay τ of the the solute between jumps. E_a is an activation energy, given by the difference in enthalpies between the initial and transition (saddle point) configurations. D_0 is the pre-exponential factor.

From harmonic transition-state theory [108, 109], the rate of transition is given by

$$\Gamma = \frac{\prod_{i=1}^{3N} \nu_i^\mathrm{I}}{\prod_{j=1}^{3N-1} \nu_j^\mathrm{S}} \exp\left(-E_\mathrm{a}/kT\right), \tag{5.12}$$

where we have the i^th normal mode frequencies of the initial and saddle point configurations as ν_i^I and ν_i^S.

The normal mode frequencies can be found by the eigenvalues of the Hessian pertaining to the initial and saddle configurations. The Hessian can be approximated for each system by evaluating numerical derivatives of atomic forces upon the displacement of each individual atom in each degree of freedom (X, Y and Z), keeping all other atoms fixed. Due to the computational expense of calculating the full Hessian using a first-order central difference scheme, which involves $2 \times 3N$ force calculations, where N is the number of atoms in the system, one only built the Hessian of atoms associated with the migration of carbon along the transition path: the first nearest neighbours of carbon in the initial, saddle and final states.

In doing the Hessian calculations on a subset of the simulation cell, one assumes that the force constants generated are not long-ranged. It was shown by Pettifor and Finnis [243, 244] in Finnis-Sinclair models that the magnitude of the force constants, out to more than six shells of neighbours, does not fall off rapidly or monotonically with distance. This long-ranged nature of force constants has also been shown in tight-binding models of zirconium [245]. To rigorously determine if this is the case for the dislocation-carbon system, one would need to analyse the properties of the

force constants using linear response theory [81]. The long-ranged nature of the force constants may hinder the predictive power of the attempt frequencies calculated in this work, and an estimate of the error cannot be given accurately without such analysis. We therefore estimate the error by the work of Finnis *et al.* [244], of whom looked at the variation of the force constants in bcc metals as a function of band filling, decomposing the contribution into n-body terms up to ten shells of neighbours. Note that the model used in this paper was based on vanadium, where the valence electrons were allowed to vary. Assuming ten shells gives reasonable convergence, one can give an estimate of the error in the force constants from the sum of contributions from three-body terms and higher in the case of a d-band with five valence electrons, accounting for ferromagnetism. The total is $\pm 1.5 \mathrm{Nm}^{-1}$, giving the percentage error as $\sim \pm 5\%$. The attempt frequency is given by the quotient of frequency products of the initial and saddle configurations as seen in equation (5.12). For an estimate of the minimum error, one assumes, that many of the frequencies in the initial and saddle point configurations are similar in magnitude—bar that of the imaginary frequency in the saddle point configuration—so the bulk of the error in the attempt frequency comes from the error of one single frequency in the initial configuration, $\sim \pm 5\%$, in addition to the error of the quotient of the resulting products, which gives an additional $\pm 10\%$ error, giving the minimum error in the attempt frequencies as $\pm 15\%$. The upper bound in the error of the attempt frequencies comes from the quotient of frequency products, which is $\sim ((3N) + (3N - 1)) \times 5\% \approx 300\%$ error, where $N = 10$ is the number of atoms included in the Hessian calculation.

5.3 Results

5.3.1 Peierls Potential

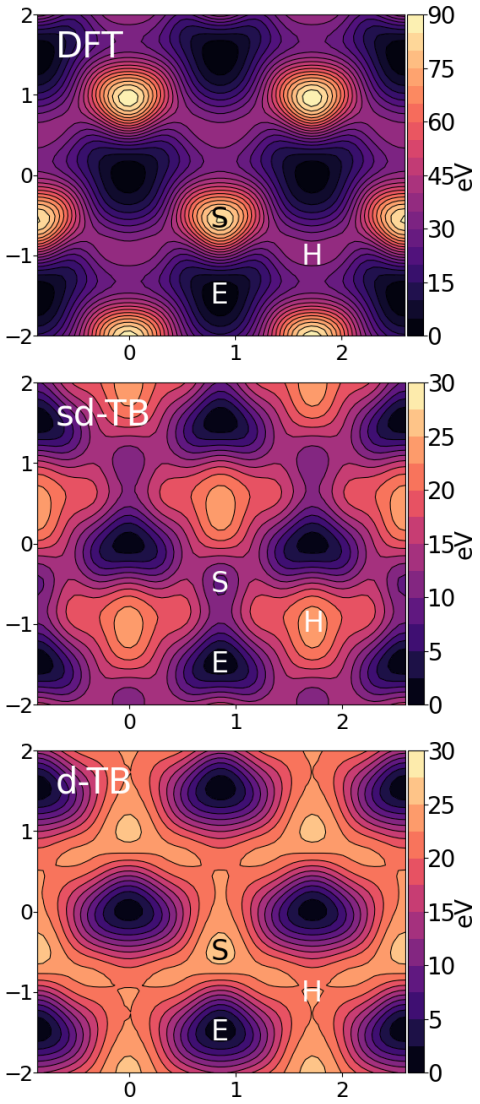

Fig. 5.4: Comparison of 2d Peierls potentials of the $1/2\langle 111\rangle$ screw dislocation between DFT [76] (top) and tight-binding (*sd* non-orthogonal middle, canonical d, bottom). $x - y$ axes in units of $d = a\sqrt{2}/3$. Energy scale is in meV. "E", "H" and "S" correspond to easy, hard and split core positions respectively, with the latter also corresponding to atomic positions. The relative energies between the different core positions is smaller in tight-binding compared to DFT. The split core as seen in tight-binding is reminiscent of EAM potentials, where the split core energy is lower than that of the hard core. The discrepancy is probably due to an insufficient repulsion at close range within the tight-binding model.

Comparison of 2d Peierls potentials of the $1/2\langle 111\rangle$ screw dislocation between DFT and tight-binding models can be found in figure 5.4, with data found in table 5.1. The sampled energies were interpolated using 2d cubic splines. The relative energies between the different core positions was found to be smaller in both tight-binding models compared to DFT. These are artefacts of the models, which have been reproduced in atomistic NEB calculations of the $1/2\langle 111\rangle$ screw dislocation Peierls barrier using the canonical *d*-band model: the Peierls barrier in this model is approximately half that of DFT [54].

The Peierls potential of the *d*-band model was found to be more reminiscent of DFT, compared to the *s*-d model; but the deviation is small: the maximum difference between the *d*/*s*-*d* models being ~ 10 meV, with the *d*-band model being, on average, $\sim +3$ meV higher.

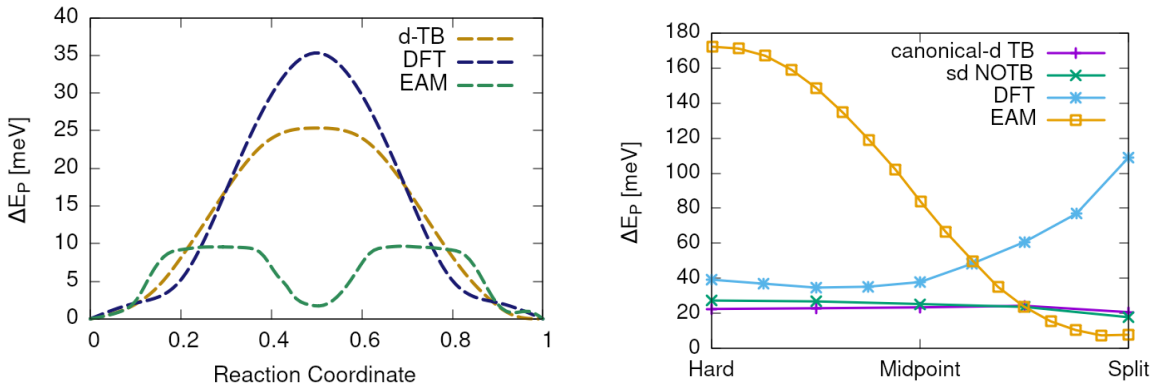

a) b)

Fig. 5.5: Left: Peierls barriers from atomistic calculations using canonical-*d*-band tight-binding, DFT and the Mendelev EAM potential, plots of the corresponding dislocation pathways can be found in figure 5.13. The EAM potential of Mendelev [116] has an unphysical well in the centre of the potential, while tight-binding and DFT produce single-humped potentials. Right: Peierls potential along the hard-split line. One can see in *s*-*d* tight-binding model pathway is more similar in shape to the EAM potential of Mendelev [116]: it decreases consistently from the hard core to the split core, but by a subtle amount in comparison. In DFT one finds a saddle point between the hard core and the midpoint.

The split core energy is lower than that of the hard core, which is reminiscent of EAM potentials [76], but not as severe, as seen in figure 5.5. Some of this discrepancy can be attributed to the to erroneous interaction term included by Itakura *et al.*, as detailed above—interaction energies can become arbitrarily high, if not made independent of truncation limit—but likely there are effects in DFT which are not

Pos	ΔE_{int}	ΔE_{tbe}	ΔE_{P}^{sd}	ΔE_{P}^{d}	$\Delta E_{\text{P}}^{\text{DFT}}$
1	0	0	0	0	0
2	–0.7	7.3	7.9	6.3	3.2
3	–1.4	16.0	17.4	15.1	19.2
4	–2.0	22.2	24.2	20.4	31.1
5	–2.5	24.8	27.4	22.6	39.3
6	–3.3	3.0	6.3	4.6	11.5
7	–6.5	7.1	13.6	12.7	39.9
8	–9.6	13.0	22.6	22.7	75.2
9	–12.5	5.4	17.9	26.8	108.9
10	–4.8	22.1	26.9	23.0	34.8
11	–7.2	18.2	25.4	23.5	37.9
12	–9.8	14.0	23.8	24.4	60.7
13	–3.8	11.5	15.3	13.2	17.6
14	–6.9	15.1	22.0	20.3	29.9
15	–4.3	18.6	22.9	20.0	39.7

Table 5.1: Table of energies used to calculate the Peierls potential. All values in meV. $\Delta E_{\text{P}}^{\text{DFT}}$ values taken from [76].

encapsulated fully within the tight-binding description, such as a lack of core electron repulsion upon deformation of the lattice, which would increase the relative energy difference. Consequences of this discrepancy on future kMC simulations are discussed in section 5.4.

The transitional kink shape from the *s*-*d* and *d*-band Peierls potentials may differ compared to DFT, with dislocation core positions possibly being situated closer to the split core position, similar to EAM potentials [76, 116]. Following the Peierls potential along the H-S direction, as seen in figure 5.5, we see that the Itakura *et al.* potential has a saddle point minimum, which corresponds to the dislocation core positions found upon kink-pair formation [76]. In the *s*-*d* model, the Peierls potential decreases monotonically along the H-S line and there is a subtle maximum found in the *d*-band model. This data suggests there may be a deviation in the dislocation path found in DFT, in moving from one Peierls valley to the next along the H-S line. Atomistic calculation of the Peierls barrier between two easy core positions in the canonical *d*-band model found core positions of the transitional kink state to go through the metastable point, similar to DFT [54], which suggest the deviation may not be severe. Section 5.3.5 discusses the effect the Peierls potential has on the pathway taken by a dislocation moving from one Peierls valley to the next.

5.3.2 Preliminary calculations

To validate the cluster simulation method, the excess energy, defined as the difference in energy between a cell with a dislocation, and a perfect reference cell, was plotted as as function of $\ln(R/r_c)$, where $R = R_2$ of the cluster and $r_c = b$, as seen in figure 5.6. In isotropic elasticity theory, this should give a linear dependence where the gradient corresponds to $\mu b^2/4\pi$, with the y intercept corresponding to the core energy E_{core}. This is well reproduced by our model, except at low $\ln(R/r_c)$ as expected, where the cell size is not large enough to accommodate for sufficient relaxation of the dislocation core, increasing the core energy, which is not accounted for in elasticity theory.

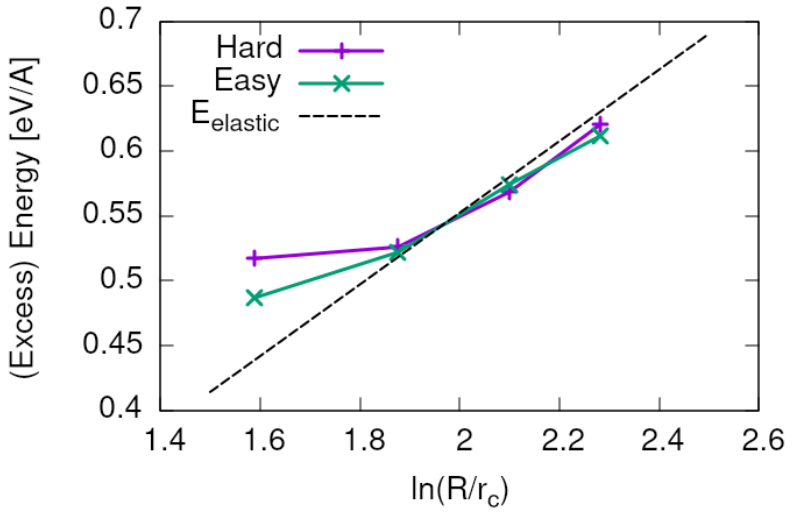

Fig. 5.6: Excess energy of dislocation clusters with differing radii for both the easy and hard core configurations. The prediction from elasticity theory is given by the black, dashed line. Deviation of both cores occurs when the cell size is small, creating an increase in the core energy, which elasticity theory cannot account for.

The energy cost to transform from the easy to the hard core can be estimated by the difference in excess energies between the cores in the limit of $\ln\left(\frac{R}{R_0}\right) \to 0$. At the smallest measured value, one finds that the core energy difference $\Delta E_{\text{core}}^{\text{Easy-Hard}} = 76$ meV/b, which is in good agreement with the DFT value of 82 meV/b [76].

5.3.3 Fe-C binding energies

As found in DFT simulations by Ventelon [232], when a carbon was placed in the vicinity of a relaxed easy dislocation core—in either of the two nearest, distinguishable,

Initial	Final
iH1, iH2	H1
iH3, iH4	H2
iH5	H3
iH6	H4
iH7	H5
iH8	H6
iH9, iH10	H7

Table 5.2: Decay relations between the initial and final sites upon relaxation of carbon interstitials around the hard core.

octahedral sites—a spontaneous reconstruction of the dislocation core occurred: from easy to hard. Upon reconstruction, the dislocation core moved to a neighbouring triangle, when looking along the $\langle 111 \rangle$ direction, where the carbon found itself situated in the centre. This will be called a prismatic site, as in Ventelon's paper. This confirms that both hard and easy dislocation cores must be studied to fully understand screw dislocation behaviour in bcc iron.

The binding energies of carbon to both the hard and easy cores can be seen in table 5.3, with the resulting distribution of carbon in figures 5.7 and 5.8. The distribution of carbon strongly depends on the type of core it finds itself situated near. The easy core only significantly modifies the position of the iE1 site, to the E1 site, situated in the centre of an adjacent triangle. All other sites are unaffected, so there is a one-to-one correspondence between all iEj and Ej sites, where $j \in \{2 \dots 10\}$. There are stable carbon positions available close to the triangular region containing the core, but not inside.

Carbon favours a prismatic site within the hard core (H1), which has the highest binding energy, 1.29 eV, of all sites considered. There are no binding sites apparent in a triangular annulus (of width $a_{\mathrm{bcc}}\sqrt{2}/2$) surrounding the hard core triangle due to the destruction/volume reduction of octahedral sites near the hard core. The initial octahedral sites, iH1 and iH2 decay to the H1 site. Similarly, iH3 and iH4 decay to the H2 site, with iH9 and iH10 decaying to a H7 site. Relations between each of the sites is given in table 5.2.

Note that interactions between carbon atoms around the core are not taken into account here: figures 5.7 and 5.8 are purely diagrammatic and not what one expects the true distribution of carbon around a screw dislocation would be. Carbon is strongly repulsive at first nearest-neighbour distances, which would modify each of

these distributions.

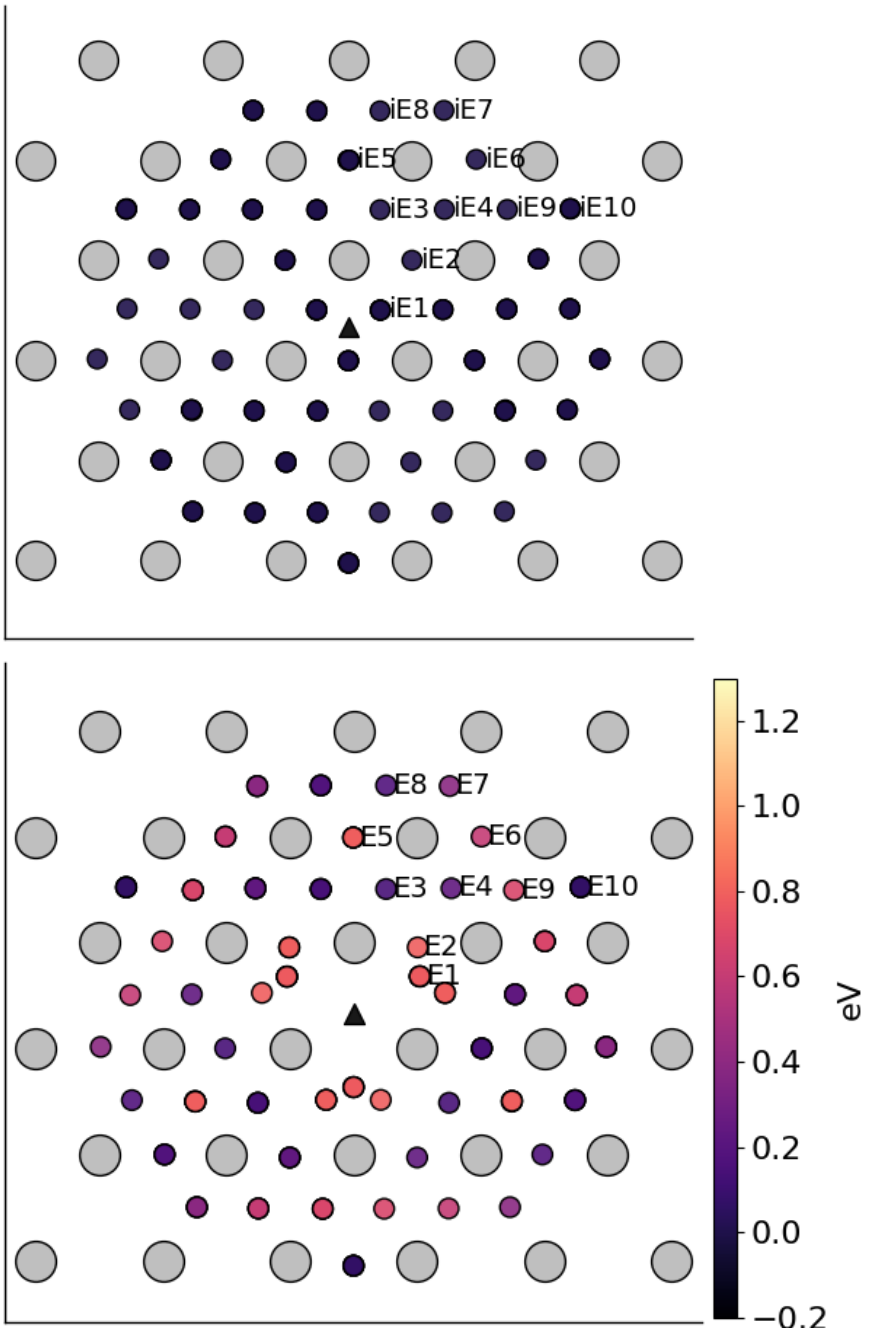

Fig. 5.7: Initial (top) and final (bottom) positions and binding energies (eV) of carbon around the easy core. Binding energies are not shown for the initial positions. Top: initial positions before relaxation. Bottom: final positions and binding energies after relaxation. The core was constrained by fixing the top and bottom three atoms surrounding each of the cores. As shown by Ventelon [232], the first and second closest octahedral sites to the hard core decay to a prismatic position inside the hard core.

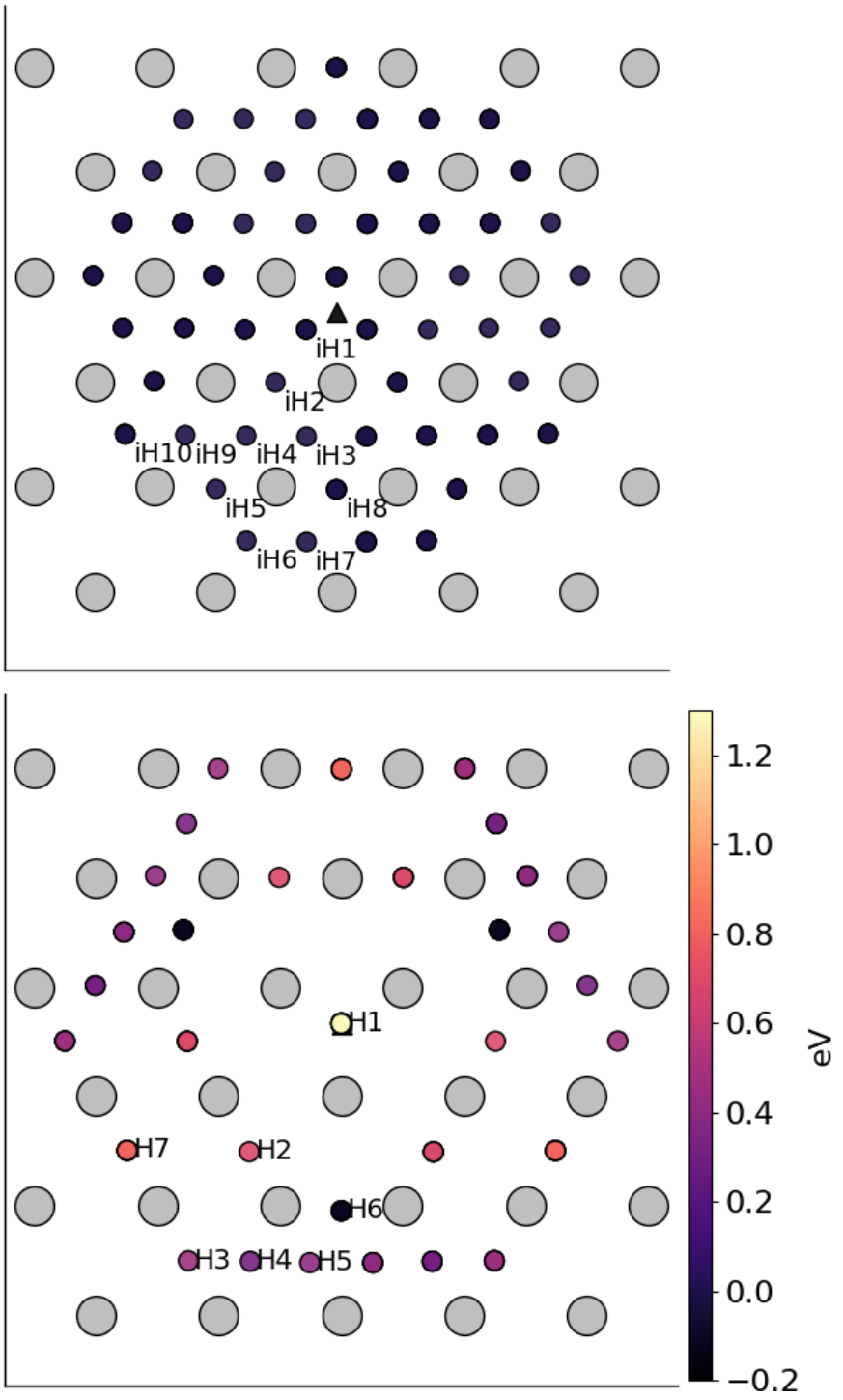

Fig. 5.8: Initial (top) and final (bottom) positions and binding energies (eV) of carbon around the hard core. The core was constrained by fixing the three atoms surrounding each of the cores in the top and bottom layers. As shown by Ventelon [232], the first and second closest octahedral sites to the hard core decay to a prismatic position inside the hard core.

Site Type	distance from core [b]	E^z [eV]	ΔE^z [eV]	E_b [eV]	E_b^z [eV]
E1	0.57	0.185	–0.018	0.793	0.775
E2	0.70	0.202	–0.001	0.793	0.793
E3	0.99	0.205	0.002	0.137	0.139
E4	1.21	0.208	0.005	0.229	0.234
E5	1.36	0.210	0.008	0.784	0.791
E6	1.66	0.209	0.007	0.597	0.603
E7	1.89	0.206	0.003	0.385	0.388
E8	1.77	0.203	0.000	0.177	0.178
E9	1.52	0.201	0.000	0.683	0.683
E10	1.95	0.202	0.000	0.067	0.067
H1	0.00	0.196	–0.006	1.298	1.291 [0.881[a], 0.790[b]]
H2	1.19	0.210	0.007	0.691	0.698
H3	2.12	0.209	0.007	0.461	0.467
H4	1.91	0.207	0.005	0.311	0.316
H5	1.80	0.208	0.006	0.403	0.409
H6	1.40	0.207	0.005	–0.119	–0.114
H7	1.35	0.206	0.006	0.825	0.819

Table 5.3: Table of energies leading to the zero-point energy corrected binding energy using the cluster method for simulation of dislocation-carbon interactions. [a] Tight-binding quadrupolar array results, starting from a fully relaxed easy core quadrupole extended to a depth of 3b with carbon introduced into the iH1 site in the middle layer, by both dislocations. [b] DFT results of Ventelon, using the same quadrupolar configuration as in [a]. In both quadrupolar simulations, carbon ended up in the H1 site.

These binding energies agree well with experiment and atomistic/elastic calculations. EAM simulations by Clouet [212, 246] found a maximum binding energy of 0.41 eV by calculating the elastic dipole tensor, as seen in Bacon, Barnett and Scattergood [169], from multiple relaxations at various volumes. Hanlumyuang et al. [214], similarly conducted DFT and EAM calculations for the interaction energy 12Å from the core, and their calculations agreed with the continuum limit of the aforementioned elastic dipole tensor, with a binding energy of 0.2 eV. In DFT calculations by Ventelon [232], the binding energy of a carbon in a hard core prism configuration was found to be 0.79 eV for a thickness in the Z direction of $3b$ (0.73eV for $6b$). This is significantly lower than the 1.29eV interaction energy of tight-binding. This discrepancy can be partially explained by the fact that the cells have not been allowed to relax with all degrees of freedom, as in the Ventelon results: the three atoms around the screw core are fixed in Z so the dislocation core position does not change upon relaxation. Repeating the calculation for the binding of a H1 carbon to a screw dislocation using a quadrupolar array, allowing for all atoms to relax, gives a binding energy of 0.88 eV.

This agrees very well with the DFT results of Ventelon [232], and suggests that core relaxation is important for determining the prismatic site binding energy.

A source of the discrepancy between DFT and tight-binding is likely the fitting of the tight-binding model itself. The Peierls barrier of this *s*-*d* model of iron, necessary for Fe-C interactions, has been shown to be half that found in DFT [54], but the solution energies for Fe-C defect complexes are well described. This implies that the relative bonding strengths between Fe-Fe and Fe-C are consistent with DFT, but there is insufficient repulsion between Fe-Fe species upon deformation. As such the energy of the dislocated lattice is not as great as it should be when simulating dislocation-carbon systems, resulting in a larger solute-dislocation binding energy from tight-binding.

5.3.4 Carbon concentration around the dislocation line

The variation of carbon concentration on the dislocation line for the binding sites of the easy and hard cores can be seen in figure 5.9. We see at low temperatures, all dislocations are decorated with carbon. As temperature increases, the amount of carbon decorating the dislocations starts to decrease. Due to the lower binding energy of carbon to the easy core, desaturation occurred at a lower temperature compared to the hard core. Dislocation densities near the upper bound of what has been observed in martensite, $\rho \approx 10^{15}\mathrm{m}^{-2}$, reduce the temperature at which carbon concentration starts to decrease on the dislocation core. Lower nominal carbon concentrations cause carbon concentrations around the dislocation to decrease at a lower temperature.

In the high-purity iron case, $C_{\mathrm{nom}} = 10$ appm, we find at dislocation densities above $\rho \approx 10^{15}\mathrm{m}^{-2}$, that there is a reduction in the maximum concentration permitted in the material, with increasing dislocation density. This is due to the fact that there is not enough carbon for all of the dislocations, as such the concentration on the dislocation line decreases.

In the operating temperature range of $40 - 90°\mathrm{C} = 310 - 360°\mathrm{K}$, we expect most hard core sites are saturated. Given the high concentrations of the E1/E2 sites around the easy core in this range, we expect all dislocations will be of the hard core type, due to reconstruction of the easy core by the adjacent carbon.

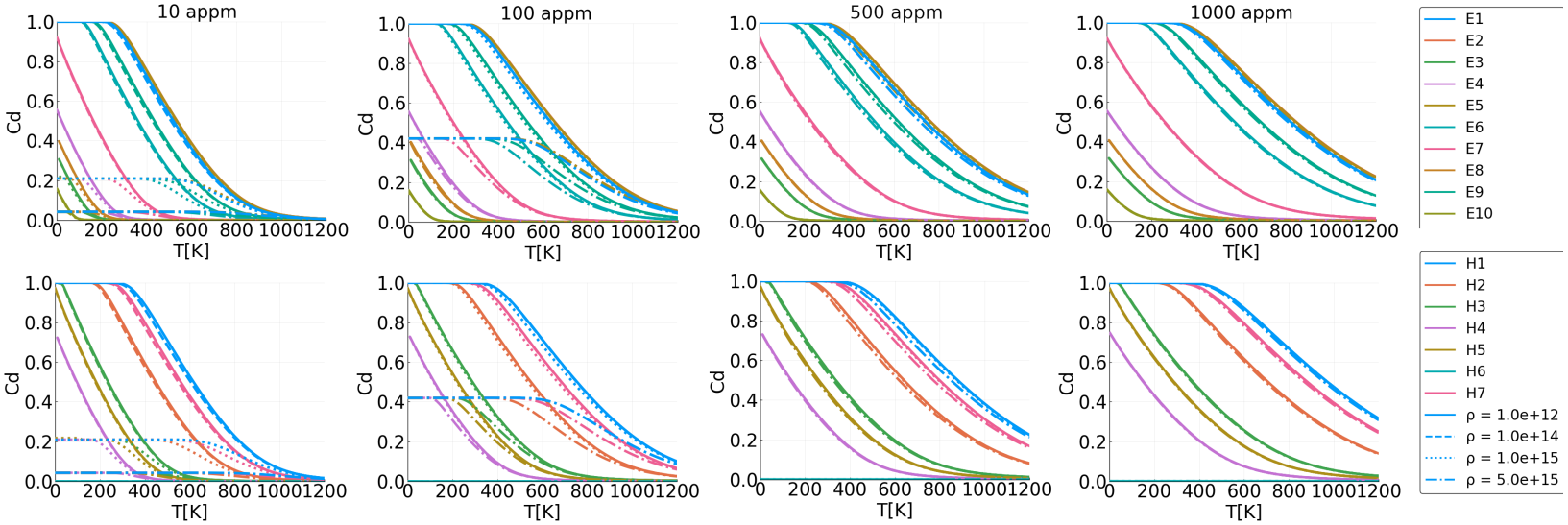

Fig. 5.9: Variation of carbon concentration on the dislocation line c_d for the binding sites of the hard core (Hi) and easy core (Ei). Solid, dashed, dotted and dash-dotted lines correspond to dislocation densities of 1×10^{12} m^{-2}, 1×10^{14} m^{-2}, 1×10^{15} m^{-2} and 5×10^{15} m^{-2} respectively. The nominal carbon concentrations are 10, 100, 500 and 1000 appm from left to right, where around 1000 appm corresponds to the concentration of carbon at the solubility limit of C in ferrite: 0.02wt%. c_d and c_{bulk} reached self-consistency, with an absolute tolerance of 1×10^{-6}. C-C interactions were taken into account with the repulsive first-neighbour interaction energy $V_{\text{CC}} = 0.30$ eV. No intersite interactions were taken into account. The maximum concentration of carbon around the easy core, drops off at a lower temperature than that of the hard core due to lower binding energy of the Ei sites compared to the Hi sites. The operating temperature is taken to be 50° C = 320° K.

5.3.5 Line Tension Model

5.3.5.1 Prerequisites

The K coefficient for the line tension model was calculated from atomistic simulations, using the method of Itakura *et al.* [76], by calculation of a Hessian from the displacement of atoms surrounding the dislocation core. Tight-binding gave $K = 0.734$ eVÅ^{-2}, which agrees well with DFT, where $K = 0.816$ eVÅ^{-2}.

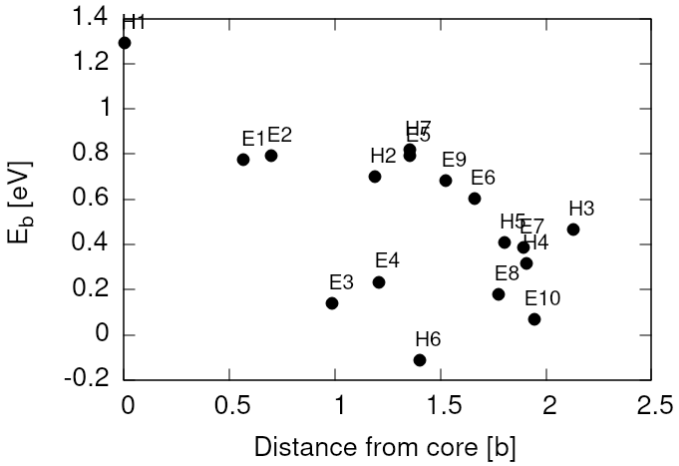

Fig. 5.10: Distance dependence of the binding energies of carbon to the $1/2\langle 111\rangle$ screw dislocation in iron. Positive binding energies denote a favourable binding.

Dislocation-carbon binding energies were found to decay with distance, as seen in figures 5.10 and 5.11. A Lorentzian was fit to specific binding energies such that a continuous function could be used to describe binding within the line tension model. This is a purely empirical model. The choice of sites used for the fitting is discussed in section 5.4.

This distance-dependence agrees well with previous calculations of the binding energy at larger distances from the core [214].

5.3.5.2 Kink-pair formation in pure iron

In figure 5.12, one can see the P_x and P_y core positions which result from the highest enthalpy image of kink-pair formation in pure iron for the canonical-d and sd tight-binding models, where the DFT comparison is from [76]. Plots of the corresponding dislocation core pathway, $P_j = (P_x^j, P_y^j)$, looking down the dislocation line, are shown in 5.13.

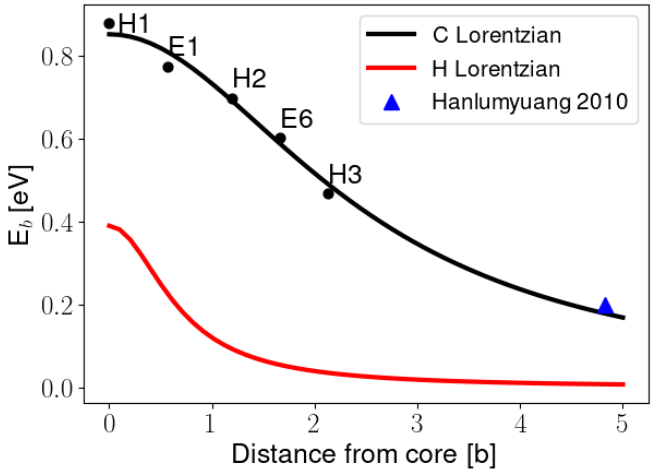

Fig. 5.11: Parameterised distance dependence of carbon binding energies to the $1/2\langle 111\rangle$ screw dislocation in iron. The sites chosen to fit to were determined by those sites a prismatic carbon in a hard core configuration would find itself, if the dislocation were to move without it along the $X = \langle \bar{2}11\rangle$ direction. The triangle, labelled Hanlumyuang, refers to the binding energy resulting from measurement of the elastic dipole tensor from DFT calculations evaluated at 12Å [214]. Binding energy of hydrogen to the $1/2\langle 111\rangle$ screw dislocation also shown for comparison [233]

The P_x line shape agrees well with the DFT-based results. The kink width was found to be slightly wider: $W_k \approx 11b$ in tight-binding from the line-tension model, compared to $10b$ in DFT and atomistic tight-binding results [54]. The larger width from tight-binding compared to DFT results from the width being proportional to $b\sqrt{K/\Delta E_P}$ [76], with the discrepancy between the K^{tbe} and K^{DFT}, being smaller than that of the Peierls potential. Differences in the P_y line shape are noticeable, with the canonical-d model reproducing the result closest to the DFT P_y line shape.

The differences in line shapes manifest themselves clearly in plots of the dislocation pathway, figure 5.13, where we see the path a dislocation takes looking down the dislocation line. The core pathway dips below the mid-line in both the d and sd models, with a more pronounced effect being shown by the sd model. Apart from this discrepancy, we see there is good agreement between tight-binding to DFT when compared to the EAM potential of Mendelev [116] in which we see a path which passes close to the split-core position. This is expected due to the low overall values of the Peierls potential of the EAM, as seen in figure 5.5.

The kink-pair formation enthalpies obtained from the tight-binding models can be

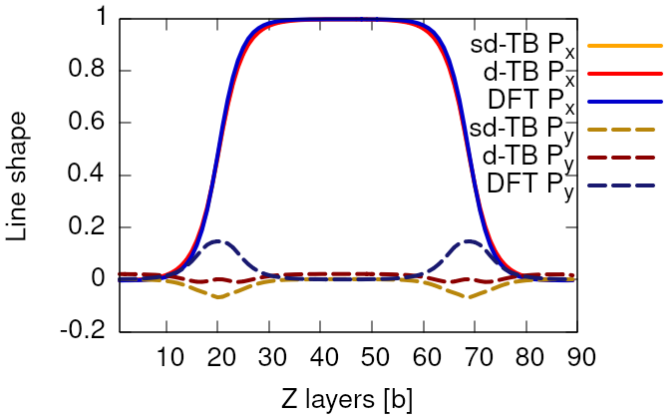

Fig. 5.12: Core positions of the line tension model from DFT (blue) and tight-binding (yellow) for the middle image corresponding to the minimum energy pathway (MEP) and the kink-pair formation energy. Images were relaxed using the ODE String method of Makri and Ortner [113]. P_x and P_y correspond to the x/y-coordinate of the dislocation core position in each of the discretised layers of the dislocation. One finds that the kink width in tight-binding is wider than that found in DFT, which corresponds with the fact that the width is proportional to $b\sqrt{K/\Delta E_P}$, where the reduction in ΔE_P^{tbe} is greater than the reduction in K_{tbe}. .

found in table 5.4. Tight-binding underestimates the kink-pair formation enthalpy by 0.18 eV, in comparison to DFT. This can be attributed to the difference in Peierls potentials between DFT and tight-binding.

Method	H_{k}
DFT	0.71 eV
s-*d* TB	0.56 eV
d TB	0.53 eV

Table 5.4: Kink-pair formation energies between DFT, and the two flavours of tight-binding used with the line-tension model .

5.3.5.3 Kink-pair formation enthalpy with a single carbon

To understand how kink-pair nucleation is affected by carbon, one can study the formation of a kink-pair but with the additional interaction of a single carbon ahead of the dislocation. With one single carbon, the dislocation core will not reconstruct, as such we perform this for a dislocation moving from from an easy core position, to an adjacent easy core position.

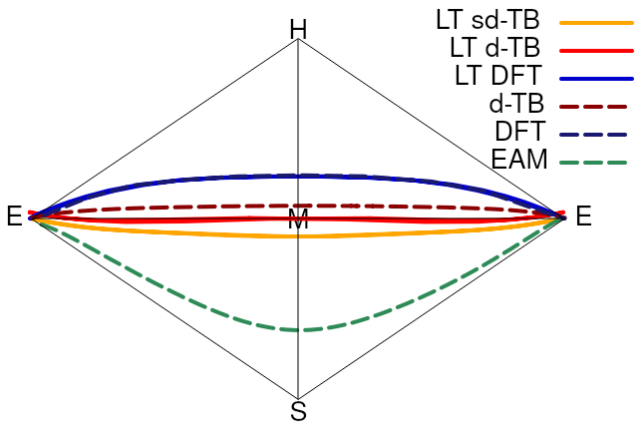

Fig. 5.13: Comparison of minimum energy pathways from atomistic calculations to the line-tension model. Dashed lines correspond to atomistic calculations. Solid lines are results from the line-tension models. Tight-binding follows a pathway much closer to that of DFT. EAM potentials predict that the dislocation core goes to the split core and then back to the easy core. Even though the Peierls landscape found in tight binding has similar characteristics to the EAM in terms of the energetic ordering of different core states, the description of the minimum energy pathway of the $1/2\langle 111\rangle$ screw dislocation as it moves between core positions is in good agreement with DFT.

We place carbon in the E1 site, the closest and one of the highest energy binding sites of carbon to the easy dislocation core. The carbon is fixed in place during kink-pair formation, as such, we are assuming a regime in which the dislocation velocity is much greater than the diffusion of carbon. Carbon-dislocation interactions are only permitted between the dislocation segment closest to the carbon.

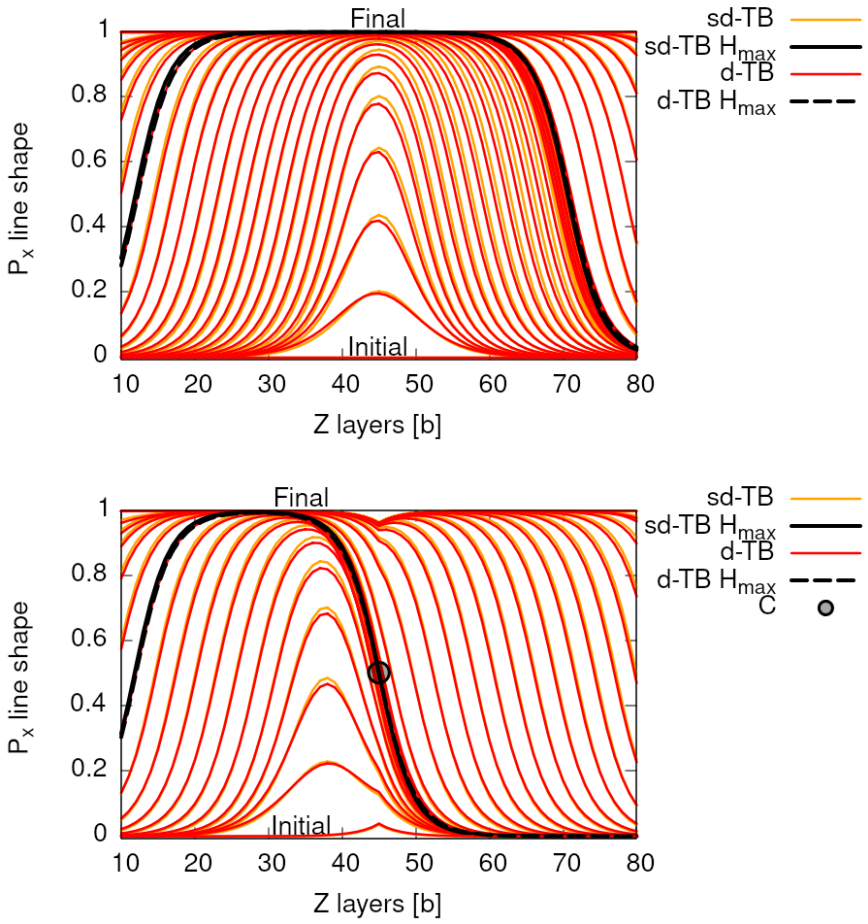

Fig. 5.14: Comparison of P_x lineshapes for the *sd* and *d* models in pure iron (top) and iron with a single carbon interacting with the central dislocation segment in an E1 site (bottom). The highest enthalpy images, $H_{\max}$, for each of the models are shown in black. In pure iron, the *d* model lineshapes are offset from the *sd* model due to the different Peierls potentials involved. With carbon along the path of migration, we find the dislocation intersects the solute, due to its large binding energy.

P_x line shapes obtained during kink-pair formation can be seen in figure 5.14. The addition of carbon causes a cusp in the dislocation line towards the carbon in the initial and final images, due to the reduction in potential the central dislocation segment experiences due to carbon interaction. As the dislocation bows out to form a kink pair, the cusp becomes less prominent. As we reach the transition state, the dislocation image intersects the carbon position, to minimise energy.

The pathway corresponding to the highest enthalpy image, can be seen in figure 5.15. Looking along a direction, we see the path a dislocation takes in going between

adjacent Peierls valleys is asymmetric, as expected due to the strong binding of carbon.

These features agree very well with the line tension model in Itakura [233], focussing on the case of dislocations undergoing kink-pair formation in the presence of a single hydrogen atom.

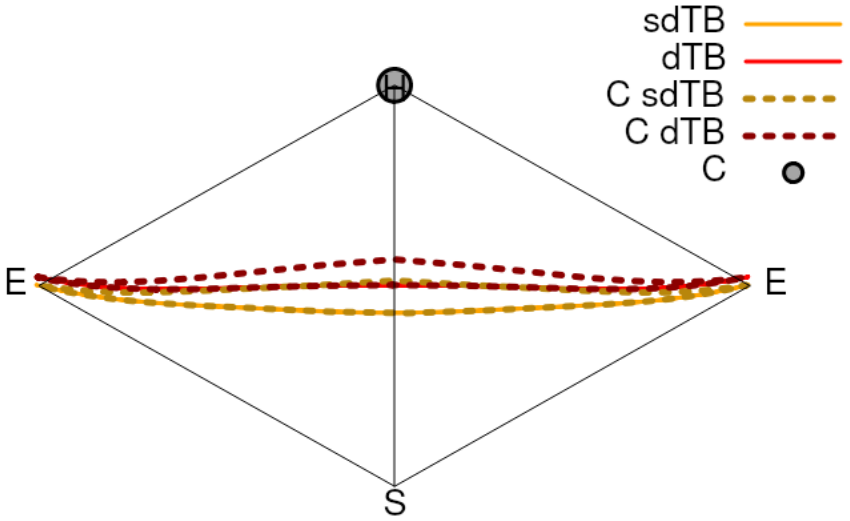

Fig. 5.15: The migration path of the highest enthalpy images for both the *sd* and *d* tight-binding models with a single carbon in an E1 site. Carbon causes a deviation of the kink-pair formation path from the pure iron case (solid lines), due to carbon-dislocation binding.

The kink-pair formation enthalpy of *sd* and *d* iron models, in both pure iron, and with carbon ahead of the dislocation line are shown in figure 5.16. The shape agrees well with results of the line tension model of Itakura *et al.* [76], and from atomistic calculations of EAM [57] and GAP [248] Fe potentials. We find that carbon produces a consistent reduction of $\sim$ 25meV to the kink-pair formation enthalpy when placed ahead of the dislocation line. The reduction is surprisingly small compared to the effect of hydrogen interaction with dislocations [233], which gives a reduction of $\sim$ 110meV. The discrepancy between carbon and hydrogen is due to the more gradual decrease of the carbon-dislocation interaction—over the distance between the initial and transition states—compared to the hydrogen-dislocation interaction, as shown in figure 5.11. Comparing the two interaction functions, we have at the Peierls valley $P_{\text{disl}} = (0, 0)$, and $P^{\text{H}} = P^{\text{C}} = (1.17\text{Å}, 0.68\text{Å})$ giving a distance $d = 0.54b$ between the dislocation and the solute. The difference in the interaction energy for a dislocation segment in

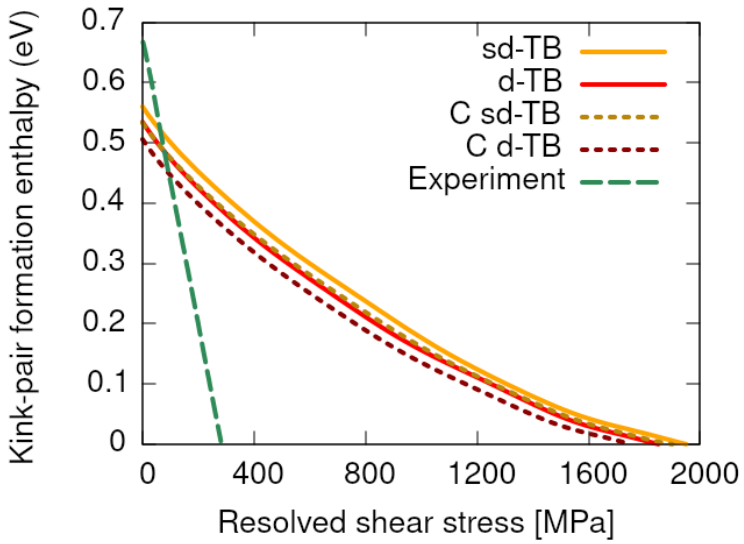

Fig. 5.16: Dependence of the kink-pair formation enthalpy with increasing stress on the $[111](1\bar{1}0)$ direction. Solid lines: pure iron. Dotted lines: carbon ahead of the dislocation line in an octahedral site. Experimental data taken from Spitzig [247].

the final position in interaction for hydrogen $\Delta E_b^{\mathrm{H}} = E_b(\mathrm{H}, 0) - E_b(\mathrm{H}, 0.54b) = 150$ meV, whereas for carbon we have $\Delta E_b^{\mathrm{C}} = E_b(\mathrm{C}, 0) - E_b(C, 0.54b) = 40$ meV. Therefore, in the dilute limit, it is the long-range of carbon-screw dislocation interactions which inhibits a strong solute-enhanced localised plasticity effect. Short-ranged dislocation-solute interactions, *i.e.* interactions which decay quickly due to an insufficient solute-induced lattice distortion—do not produce a long-ranged elastic field which binds the solute to the dislocation—which results in significant enhancements in local plasticity.

Due to the longer range of the interaction function, we expect that a single carbon will provide comparable decreases to the kink-pair formation up to distances up to 5b, if placed ahead of the dislocation line. At equilibrium, where carbon exhibits long-range ordering along the dislocation line in the H1 and H2 sites [249], we can expect a much larger decrease in the kink-pair formation enthalpy. Line-tension simulations in ordered carbon environments are necessary to account for this properly. We can approximately treat some of these effects using an effective carbon-dislocation interaction along the dislocation line during kink-pair formation, as shown in section 5.3.6.2.

The stress at which the kink-pair formation enthalpy becomes zero is the Peierls stress. In the zero temperature limit, we can approximately account for quantum effects, such as tunnelling and zero-point energy, by subtracting the Wigner correc-

tion, determined by quantum transition state theory [57, 250], from the kink-pair formation enthalpy. Calculating this correction within atomistic tight-binding simulations is currently intractable. The correction has been calculated using the Mendelev EAM potential [116] for a screw dislocation undergoing kink-pair nucleation [57]. The Wigner correction obtained is 0.09eV. We find that the Peierls stress obtained for both the *sd* and *d* models is $\approx$ 1.2GPa, see table 5.5.

Model	Peierls Stress [GPa]	Wigner-corrected Peierls Stress [GPa]
sd-TB	1.95	1.35
C *sd*-TB	1.90	1.30
d-TB	1.85	1.30
C *d*-TB	1.75	1.20
DFT [Kraych, 2019]	2.00	1.20
DFT [Itakura, 2012]	1.00 [*2.10]	0.80 [*1.60]

Table 5.5: Peierls stress of screw dislocation taken from the line tension model with the effect of the correction to the Peierls stress from quantum effects, estimated by Proville [57]. DFT results are found from papers of Itakura *et al.* and Kraych [76, 251], where Itakura *et al.* used a DFT-derived line-tension model, and Kraych used DFT NEB calculations. * corresponds to use of Itakura *et al.* DFT data in this implementation of the line-tension model. In accordance with other DFT-derived line-tension models, their Peierls stress is a factor of two out.

Discrepancies in the kink-pair formation enthalpy compared to experimental measurements of Spitzig [247], can be attributed to multiple sources. In bcc metals, experimental measurements of the CRSS, which can be linked to the kink-pair formation enthalpy, are thought to measure the stress required to operate Frank-Read sources which have been blocked due to the back stress of generated screw dislocations [252]. As mixed dislocations bow out from the source, long screw segments form—due to the higher mobility of mixed/edge character segments compared to screw segments. Between the source and the screw dislocations, there are non-screw dislocations, stresses from which act in conjunction with applied stress to reduce the necessary CRSS by 2-3 times. As such the enthalpy barrier obtained from the experimental CRSS measurements of Spitzig, cannot be directly compared to the true kink-pair formation enthalpy necessary for a single screw dislocation to undergo thermally-activated movement.

5.3.5.4 Kink-pair nucleation rate

One can use the Arrhenius law in equation (5.11), to calculate the attempt frequency of a process p, given an activation energy barrier E_{a} [110],

$$\Gamma_{\mathrm{p}}(E_{\mathrm{a}}, T) = \nu^{*}_{\mathrm{p}} \exp\Big(- \frac{E_{\mathrm{a}}}{k_{\mathrm{B}} T}\Big), \tag{5.13}$$

where, considering the process of kink-pair formation, Γ is the inverse of the mean time-of-stay of the dislocation in a Peierls valley before forming a kink-pair $\Gamma = \frac{1}{\tau_{\mathrm{disl.}}}$ and $\nu^{*} = \frac{\prod_{i=1}^{3N} \nu_i^{\mathrm{init.}}}{\prod_{j=1}^{3N-1} \nu_j^{S}}$ is an attempt frequency for the transition of the kink-pair over the activation barrier E_{a}.

The kink-pair nucleation rate of a dislocation depends linearly on the number of **b** length segments of which it is composed: the greater the length, the more likely that a stable kink-pair will be formed under thermal fluctuations. For a dislocation of length N_d Burgers vectors, the attempt frequency is given by, as in as Itakura *et al.* [233]:

$$\Gamma_{\mathrm{d}}(H_k(\sigma), T) = \Gamma_{\mathrm{k}}(H_k(\sigma), T) N_d, \tag{5.14}$$

where $H_k(\sigma)$ is the kink-pair formation enthalpy. Experimental results of *in situ* straining of Fe from Caillard [253], enable calculation of the stable kink-pair nucleation rate: assuming $b = 2\mu$m, $T = 300$K and an applied stress of 33MPa one obtains $\Gamma_{\mathrm{d}}(H_k(33\mathrm{MPa}), T = 300\mathrm{K}) = 81 s^{-1}$.

There will be an enhancement of the rate due to carbon occupying sites ahead of the dislocation, in the limit of fast glide. Given a concentration of carbon on the dislocation line, c_d, for the sites ahead of the dislocation, we can define a rate enhancement factor,

$$f_r(c_d, \Delta H_k, T) = 1 + c_d W_k \{\exp(\Delta H_k / k_{\mathrm{B}} T) - 1\}. \tag{5.15}$$

where $\Delta H_k = H_k - H_k^{\mathrm{C}} = 25$meV and $W_k \approx 11b$ is the kink-width [77]. This assumes the increase in the rate comes only from kink segments which all interact equally strongly with the carbon ahead. Assuming $T = 300$ K, and assuming the concentration of carbon is that of the E2 site, c_d^{E2}, we obtain enhancement factors as shown in table 5.6.

These rate enhancements are an order of magnitude less compared to what one finds with hydrogen in iron [54], due to the small reduction to the kink-pair formation enthalpy with carbon.

c_{nom} [appm]	f_r, Rate Enhancement factor	T_{U} [K]
10	4.4	745
100	7.9	1329
500	17.3	3043
1000	17.3	3043

Table 5.6: Enhancement factors to the kink nucleation rate and corresponding critical temperatures. c_d was taken as the value reached from self-consistency at T=300K for the E2 site, at a dislocation density of $\rho = 10^{15}$ m^{-2}, as seen in figure 5.9. Kink-pair nucleation rate enhancements steadily increase until concentrations at which all dislocations are decorated with carbon, in the cases of $C_{\text{nom}} \geq 500$ appm. The critical temperatures are all well above operating temperature, so we can expect rate enhancements during operation.

Significant enhancement of the nucleation rate occurs when the rate enhancement factor is on the order of $f_r \sim 1$ or greater. Defining $c_d^E = \frac{1}{W_k\{\exp(\Delta H_k/k_{\text{B}}T)-1\}}$, one can impose a condition when $c_d^E > c_d$, defining a critical temperature T_{U} after which these enhancements are not deemed important. See table 5.6. All the critical temperatures are found to be well above operating temperature.

These results only account for the effect of a single carbon just ahead of the core in the dilute limit. There are multiple, strong binding sites, and the influence of carbon is significant even at long distances from the core, as seen in figure 5.11. With the introduction of more carbon, there will be a reconstruction from the easy to the hard core. With reconstruction, ordering phenomena of carbon has been found along the screw dislocation in Fe, which would decrease the kink-nucleation rate [249]. Ising models parameterised on *ab-initio* data give equilibrium concentrations of different carbon trap sites along the dislocation core, accounting for carbon-carbon repulsion. They predict H1 and H2-type sites in adjacent layers can have concentrations which are ~ 0.55 and ~ 0.22 respectively, when the nominal carbon concentration is 1000 appm, at 300K. With the larger concentration of carbon in the H1 site, one expects an increase in the kink-pair formation enthalpy, due to carbon in other sites not being able to overcome the strong binding of the prismatic carbon to the core. The mean effect of carbon at different concentrations, in the limit of slow glide is discussed in section 5.3.6.

5.3.5.5 Kink-trapping

Kink-trapping is the energetic barrier to kink-migration along the dislocation line due to the change in binding energy of a kink sweeping past a defect. The kink-

trapping effect due to carbon can be estimated in the dilute limit as follows [233]. If a kink-pair were to form with a carbon in an E1 site behind the dislocation, the carbon-dislocation binding energy will change. We can assume carbon remains in its site upon movement: the barrier to kink-migration has been shown to be small [54, 233, 238], as such kink-migration is orders of magnitude faster than that of carbon and even hydrogen diffusion.

As the kink sweeps past, the E1 site becomes an E6 site, resulting in a difference in binding energy of $\Delta E_b^{\mathrm{E1}\rightarrow\mathrm{E6}} = 0.775 - 0.603 = 172$ meV. This trapping effect is expected to decrease with applied stress, as shown in Itakura *et al.*, but this is left for future work.

This is an important effect to account for, in the context of a SCkMC models, as solute drag has been shown to reduce the kink-migration velocity sufficiently, such that jogs can form on dislocations due to the collision of kinks on different glide planes causing pinning and the formation of edge dipoles seen in experiment [238].

5.3.6 Line-tension equilibrium conditions

5.3.6.1 Dynamics of straight 1/2⟨111⟩ screw dislocation

Figure 5.17 shows the potential a straight screw dislocation experiences as it moves between Peierls valleys in an equilibrium carbon environment, allowing carbon to redistribute between trap sites upon glide. The same carbon binding energies were used for both the *sd* and *d* models. The potential a dislocation experiences decreases as carbon concentration is increased. This is due to the stabilisation of the hard core position with increases in carbon content. With stabilisation, E1/2 sites are distorted into H1 sites. At concentrations $>$ 20appm, the mean carbon-dislocation interaction energy becomes greater in magnitude than the bare Peierls potential, resulting in a potential well.

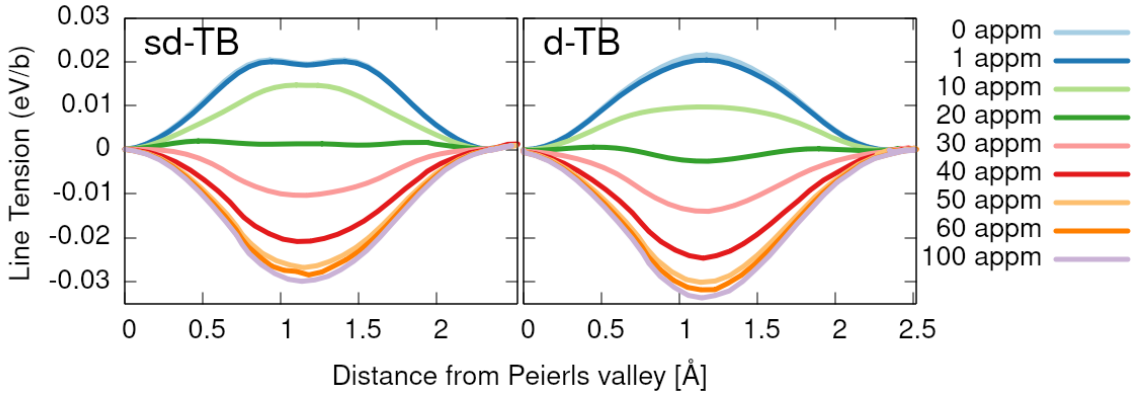

Fig. 5.17: Enthalpies of straight screw dislocation in the line-tension model in an environment of carbon with concentrations determined by thermodynamical mean field model. Carbon concentration on the dislocation on the dislocation line is in equilibrium with the bulk according to the concentration given by the H1 site, where carbon is able to redistribute between the sites according to Maxwell-Boltzmann statistics.

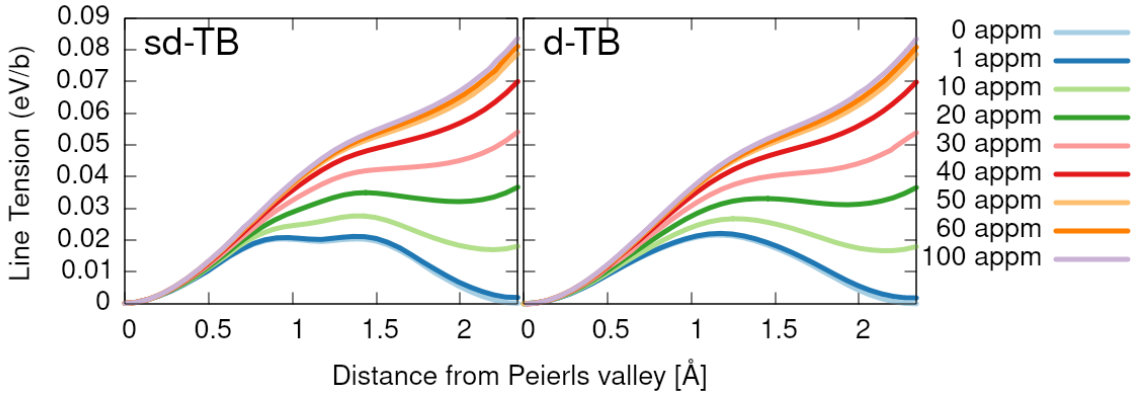

Fig. 5.18: Enthalpies of straight screw dislocation in the line-tension model in an environment of carbon with concentrations determined by thermodynamical mean field model. Concentration of carbon in each of the sites is fixed to its initial value, simulating the limit where carbon does not have time to equilibriate with dislocation movement.

Figure 5.18 shows the case where the concentration of carbon is not allowed to equilibriate: simulating the limit of rapid glide, where the occupancy of carbon in all trap sites is fixed to the value determined at the initial easy-core configuration of the straight dislocation. The occupancies decrease rapidly with distance from the core. As such, the energy a straight dislocation experiences, relative to the initial dislocation position, increases with distance from the Peierls valley, due to a reduction in the

dislocation-carbon interaction energy from a lack of carbon occupancy.

In reality, we have a situation which is between the two limiting cases. This can be accounted for by a continuity term which is dependent on dislocation velocity [238].

5.3.6.2 Dynamics of kink-pair formation in equilibrium

The line-tension upon kink-pair formation, in the limit of slow glide, can be seen in figure 5.19. One finds the spring term, which is zero for the aforementioned straight dislocation dynamics, gives a large contribution in the maximum enthalpy images. It is significantly larger than the Peierls potential, such that the double-humped nature of the *sd*-model is smoothed out. As the hard core is stabilised with increasing carbon content at 320K, the line tension decreases, due to the negation of the bare Peierls potential with increasing carbon-dislocation interaction energy. At nominal concentrations greater than 20 appm, the string method finds lower energy dislocation configurations away from the straight initial easy core position favoured at lower concentrations.

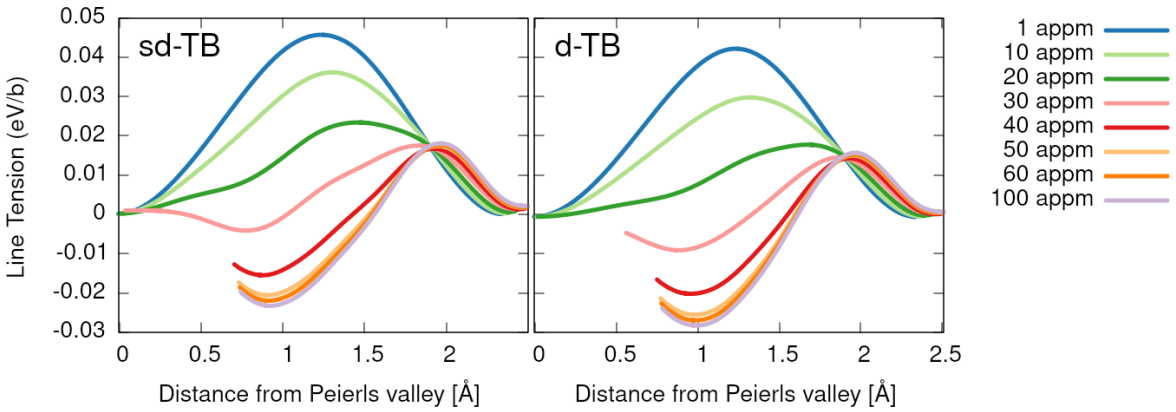

Fig. 5.19: Enthalpies of the maximum enthalpy images upon kink-pair formation with increasing carbon content. Carbon interaction causes a reduction in the enthalpy barrier as due to the negation of the effect of the bare Peierls potential. As the nominal carbon concentration passes 20 appm, the hard core is stabilised, thus causing the string method algorithm to find a global minimum closer to the hard core position.

With increasing carbon concentration, both tight-binding models exhibit a deviation of the maximum enthalpy pathway towards the hard core, as shown in figure 5.20. At each concentration, the path a dislocation takes in the *d* tight-binding model is closer to the hard core, due to the morphology of its Peierls potential.

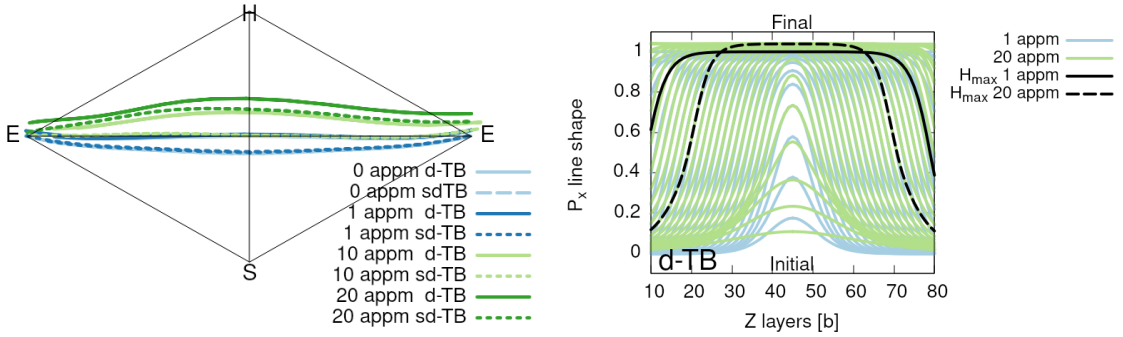

Fig. 5.20: Maximum enthalpy pathways and lineshapes found upon kink-pair formation in an environment of carbon for both tight-binding models at different nominal carbon concentrations. Concentrations shown are before the easy core becomes unstable. With an increase in carbon content, the path starts to deviate towards the hard core. Right: P_x lineshape corresponding to different carbon concentrations of the canonical-d tight-binding model.

The lineshapes of the P_x dislocation coordinate on kink-pair formation, figure 5.20, broaden with carbon content due to the attraction of the dislocation line to the carbon sites which are distributed across the length of the dislocation.

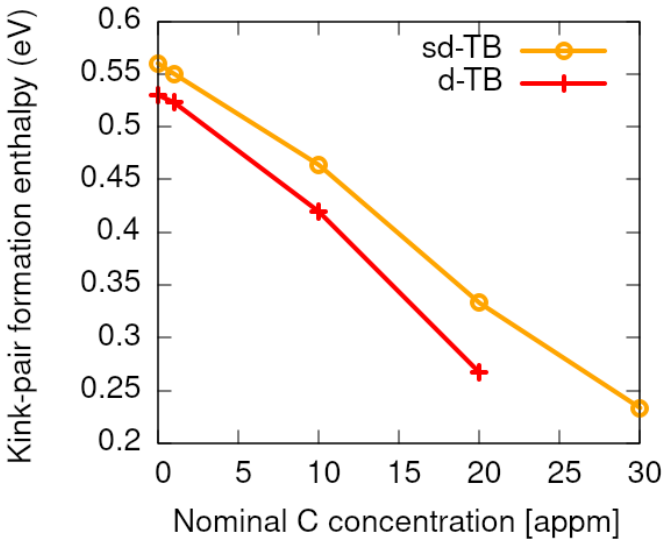

Fig. 5.21: Kink-pair formation enthalpy dependence on nominal carbon concentration without the application of stress. There is a consistent decrease in the mean kink-pair formation enthalpy with carbon content.

The kink-pair formation enthalpy in an effective carbon concentration can be seen

to decrease with increasing carbon content. At concentrations greater than 20 appm, the hard core is stabilised.

Line-tension simulations of the transition from a carbon-stabilised hard-core, to an adjacent carbon-stabilised hard core were performed. It was found that the string method would move the initial and final images to minima which were offset from the actual hard core positions, as these were positions which minimised the Peierls potential, while the dislocation core could still be close to carbon. These positions were related to the interpolated site positions, which were between the true trap-sites, which are not physical. With increasing concentration, the kink-pair formation enthalpies larger, from $0.7 - 1.5$ eV. As the cores settled in fictitious positions, the results from these simulations were not included in this thesis.

Line-tension calculations of the kink-pair formation of a dislocation moving from the stabilised hard core to an adjacent hard-core position, using a different methodology for carbon-dislocation interaction energies in the limit of slow glide, are necessary to ascertain the kink-pair formation enthalpy at higher carbon contents. We expect, as was seen in self-consistent calculations of the kink-pair formation enthalpy in hydrogen [238], that the trend will be reversed: the kink-pair formation enthalpy will increase with carbon content, once the hard core has been stabilised, as observed in the calculations performed in the previous paragraph.

One can see the effect that these mean enthalpies have on the kink-pair nucleation rate. Using the results of the kink-pair formation enthalpy from the canonical-d tight-binding model, and using equations (5.14) and (5.13) we have the rates as shown in table 5.7. The rate enhancement factor is not included here as the concentration term is taken into account in the kink-pair formation calculation itself.

c_{nom} [appm]	$\Gamma_{\text{d}}(T = 320\text{K})$ $[s^{-1}]$	$\bar{v}_{\text{d}}(T = 320\text{K})$ $[\text{Å}s^{-1}]$
10	8.7	20.4
20	2881.8	6753.1

Table 5.7: Kink-pair nucleation rate in an environment of carbon using the results of the canonical d-band model, from equations (5.14) and (5.13).

Allowing carbon to equilibriate between trap sites during kink-pair formation, we see a large enhancement to the kink pair nucleation rate, increasing dislocation velocity. Discussion of these results are left for section 5.3.7.1.

5.3.7 Diffusion Barriers

EAM calculations of the diffusion barriers of carbon close to the easy core have shown a decrease in barrier height from 0.87eV for bulk diffusion, to 0.2eV around the dislocation core [56]. The lowering of the diffusion barrier around the dislocation line is crucial to the validity of dislocation-assisted carbon migration. As will be shown in section 5.3.7.1, carbon is only able to keep up with screw dislocations at temperatures $\sim$ 300K, if the diffusion barrier is lowered below $\sim$ 0.7 eV. However, the predictive power of the EAM potential used to obtain these barriers is limited. The Mendelev EAM potential is unable to reproduce: the 2D Peierls potential, which is double-humped, instead of single-humped [116]; the metastable hard core structure, which exhibits a spontaneous reconstruction to the hard core from the easy core and, the binding energies of carbon close to the dislocation core—being half that found in Ventelon and this work [232, 246]. These discrepancies are likely due to the inherent lack of quantum mechanical bonding information included in the EAM description, which seems necessary for an accurate description of energetics close to the dislocation core in iron. As such, it remains to be seen if the diffusion barriers, and consequent diffusion rates obtained from this EAM potential are faithful, when compared to quantum methods, such as DFT and tight-binding.

As seen in figure 5.9, at moderate dislocation densities, we expect all dislocations to be decorated with carbon, and be of hard-core type. As such, it is important to ascertain the diffusion barriers of carbon around the hard core, as it is the core we expect to find most commonly in steels. From this, we can ascertain if there exists a high-mobility zone around dislocations in bcc iron, validating the EAM results of Nematollahi and the Fe-C potential of Becquart [56, 246], in addition to providing a mechanism as to how carbon can travel with dislocations.

The diffusion barriers of carbon around the hard core from tight-binding can be seen in figure 5.22. As found in DFT diffusion barrier calculations of carbon in iron [240], the barrier for carbon displaced by a single lattice parameter is double-humped, which corresponds to carbon travelling through an intermediate octahedral site, which is of the same energy as the initial and final sites. Only one of these humps is shown in figure 5.22, as they are identical. The bulk diffusion barrier obtained agrees very well with DFT calculations. One obtains a value of 0.82 eV, compared to 0.87 eV found by Jiang and Carter [240]. As such one may expect that the actual energy barriers energies found below may be lower than from what one may expect from DFT.

The diffusion coefficient prefactor calculated by finding the attempt frequency from

the normal modes of the Hessian of all first neighbour atoms to the carbon in the initial and transition states and using the standard equations (5.11) and (5.12). The predicted value of the diffusion coefficient prefactor $D_0^{\text{tbe bulk}} = 6.07 \times 10^{-7}$ m^2 s^{-1} in bulk diffusion lies close to the DFT value and the average experimental value, with values of $D_0^{\text{DFT bulk}} = 1.44 \times 10^{-7}$ m^2 s^{-1} and $D_0^{\text{Exp. bulk}} = 1.67 \times 10^{-7}$ m^2 s^{-1} [240, 254]. Note, the average experimental value varies over several orders of magnitude.

The discrepancy between DFT and tight-binding for the diffusion prefactor may arise from the size of the supercell used (a 250 atom cell was used in tight-binding compared to 125 atoms in DFT) and the construction of the Hessian: Jiang and Carter constructed a rather small Hessian which only pertained to the three atom system of carbon and the two iron atoms which were between the initial and final octahedral sites, rather than including the effect of the first nearest neighbours of carbon in each image of the transition path considered. As carbon produces a large tetragonal distortion of bcc Fe octahedral sites, it is expected that the first nearest neighbours would all have a sizeable effect on the vibrational frequencies and the mode of vibration associated with transition, which would thereby modify the value of Γ and the diffusion coefficient prefactor. For completeness, using the same method of Hessian construction as Jiang and Carter, one obtains $D_0^{\text{tbe bulk JC}} = 7.44 \times 10^{-8}$ m^2 s^{-1}, which is roughly half that of the DFT calculated value.

The migration barriers around the hard dislocation core vary. One finds that the migration energy barriers are significantly lower around the hard core compared to the bulk value of 0.82 eV, however, they are not all around 0.2 eV as calculations of diffusion around the easy core by Nematollahi suggest: the barriers vary from $0.2 - 1.8$ eV. One finds that the lowest energy barrier is that found by the transition of the H4 site to the H3 site, which results in an energy barrier of 0.2 eV.

Considering the H1 to H2 transition, one finds a large barrier of 1.8 eV. This high barrier can partially be attributed to the constraint of keeping the core atoms in the top and bottom layer fixed in the Z direction during the saddle point search. As seen in section 5.3.3, performing relaxations of carbon-dislocation systems within a quadrupolar array, with the same tight-binding model, reduced the binding energy of the H1 site by 0.4 eV.

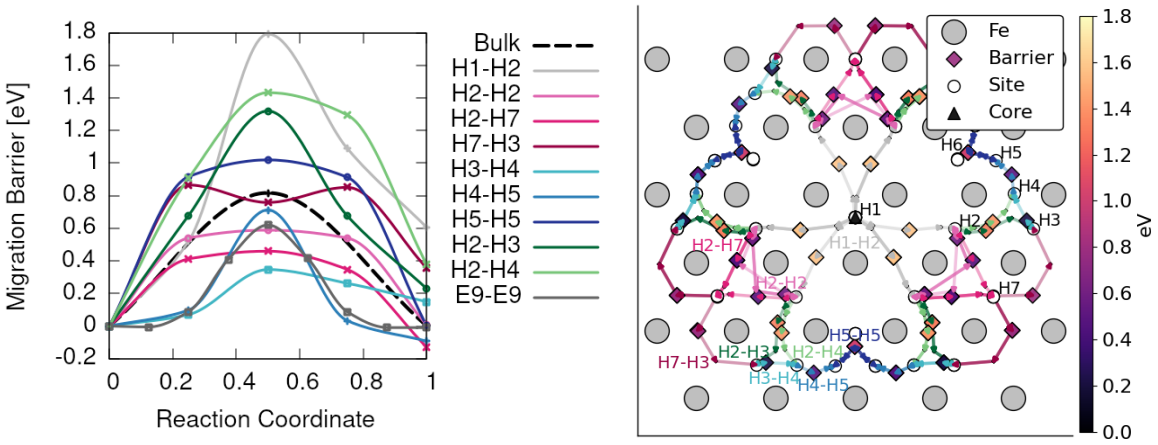

Fig. 5.22: Left: energy barriers for carbon migration around a static hard-core dislocation. The bulk migration barrier was calculated using tight-binding for comparison. Many barriers around the hard dislocation core are reduced compared to that of the bulk, with some being higher due to the constraints imposed on some core atoms during relaxation. Right: Paths of migration, where the saddle points are denoted by large markers, where the colormap gives the migration barrier relative to the first site.

Transition	E_a [eV]	ν^* [THz]
Bulk → Bulk	0.817	44.19
H1 → H2	1.790	24.58
H2 → H1	1.180	30.01
H3 → H4	0.347	20.77
H4 → H3	0.197	4.39
H4 → H5	0.484	48.52
H5 → H4	0.576	49.85
H5 → H5	1.016	26.25
H2 → H2	0.589	36.03
H2 → H7	0.460	27.15
H7 → H2	0.588	6.07
H3 → H7	0.418	30.07
H7 → H3	0.776	29.67

Table 5.8: Table of energy barriers, with the value of ν^*, the attempt frequency calculated as in Vineyard [109] from tight binding.

From the resultant paths, one can see potential mechanisms for carbon to keep up with the dislocation. At equilibrium around 300K, a screw dislocation is in a hard core configuration, with carbon segregated to binding sites around the core. Applying a shear stress such that the dislocation moves along the $X = \langle 2\bar{1}1 \rangle$ direction, the

dislocation will move to the next hard core site, which is stabilised by the carbon atoms at the H2 site. Assuming only barriers below 0.6 eV are able to be activated, as the velocity of carbon is an order of magnitude greater than that of the dislocation, as seen in figure 5.23 at $T = 300$ K, then we have the following mechanisms.

Considering sites ahead of the dislocation, before the dislocation moves, we have a H7 site which is occupied, which is likely due to its large binding energy of 0.82 eV. Once the dislocation has moved, assuming all carbon remains in place during dislocation movement, it becomes a H2 site. The carbon in the H2 site can freely diffuse to the new H7 site immediately ahead, as the H2 $\rightarrow$ H7 barrier is 0.46 eV. This is probable as the binding energy of the H7 site is higher than that of the H2 site, and there is likely not a carbon in the new H7 site due to the lower binding energy of carbon as we go out from the core. The binding energy of carbon at a distance of 3b distance is around ≈ 0.4 eV, assuming the parameterised Lorentzian curve in figure 5.11 is accurate. As we assume carbon stays in place during the transition of the dislocation from one hard core site to the next, and taking into account that the maximum concentration of the H2 site (of $E_\mathrm{b} = 0.698$ eV) was around 0.22 at 1000 appm and 300K, as found by the Ising model incorporating carbon repulsion of Lüthi [249], one can safely assume that the concentration of carbon in the newly minted H7 site would be lower. The sites previously H3, H4 and H5 will become new H2 sites, which can diffuse by the same mechanism, to the new H7 site.

Considering sites parallel to dislocation motion, the H3 site will become a new H5 site, which can take the transition path H5 $\leftrightarrow$ H4 $\leftrightarrow$ H3 $\rightarrow$ H7. This carbon is marginally more likely to stay in the new H3 site than the H5 site, and so the cycle could repeat upon further motion of the dislocation. For H4 and H5 sites we see that they can diffuse by H3 $\rightarrow$ H4 $\rightarrow$ H5, where these carbon atoms will now stay behind the dislocation due to the large barrier of the H5 $\rightarrow$ H5 transition.

For sites behind the dislocation, we find that the H1 site becomes H2. Carbon is able to redistribute itself between the H7 and adjacent H2 site. The H2 site becomes H7, and that the H7 $\rightarrow$ H2 transition is possible, yet less likely to occur due to the tendency for carbon to stay in the sites of the highest binding energy.

In some particular site-transitions, the preferred path of carbon is to go through slightly deformed, metastable, octahedral-like sites. These can be seen in the transitions of the H2-H2, H7-H3 transitions.

5.3.7.1 Comparison of velocities of carbon and dislocations by thermal activation.

We can calculate and compare the velocities of carbon undergoing diffusion and dislocations undergoing kink-pair formation using information from literature, and from the migration barriers around the core, as detailed below. A figure showing the calculation for a range of temperatures can be seen in figure 5.23.

The average velocity associated with a process undergoing thermal activation of a barrier is given by $\bar{v} = d_a \Gamma$, where d_a is the distance between the the initial and final states of the barrier and $\Gamma = \nu_0 \exp\{(-E_a/k_B T)\}$ is the jump rate at a given temperature over an activation barrier E_a. For dislocations in bcc we have $d_d = a\sqrt{2/3} = 2.34$Å, the jump distance between Peierls valleys, and for kink-pair formation and $d_C = 1.435$Å, the distance between octahedral sites which carbon can jump to.

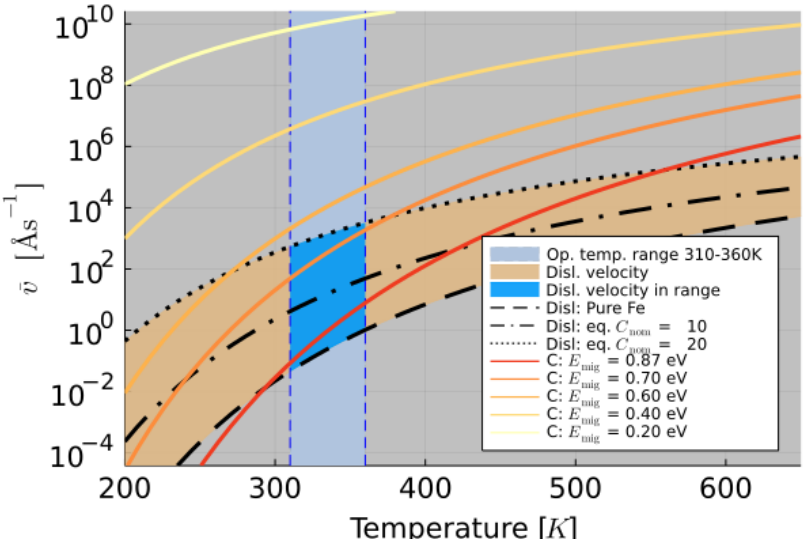

Fig. 5.23: Average velocity of dislocations moving by kink-pair formation compared to the velocity of carbon diffusion at various temperatures and migration barriers. With a migration barrier smaller than 0.6 eV, carbon is able to move with dislocations. The effect of the rate enhancement factors were negligible on the log velocity, as such, they were omitted for clarity.

The experimental diffusion coefficient prefactor of carbon in bcc Fe has been calculated as $D_0^C = 1.67 \times 10^{-7} \mathrm{m^2 s^{-1}}$ [240, 254]. The attempt frequency is related to the diffusion coefficient prefactor by $\nu_0 = 6D_0/a^2$ [241, 255], which gives the attempt frequency of carbon as $\nu_0^C = 1.21 \times 10^{13} s^{-1}$ [56]. Given that the migration energy barrier of carbon in bulk bcc Fe is $E_{\mathrm{m\ bulk}}^C = 0.87$eV from DFT calculations, rate of

transition for carbon at $T = 300$ K is $\Gamma_{\mathrm{C}} = \nu_0^{\mathrm{C}} \exp\left\{-E^{\mathrm{C}}_{\mathrm{m\ bulk}}/k_{\mathrm{B}}T\right\} = 2.95 \times 10^{-2} s^{-1}$, resulting in a velocity of $v_{\mathrm{C}} = 4.23 \times 10^{-2} \text{Å} s^{-1}$.

From the experimental rate of stable kink-pair nucleation in pure iron as $\Gamma_{\mathrm{d}} = 81 s^{-1}$ from the work of Caillard [253], we can estimate the attempt frequency $\nu_{\mathrm{d}}^0 = 0.99 \times 10^8 \mathrm{s}^{-1}$ using the experimental kink-pair formation enthalpy at 33 MPa $H_{\mathrm{k}} = 0.595$ eV as in Itakura *et al.* [233]. This gives the velocity, as $v_{\mathrm{d}} = d_{\mathrm{d}} \Gamma_{\mathrm{d}}(H_{\mathrm{k}}, 300) = 2.0 \text{Å} s^{-1}$.

This shows that in the bulk, carbon cannot be assumed to move with the dislocation, as the velocity of carbon is less than that of kink-pair formation.

However, with lower carbon migration barriers in the vicinity of screw dislocations, carbon is able to be dragged along with the dislocation during glide. Assuming only carbon barriers below 0.6 eV can be activated at 300K, and that the attempt frequencies range from 6–30 THz from table 5.8, one finds the average velocity of carbon ranges from $v_{\mathrm{C}} = 6.0 \times 10^2$ – $3.0 \times 10^3 \text{Å} s^{-1}$. The lower bound of the carbon velocity is much greater than that of dislocations undergoing thermally-activated movement, as such we can assume that in the high-mobility zone that carbon is able to move with dislocations.

One can determine an upper bound to the average screw dislocation velocity in an environment of carbon, by the plotting of the dislocation velocities with the kink-pair formation enthalpies found in equilibrium, as seen in figure 5.21. The corresponding equilibrium dislocation velocities seen in figure 5.23, do not account for the self-consistency of the kink-pair formation enthalpy and the average dislocation velocity. Applying self-consistency is necessary, as with an increase in dislocation velocity, there is a reduction in the occupation of trap sites, which in-turn increases the kink-pair formation enthalpy, reducing the velocity from the original value. The average velocity of the screw dislocation at 20 appm C—which gives the lowest kink-pair formation enthalpy, resulting in the highest velocity—represents an upper bound to dislocation velocity modified by the carbon environment, as seen in figure 5.23. This upper bound is assumed to be reasonably accurate in the operating temperature range of 310-360K, despite the kink-pair formation enthalpy only being sampled at 320K. Future work would be to improve on these results by adding in self-consistency, with extended sampling over the operating temperature range.

The timescale of carbon redistribution with dislocation movement remains negligible as long as the kink-pair formation enthalpy with carbon $H_{\mathrm{k}}^{\mathrm{C}}(\sigma)$ is greater than the migration barrier energy in high mobility zone [77]: $H_{\mathrm{k}}(\sigma) - \Delta H_{\mathrm{k}}^{\mathrm{C}}(\sigma) > E_{\mathrm{C}}^{\mathrm{m}}$ [77]. Using

value of $E_{\mathrm{C}}^{\mathrm{m}} = 0.6$ eV, one obtains a critical shear of $\sigma_c^{\mathrm{U}} \sim 25$MPa; using the smallest barrier of $E_{\mathrm{C}}^{\mathrm{m}} = 0.2$ eV, we can obtain an upper critical stress $\sigma_c^{\mathrm{U}} \sim 210$MPa, above which carbon cannot enhance dislocation mobility. These are approximate bounds. Strain has been shown to increase the binding energy of solute sites by the easy core [56], and it is uncertain how shear strains will affect the migration barriers of carbon around the hard screw dislocation.

5.4 Discussion

The Peierls potential is reproduced well by tight-binding. The change in core energy agrees well with the calculated change of dislocation core energies of the in-situ Fe straining experiments of Caillard [253], despite these simulations being performed at 0K, using the ferromagnetic ground state of iron during dislocation relaxations. For a Peierls potential more reminiscent of iron at finite temperature, one could have given a more thorough treatment of magnetism, performing multiple dislocation relaxations using the non-collinear disordered local moment approximation to handle paramagnetism, as was achieved by Casillas and Ventelon [256]. Their calculations showed that the energy difference between the hard and easy cores is lowered to 26 ± 20meV$/b$, from 40meV$/b$. The error bars are too large to confirm the hypothesis that the Peierls potential is significantly different, and the tight-binding results coincidentally fall exactly into the middle of their range. As such, the resultant Peierls potential from ferromagnetic calculations within tight-binding was deemed suitable for the line-tension model.

We see a reduction in the kink-pair formation enthalpy of pure iron in tight-binding, by 0.15eV compared to DFT, due to the smaller overall Peierls potential in both the *sd* and *d* tight-binding models. This would increase the rate of kink nucleation in kMC models, causing a higher overall dislocation velocity. We do not expect this discrepancy will significantly change the principal mechanisms observed, or results obtained, from kMC simulations.

As in Lüthi [249], carbon interactions were found to be vital in understanding how screw dislocations move in steels, due to the spontaneous reconstruction of the pure iron ground state (easy core) upon introduction of carbon. From the large binding energy of the H1 site, one would expect a hard core with carbon in a prismatic site as the ground state configuration for pinned dislocations. In normal operating temperatures of the bearings, one expects all dislocations to be hard cores saturated with carbon in most of the H_j sites, as seen in the concentration analysis. In ferrite that

has just transformed, assuming a C concentration of 0.6 wt% as seen in martensite, we expect similar behaviour to the 1000 appm case as seen in figure 5.9.

In the context of dislocation-assisted carbon migration, with sufficient contact stress, dislocations in their hard core ground state will be forced to move along the $X = \langle\bar{2}11\rangle$ direction along a $\{110\}$ plane, the elementary slip plane for screw dislocations in Fe [253]. This results in the hard core reconstructing to an easy core. In the limit of rapid glide, the prismatic carbon will stay in-place, becoming an E1 site. A drag force now acts to impede motion of the dislocation, due to the binding of the carbon in the E1 site. Progression of dislocation glide results in further reconstruction of the dislocation core to hard and easy states, with the original carbon being situated in H2, E6 and H3 sites, relative to the dislocation centre. From this reasoning, the Lorentzian which parameterised the carbon interaction was fit to the H1, E1, H2, E6 and H3 sites, as seen in figure 5.11. As the dislocation moves, there is a significant drag force acting on the dislocation, which decreases the further the dislocation moves from carbon. As seen from the line-tension equilibrium results of straight dislocations, figure 5.18, right, the energy of the straight segments increase greatly due to this drag force.

However, due to the reduced barriers for carbon migration within the vicinity of a dislocation, as shown by the explicit calculation of diffusion barriers, there can be an average velocity of carbon orders of magnitude greater than that of screw dislocations, so carbon is indeed very much able to keep up with the dislocation in normal operating temperature conditions. The migration barriers key to carbon keeping up with dislocations are the H2 $\leftrightarrow$ H7 and H3 $\leftrightarrow$ H5 barriers. Assuming that the stress does not hinder carbon migration barriers significantly, the limit of slow glide applies during operation, where carbon is able to keep up with the dislocation and equilibriate between sites. It is found that the kink-pair formation enthalpy decreases significantly up to the critical concentration of 20 appm at which the dislocation becomes a hard core; and the velocity of the dislocation will increase due to the rate enhancement from the ability of carbon to equilibriate with the sites around the dislocation from the reduced migration barriers. Increasing the concentration of carbon further increases the kink-pair formation enthalpy, as seen in hydrogen. In reality, the actual rate enhancement is dependent on the amount of carbon which can equilibriate, which itself is a function of dislocation velocity. As such, in future SCkMC simulations, one will be able to find the dislocation velocity and kink-pair formation enthalpy in a self-consistent matter, allowing for accurate simulation of carbon drag by dislocations.

Within the context of the softening effect of carbon in ferrite, as seen in the temperature dependence of the flow stress [16, 48], one sees that the origin of the softening effect may be due to the activation of carbon diffusion, which decreases the kink-pair formation enthalpy. The softening effect is found in the dependence of flow stress 150 to 300K. Comparing this with the screw dislocation velocities in figure 5.23, one sees that diffusion barriers which are < 0.6 eV can be activated in this range, which give a comparable velocity to dislocations which are in the lower range of dislocation velocities seen here. The increased activation of these barriers causes softening by the enhancement of kink-pair formation. The hardening effect of carbon > 300K has been seen to be attributed to the inversion of the screw/edge mobility ratio, as seen in *in-situ* straining experiments [48].

5.5 Future work

Using the kink-pair formation enthalpies and the binding energies of carbon to screw dislocations, one can proceed with self-consistent kinetic Monte Carlo simulations of dislocation glide in an environment of carbon to understand how dislocations move carbon under applied stress, in different temperature and nominal carbon concentration regimes.

It would be of interest to pursue atomistic calculations of carbon bound to edge dislocations. DFT/elastic dipole tensor calculations by Maugis *et al.* [257], show under *compressive* stress, carbon diffusivity is *enhanced*. This was also seen in the work of Simpson with hydrogen [54]. Pipe diffusion along edge dislocations could therefore be an important aspect to consider in carbon transport, in addition to the higher mobility of edge dislocations in bcc iron. As such, edge dislocations could be quite important within the mechanism of dislocation-assisted carbon migration. Furthermore, the effect of stress on the migration barriers of carbon around the screw cores is yet to be determined.

Ising and Monte Carlo models of intersite carbon interactions have been performed using the results of DFT carbon-dislocation binding energies [249]. These calculations only considered the hard core, with carbon binding sites of the H1 prismatic site and a H2 site, (which they name P and $O^{(4)}$ respectively). First neighbour C-C interactions were taken into account, both along the dislocation line and between carbon sites. Using the tight-binding calculations as detailed in section 5.2.3, one can easily apply and extend this analysis to consider more binding sites around the hard

core, and observe stable carbon distributions around the easy core. From these models, one could calculate the kink-pair formation enthalpy in an environment of multiple carbons within the line-tension model explicitly accounting for the long-range ordering exhibited by carbon.

5.5.1 Modification of occupancies in SCkMC due to diffusion barriers

To model the solute atmosphere around a dislocation in an environment of carbon, which is allowed to diffuse, we can use a discrete diffusion model, as detailed in Yoshinaga [258]. One could use this to extend the line-tension model and the SCkMC model and estimate the amount of carbon dragged by the dislocation [56].

Using the carbon migration barriers, and attempt frequencies around the dislocation core, one can determine the evolution of carbon concentration with time. Nematollahi *et al.* [56] extended this model to include the effect of changes in occupancy upon dislocation movement.

The total change in occupancy can be described by the equation

$$\frac{\partial \chi_i}{\partial t} = \sum_{j=1}^{4} \Big\{ \chi_j(1-\chi_i)\nu_0^{i\to j} \exp\Big\{\Big[-E_{\mathrm{a}}^{i\to j}/k_{\mathrm{B}}T\Big]\Big\} - \chi_i(1-\chi_j)\nu_0^{j\to i} \exp\Big\{\Big[-E_{\mathrm{a}}^{j\to i}/k_{\mathrm{B}}T\Big]\Big\}\Big\} + \frac{\bar{v}_{\mathrm{disl}}}{a/2}[\chi_{j+} - \chi_i], \tag{5.16}$$

where χ_i, is the occupancy of a particular carbon site, $E_{\mathrm{a}}^{j\to i}$, is the migration barrier of carbon from site j to site i, ν_0 is the associated attempt frequency. The summation is over the four nearest sites available for carbon to diffuse to. The last term in equation (5.16), is a convection term, allowing concentrations to change upon a dislocation moving with average velocity $\bar{v}_{\mathrm{disl}}$. We use the convention of a dislocation moving along the positive x-axis; as such, χ_{j+} is the occupation of a site to the right of site i the dislocation, which is biased to move towards the χ_i upon dislocation movement, and similarly site i will move the the $j-$ site, to the left of the dislocation.

In the paper of Gong *et al.* [238], the diffusion model has a different form. The occupancy of carbon is taken as a proportion of the difference between the limiting cases of dislocation movement: slow dislocation movement, where carbon is able to equilibriate with the dislocation, and fast dislocation movement, where carbon occupancies are fixed. This has the form of

$$\frac{\partial \chi_i}{\partial t} = \bar{v}_{\text{disl}} \frac{\partial \chi_i}{\partial x} = \left(\chi_i^e(x) - \chi_i(x, \bar{v})\right) \nu_0^{\text{solute escape}} \exp\{-E_i(r)/k_{\text{B}}T\}, \tag{5.17}$$

where χ_i^e is the equilibrium occupancy of site i, χ_i is the true occupancy of the site, which is solved for, $\nu_0^{\text{solute escape}}$ is the attempt frequency for carbon to escape the solute atmosphere, and $E_i(r)$ is the *binding* energy of carbon to the i^{th} site, which has been parameterised by a dependence on the distance from the dislocation core r. This equation can be solved self-consistently with

$$\bar{v}_{\text{disl}}(H_{\text{k}}) = h\nu_{\text{k}}^0 \exp\left(-H_{\text{k}}(C_{\text{C}}, \sigma, \bar{v}_{\text{disl}})/k_{\text{B}}T\right), \tag{5.18}$$

where $h = a\sqrt{2/3}$ is the distance between two Peierls valleys, $\nu_{\text{k}}^0 = 2.31 \times 10^9 \text{s}^{-1}$ is the attempt frequency for stable kink-pair formation, which is fit to obtain the measured dislocation velocity in pure Fe, and H_{k} is the kink-pair formation enthalpy at a given carbon concentration, stress and average dislocation velocity.

One could extend the SCkMC model to include the discrete diffusion model of carbon into different sites around the dislocation, using the attempt frequencies of the various diffusion barriers calculated. The steps being

1. Assume an initial H_k
2. Calculate the the dislocation velocity $\bar{v}_{\text{disl}}(H_{\text{k}})$ using equation (5.18).
3. Solve for the occupancies of the sites in equation (5.16).
4. Calculate the kink-pair formation enthalpy $H_k(C_{\text{C}}, \sigma, \bar{v}_{\text{disl}})$ using the string/NEB method.

5.6 Conclusion

Dislocation-assisted carbon migration is thought to be a viable mechanism by which martensite decays to form DER regions—areas composed mostly of ferrite interspersed in a martensitic matrix—which enhances failure risk by RCF. There is dispute over where excess carbon from the martensitic matrix finds itself upon transformation to ferrite, of much lower carbon solubility. The current leading mechanism suggests carbon segregates to pre-existing carbides, yet experimental results show in the late stages of DER formation, pre-existing carbides are partially dissolved in areas of highly

localized plasticity, implying segregation of carbon to dislocations. As such, a thorough investigation of carbon-dislocation interactions is vital to understanding how DER initially forms and progresses.

In this chapter, the preliminary work for an SCkMC model, which can be used to investigate carbon can migrate with dislocations has been achieved: tight-binding atomistic calculations were used to obtain carbon-dislocation binding energies for both screw core configurations, the 2d Peierls potential, and line-tension parameters, which were necessary for a line-tension model of a dislocation, from which one could obtain the kink-pair formation enthalpy of screw dislocations in the limit of fast glide in the dilute carbon limit, and in the limit of slow glide at equilibrium concentrations, thereby simulating carbon migration. Tight-binding calculations were also used to find carbon migration barriers around hard core, which were greatly reduced, as in the easy core, thereby giving weight to a mechanism for dislocation-assisted carbon migration by carbon diffusing with the dislocation in the direction of dislocation motion.

The Peierls potential found by tight-binding gave characteristics comparable to both EAM/DFT results. Carbon distribution around the easy and hard cores were found to differ significantly, with the largest binding energy being found by carbon being situated in a prismatic site in the hard core. Carbon within 3Å of the easy core caused reconstruction to the hard core, with carbon in a prismatic site. The carbon-dislocation binding energies decrease with distance, and are in good agreement with the literature.

Equilibrium carbon concentration calculations around the hard/easy cores at normal operating temperatures and dislocation densities suggest that *all dislocations are of hard core type* with carbon situated in an H1/prismatic site, with reconstruction of all easy core dislocations to hard core, resulting in all dislocations being pinned. Therefore in bearing steels, one predicts that all the cores are saturated, showing that dislocations can indeed act as a reservoir for carbon during DER development.

One can determine what happens in the two limiting cases of dislocation velocity, where dislocation speed is much greater than that of carbon diffusion, and where dislocation speed is slow compared to carbon diffusion.

In the former limit, the limit of fast glide, if there is sufficient stress, a dislocation can escape the hard core, equilibrium ground state—where it is pinned by carbon—and move to adjacent easy/hard core positions. Throughout the transition, it experiences a large drag force from the strong binding energy of prismatic carbon to the dislocation. Once it has escaped the environment of carbon, one finds, by calculation of

the kink-pair formation enthalpy, that if a single carbon is found ahead of the dislocation, then the solute-enhanced localised plasticity effect, due to the reduction of the kink-pair formation enthalpy, is surprisingly subtle, due to the long range of its interaction. There is a kink-trapping effect which hinders the migration of kinks along the dislocation line, which is found to be much stronger for the hard core than the easy core.

Allowing for carbon to equilibriate between trap sites, in the limit of slow glide relative to carbon migration, we see the average kink-pair formation enthalpy decreases significantly upon stabilisation of the hard core, with an expected increase in the kink-pair formation enthalpy for carbon concentrations greater than 20 appm. A self-consistent method is necessary to obtain more accurate estimates of the kink-pair formation enthalpy and average dislocation velocity with carbon concentration.

Through diffusion barrier calculations of carbon around the hard core, one confirms that there is indeed sufficient reduction of some migration barriers in the vicinity of the hard core which allows for carbon to move with dislocations in normal operating temperatures, proving that a dislocation-assisted carbon migration mechanism is a feasible mechanism for DER formation. Carbon is able to stay ahead of the dislocation due to the H2 $\rightarrow$ H7 transition, which allows for a consistent, albeit reasonably subtle, carbon-enhanced localised plasticity effect. Other sites around and behind the dislocation also allow for carbon to stay with the dislocation: the H2 $\leftrightarrow$ H7 and H3 $\leftrightarrow$ H5 transitions.

The reduction of these barriers explain the softening effect of carbon between 150 to 300K, due to the activation of the lower carbon diffusion barriers, allowing for a reduction in the kink-pair formation enthalpy.

From these results, one has demonstrated the applicability of simple tight-binding models to describe and validate fundamental mechanisms in iron, with the limits of scalability and feasible computational time being shown by the dislocation/diffusion barrier calculations. This work allows for the construction of an advanced SCkMC model, which simulates the movement of dislocations by kink-pair formation, and carbon diffusion by a discrete diffusion model. The dislocation velocity and concentration of carbon arising from the discrete diffusion model—explicitly simulating carbon migration—would be solved self-consistently, giving rise to well-informed predictions of how and where carbon is situated during thermally-activated movement of dislocations at different nominal concentrations, stresses and temperatures. These can provide predictions of flow stress and dislocation configurations with carbon content.

Chapter 6

Conclusion

In this thesis, an exhibition of what can be achieved with simple tight-binding models, in terms of both scale and transferability, has been shown through an investigation of defects in metals.

The parameterisations achieved in this thesis push the limits of transferability, allowing for many novel simulations with multiple phases. The models were fit without the need for vast quantities of *ab-inito* data—as would be necessary in modern data-driven approaches—while explicitly describing quantum mechanical bonding and phenomena, unlike empirical descriptions.

Scalability of the models was exhibited by investigation of fundamental hardening mechanisms of oxygen in titanium, and dislocation-assisted carbon migration/carbon-induced softening in iron. This necessitated large simulation cells such that one could obtain accurate core structure resolution in reaction to solutes. The simulations were at the limits of scale in tight-binding, both in terms of: size, where $\sim$ 1000 atoms were used to simulate dislocations in titanium; and in time, where more than 10^6 core hours of time were necessary to ascertain the diffusion barriers of carbon around the hard screw dislocation core in iron.

The central points pertaining to titanium are as follows.

- The first self-consistent polarisable-ion tight-binding model which can describe bulk Ti along with TiO_2, TiH_2, H_2 and H_2O was successfully created.
- This model gave cohesive energies of rutile TiO_2 and fluorite TiH_2 in agreement with DFT, in addition to titanium cohesive energies commensurate with experiment, allowing for comparable solution energies of H and O in bulk Ti to DFT.

- The first tight-binding simulations of water on titanium found that the model was stable under NVT molecular dynamics. Water was found to dissociate on the titanium surface, forming a H^- ion which penetrated the metal and an OH group which adsorbed on the surface.
- The morphology of γ-surfaces in hcp Ti was in accordance with DFT, with the *d*-model showing the correct energetic ordering of stable stacking faults for the basal and prismatic planes.
- Investigation of dislocations in titanium gave dissociations of the $\langle a \rangle$ screw dislocation in agreement with experimental observations of screw dislocation glide and some DFT core structures. This is the first modern tight-binding model to do so. Furthermore, the Peierls stress on the prismatic plane was in agreement with experiment.
- Oxygen-screw dislocation interactions were found to be repulsive, causing the generation of jogs on the dislocation line, as found in DFT and experimental observations. These jogs explain the origin of the dramatic increase in yield strength with oxygen content in titanium due to the pinning of dislocations.
- The prediction of a new mechanism of jog formation was seen in tight-binding, due to oxygen interacting with the dislocation out of the prismatic glide plane, which is commensurate with *ab-initio* calculations. This could explain the prevalence of slip planarity with oxygen content more satisfactorily than the interstitial shuffling mechanism.
- Estimation of oxygen-jog interactions show it is preferable for oxygen to bind to the jogs upon formation, inhibiting jog-dipole annihilation and further pinning the dislocation by bound oxygen. This can be important in the modelling of creep in titanium, which is theorised to be controlled by jogged screw dislocations.
- The glide of screw dislocations in titanium is likely governed by a locking-unlocking mechanism, where a sessile pyramidal core is the ground-state, and glide occurs by transition to a glissile metastable prismatic core. But errors apparent in core energies from atomistic calculations still leave the true ground-state core structure in question.

The main results pertaining to iron are as follows.

- Investigation of carbon in bcc iron found a reconstruction of the easy screw core to a hard screw core, in agreement with DFT. This has not been shown in empirical potentials, demonstrating the necessity of a quantum mechanical description of bonding for dislocation-solute interactions in iron.
- A thermodynamical mean-field model showed that most cores in iron, for a wide range of operating temperatures, are the *hard* core, even in high-purity iron.
- A line-tension model parameterised on atomistic data found increases in carbon content caused a reduction in the kink-pair formation enthalpy, in the limit of slow glide.
- Migration barriers of carbon around the hard screw dislocation core were found to be reduced, resulting in the discovery of diffusion mechanisms allowing carbon to keep up with dislocations upon glide.
- The average velocity of carbon around the dislocation, in the range of bearing operation temperatures, was shown to be greater than the average dislocation velocity due to these reduced barriers.
- This validates the feasibility of a dislocation-assisted carbon migration mechanism to explain dark-etching region formation in bearing steels. This effect could further explain the origin of the softening effect of carbon in iron.
- The data generated from these atomistic simulations can form the basis of an SCkMC model of dislocation glide, incorporating carbon diffusion. From such a model, one can ascertain the regimes of temperature, stress and carbon concentration in which carbon can keep up with dislocations, and the dislocation networks which result.

There is scope for more research with the models created/used here. The combined Ti, TiO_2, TiH_2, H_2O and H_2 model has many applications. The interface structure between titanium and its oxide and hydride is of interest. The structure of water on the surface of titanium/titanium dioxide/titanium hydride can be discerned. Electrochemical simulations involving titanium electrodes could be achieved using "hairy probes" [259]. The plasticity of titanium could be investigated further, with the exploration of edge dislocation-oxygen interactions, which would be useful in creep modelling. In addition, diffusion barriers around the core can be determined, to see if they are reduced in the vicinity of screw/edge cores, allowing for kMC models of

dislocation glide/diffusion. Novel stress-corrosion cracking simulations of titanium by oxygen can be attempted. With application of an $\mathcal{O}(N)$ bond-order potential scheme, scalability can be greatly enhanced, allowing for simulations of grain/twin boundaries, dislocation loops and dislocation pile-ups in titanium.

With the iron-carbon model, the effect carbon and its pinning of edge dislocations at higher temperatures in iron [48] could be explored by calculation of edge dislocation-carbon binding energies. The Peierls potential for edge dislocations can be determined allowing for line-tension modelling, as has been achieved here for screw dislocations. The SCkMC can be extended with the explicit inclusion of attempt frequencies and diffusion barriers of carbon around dislocations, as detailed.

References

[1] D. Banerjee and J. Williams, "Perspectives on Titanium Science and Technology," *Acta Materialia*, vol. 61, pp. 844–879, Feb. 2013.

[2] S. Kadkhodaei, Q.-J. Hong, and A. van de Walle, "Free energy calculation of mechanically unstable but dynamically stabilized bcc titanium," *Physical Review B*, vol. 95, p. 064101, Feb. 2017.

[3] D. R. Trinkle, R. G. Hennig, S. G. Srinivasan, D. M. Hatch, M. D. Jones, H. T. Stokes, R. C. Albers, and J. W. Wilkins, "New Mechanism for the α to ω Martensitic Transformation in Pure Titanium," *Physical Review Letters*, vol. 91, p. 025701, July 2003.

[4] R. G. Hennig, D. R. Trinkle, J. Bouchet, S. G. Srinivasan, R. C. Albers, and J. W. Wilkins, "Impurities block the α to ω martensitic transformation in titanium," *Nature Materials*, vol. 4, pp. 129–133, Feb. 2005.

[5] Y. K. Vohra and P. T. Spencer, "Novel γ-Phase of Titanium Metal at Megabar Pressures," *Physical Review Letters*, vol. 86, pp. 3068–3071, Apr. 2001.

[6] Y. Akahama, H. Kawamura, and T. Le Bihan, "New delta (distorted-bcc) titanium to 220 GPa," *Physical Review Letters*, vol. 87, p. 275503, Dec. 2001.

[7] P. M. Anderson, J. P. Hirth, and J. Lothe, *Theory of Dislocations*. Cambridge: Cambridge University Press, 2017 edition ed., 2017.

[8] T. Furuhara and H. Aaronson, "Crystallography and interfacial structure of proeutectoid α grain boundary allotriomorphs in a hypoeutectoid TiCr alloy," *Acta Metallurgica et Materialia*, vol. 39, pp. 2887–2899, Nov. 1991.

[9] R. Sandala, *Deformation Mechanisms of Two-Phase Titanium Alloys*. The University of Manchester (United Kingdom), 2014.

[10] E. Schmid and W. Boas, *Kristallplastizität*. Berlin, Heidelberg: Springer Berlin Heidelberg, 1935.

[11] A. Argon, *Strengthening Mechanisms in Crystal Plasticity*. Oxford University Press, Aug. 2007.

[12] S. Naka, A. Lasalmonie, P. Costa, and L. P. Kubin, "The low-temperature plastic deformation of α-titanium and the core structure of a-type screw dislocations," *Philosophical Magazine A*, vol. 57, pp. 717–740, May 1988.

[13] M. Šob, "Sessile Splittings of Screw Dislocations in H.C.P. Metals," *Physica Status Solidi (a)*, vol. 24, pp. K133–K136, Aug. 1974.

[14] A. Akhtar, "Basal slip and twinning in α-titanium single crystals," *Metallurgical Transactions A*, vol. 6, pp. 1105–1113, May 1975.

[15] B. Barkia, J. Couzinié, S. Lartigue-Korinek, I. Guillot, and V. Doquet, "In situ TEM observations of dislocation dynamics in α titanium: Effect of the oxygen content," *Materials Science and Engineering: A*, vol. 703, pp. 331–339, Aug. 2017.

[16] D. Caillard and J.-L. Martin, *Thermally Activated Mechanisms in Crystal Plasticity*. No. 8 in Pergamon Materials Series, Amsterdam ; Boston, Mass: Pergamon, 2003.

[17] S. Farenc, D. Caillard, and A. Couret, "A new model for the peak of activation area of α titanium," *Acta Metallurgica et Materialia*, vol. 43, pp. 3669–3678, Oct. 1995.

[18] S. Farenc, D. Caillard, and A. Couret, "An in situ study of prismatic glide in α titanium at low temperatures," *Acta Metallurgica et Materialia*, vol. 41, pp. 2701–2709, Sept. 1993.

[19] E. Clouet, D. Caillard, N. Chaari, F. Onimus, and D. Rodney, "Dislocation locking versus easy glide in titanium and zirconium," *Nature Materials*, vol. 14, pp. 931–936, Sept. 2015.

[20] E. D. Levine, "Deformation mechanisms in titanium at low temperatures," vol. 236, no. 11, pp. 1558–1565, 1966.

[21] A. Akhtar and E. Teghtsoonian, "Prismatic slip in α-titanium single crystals," *Metallurgical Transactions A*, vol. 6, p. 2201, Dec. 1975.

[22] M. P. Biget and G. Saada, "Low-temperature plasticity of high-purity α-titanium single crystals," *Philosophical Magazine A*, vol. 59, pp. 747–757, Apr. 1989.

[23] R. Symposium on Internal Stresses and Fatigue in Metals, Gerald Mark and W. L. Grube, eds., *Internal Stresses and Fatigue in Metals; Proceedings.* Amsterdam; New York: Elsevier Pub. Co., 1959.

[24] J. C. Williams, A. W. Sommer, and P. P. Tung, "The influence of oxygen concentration on the internal stress and dislocation arrangements in α titanium," *Metallurgical and Materials Transactions B*, vol. 3, pp. 2979–2984, Nov. 1972.

[25] R. Orawa, "On the deformation mechanisms in alpha-titanium below 0.4 Tm," *Scripta Metallurgica*, vol. 1, pp. 153–156, Dec. 1967.

[26] Q. Yu, L. Qi, T. Tsuru, R. Traylor, D. Rugg, J. W. Morris, M. Asta, D. C. Chrzan, and A. M. Minor, "Origin of dramatic oxygen solute strengthening effect in titanium," *Science*, vol. 347, pp. 635–639, Feb. 2015.

[27] H. Conrad, "Effect of interstitial solutes on the strength and ductility of titanium," *Progress in Materials Science*, vol. 26, pp. 123–403, Jan. 1981.

[28] Y. Chong, M. Poschmann, R. Zhang, S. Zhao, M. S. Hooshmand, E. Rothchild, D. L. Olmsted, J. W. Morris, D. C. Chrzan, M. Asta, and A. M. Minor, "Mechanistic basis of oxygen sensitivity in titanium," *Science Advances*, vol. 6, p. eabc4060, Oct. 2020.

[29] R. L. Fleischer, "Solution hardening by tetragonal dist ortions: Application to irradiation hardening in F.C.C. crystals," *Acta Metallurgica*, vol. 10, pp. 835–842, Sept. 1962.

[30] G. Leyson and W. Curtin, "Friedel vs. Labusch: The strong/weak pinning transition in solute strengthened metals," *Philosophical Magazine*, vol. 93, pp. 2428–2444, July 2013.

[31] E. Conforto, I. Guillot, and X. Feaugas, "Solute hydrogen and hydride phase implications on the plasticity of zirconium and titanium alloys: A review and some recent advances," *Philosophical Transactions of the Royal Society A: Mathematical, Physical and Engineering Sciences*, vol. 375, p. 20160417, July 2017.

[32] Churchman, "The slip modes of titanium and the effect of purity on their occurrence during tensile deformation of single crystals," *Proceedings of the Royal Society of London. Series A. Mathematical and Physical Sciences*, vol. 226, pp. 216–226, Nov. 1954.

[33] S. Zaefferer, "A study of active deformation systems in titanium alloys: Dependence on alloy composition and correlation with deformation texture," *Materials Science and Engineering: A*, vol. 344, pp. 20–30, Mar. 2003.

[34] S. Ooi, J. Lai, S. Restrepo, E. Vegter, and Y. Rose, "Dark etching regions under rolling contact fatigue: A review," 2019.

[35] H. Fu, E. Galindo-Nava, and P. Rivera-Díaz-del-Castillo, "Modelling and characterisation of stress-induced carbide precipitation in bearing steels under rolling contact fatigue," *Acta Materialia*, vol. 128, pp. 176–187, Apr. 2017.

[36] "Microstructural Alterations in Rolling Contact Fatigue," in *Advances in Electron Metallography: Vol. 6* (B. R. Banerjee, ed.), pp. 74–74–15, 100 Barr Harbor Drive, PO Box C700, West Conshohocken, PA 19428-2959: ASTM International, Jan. 1966.

[37] A. B. Jones, "Metallographic Observations of Ball Bearing Fatigue Phenomena," in *Symposium on Testing of Bearings* (Administrative Committee on Simulated Service Testing, ed.), pp. 35–35–18, 100 Barr Harbor Drive, PO Box C700, West Conshohocken, PA 19428-2959: ASTM International, Jan. 1947.

[38] J. J. Bush and W. L. Grube, "Microstructural, microhardness and residual stress changes due to rolling contact," *Tribology*, vol. 3, p. 249, Nov. 1970.

[39] H. Swahn, P. C. Becker, and O. Vingsbo, "Martensite decay during rolling contact fatigue in ball bearings," *Metallurgical Transactions A*, vol. 7, pp. 1099–1110, Aug. 1976.

[40] T. Taoka, S. Takeuchi, and E. Furubayashi, "Slip Systems and Their Critical Shear Stress in 3% Silicon Iron," *Journal of the Physical Society of Japan*, vol. 19, pp. 701–711, May 1964.

[41] B. Šesták and N. Zárubová, "Asymmetry of Slip in Fe-Si Alloy Single Crystals," *physica status solidi (b)*, vol. 10, no. 1, pp. 239–250, 1965.

[42] A. Argon and S. Maloof, "Plastic deformation of tungsten single crystals at low temperatures," *Acta Metallurgica*, vol. 14, pp. 1449–1462, Nov. 1966.

[43] D. K. Bowen, J. M. Capus, and C. E. Silverstone, "Plastic flow of martensite," *Philosophical Magazine*, vol. 15, pp. 1041–1044, May 1967.

[44] M. Duesbery and V. Vitek, "Plastic anisotropy in b.c.c. transition metals," *Acta Materialia*, vol. 46, pp. 1481–1492, Mar. 1998.

[45] D. Quesnel, A. Sato, and M. Meshii, "Solution softening and hardening in the IronCarbon system," *Materials Science and Engineering*, vol. 18, pp. 199–208, Apr. 1975.

[46] D. Brunner and J. Diehl, "The Effect of Atomic Lattice Defects on the Softening Phenomena of High-Purity α-Iron," *physica status solidi (a)*, vol. 160, pp. 355–372, Apr. 1997.

[47] E. Kuramoto, Y. Aono, and K. Kitajima, "Thermally activated slip deformation of high purity iron single crystals between 4.2 K and 300 K," *Scripta Metallurgica*, vol. 13, pp. 1039–1042, Nov. 1979.

[48] D. Caillard, "An in situ study of hardening and softening of iron by carbon interstitials," *Acta Materialia*, vol. 59, pp. 4974–4989, July 2011.

[49] A. H. Cottrell and B. A. Bilby, "Dislocation Theory of Yielding and Strain Ageing of Iron," *Proceedings of the Physical Society. Section A*, vol. 62, pp. 49–62, Jan. 1949.

[50] V. Šmeļova, A. Schwedt, L. Wang, W. Holweger, and J. Mayer, "Electron microscopy investigations of microstructural alterations due to classical Rolling Contact Fatigue (RCF) in martensitic AISI 52100 bearing steel," *International Journal of Fatigue*, vol. 98, pp. 142–154, May 2017.

[51] H. Fu, W. Song, E. I. Galindo-Nava, and P. E. Rivera-Díaz-del-Castillo, "Strain-induced martensite decay in bearing steels under rolling contact fatigue: Modelling and atomic-scale characterisation," *Acta Materialia*, vol. 139, pp. 163–173, Oct. 2017.

[52] A. Warhadpande, F. Sadeghi, and R. D. Evans, "Microstructural Alterations in Bearing Steels under Rolling Contact Fatigue Part 1—Historical Overview," *Tribology Transactions*, vol. 56, pp. 349–358, May 2013.

[53] A. Warhadpande, F. Sadeghi, and R. D. Evans, "Microstructural Alterations in Bearing Steels under Rolling Contact Fatigue: Part 2—Diffusion-Based Modeling Approach," *Tribology Transactions*, vol. 57, pp. 66–76, Jan. 2014.

[54] E. L. Simpson, *A Tight Binding Study of Dislocations in Iron and Their Interaction with Hydrogen*. PhD thesis, King's College London, 2018.

[55] E. L. Simpson and A. T. Paxton, "Effect of applied strain on the interaction between hydrogen atoms and 1 2 ⟨ 111 ⟩ screw dislocations in α-iron," *International Journal of Hydrogen Energy*, vol. 45, pp. 20069–20079, July 2020.

[56] G. A. Nematollahi, B. Grabowski, D. Raabe, and J. Neugebauer, "Multiscale description of carbon-supersaturated ferrite in severely drawn pearlitic wires," *Acta Materialia*, vol. 111, pp. 321–334, June 2016.

[57] L. Proville, D. Rodney, and M.-C. Marinica, "Quantum effect on thermally activated glide of dislocations," *Nature Materials*, vol. 11, pp. 845–849, Oct. 2012.

[58] R. Hulse and C. Race, "An Atomistic Modelling Study of the Properties of Dislocation Loops in Zirconium," *Journal of Nuclear Materials*, vol. 546, p. 152752, Apr. 2021.

[59] N. Mardirossian and M. Head-Gordon, "Thirty years of density functional theory in computational chemistry: An overview and extensive assessment of 200 density functionals," *Molecular Physics*, vol. 115, pp. 2315–2372, Oct. 2017.

[60] S. G. Louie and M. S. Hybertsen, "Theory of quasiparticle energies: Band gaps and excitation spectra in solids," *International Journal of Quantum Chemistry*, vol. 32, pp. 31–44, Mar. 1987.

[61] P. Mori-Sánchez, A. J. Cohen, and W. Yang, "Localization and Delocalization Errors in Density Functional Theory and Implications for Band-Gap Prediction," *Physical Review Letters*, vol. 100, p. 146401, Apr. 2008.

[62] M. S. Daw and M. I. Baskes, "Embedded-atom method: Derivation and application to impurities, surfaces, and other defects in metals," *Physical Review B*, vol. 29, pp. 6443–6453, June 1984.

[63] M. W. Finnis and J. E. Sinclair, "A simple empirical N -body potential for transition metals," *Philosophical Magazine A*, vol. 50, pp. 45–55, July 1984.

[64] M. I. Baskes, "Modified embedded-atom potentials for cubic materials and impurities," *Physical Review B*, vol. 46, pp. 2727–2742, Aug. 1992.

[65] S. M. Rassoulinejad-Mousavi and Y. Zhang, "Interatomic Potentials Transferability for Molecular Simulations: A Comparative Study for Platinum, Gold and Silver," *Scientific Reports*, vol. 8, p. 2424, Feb. 2018.

[66] A. P. Bartók and G. Csányi, "Gaussian Approximation Potentials: A brief tutorial introduction," *arXiv:1502.01366 [cond-mat, physics:physics]*, Feb. 2020.

[67] A. P. Bartók, R. Kondor, and G. Csányi, "On representing chemical environments," *Physical Review B*, vol. 87, p. 184115, May 2013.

[68] A. P. Bartók, M. C. Payne, R. Kondor, and G. Csányi, "Gaussian Approximation Potentials: The Accuracy of Quantum Mechanics, without the Electrons," *Physical Review Letters*, vol. 104, p. 136403, Apr. 2010.

[69] A. P. Bartók, J. Kermode, N. Bernstein, and G. Csányi, "Machine Learning a General-Purpose Interatomic Potential for Silicon," *Physical Review X*, vol. 8, p. 041048, Dec. 2018.

[70] R. Drautz, "Atomic cluster expansion for accurate and transferable interatomic potentials," *Physical Review B*, vol. 99, p. 014104, Jan. 2019.

[71] R. Drautz, "Atomic cluster expansion of scalar, vectorial, and tensorial properties including magnetism and charge transfer," *Physical Review B*, vol. 102, p. 024104, July 2020.

[72] N. Chaari, E. Clouet, and D. Rodney, "First-Principles Study of Secondary Slip in Zirconium," *Physical Review Letters*, vol. 112, p. 075504, Feb. 2014.

[73] N. Chaari, E. Clouet, and D. Rodney, "First order pyramidal slip of 1/3 <1-210> screw dislocations in zirconium," *Metallurgical and Materials Transactions A*, vol. 45, pp. 5898–5905, Dec. 2014.

[74] N. Chaari, D. Rodney, and E. Clouet, "Oxygen - Dislocation interaction in zirconium from first principles," *Acta Materialia*, vol. 132, pp. 416–424, June 2017.

[75] N. Chaari, D. Rodney, and E. Clouet, "Oxygen-dislocation interaction in titanium from first principles," *Scripta Materialia*, vol. 162, pp. 200–203, Mar. 2019.

[76] M. Itakura, H. Kaburaki, and M. Yamaguchi, "First-principles study on the mobility of screw dislocations in bcc iron," *Acta Materialia*, vol. 60, pp. 3698–3710, May 2012.

[77] M. Itakura, H. Kaburaki, M. Yamaguchi, and T. Okita, "The effect of hydrogen atoms on the screw dislocation mobility in bcc iron: A first-principles study," *Acta Materialia*, vol. 61, pp. 6857–6867, Oct. 2013.

[78] M. Aoki, A. P. Horsfield, and D. G. Pettifor, "Tight-binding bond order potential a forces for atomistic simulations," *Journal of Phase Equilibria*, vol. 18, pp. 614–623, Dec. 1997.

[79] D. Nguyen-Manh, D. G. Pettifor, D. J. H. Cockayne, M. Mrovec, S. Znam, and V. Vitek, "Environmentally dependent bond-order potentials: New developments and applications," *Bulletin of Materials Science*, vol. 26, pp. 43–51, Jan. 2003.

[80] A. P. Horsfield, A. M. Bratkovsky, M. Fearn, D. G. Pettifor, and M. Aoki, "Bond-order potentials: Theory and implementation," *Physical Review B*, vol. 53, pp. 12694–12712, May 1996.

[81] M. Finnis, *Interatomic Forces in Condensed Matter*. Oxford University Press, Oct. 2003.

[82] R. M. Martin, *Electronic Structure: Basic Theory and Practical Methods*. Cambridge University Press, first ed., Apr. 2004.

[83] O. Madelung, *Introduction to Solid-State Theory*, vol. 2 of *Springer Series in Solid-State Sciences*. Berlin, Heidelberg: Springer Berlin Heidelberg, 1978.

[84] W. A. Harrison, *Electronic Structure and the Properties of Solids: The Physics of the Chemical Bond*. New York: Dover Publications, dover ed ed., 1989.

[85] E. Pavarini, E. Koch, F. Anders, M. Jarrell, Institute for Advanced Simulation, and German Research School for Simulation Sciences, eds., *Correlated Electrons: From Models to Materials: Lecture Notes of the Autumn School Correlated Electrons 2012: At Forschungszentrum Jülich, 3-7 September 2012*. No. Band 2 in Schriften Des Forschungszentrums Jülich. Reihe Modeling and Simulation, Jülich: Forschungszentrum Jülich, Zentralbibliothek, Verl, 2012.

[86] P. Hohenberg and W. Kohn, "Inhomogeneous Electron Gas," *Physical Review*, vol. 136, pp. B864–B871, Nov. 1964.

[87] W. Kohn and L. J. Sham, "Exchange and Correlation Effects in an Inhomogeneous Electron Gas," tech. rep., Defense Technical Information Center, Fort Belvoir, VA, May 1965.

[88] M. Levy, "Universal variational functionals of electron densities, first-order density matrices, and natural spin-orbitals and solution of the v -representability problem," *Proceedings of the National Academy of Sciences*, vol. 76, pp. 6062–6065, Dec. 1979.

[89] A. T. Paxton, "An introduction to the tight binding approximation— implementation by diagonalisation," tech. rep., 2009.

[90] A. P. Sutton, M. W. Finnis, D. G. Pettifor, and Y. Ohta, "The tight-binding bond model," *Journal of Physics C: Solid State Physics*, vol. 21, pp. 35–66, Jan. 1988.

[91] J. C. Slater and G. F. Koster, "Simplified LCAO Method for the Periodic Potential Problem," *Physical Review*, vol. 94, pp. 1498–1524, June 1954.

[92] F. R. Boer and D. G. Pettifor, *The Structures of Binary Compounds*. No. v. 2 in Cohesion and Structure, Amsterdam New York: North-Holland Sole distributors for the USA and Canada, Elsevier Science Pub. Co, 1989.

[93] L. E. Ballentine and M. Kolar, "Recursion, non-orthogonal basis vectors, and the computation of electronic properties," *Journal of Physics C: Solid State Physics*, vol. 19, pp. 981–993, Mar. 1986.

[94] G. Bester and M. Fähnle, "Interpretation of *ab initio* total energy results in a chemical language: I. Formalism and implementation into a mixed-basis pseudopotential code," *Journal of Physics: Condensed Matter*, vol. 13, pp. 11541–11550, Dec. 2001.

[95] D. G. Pettifor, "Theory of energy bands and related properties of 4d transition metals : I. Band parameters and their volume dependence," p. 22, 1976.

[96] D. G. Pettifor, "Theory of energy bands and related properties of 4d transition metals. III. s and d contributions to the equation of state," *Journal of Physics F: Metal Physics*, vol. 8, pp. 219–230, Feb. 1978.

[97] J. Smutna, R. M. Fogarty, M. R. Wenman, and A. P. Horsfield, "Systematic development of *ab initio* tight-binding models for hexagonal metals," *Physical Review Materials*, vol. 4, p. 043801, Apr. 2020.

[98] H. Hasegawa and D. G. Pettifor, "Microscopic Theory of the Temperature-Pressure Phase Diagram of Iron," *Physical Review Letters*, vol. 50, pp. 130–133, Jan. 1983.

[99] H. Hasegawa, "A spin fluctuation theory of degenerate narrow bands-finite-temperature magnetism of iron," *Journal of Physics F: Metal Physics*, vol. 13, pp. 1915–1929, Sept. 1983.

[100] E. C. Stoner, "LXXX. *Atomic moments in ferromagnetic metals and alloys with non-ferromagnetic elements*," *The London, Edinburgh, and Dublin Philosophical Magazine and Journal of Science*, vol. 15, pp. 1018–1034, May 1933.

[101] Stoner, "Collective electron ferromagnetism II. Energy and specific heat," *Proceedings of the Royal Society of London. Series A. Mathematical and Physical Sciences*, vol. 169, pp. 339–371, Feb. 1939.

[102] G. Liu, D. Nguyen-Manh, B.-G. Liu, and D. G. Pettifor, "Magnetic properties of point defects in iron within the tight-binding-bond Stoner model," *Physical Review B*, vol. 71, p. 174115, May 2005.

[103] A. T. Paxton and M. W. Finnis, "Magnetic tight binding and the iron-chromium enthalpy anomaly," *Physical Review B*, vol. 77, p. 024428, Jan. 2008.

[104] D. G. Pettifor, *Bonding and Structure of Molecules and Solids*. Oxford : New York: Clarendon Press ; Oxford University Press, 1995.

[105] H. Hellmann, "Einführung in die Quantenchemie," in *Hans Hellmann: Einführung in die Quantenchemie* (D. Andrae, ed.), pp. 19–376, Berlin, Heidelberg: Springer Berlin Heidelberg, 2015.

[106] R. P. Feynman, "Forces in Molecules," *Physical Review*, vol. 56, pp. 340–343, Aug. 1939.

[107] E. L. Simpson, "A Tight Binding Study of Dislocations in Iron and Their Interaction with Hydrogen," p. 230.

[108] H. Eyring, "The Activated Complex in Chemical Reactions," *The Journal of Chemical Physics*, vol. 3, pp. 107–115, Feb. 1935.

[109] G. H. Vineyard, "Frequency factors and isotope effects in solid state rate processes," *Journal of Physics and Chemistry of Solids*, vol. 3, pp. 121–127, Jan. 1957.

[110] G. Henkelman, B. P. Uberuaga, and H. Jónsson, "A climbing image nudged elastic band method for finding saddle points and minimum energy paths," *The Journal of Chemical Physics*, vol. 113, pp. 9901–9904, Dec. 2000.

[111] W. E, W. Ren, and E. Vanden-Eijnden, "String method for the study of rare events," *Physical Review B*, vol. 66, p. 052301, Aug. 2002.

[112] W. E, W. Ren, and E. Vanden-Eijnden, "Simplified and improved string method for computing the minimum energy paths in barrier-crossing events," *The Journal of Chemical Physics*, vol. 126, p. 164103, Apr. 2007.

[113] S. Makri, C. Ortner, and J. R. Kermode, "A preconditioning scheme for minimum energy path finding methods," *The Journal of Chemical Physics*, vol. 150, p. 094109, Mar. 2019.

[114] A. P. Sutton, *Physics of Elasticity and Crystal Defects*. Oxford Series on Materials Modelling, Oxford ; New York, NY: Oxford University Press, first edition ed., 2020.

[115] A. N. Stroh, "Steady State Problems in Anisotropic Elasticity," *Journal of Mathematics and Physics*, vol. 41, pp. 77–103, Apr. 1962.

[116] M. I. Mendelev, S. Han, D. J. Srolovitz, G. J. Ackland, D. Y. Sun, and M. Asta, "Development of new interatomic potentials appropriate for crystalline and liquid iron," *Philosophical Magazine*, vol. 83, pp. 3977–3994, Dec. 2003.

[117] C. Domain, C. S. Becquart, and J. Foct, "*Ab Initio* study of foreign interstitial atom (C, N) interactions with intrinsic point defects in α -Fe," *Physical Review B*, vol. 69, p. 144112, Apr. 2004.

[118] D. R. Trinkle, M. D. Jones, R. G. Hennig, S. P. Rudin, R. C. Albers, and J. W. Wilkins, "Empirical tight-binding model for titanium phase transformations," *Physical Review B*, vol. 73, p. 094123, Mar. 2006.

[119] P. B. Legrand, "Relations entre la structure électronique et la facilité de glissement dans les métaux hexagonaux compacts," *Philosophical Magazine B*, vol. 49, pp. 171–184, Feb. 1984.

[120] P. B. Legrand, "Structure du coeur des dislocations vis $1/3\langle 11\ 2\ 0\rangle$ dans le titane," *Philosophical Magazine A*, vol. 52, pp. 83–97, July 1985.

[121] O. Jepsen, "Electronic structure and magnetic breakdown in titanium," *Physical Review B*, vol. 12, pp. 2988–2997, Oct. 1975.

[122] F. Ducastelle and F. Cyrot-Lackmann, "Moments developments and their application to the electronic charge distribution of d bands," *Journal of Physics and Chemistry of Solids*, vol. 31, pp. 1295–1306, June 1970.

[123] F. Ducastelle, "Modules élastiques des métaux de transition," *Journal de Physique*, vol. 31, no. 11-12, pp. 1055–1062, 1970.

[124] R. Haydock, V. Heine, and M. J. Kelly, "Electronic structure based on the local atomic environment for tight-binding bands," *Journal of Physics C: Solid State Physics*, vol. 5, pp. 2845–2858, Oct. 1972.

[125] A. Girshick, A. M. Bratkovsky, D. G. Pettifor, and V. Vitek, "Atomistic simulation of titanium. I. A bond-order potential," *Philosophical Magazine A*, vol. 77, pp. 981–997, Apr. 1998.

[126] A. Girshick, D. G. Pettifor, and V. Vitek, "Atomistic simulation of titanium. II. Structure of $\frac{1}{3}\ \langle\ 1\ 2\ 1\ 0\rangle$ screw dislocations and slip systems in titanium," *Philosophical Magazine A*, vol. 77, pp. 999–1012, Apr. 1998.

[127] D. R. Trinkle, "Private communications.," 2018.

[128] A. Urban, M. Reese, M. Mrovec, C. Elsässer, and B. Meyer, "Parameterization of tight-binding models from density functional theory calculations," *Physical Review B*, vol. 84, p. 155119, Oct. 2011.

[129] P.-O. Löwdin, "On the Non-Orthogonality Problem Connected with the Use of Atomic Wave Functions in the Theory of Molecules and Crystals," *The Journal of Chemical Physics*, vol. 18, pp. 365–375, Mar. 1950.

[130] A. Ferrari, M. Schröder, Y. Lysogorskiy, J. Rogal, M. Mrovec, and R. Drautz, "Phase transitions in titanium with an analytic bond-order potential," *Modelling and Simulation in Materials Science and Engineering*, vol. 27, p. 085008, Dec. 2019.

[131] P. Kwasniak and E. Clouet, "Basal slip of ⟨a⟩ screw dislocations in hexagonal titanium," *Scripta Materialia*, vol. 162, pp. 296–299, Mar. 2019.

[132] N. Tarrat, M. Benoit, and J. Morillo, "Core structure of screw dislocations in hcp Ti: An ab initio DFT study," *International Journal of Materials Research*, vol. 100, pp. 329–332, Mar. 2009.

[133] N. Tarrat, M. Benoit, D. Caillard, L. Ventelon, N. Combe, and J. Morillo, "Screw dislocation in hcp Ti : DFT dislocation excess energies and metastable core structures," *Modelling and Simulation in Materials Science and Engineering*, vol. 22, p. 055016, July 2014.

[134] C. M. Bishop, *Pattern Recognition and Machine Learning*. Information Science and Statistics, New York: Springer, 2006.

[135] T. Hastie, R. Tibshirani, and J. Friedman, *The Elements of Statistical Learning*. Springer Series in Statistics, New York, NY: Springer New York, 2009.

[136] A. Y. Lozovoi, D. L. Pashov, T. J. Sheppard, J. J. Kohanoff, and A. T. Paxton, "Universal tight binding model for chemical reactions in solution and at surfaces. III. Stoichiometric and reduced surfaces of titania and the adsorption of water," *The Journal of Chemical Physics*, vol. 141, p. 044505, July 2014.

[137] V. Heine, "$s\ensuremath{-}d$ Interaction in Transition Metals," *Physical Review*, vol. 153, pp. 673–682, Jan. 1967.

[138] V. Heine, "Electronic Structure from the Point of View of the Local Atomic Environment," in *Solid State Physics*, vol. 35, pp. 1–127, Elsevier, 1980.

[139] Andersen, O. and Jepsen, O. and Glötzel, D. and Bassani, F. and Fumi, F. and Tosi, M.P., "Canonical Description of the Band Structure of Metals," pp. 59–176, Jan. 1985.

[140] A. J. Skinner and D. G. Pettifor, "Transferability and the pair potential within the tight-binding bond model: An analytic study for hydrogen," *Journal of Physics: Condensed Matter*, vol. 3, pp. 2029–2047, Apr. 1991.

[141] A. T. Paxton and C. Elsässer, "Electronic structure and total energy of interstitial hydrogen in iron: Tight-binding models," *Physical Review B*, vol. 82, p. 235125, Dec. 2010.

[142] A. T. Paxton, A. P. Sutton, and C. M. M. Nex, "Structural stability of silicon in tight-binding models," *Journal of Physics C: Solid State Physics*, vol. 20, pp. L263–L269, May 1987.

[143] A. Paxton and A. Sutton, "A tight-binding study of grain boundaries in silicon," *Acta Metallurgica*, vol. 37, pp. 1693–1715, July 1989.

[144] A. Ferrari, M. Schröder, Y. Lysogorskiy, J. Rogal, M. Mrovec, and R. Drautz, "Phase transitions in titanium with an analytic bond-order potential," *Modelling and Simulation in Materials Science and Engineering*, vol. 27, p. 085008, Dec. 2019.

[145] D. Pashov, *Electronic Structure of Certain Titanium-Aluminium Superalloys: From First Principles to Bond Order Potentials*. Ph.D. Thesis, Queen's University Belfast, Belfast, 2012.

[146] D. Nguyen-Manh, D. G. Pettifor, and V. Vitek, "Analytic Environment-Dependent Tight-Binding Bond Integrals: Application to MoSi 2," *Physical Review Letters*, vol. 85, pp. 4136–4139, Nov. 2000.

[147] D. Pashov, S. Acharya, W. R. L. Lambrecht, J. Jackson, K. D. Belashchenko, A. Chantis, F. Jamet, and M. van Schilfgaarde, "Questaal: A package of electronic structure methods based on the linear muffin-tin orbital technique," *Computer Physics Communications*, vol. 249, p. 107065, Apr. 2020.

[148] B. Barzdajn, A. M. Garrett, T. M. Whiting, and C. P. Race, "Development of data-driven spd tight-binding models of Fe—parameterisation based on QSGW

and DFT calculations including information about higher-order elastic constants," *Modelling and Simulation in Materials Science and Engineering*, vol. 29, p. 085006, Dec. 2021.

[149] N. Hansen, Y. Akimoto, and P. Baudis, "CMA-ES/pycma on Github." Zenodo, DOI:10.5281/zenodo.2559634, Feb. 2019.

[150] N. Hansen, "The CMA Evolution Strategy: A Tutorial," *arXiv:1604.00772 [cs, stat]*, Apr. 2016.

[151] G. Jastrebski and D. Arnold, "Improving Evolution Strategies through Active Covariance Matrix Adaptation," in *2006 IEEE International Conference on Evolutionary Computation*, (Vancouver, BC, Canada), pp. 2814–2821, IEEE, 2006.

[152] N. Hansen, R. Ros, N. Mauny, M. Schoenauer, and A. Auger, "Impacts of invariance in search: When CMA-ES and PSO face ill-conditioned and non-separable problems," *Applied Soft Computing*, vol. 11, pp. 5755–5769, Dec. 2011.

[153] L. Fast, J. M. Wills, B. Johansson, and O. Eriksson, "Elastic constants of hexagonal transition metals: Theory," *Physical Review B*, vol. 51, pp. 17431–17438, June 1995.

[154] A. Girshick, D. G. Pettifor, and V. Vitek, "Atomistic simulation of titanium. II. Structure of $\frac{1}{3}\langle 1\ 2\ 1\ 0\rangle$ screw dislocations and slip systems in titanium," *Philosophical Magazine A*, vol. 77, pp. 999–1012, Apr. 1998.

[155] E. Clouet, "Screw dislocation in zirconium: An *ab initio* study," *Physical Review B*, vol. 86, p. 144104, Oct. 2012.

[156] C. S. G. Cousins, "Electrostatic contributions to the second- and third-order inner elastic constants of HCP metals for a range of axial ratios," *Journal of Physics C: Solid State Physics*, vol. 12, pp. 989–994, Mar. 1979.

[157] D. C. Wallace, *Thermodynamics of Crystals*. Mineola, N.Y: Dover Publications, 1998.

[158] J. F. Nye, *Physical Properties of Crystals: Their Representation by Tensors and Matrices*. Oxford [Oxfordshire] : New York: Clarendon Press ; Oxford University Press, 1st published in pbk. with corrections, 1984 ed., 1984.

[159] A. Togo and I. Tanaka, "First principles phonon calculations in materials science," *Scripta Materialia*, vol. 108, pp. 1–5, Nov. 2015.

[160] D. Rodney, L. Ventelon, E. Clouet, L. Pizzagalli, and F. Willaime, "Ab initio modeling of dislocation core properties in metals and semiconductors," *Acta Materialia*, vol. 124, pp. 633–659, Feb. 2017.

[161] B. Yin, Z. Wu, and W. Curtin, "Comprehensive first-principles study of stable stacking faults in hcp metals," *Acta Materialia*, vol. 123, pp. 223–234, Jan. 2017.

[162] M. Benoit, N. Tarrat, and J. Morillo, "Density functional theory investigations of titanium γ -surfaces and stacking faults," *Modelling and Simulation in Materials Science and Engineering*, vol. 21, p. 015009, Jan. 2013.

[163] A. Girshick, A. M. Bratkovsky, D. G. Pettifor, and V. Vitek, "Atomistic simulation of titanium. I. A bond-order potential," *Philosophical Magazine A*, vol. 77, pp. 981–997, Apr. 1998.

[164] S. Znám, *Bond Order Potentials for Atomistic Studies of Dislocations and Other Extended Defects in TiAl*. PhD thesis, University of Pennsylvania, 2001.

[165] A. J. Ready, A. P. Sutton, P. D. Haynes, and D. Rugg, "Stacking faults and the {\gamma}-surface on {1-101} pyramidal planes in {\alpha}-titanium," *arXiv:1608.00923 [cond-mat]*, Oct. 2016.

[166] B. Yin, Z. Wu, and W. Curtin, "Comprehensive first-principles study of stable stacking faults in hcp metals," *Acta Materialia*, vol. 123, pp. 223–234, Jan. 2017.

[167] A. Serra, R. Pond, and D. Bacon, "Computer simulation of the structure and mobility of twinning disclocations in H.C.P. Metals," *Acta Metallurgica et Materialia*, vol. 39, pp. 1469–1480, July 1991.

[168] P. Kwasniak, H. Garbacz, and K. Kurzydlowski, "Solid solution strengthening of hexagonal titanium alloys: Restoring forces and stacking faults calculated from first principles," *Acta Materialia*, vol. 102, pp. 304–314, Jan. 2016.

[169] D. Bacon, D. Barnett, and R. Scattergood, "Anisotropic continuum theory of lattice defects," *Progress in Materials Science*, vol. 23, pp. 51–262, Jan. 1980.

[170] M. M. Savin, V. M. Chernov, and A. M. Strokova, "Energy factor of dislocations in hexagonal crystals," *Physica Status Solidi (a)*, vol. 35, pp. 747–754, June 1976.

[171] A. Foreman, "Dislocation energies in anisotropic crystals," *Acta Metallurgica*, vol. 3, pp. 322–330, July 1955.

[172] A. Y. Lozovoi, D. L. Pashov, T. J. Sheppard, J. J. Kohanoff, and A. T. Paxton, "Universal tight binding model for chemical reactions in solution and at surfaces. III. Stoichiometric and reduced surfaces of titania and the adsorption of water," *The Journal of Chemical Physics*, vol. 141, p. 044505, July 2014.

[173] L. Goodwin, A. J. Skinner, and D. G. Pettifor, "Generating Transferable Tight-Binding Parameters: Application to Silicon," *Europhysics Letters (EPL)*, vol. 9, pp. 701–706, Aug. 1989.

[174] R. Wood, "The Lattice Constants of High Purity Alpha Titanium," *Proceedings of the Physical Society*, vol. 80, p. 783, Dec. 2002.

[175] E. S. Fisher and C. J. Renken, "Single-Crystal Elastic Moduli and the hcp → bcc Transformation in Ti, Zr, and Hf," *Physical Review*, vol. 135, pp. A482–A494, July 1964.

[176] C. Kittel, *Introduction to Solid State Physics*. Hoboken, NJ: Wiley, 8th ed ed., 2005.

[177] A. Tunde Raji, S. Scandolo, R. Mazzarello, S. Nsengiyumva, M. Härting, and D. Thomas Britton, "*Ab Initio* pseudopotential study of vacancies and self-interstitials in hcp titanium," *Philosophical Magazine*, vol. 89, pp. 1629–1645, July 2009.

[178] E. Hashimoto, E. A. Smirnov, and T. Kino, "Temperature dependence of the Doppler-broadened lineshape of positron annihilation in $\upalpha$-Ti," *Journal of Physics F: Metal Physics*, vol. 14, pp. L215–L217, Oct. 1984.

[179] P. Hidnert, "Thermal expansion of titanium," *Journal of Research of The National Bureau of Standards*, vol. 30, p. 5, 1943.

[180] P. Souvatzis, O. Eriksson, M. Katsnelson, and S. Rudin, "The self-consistent ab initio lattice dynamical method," *Computational Materials Science*, vol. 44, pp. 888–894, Jan. 2009.

[181] S. Kadkhodaei and A. Davariashtiyani, "Phonon-assisted diffusion in bcc phase of titanium and zirconium from first principles," *Physical Review Materials*, vol. 4, p. 043802, Apr. 2020.

[182] M. Ghazisaeidi and D. Trinkle, "Core structure of a screw dislocation in Ti from density functional theory and classical potentials," *Acta Materialia*, vol. 60, pp. 1287–1292, Feb. 2012.

[183] A. de Crecy, A. Bourret, S. Naka, and A. Lasalmonie, "High resolution determination of the core structure of $1/3\langle 11\,2\,0\rangle$ $\{10\,1\,0\}$ edge dislocation in titanium," *Philosophical Magazine A*, vol. 47, pp. 245–254, Feb. 1983.

[184] J. K. Burdett, T. Hughbanks, G. J. Miller, J. W. Richardson, and J. V. Smith, "Structural-electronic relationships in inorganic solids: Powder neutron diffraction studies of the rutile and anatase polymorphs of titanium dioxide at 15 and 295 K," *Journal of the American Chemical Society*, vol. 109, pp. 3639–3646, June 1987.

[185] H. Tang, H. Berger, P. Schmid, F. Lévy, and G. Burri, "Photoluminescence in TiO2 anatase single crystals," *Solid State Communications*, vol. 87, pp. 847–850, Sept. 1993.

[186] J. K. Dewhurst and J. E. Lowther, "High-pressure structural phases of titanium dioxide," *Physical Review B*, vol. 54, pp. R3673–R3675, Aug. 1996.

[187] S. J. Smith, R. Stevens, S. Liu, G. Li, A. Navrotsky, J. Boerio-Goates, and B. F. Woodfield, "Heat capacities and thermodynamic functions of TiO2 anatase and rutile: Analysis of phase stability," *American Mineralogist*, vol. 94, pp. 236–243, Feb. 2009.

[188] L.-c. Ming and M. H. Manghnani, "Isothermal compression of TiO_2 (Rutile) under hydrostatic pressure to 106 kbar," *Journal of Geophysical Research*, vol. 84, no. B9, p. 4777, 1979.

[189] T. Arlt, M. Bermejo, M. A. Blanco, L. Gerward, J. Z. Jiang, J. Staun Olsen, and J. M. Recio, "High-pressure polymorphs of anatase ${\mathrm{TiO}}_{2}$," *Physical Review B*, vol. 61, pp. 14414–14419, June 2000.

[190] J. Pascual, J. Camassel, and H. Mathieu, "Resolved Quadrupolar Transition in TiO2," *Physical Review Letters*, vol. 39, pp. 1490–1493, Dec. 1977.

[191] M. Ghazisaeidi and D. Trinkle, "Core structure of a screw dislocation in Ti from density functional theory and classical potentials," *Acta Materialia*, vol. 60, pp. 1287–1292, Feb. 2012.

[192] L. Zhang, D.-Y. Lin, H. Wang, R. Car, and W. E, "Active learning of uniformly accurate interatomic potentials for materials simulation," *Physical Review Materials*, vol. 3, p. 023804, Feb. 2019.

[193] T. Wen, R. Wang, L. Zhu, L. Zhang, H. Wang, D. J. Srolovitz, and Z. Wu, "Specialising neural network potentials for accurate properties and application to the mechanical response of titanium," *npj Computational Materials*, vol. 7, pp. 1–11, Dec. 2021.

[194] I. Betova, "Effect of potential on dissociative adsorption of water on titanium assessed by density functional theory calculations," *Computational Materials Science*, p. 9, 2020.

[195] M. Stancheva, B. Diawara, F. Lebreau, and M. Bojinov, "Multi-Scale Modeling of the Initial Stages of Anodic Oxidation of Titanium," *Journal of The Electrochemical Society*, vol. 161, no. 8, pp. E3188–E3195, 2014.

[196] L. Liang, *Ab Initio Simulation of Extended Defects of -Ti in Presence of Interstitial Atoms H O*. PhD thesis, Université Paris-Saclay,, Oct. 2016.

[197] F. R. N. Nabarro, "The theory of solution hardening," *Philosophical Magazine*, vol. 35, pp. 613–622, Mar. 1977.

[198] R. Labusch, "A Statistical Theory of Solid Solution Hardening," *physica status solidi (b)*, vol. 41, no. 2, pp. 659–669, 1970.

[199] D. Hull and D. J. Bacon, *Introduction to Dislocations*. Amsterdam Heidelberg: Butterworth Heinemann, Elsevier, 5. ed ed., 2011.

[200] G. A. Nematollahi, B. Grabowski, D. Raabe, and J. Neugebauer, "Multiscale description of carbon-supersaturated ferrite in severely drawn pearlitic wires," *Acta Materialia*, vol. 111, pp. 321–334, June 2016.

[201] A. Ishii, J. Li, and S. Ogata, ""Conjugate Channeling" Effect in Dislocation Core Diffusion: Carbon Transport in Dislocated BCC Iron," *PLoS ONE*, vol. 8, p. e60586, Apr. 2013.

[202] M. Monavari and M. Zaiser, "Annihilation and sources in continuum dislocation dynamics," *Materials Theory*, vol. 2, p. 3, Dec. 2018.

[203] D. Caillard, M. Rautenberg, and X. Feaugas, "Dislocation mechanisms in a zirconium alloy in the high-temperature regime: An in situ TEM investigation," *Acta Materialia*, vol. 87, pp. 283–292, Apr. 2015.

[204] G. Viswanathan, "Creep behaviour of Ti-6Al-2Sn-4Zr-2Mo: II. Mechanisms of deformation," *Acta Materialia*, vol. 50, pp. 4965–4980, Dec. 2002.

[205] G. B. Viswanathan, S. Karthikeyan, M. J. Mills, and R. W. Hayes, "Application of a modified jogged-screw model for creep of TiAl and α-Ti alloys," *Metallurgical and Materials Transactions A*, vol. 33, pp. 329–336, Feb. 2002.

[206] A. T. Paxton and C. Elsässer, "Analysis of a carbon dimer bound to a vacancy in iron using density functional theory and a tight binding model," *Physical Review B*, vol. 87, p. 224110, June 2013.

[207] B. deB Darwent, "Bond dissociation energies in simple molecules," Tech. Rep. NBS NSRDS 31, National Bureau of Standards, Gaithersburg, MD, 1970.

[208] D. E. Jiang and E. A. Carter, "Diffusion of interstitial hydrogen into and through bcc Fe from first principles," *Physical Review B*, vol. 70, p. 064102, Aug. 2004.

[209] V. V. Bulatov and W. Cai, *Computer Simulations of Dislocations*. No. 3 in Oxford Series on Materials Modelling, Oxford ; New York: Oxford University Press, 2006.

[210] W. Cai, V. V. Bulatob, J. Chang, J. Li, and S. Yip, "Periodic image effects in dislocation modelling," *Philosophical Magazine*, vol. 83, pp. 539–567, Jan. 2003.

[211] Z. M. Chen, M. Mrovec, and P. Gumbsch, "Atomistic aspects of 1/2<111> screw dislocation behavior in alpha-iron and the derivation of microscopic yield criterion," *Modelling and Simulation in Materials Science and Engineering*, vol. 21, p. 055023, June 2013.

[212] E. Clouet, S. Garruchet, H. Nguyen, M. Perez, and C. S. Becquart, "Dislocation interaction with C in α-Fe: A comparison between atomic simulations and elasticity theory," *Acta Materialia*, vol. 56, pp. 3450–3460, Aug. 2008.

[213] E. Clouet, C. Varvenne, and T. Jourdan, "Elastic modeling of point-defects and their interaction," *Computational Materials Science*, vol. 147, pp. 49–63, May 2018.

[214] Y. Hanlumyuang, P. Gordon, T. Neeraj, and D. Chrzan, "Interactions between carbon solutes and dislocations in bcc iron," *Acta Materialia*, vol. 58, pp. 5481–5490, Sept. 2010.

[215] R. Douthwaite and J. Evans, "Interaction between a tetragonal distortion and a $\langle 111 \rangle$ screw dislocation in an anisotropic cubic crystal," *Scripta Metallurgica*, vol. 7, pp. 1019–1026, Oct. 1973.

[216] R. Kapoor, "Huang diffuse scattering from interstitials in an hcp lattice," *Pramana*, vol. 14, pp. 209–217, Mar. 1980.

[217] R. Veiga, M. Perez, C. Becquart, E. Clouet, and C. Domain, "Comparison of atomistic and elasticity approaches for carbon diffusion near line defects in α-iron," *Acta Materialia*, vol. 59, pp. 6963–6974, Oct. 2011.

[218] L. Scotti and A. Mottura, "Interstitial diffusion of O, N, and C in α -Ti from first-principles: Analytical model and kinetic Monte Carlo simulations," *The Journal of Chemical Physics*, vol. 144, p. 084701, Feb. 2016.

[219] S. K. Nayak, C. J. Hung, V. Sharma, S. P. Alpay, A. M. Dongare, W. J. Brindley, and R. J. Hebert, "Insight into point defects and impurities in titanium from first principles," *npj Computational Materials*, vol. 4, pp. 1–10, Mar. 2018.

[220] D. Connétable, J. Huez, É. Andrieu, and C. Mijoule, "First-principles study of diffusion and interactions of vacancies and hydrogen in hcp-titanium," *Journal of Physics: Condensed Matter*, vol. 23, p. 405401, Oct. 2011.

[221] C. S. Hartley and Y. Mishin, "Representation of dislocation cores using Nye tensor distributions," *Materials Science and Engineering: A*, vol. 400-401, pp. 18–21, July 2005.

[222] P. Zhang and D. R. Trinkle, "A modified embedded atom method potential for interstitial oxygen in titanium," *Computational Materials Science*, vol. 124, pp. 204–210, Nov. 2016.

[223] D. A. Aksyonov, T. Hickel, J. Neugebauer, and A. G. Lipnitskii, "The impact of carbon and oxygen in alpha-titanium: *Ab Initio* study of solution enthalpies and grain boundary segregation," *Journal of Physics: Condensed Matter*, vol. 28, p. 385001, Sept. 2016.

[224] A. Voskamp, "Fatigue and Material Response in Rolling Contact," in *Bearing Steels: Into the 21st Century* (J. Hoo and W. Green, eds.), pp. 152–152–15, 100 Barr Harbor Drive, PO Box C700, West Conshohocken, PA 19428-2959: ASTM International, Jan. 1998.

[225] A. P. Voskamp and E. J. Mittemeijer, "State of residual stress induced by cyclic rolling contact loading," *Materials Science and Technology*, vol. 13, pp. 430–438, May 1997.

[226] I. Polonsky, "On white etching band formation in rolling bearings," *Journal of the Mechanics and Physics of Solids*, vol. 43, pp. 637–669, Apr. 1995.

[227] R. Österlund and O. Vingsbo, "Phase changes in fatigued ball bearings," *Metallurgical Transactions A*, vol. 11, pp. 701–707, May 1980.

[228] N. Mitamura, H. Hidaka, and S. Takaki, "Microstructural Development in Bearing Steel during Rolling Contact Fatigue," *Materials Science Forum*, vol. 539-543, pp. 4255–4260, Mar. 2007.

[229] A. P. Voskamp, R. Österlund, P. C. Becker, and O. Vingsbo, "Gradual changes in residual stress and microstructure during contact fatigue in ball bearings," *Metals Technology*, vol. 7, pp. 14–21, Jan. 1980.

[230] S. Hashemi, "Strength–hardness statistical correlation in API X65 steel," *Materials Science and Engineering: A*, vol. 528, pp. 1648–1655, Jan. 2011.

[231] H. K. D. H. Bhadeshia, "Solution to the Bagaryatskii and Isaichev ferrite–cementite orientation relationship problem," *Materials Science and Technology*, vol. 34, pp. 1666–1668, Sept. 2018.

[232] L. Ventelon, B. Lüthi, E. Clouet, L. Proville, B. Legrand, D. Rodney, and F. Willaime, "Dislocation core reconstruction induced by carbon segregation in bcc iron," *Physical Review B*, vol. 91, p. 220102, June 2015.

[233] M. Itakura, H. Kaburaki, M. Yamaguchi, and T. Okita, "The effect of Hydrogen atom on the Screw Dislocation Mobility in BCC Iron: A First-Principles Study," *arXiv:1304.0602 [cond-mat]*, Aug. 2013.

[234] E. Clouet, L. Ventelon, and F. Willaime, "Dislocation Core Energies and Core Fields from First Principles," *Physical Review Letters*, vol. 102, p. 055502, Feb. 2009.

[235] G. Tréglia, B. Legrand, F. Ducastelle, A. Saúl, C. Gallis, I. Meunier, C. Mottet, and A. Senhaji, "Alloy surfaces: Segregation, reconstruction and phase transitions," *Computational Materials Science*, vol. 15, pp. 196–235, June 1999.

[236] D. McLean and A. Maradudin, "*Grain Boundaries in Metals*," *Physics Today*, vol. 11, pp. 35–36, July 1958.

[237] S. Morito, J. Nishikawa, and T. Maki, "Dislocation Density within Lath Martensite in Fe-C and Fe-Ni Alloys," *ISIJ International*, vol. 43, no. 9, pp. 1475–1477, 2003.

[238] P. Gong, I. H. Katzarov, J. Nutter, A. T. Paxton, and W. M. Rainforth, "The influence of hydrogen on plasticity in pure iron—theory and experiment," *Scientific Reports*, vol. 10, p. 10209, Dec. 2020.

[239] B. Berne, G. Ciccotti, and D. Coker, *Classical and Quantum Dynamics in Condensed Phase Simulations: Proceedings of the International School of Physics*. World Scientific Publishing Company, 1998.

[240] D. E. Jiang and E. A. Carter, "Carbon dissolution and diffusion in ferrite and austenite from first principles," *Physical Review B*, vol. 67, p. 214103, June 2003.

[241] C. Wert and C. Zener, "Interstitial Atomic Diffusion Coefficients," *Physical Review*, vol. 76, pp. 1169–1175, Oct. 1949.

[242] Y. Lu, F. Zheng, and P. Zhang, "First-principles study of temperature-dependent diffusion coefficients for helium in α-Ti," *Journal of Applied Physics*, vol. 114, p. 153507, Oct. 2013.

[243] D. G. Pettifor, D. L. Weaire, M. Cardona, P. Fulde, K. von Klitzing, and H.-J. Queisser, eds., *The Recursion Method and Its Applications*, vol. 58 of *Springer Series in Solid-State Sciences*. Berlin, Heidelberg: Springer Berlin Heidelberg, 1987.

[244] M. W. Finnis, K. L. Kear, and D. G. Pettifor, "Interatomic Forces and Phonon Anomalies in bcc $3d$ Transition Metals," *Physical Review Letters*, vol. 52, pp. 291–294, Jan. 1984.

[245] I. Schnell, M. D. Jones, S. P. Rudin, and R. C. Albers, "Tight-binding calculations of the elastic constants and phonons of hcp Zr: Complications due to anisotropic stress and long-range forces," *Physical Review B*, vol. 74, p. 054104, Aug. 2006.

[246] C. Becquart, J. Raulot, G. Bencteux, C. Domain, M. Perez, S. Garruchet, and H. Nguyen, "Atomistic modeling of an Fe system with a small concentration of C," *Computational Materials Science*, vol. 40, pp. 119–129, July 2007.

[247] W. Spitzig and A. Keh, "Orientation dependence of the strain-rate sensitivity and thermally activated flow in iron single crystals," *Acta Metallurgica*, vol. 18, pp. 1021–1033, Sept. 1970.

[248] F. Maresca, D. Dragoni, G. Csányi, N. Marzari, and W. A. Curtin, "Screw dislocation structure and mobility in body centered cubic Fe predicted by a Gaussian Approximation Potential," *npj Computational Materials*, vol. 4, p. 69, Dec. 2018.

[249] B. Lüthi, F. Berthier, L. Ventelon, B. Legrand, D. Rodney, and F. Willaime, "*Ab Initio* thermodynamics of carbon segregation on dislocation cores in bcc iron," *Modelling and Simulation in Materials Science and Engineering*, vol. 27, p. 074002, Oct. 2019.

[250] G. Henkelman, A. Arnaldsson, and H. Jónsson, "Theoretical calculations of CH4 and H2 associative desorption from Ni(111): Could subsurface hydrogen play an important role?," *The Journal of Chemical Physics*, vol. 124, p. 044706, Jan. 2006.

[251] A. Kraych, E. Clouet, L. Dezerald, L. Ventelon, F. Willaime, and D. Rodney, "Non-glide effects and dislocation core fields in BCC metals," *npj Computational Materials*, vol. 5, pp. 1–8, Nov. 2019.

[252] R. Gröger and V. Vitek, "Explanation of the discrepancy between the measured and atomistically calculated yield stresses in body-centred cubic metals," *Philosophical Magazine Letters*, vol. 87, pp. 113–120, Feb. 2007.

[253] D. Caillard, "Kinetics of dislocations in pure Fe. Part I. In situ straining experiments at room temperature," *Acta Materialia*, vol. 58, pp. 3493–3503, May 2010.

[254] J. da Silva and R. B. McLellan, "Diffusion of carbon and nitrogen in B.C.C. iron," *Materials Science and Engineering*, vol. 26, pp. 83–87, Nov. 1976.

[255] A. Ramasubramaniam, M. Itakura, M. Ortiz, and E. Carter, "Effect of atomic scale plasticity on hydrogen diffusion in iron: Quantum mechanically informed and on-the-fly kinetic Monte Carlo simulations," *Journal of Materials Research*, vol. 23, pp. 2757–2773, Oct. 2008.

[256] L. Casillas-Trujillo, D. Gambino, L. Ventelon, and B. Alling, "Screw dislocation core structure in the paramagnetic state of bcc iron from first-principles calculations," *Physical Review B*, vol. 102, p. 094420, Sept. 2020.

[257] P. Maugis and D. Kandaskalov, "Revisiting the pressure effect on carbon migration in iron," *Materials Letters*, vol. 270, p. 127725, July 2020.

[258] H. Yoshinaga and S. Morozumi, "The solute atmosphere round a moving dislocation and its dragging stress," *The Philosophical Magazine: A Journal of Theoretical Experimental and Applied Physics*, vol. 23, pp. 1367–1385, June 1971.

[259] A. P. Horsfield, M. Boleininger, R. D'Agosta, V. Iyer, A. Thong, T. N. Todorov, and C. White, "Efficient simulations with electronic open boundaries," *Physical Review B*, vol. 94, p. 075118, Aug. 2016.

[260] D. Rodney and L. Proville, "Stress-dependent Peierls potential: Influence on kink-pair activation," *Physical Review B*, vol. 79, p. 094108, Mar. 2009.

Appendix A

Estimation of jog width from oxygen-induced cross-slip

One has approximated here that the jogs on the screw dislocation are straight and of no width. This is not the case in reality. There will be a width to the jogs of a few atomic spacings, and if the width is very wide, then the elastic analysis of oxygen binding to a straight edge segment becomes less applicable to the case of jogs on a screw dislocation. We can approximately calculate the width of the jogs to determine if the approximation of straightness is reasonable, using a line-tension model. Assuming a constant line-tension with angular variation, we can determine the width of the jogs from the exact same analysis as that for the kink width from a line-tension model [7]

$$w \approx b\sqrt{\frac{T}{2E_{\mathrm{P}}}}, \tag{A.1}$$

where w is the kink width, T is the line-tension and E_{P} is the value of the Peierls potential, which is dependent on the glide plane. The line tension T can be estimated from the dislocation line energy $T = E_{\mathrm{elastic}} + E_{\mathrm{core}}$ [260], it can also be estimated by calculation finite difference methods in atomistic simulation [76]. The elastic term can be estimated by use of the anisotropic prelogarithmic factors, and the standard equation $E_{\mathrm{elastic}} = b^i K_{ij} b^j \ln R/r_{\mathrm{c}}$. The core radius, r_{c} was taken to be the dislocation half-width as above. The radius, R of the dislocation was arbitrarily taken to be $12b$, as in Rodney *et al.* [260]. The Peierls potential was simply taken to be the stable stacking fault energy for that particular plane, which is therefore underestimated by a neglect of the dislocation core energy, as would be apparent in the true Peierls energy landscape of the dislocation. The core energy in the above equation for T is not able

to be accounted for without explicit atomistic simulation of the dislocation, and is a large source of error in the estimation of T, as evidenced in the paper of Rodney *et al.* [7, 260]. As the Peierls potential on the basal plane is much higher than that on the prismatic plane, as evidenced by unstable basal cores in DFT calculations [131], one may expect that the width of the kink on the basal plane is much smaller than on the π_1 plane. However one finds, using purely an elastic analysis, that widths are, from the *sd*-model, $w_{\text{basal}}^{\text{sd-TB}} = 3.10b$, $w_{\pi_1}^{\text{sd-TB}} = 1.50b$ and $w_{\text{pris.}}^{\text{sd-TB}} = 3.33b$, and from Curtin *et al.* DFT [166], one finds $w_{\text{basal}}^{\text{DFT}} = 2.47b$, $w_{\pi_1}^{\text{DFT}} = 2.56b$ and $w_{\text{pris.}}^{\text{DFT}} = 3.16b$. These widths are very narrow compared to that of screw dislocations in iron which are around $10b$ [76, 107], but comparable to those in aluminium [260], estimated from EAM potentials. Therefore the approximation of a straight jog/kink is not unreasonable, and the binding energy analysis by elasticity becomes more accurate as oxygen undergoes migration events to the jog, until it migrates a distance of $w/2$ to the centre of the jog, which is straight.

Appendix B

Regularisation of interaction energy in quadrupolar array

In isotropic elasticity, the elastic energy of a single dislocation dipole in an infinite lattice is given by

$$E_{\mathrm{el}}^{\infty} = \frac{\mu b^2}{4\pi} \ln\left(\frac{r}{r_c}\right)$$

The contribution from periodic images to the correction is

$$E_{\mathrm{img}} = E_{\mathrm{el}}(\mathbf{a}, \mathbf{c}_i, r_c) - E_{\mathrm{el}}^{\infty}(\mathbf{a}, r_c),$$

"Ghost" dipoles are introduced to account for the conditional convergence of the sum at $\pm\alpha\mathbf{b}$ and $\pm\beta\mathbf{b}$, where $\alpha = \beta = 0.5$. We define $E_{\mathrm{dg}}(\mathbf{R})$ as the interaction energy of a ghost dislocation and a dipole at $\mathbf{R}$ anisotropic elasticity equations as shown in [210].

Defining,

$$E_{\mathrm{dd}}(\mathbf{R}) = \frac{\mu b^2}{2\pi} \ln \frac{|\mathbf{R}|^2}{|\mathbf{R}+\mathbf{a}| \cdot |\mathbf{R}-\mathbf{a}|},$$

we obtain,

$$E_{\mathrm{img}} = \frac{1}{2} \sum_{\mathbf{R}} [E_{\mathrm{dd}}(\mathbf{R}) - E_{\mathrm{dg}}(\mathbf{R})] - \frac{1}{2} E_{\mathrm{dg}}(\mathbf{R} = 0),$$

which can be subtracted from the total energy as given from atomistic calculations, for a regularised interaction energy.

Appendix C

Zero-point energy calculation

After relaxation of the C-dislocation system, a 3x3 Hessian matrix is constructed by taking the numerical derivative of forces observed on the carbon atom after displacement by ± 0.015Å in each of the X, Y and Z directions. The three atoms surrounding the core on the first and third layers were again fixed in Z coordinate. The zero-point energy is given by

$$E_z = \frac{1}{2} \sum_{i=1}^{3} \frac{h}{2\pi} \sqrt{k_i / m_{\mathrm{C}}},$$

where k_i are the eigenvalues of the Hessian and m_{C} is the mass of carbon.

Appendix D

Smooth mapping of sites in equilibrium line-tension model

To approximate the position of trap sites upon dislocation movement, the x-coordinate of the dislocation core position, P_x, was used to obtain the trap site positions around the core.

Focussing on one half of the the path of a dislocation between peierls valleys, the segment of a dislocation going between an easy core to hard core, one can define forward and backwards paths, a dislocation travelling from the easy core towards the hard core, and vice versa. The trap sites at the end points are well-defined: when $P_x = P_x^{\text{easy}} = 0$, the trap sites are exactly those found upon relaxation of the easy core, similarly, when $P_x = P_x^{\text{hard}} = a\sqrt{2}/(2\sqrt{3}) = d$, the trap sites are those found upon relaxation of the hard core. These positions can be seen in section 5.3.3.

One can define trap site mappings for these forward and backwards paths: for an easy core site to a hard core site, $E_j^\alpha \to H_k^\beta$, and from hard core to easy core $H_l^\gamma \to E_m^\delta$, where j, k, l, m denote a particular trap site position, with labels defined in section 5.3.3 and $\alpha, \beta, \gamma, \delta$ are labels which denote which of the six possible sectors the site belongs to. These six sectors arise from the combination of the three-fold rotational and reflection symmetry found in the crystal—thus one need only have the trap sites for one sector and apply the appropriate rotation and/or reflection to obtain the necessary trap site position at the given endpoint. These mappings are not symmetric for the forward and backwards paths, *e.g.* are many easy core trap sites which map to the H1 site, due to its strong binding energy, as found in atomistic simulations of reconstruction, but, quite clearly, these mappings

For a given mapping, one can linearly interpolate between the two positions to give

a trap site position for an intermediate dislocation core.

$$P_{j,k}^{\text{trap forward}}(P_x) = \left(1 - \frac{P_x}{d}\right) E_j^{\alpha} + \frac{P_x}{d} H_k^{\beta},$$

$$P_{l,m}^{\text{trap backward}}(P_x) = \left(1 - \frac{P_x}{d}\right) E_m^{\delta} + \frac{P_x}{d} H_l^{\gamma}.$$

To define trap site mappings for core positions at $P_x > d$, one need only swap the forward for the backwards path, due to reflection symmetry about $P_x = d$, thus allowing for well defined trap sites for all core positions between the peierls valleys. This can be seen in the kink-pair formation of the canonical-d tight-binding model in figure D.1.

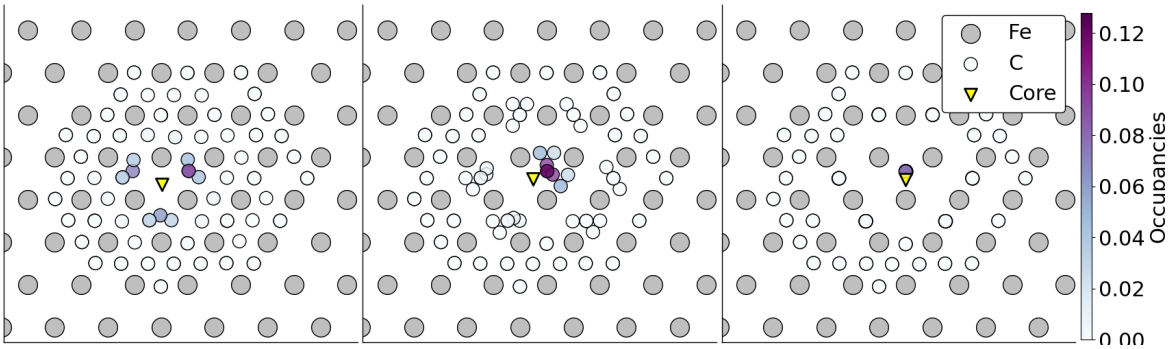

Fig. D.1: Positions of trap sites around dislocation segments upon kink-pair formation at a nominal carbon concentration of 30 appm. Path only shown to the hard core to demonstrate smooth mapping of trap sites going from easy to hard core. Equilibrium occupancies shown by coloured circles.